COLLEGE DOCTORAL PAYS DE LA LOIRE
ED MATIERE,MOLECULES MATERIAUX ET GEOSCIENCES

université angers

Thèse de doctorat

De
L'UNIVERSITÉ D'ANGERS
Sous le sceau de
LA COMUE ANGERS – LE MANS

ECOLE DOCTORALE N° 596
Matière, Molécules, Matériaux et Géosciences
Spécialité : Chimie moléculaire et macromoléculaire

Par

Federica SOLANO

Functionalized BVDT-TTF for electro-active coordination polymers and molecular conductors

Thèse présentée et soutenue à Angers, le 06/12/23

Unité de recherche : Laboratoire MOLTECH-Anjou – CNRS UMR 6200

Rapporteurs avant soutenance :

Stéphane Baudron — Directeur de Recherche CNRS, Université de Strasbourg
Aude Demessence — Chargée de Recherche CNRS, Université de Lyon

Composition du Jury :

Examinateurs : Marc Salle — Professeur, Université d'Angers
Maria Laura Mercuri — Professeure, Université de Cagliari

Dir. de thèse : Narcis Avarvari — Directeur de Recherche CNRS, Université d'Angers
Co-dir. de thèse : Nicolas Zigon — Maître de Conférences, Université d'Angers

Acknowledgements

I would like to express my gratitude to the director of the Moltech Anjou laboratory, Dr. Philippe Blanchard, where I had the chance to do my thesis.

I want to express my gratitude to my supervisor, Dr. Narcis Avarvari for allowing me to be part of the CIMI team. Thank you for your availability and guidance. Working with such a compassionate and enthusiastic mentor has ignited a profound passion for science in me, growing into an unstoppable curiosity and dedication.

I would like to express my gratitude to my co- supervisor, Dr. Nicolas Zigon, for his guidance, unwavering support, and the kindness he demonstrated during these last few years. I am thankful for his exceptional patience. I look up to you for inspiration in spirit, humility, and expertise.

Special thanks should be given to our collaborators for their aid, without it this project would have proved impossible to complete:
Dr. Enric Canadell (ICMAB, Spain), Dr. Pere Alemany (University of Barcelona, Spain) and Dr. Pascale Auban-Senzier (LPS, Université d'Orsay). Thanks to Dr. Iwona Olejniczak, Dr. Bolesław Barszcz and Dr. Arek Frąckowiak (Institute of Molecular Physics Polish Academy of Sciences, Poznań, Poland) for graciously welcoming me into their institute, teaching me the Raman technique, showcasing the beauty of Poland, and for their kindness and warmth.

I would like to express my gratitude to the CIMI group, Dr. Nicolas Mercier, Dr. Abdelkrim El-Ghayoury, Dr. Thomas Cauchy, Dr. Marie-Claire Dul, Dr. Flavia Pop, Dr. Alexandre Abhervé, Dr. Ryota Nakajima, Clémence Cazals, Axel Houssin, Alla Skorokhod, Dr. Maroua Ben Haj Salah, Dr. Faten Hleli and Dr. Alexandra Bodgan for warmly welcoming me and seamlessly integrating me into the team.
In particular:
To Dr. Ingrid Freuze, Cécile Mézière, and Dr. Magali Allain for being always available to assist me in comprehending MS and electrocrystallization experiments and crystallography.
To Dr. Yohan Cheret for sharing an office and laboratory with me over these years. Without your support and shared laughter, the days would have felt much longer. Thank you for being a friend before being a colleague.
To my Italian team, Dr. Maurizio Mastropasqua and Fabio Manna for making me feel less homesick (and for treating me to delicious Italian meals).
To Dr. Nataliya Plyuta for always being there during the good and challenging days, which we overcome by sharing laughter over our misadventures.
To Yuliia Oleksii for the complicity and for making my coffee breaks sweeter.

I am very thankful to every member in the Moltech Anjou laboratory, for the nice atmosphere they created in this place.
In particular:
To Dr. Slava Shkirskiy for being by my side throughout. I will forever remember our walks from work to home, with the break on the bench by the river, enjoying a beer along the way.
To Aline Makhloutah and Dr. Julien Billon for welcoming me into the French-Lebanese culture. I will never forget our wonderful moments spent together.
To Dario Puchan and Chloé Billiaux for experiences, memories and laughter that will forever stay imprinted within me.
To Dr. Clement Drou, Dr. Anna Popczyk, Tatiana Ghanem, Soussana Azar, Elie Bou Rahhal, Louis Hardoin, Korentin Morice, Dr. Youssef Aidibi, Kelvine Letellie, Dr. Pierre Josse, Khaled Youssef, Dr. Oksana Kharchenko, Dr. Augustin Ayoub and Dr. Fanny Peigneguy for being wonderful companions and gifting me many smiles.

I would like to express my gratitude to Dr. Claudio Fontanesi, Dr. Agnese Giacomino and Dr. Paolo Inaudi for encouraging me to embark on this new adventure.

Thanks to Dr. Carlotta Tornaturi, I was incredibly lucky to find a great Italian friend in the heart of France. Thanks to Arianna Tiozzo for always being on the same wavelength with me despite the kilometers of distance.

And finally, I want to thank my entire family for supporting and encouraging my choices.

SUMMARY

LIST OF FIGURES AND TABLES

ABBREVIATIONS AND SYMBOLS

GENERAL INTRODUCTION

CHAPTER I: TETRATHIAFULVALENE: DONOR AND LIGAND

1. Tetrathiafulvalene: structure, properties, applications 2
1.1. Structure, generalities and properties 2
1.2. Applications 4
2. Alkylthio-tetrathiafulvalenes (RS)nTTF 7
2.1. Synthesis of functionalized TTF and $(RS)_nTTF$ 7
2.2. Synthesis of Substituted BEDT-TTF 11
2.3. Properties of electron-withdrawing substituents on TTF 12
2.4. Properties of Alkylthio tetrathiafulvalenes $(RS)_nTTF$ 13
3. Electrocrystallization 14
3.1. Definition, principles 14
3.2. Electrocrystallization of $(RS)_nTTFs$ 16
3.3. Electrocrystallization of BEDT-TTF 17
3.4. Synthesis and electrocrystallization of BVDT-TTF 24
4. Metal Organic Framework, MOFs 26
4.1. Definition, properties 26
4.2. Applications 32
4.3. Conductivity in MOFs 34
4.4. TTF as ligand for conductive MOFs 38
4.5. BVDT-TT as ligand for electro-active MOFs 41

CHAPTER II: SYNTHESIS OF FUNCTIONALIZED BVDT-TTF

1. Electro-active MOFs : ligand design 42
2. Synthetic strategy for a direct functionalization of the BVDT-TTF 44
2.1. Synthesis of BVDT-TTF and functionalized BVDT-TTF in prior studies 44
2.2. Transition-metal-catalyzed direct C–H arylation of BVDT-TTF with aryl halides 47
2.3. Lithiation/Iodination of VDT 49
2.4. Synthesis of methyl 4-((2-thioxo-[1,3]dithiolo[4,5-b][1,4]dithiin-5-yl)ethynyl)benzoate 50
2.5. Synthesis of BVDT-TTF $(Dipicolinic\ acid)_4$ 52
2.6. Tetrabromo(dibenzodithio)tetrathiafulvalene 57
2.7. Diiododibenzoate(dibenzodithio)tetrathiafulvalene 59
3. Conclusions 61

CHAPTER III : SYNTHESIS AND STUDIES OF COORDINATION NETWORKS BASED ON ELECTROACTIVE LIGANDS

1. Electroactive MOFs based on TTF 62
2. BVDT-TTF-Py_4 as a ligand for electroactive MOFs 63
2.1. Synthesis of BVDT-TTF-Py_4 64
3. Isostructural MOFs containing Hg(II), Cu(II), Cd(II), Zn(II) and BVDT-TTF-Py_4 66
3.1. Synthesis and structure of MOFs 66
3.2. Solid state voltammetry 69
3.3. Post-synthetic Oxidation 73
3.4. Structure of BVDT-TTF-$Py_4{}^{\bullet+}CdCl_2\ I_3^-$ 74
3.5. Band structure calculations 75
3.6. Powder X-ray Diffraction (PXRD) 79
3.7. Raman measurements: comparison between neutral and oxidised MOFs 80
3.8. Conductivity measurements: comparison between neutral and oxidised MOFs 85
4. BVDT-TTF-Py_4-$[CuCl_2]_2$ 86

4.1. Synthesis and structure 86
4.2 Post-synthetic Oxidation 88
4.3 Powder X-ray Diffraction (PXRD) 88
4.4 Thermogravimetric analysis (TGA) 89
4.5 Solid state voltammetry 90
4.6 Raman measurements 91
4.7 Conductivity measurements 93
4.8 Ligand exchange in BVDT-TTF-Py_4-$[CuCl_2]_2$ 94
5 TTF(isophthalic acid)$_4$ as ligand for electroactive MOF 96
5.1 Synthesis and properties of H_8TTFOC 97
5.2 Synthesis and structure of Zn_2-TTFOC 99
5.3 Synthesis and structure of Ni_3-TTFOC 101
5.4 Synthesis and structure of Cu_3-TTFOC 103
2. Conclusion 105

CHAPTER IV: BVDT-TTF AND EVT-TTF AS ORGANIC DONORS

1. BVDT-TTF and EVT-TTF salts 107
2. (BVDT-TTF)(TaF_6) 109
2.1. Crystal structure description 109
2.2. Conductivity measurement 111
2.3. Band structure calculations 111
3. (BVDT-TTF)$_{2.5}$ (I_3) 113
3.1. Crystal structure description 113
3.2. Conductivity measurement 114
3.3. Band structure calculations 115
4. (BVDT-TTF)$_2$(ReO_4) 117
4.1. Crystal structure 117
4.2. Conductivity measurement 119
5. EVT-TTF 119
5.1. Synthesis and properties 119
5.2. (EVT-TTF)(ClO_4) crystal structure description 122
5.3. Conductivity measurement 124
5.4. Band structure calculations 125
6. Raman measurements 126
7. Conclusions 132

GENERAL CONCLUSION AND PERSPECTIVES

EXPERIMENTAL SECTION

1. General Information 136
1.1. NMR spectra 136
1.2. Mass spectra 136
1.3. Elemental Analyses 136
1.4. Cyclic voltammetry 136
1.5. Solid state cyclic voltammetry 136
1.6. X-Ray Diffraction 137
1.7. Single Crystal Conductivity Measurements 137
1.8. Raman measurements 137
1.9. Computational methods 138
1.10. Band structure calculations 138
2. Experimental Procedures 140
3. Crystallographic Data 154

List of Figures and Tables

Figure 1- 1. TTF structure 2
Figure 1- 2. TTF, radical cation and dication species and their geometries 3
Figure 1- 3. Applications of TTFs. 4
Figure 1- 4. Push-pull chromophores based on TTF. 5
Figure 1- 5. Tetrakis-TTF-calix[4]pyrrole and the two distinct conformers assuming in the presence and absence of an anion. 6
Figure 1- 6. Biscondensation of 1,2-Dichalcogenolates with Tetrachloroethylene 7
Figure 1- 7. Second strategy for substituted TTFs 8
Figure 1- 8. Mechanism of phosphite coupling (II e) 9
Figure 1- 9. Lithiation of the TTF molecule followed by reaction with electrophilic agents 10
Figure 1- 10. Synthesis of 2,3,6,7-Tetrakis(2'-cyanoethylthio)tetrathiafulvalene followed by deprotection and alkylation to afford on $(RS)_n$TTF 11
Figure 1- 11. Synthesis pathway of substituted BEDT- TTF 11
Figure 1- 12. MOs of DN-TTF, DA-TTF, and DTet-TTF.[36] 12
Figure 1- 13. Configuration of an electrocrystallization cell and the crystals of radical cation salts obtained on the electrode. 15
Figure 1- 14. Salts stoichiometry. 15
Figure 1- 15. Main packing.[45] 16
Figure 1- 16. (TMT-TTF)I_3 packing diagram. 17
Figure 1- 17. BEDT-TTF structure. 17
Figure 1- 18. Different packing types of BEDT-TTF salts. 18
Figure 1- 19. $(BEDT\text{-}TTF)_2(ClO_4)$ packing diagram. 19
Figure 1- 20. $(BEDT\text{-}TTF)_2(ReO_4)$ packing diagram. 19
Figure 1- 21. "Corrugated sheet" network of β-$(BEDT\text{-}TTF)_2I_3$ and the interstack S···S contacts and temperature dependence of the conductivity of β-$(BEDT\text{-}TTF)_2I_3$. 20
Figure 1- 22. $(BEDT\text{-}TTF)_2Cu(SCN)_2$ showing donor stacking and a view of the κ-phase. 21
Figure 1- 23. Intermolecular S···S contact between neighbouring stacks of β-$(BEDT\text{-}TTF)_2PF_6$. 22
Figure 1- 24. δ-m $(BEDT\text{-}TTF)_2TaF_6$ (**a**) and the δ-o $(BEDT\text{-}TTF)_2TaF_6$ phase (**b**). 23
Figure 1- 25. Intermolecular S···S distances of $(BEDT\text{-}TTF)_2(TaF_6)_2CH_2Cl_2$.[67] 23
Figure 1- 26. BVDT-TTF structure. 24
Figure 1- 27. Pathways for the synthesis of BVDT-TTF. 25
Figure 1- 28. BVDT-TTF_2PF_6 along c axis. 25
Figure 1- 29. Synthesis of MOFs. 27
Figure 1- 30. Levels of construction in MOFs. 27
Figure 1- 31. Hofmann network: $Ni(CN)_2(NH_3)\cdot C_6H_6$. 28
Figure 1- 32. $Cd(HMDA)Ni(CN)_4(C_7H_9N)$ 29

Figure 1- 33. a) coordination ligand-metal cluster b) cavities in the MOF-5 framework. 30
Figure 1- 34. a) metal exchange b) metal incorporation c) ligand exchange d) ligand installation e) ligand removal f) guest inclusion within the pores.[98].....32
Figure 1- 35. Asymmetric alkyl- and alkynylzinc additions catalyzed by the CMOF/Ti-BINOLate catalyst within large open channels.[105] 33
Figure 1- 36. Electronic structures of a generic insulator, semiconductor, and metal. 34
Figure 1- 37. Poor electronic communication between the interface of the inorganic and organic regions and the resulting electronic band structure.[108].....35
Figure 1- 38. Pathways for conductive MOFs.[119] 37
Figure 1- 39. a) Helical stacking of TTF cores with S···S distances contact, b) 1D channels parallel to the stacking direction. 39
Figure 1- 40. Calculated band structure and projected density of states of Zn_2(TTFTB).[122] 39
Figure 1- 41. 3D network of Fe(dca)[TTF(py)$_4$](ClO_4) before and after insertion.[123] 40
Figure 1- 42. Overview of TTF, BEDT-TTF and BVDT-TTF as building blocks. 41

Table 1- 1. $E1/2$ of TTF, Tetrakis(methylthio)tetrathiafulvalene TMT-TTF and BEDT-TTF, conductivity and charge transfer values in TCNQ salts. 14
Table 1- 2. Charge transfer complexes. 26
Table 1- 3. Correlation between ionic radius of metals and S···S distance of TTF filaments. 38

Figure 2- 1. Construction of MOFs based on BVDT-TTF building block. 43
Figure 2- 2. Target BVDT-TTF tetrabenzoic acid. 44
Figure 2- 3. Synthesis of BVDT-TTF molecules with fused thiophene and 1,4-dithiin rings. 45
Figure 2- 4. Synthesis of tetraphenyl-BVDT-TTF. 45
Figure 2- 5. Synthesis of BVDT-TTF. 46
Figure 2- 6. Cyclic voltammetry of a **5** solution 10^{-3} M, $TBAPF_6$ 0.1M in DCM. Platinum electrode as WE, platinum wire as CE and an Ag/AgCl/Saturated KCl electrode as RE at scan rate 20/50/100 $mV \cdot cm^{-1}$. Values were converted with respect to the standard calomel electrode (SCE). 47
Figure 2- 7. Protocol for direct C–H arylation on TTF. 48
Figure 2- 8. Protocol for direct C–H arylation on BVDT-TTF. 48
Figure 2- 9. X-ray structure of the undesired product: dimethyl 4,4'-thiodibenzoate. 49
Figure 2- 10. Possible mechanism for 1,4-dithiin ring rearrangement. 49
Figure 2- 11. Pd-catalyzed cross-coupling reactions. 49
Figure 2- 12. Lithiation-iodination of compound **3**. 50
Figure 2- 13. Suzuki-Miyaura coupling between **6** and (4-(methoxycarbonyl)phenyl)boronic acid. 51
Figure 2- 14. Main condition used for Suzuki-Miyaura coupling. 51
Figure 2- 15. Sonogashira cross-coupling reaction. 51
Figure 2- 16. MUV-5 networks.[39] 53
Figure 2- 17. BVDT-TTF (Dipicolinic acid)$_4$, **13**. 54

Figure 2- 18. Synthesis of BVDT-TTF (Dipicolinic acid)$_4$ **13**.....54
Figure 2- 19. Cyclic voltammetry of a solution of **12** (10^{-3} M, $TBAPF_6$ 0.1M in DCM). Platinum electrode as WE, platinum wire as CE and an Ag/AgCl/Saturated KCl electrode as RE at scan rate 20/50/100 mV·cm^{-1}. Values were converted with respect to SCE electrode. 55
Figure 2- 20. Metals and reaction conditions to synthetize MOFs using BVDT-TTF (Dipicolinic acid)$_4$ **13** as ligand. 56
Figure 2- 21. Cu_2O-catalyzed C–S coupling between aryl iodides and zincate salt as reported by Sun et al. 57
Figure 2- 22. BVDT-TTF bisphenyl-tetrabenzoic acid. 57
Figure 2- 23. Cu_2O-catalyzed C–S coupling between aryl bromide and zincate salt. 58
Figure 2- 24. Pathway for the synthesis of tetrabromo(dibenzodithio)tetrathiafulvalene **18**. 58
Figure 2- 25. Catalyst and substrates for Suzuki-Miyaura and Sonogashira coupling on the compound **16**. 59
Figure 2- 26. Suzuki-Miyaura coupling to obtain 4,5-dimethylbenzoate 1,2-diiodobenzene. 60
Figure 2- 27. Diiodo, dibenzoate(dibenzodithio)tetrathiafulvalene synthesis. 60
Figure 2- 28. Four and Two-contact method commonly used for measuring electrical conductivity of MOFs. I and V denote current and voltage, respectively, and L, w, and t denote the length, width, and thickness of the samples, respectively. 85

Table 2- 1. Potential oxidation, $\boldsymbol{EOx}$ and reduction, $\boldsymbol{ERed}$ potentials and $\boldsymbol{E1/2}$ of **5** vs SCE at different scan rates. 47
Table 2- 2. Potential oxidation, $\boldsymbol{EOx}$ and reduction, $\boldsymbol{ERed}$ potentials and $\boldsymbol{E1/2}$ of **12** at different scan rates in DCM and ACN vs SCE. 56

Figure 3- 1. BVDT-TTF-Py$_4$. 63
Figure 3- 2. Synthesis of BVDT-TTF-Py$_4$. 65
Figure 3- 3. Cyclic voltammetry of a solution of **L** 10^{-3} M, $TBAPF_6$ 0.1M in DCM. Platinum electrode as WE, platinum wire as CE and an Ag/AgCl/Saturated KCl electrode as RE at scan rate 20/50/100 mV·cm^{-1}. Values were converted with respect to the standard calomel electrode (SCE). 65
Figure 3- 4. Single crystal X-ray structure for BVDT-TTF-Py$_4$-$ZnCl_2$. a) Side view of the BVDT-TTF stacking, b) view of a single 2D layer and c) packing (solvent molecules and H atoms have been omitted for the sake of clarity. C: grey; S: yellow; N: blue; Cl: green and Zn: dark blue). 68
Figure 3- 5. Solid-state electrochemical configuration. 70
Figure 3- 6. CV curves of a) 1 mM ligand in solution in 0.1 M $TBAPF_6$ DCM solution and (b) ligand powder with Nafion. WE/GCE for a) and GCP for b). RE: Ag wire, CE: Pt wire. CV profiles were obtained at 20 mV s^{-1} scan rate. 71
Figure 3- 7. CV curve of **L**-$HgCl_2$, **L**-$CdCl_2$, **L**-$ZnCl_2$, **L**-$CuCl_2$ crystalline powder with Nafion. WE/GCP, RE: Ag wire. CE: Pt wire. CV profiles were obtained at a 20 mV s^{-1} scan rate. 72
Figure 3- 8. Crystal of **L**-$HgCl_2$ before and after oxidation. 73

Figure 3- 9. Single crystal X-ray structure for **L**$^{\bullet+}$$CdCl_2$ I_3^- along the c axis. 75
Figure 3- 10. Crystal structure of **L**-$CdCl_2$ where the short S···S contacts are shown as red dotted lines; for clarity solvent molecules are not displayed and the pyridine ligands have been omitted in b), c) and d). a) Projection view along the b-direction, b) top view of a double layer, c) overlap mode between pairs of **L** donors where the inner (i) and outer (o) types of S atoms are noted, and d) schematic lateral view showing that the double layers are step-layers with successive steps built from donors turning in opposite senses. 76
Figure 3- 11. DFT band structure for **L**-$CdCl_2$ (a). DFT band structure for the metallic (b), ferromagnetic (FM) (c) and fully antiferromagnetic states (AF) (d) of **L**$^{\bullet+}$-$CdCl_2$-I_3^-. Γ=(0, 0, 0), X=(a*/2, 0, 0), Y=(0, b*/2, 0) and Z=(0, 0, c*/2); M=(0, b*/2, c*/2) in a) but (a*/2, b*/2, 0) in b), c) and d). The dashed line refers to the highest occupied level in all cases. All levels up to the energy zero are doubly filled in a) and b). Spin-up and spin-down bands are shown in red and blue, respectively in (c) and (d). The spin-up and spin-down bands are identical although located in spatially different but equivalent sites in (d) so that they superpose and only the blue bands are visible. Note the larger energy scale in a). 78
Figure 3- 12. 1) Theoretical PXRD pattern of (a) **L**-$CdCl_2$ and (c) **L**$^{\bullet+}$-$CdCl_2$-I_3^- ; Experimental PXRD pattern of (b) **L**-$CdCl_2$ and (d) **L**$^{\bullet+}$-$CdCl_2$-I_3^-. 2) (a) Theoretical PXRD pattern of **L**-$HgCl_2$, (b) experimental PXRD pattern of **L**-$HgCl_2$ and (c) of **L**$^{\bullet+}$-$HgCl_2$-I_3^-. 3) (a) Theoretical PXRD pattern of **L**-$CuCl_2$, (b) experimental PXRD pattern of **L**-$CuCl_2$ and (c) of **L**$^{\bullet+}$-$CuCl_2$-I_3^-. 80
Figure 3- 13. Frontier molecular orbitals: HOMO (Highest Occupied Molecular Orbital) of neutral BVDT-TTF-Py_4 (left), and α-SOMO (Single Occupied MO) of the BVDT-TTF-$Py_4^{\bullet+}$ cation (right), calculated using DFT methods.....82
Figure 3- 14. Schematic view of the symmetric C=C stretching ν_C mode of the neutral BVDT-TTF-Py_4 molecule (left) and BVDT-TTF-$Py_4^{\bullet+}$ radical cation (right), as it results from DFT calculations. 82
Figure 3- 15. (a) Raman spectra of selected BVDT-TTF-Py_4 coordination networks; (b) Raman spectrum of neutral BVDT-TTF-Py_4, together with the respective theoretical Raman spectrum calculated at the B3LYP/6-31+ +G(d,p) level of theory. (c) Raman spectra of **L**$^{\bullet+}$$CdCl_2$ I_3^- and **L**$^{\bullet+}$$ZnCl_2$ $I_3^{-\cdot}$ (d) Theoretical Raman spectrum of BVDT-TTF-$Py_4^{\bullet+}$ calculated at the B3LYP/6-31+ +G(d,p) level of theory. The charge-sensitive νC mode is labelled as $\nu C + 1$ for the cation. (a), (b) and (c) are measured at room temperature with the 785 nm excitation line at room temperature. 83
Figure 3- 16. Raman spectra of **L**$^{\bullet+}$-$CdCl_2$-I_3^- measured at room temperature with the 632.8 nm excitation line, in the frequency range of the stretching polyiodide modes; the spectra are offset for clarity. 84
Figure 3- 17. Single crystal X-ray structure for **L**-$[CuCl_2]_2$. a) Secondary building unit b) packing c) side view of the BVDT-TTF-Py_4 stacking sequences along b-axis (C: grey; N: blue; Cl: green; Cu: orange). ..87
Figure 3- 18. Crystal before and after oxidation. 88
Figure 3- 19. a) theoretical pattern of **L**-$[CuCl_2]_2$ b) pattern of **L**-$[CuCl_2]_2$ c) theoretical pattern of **L**-$[CuCl_2]$ and d) pattern of **L**-$CuCl_2$ d) PXRD pattern of **L**$^{\bullet+}$-$[CuCl_2]_2$-I_3^-.....89
Figure 3- 20. Thermogravimetric analysis (TGA) data for **L**-$[CuCl_2]_2$. 90

Figure 3- 21. CV curve of **L**-$[CuCl_2]_2$ crystalline powder with Nafion. WE/GCP, RE: Ag wire. CE: Pt wire. CV profile was obtained at 20 mV s^{-1} scan rate. 91
Figure 3- 22. Raman spectra of selected neutral **L**-$[CuCl_2]_2$and of oxidized **L**-$[CuCl_2]_2$. The charge-sensitive νC mode is labelled as $\nu C + 1$ for the cation and $\nu C0$ for the neutral. Both are measured at room temperature with the 785 nm excitation line at room temperature. 92
Figure 3- 23. Raman spectra of $\mathbf{L}^{\bullet+}$-$[CuCl_2]_2$-I_3^- measured at room temperature with the 632.8 nm excitation line, in the frequency range of the stretching polyiodide modes. 93
Figure 3- 24. Single crystal X-ray structure for **L**-$(CuCl_2)_2(CH_3OH)_2$. a) Secondary building unit b) packing c) side view of the BVDT-TTF-Py_4 stacking sequences (C: grey; N: blue; Cl: green; Cu: orange; O: red). 95
Figure 3- 25. H_8TTFOC structure. 96
Figure 3- 26. Synthesis of H_8TTFOC. 97
Figure 3- 27. Cyclic voltammetry of H_8TTFOC solution (10^{-3} M, $TBAPF_6$ 0.1 M in THF). Platinum electrode as WE, platinum wire as CE and an Ag/AgCl/Saturated KCl electrode as RE at scan rate 20/50/100 mV·cm^{-1}. Values were converted with respect to the standard calomel electrode (SCE). 98
Figure 3- 28. Single crystal X-ray structure for Zn_2-TTFOC. a) Secondary building unit b) packing along a-axis c) side view of the Zn_2-TTFOC along b-axis (C: grey; S: yellow; O: red; Zn: green). 100
Figure 3- 29. Single crystal X-ray structure for Ni_3-TTFOC. a) Secondary building unit b) packing along b-axis c) packing along c-axis (C: grey; S: yellow; O: red; Ni: green) d) side view of the Ni_3-TTFOC stacking sequences. 102
Figure 3- 30. Alternative SBU. 102
Figure 3- 31. Single crystal X-ray structure for Cu_3-TTFOC. a) Secondary building unit b) packing c) side view of the Cu_3-TTFOC (C: grey; S: yellow; O: red; Cu: orange). 104
Figure 3- 32. Theoretical PXRD pattern of Cu_3-TTFOC (black) and experimental PXRD pattern (red). 105

Table 3- 1. Potential oxidation, $\boldsymbol{EOx}$ and reduction, $\boldsymbol{ERed}$ potentials and $\boldsymbol{E1/2}$ of **L** vs SCE at different scan rates. 66
Table 3- 2. Crystallographic data **L** -MCl_2 (M=Cu, Zn, Cd or Hg). 67
Table 3- 3. Selected bond distances and angles for **L**-MCl_2. i and o correspond to the S atoms located on the inner rings and outer rings of **L**, respectively. 69
Table 3- 4. Oxidation potential, $\boldsymbol{EOx}$, and reduction potential, $\boldsymbol{ERed}$ of BVDT-TTF-Py_4, **L**-$HgCl_2$, **L**-$CdCl_2$, **L**-$ZnCl_2$, **L**-$CuCl_2$ WE/GCE for a) and GCP for b). RE: Ag wire CE: Pt wire. 72
Table 3- 5. Crystal data of **L**-$CdCl_2$ and $\mathbf{L}^{\bullet+}CdCl_2$ I_3^- 74
Table 3- 6. The positions in cm^{-1} of the charge-sensitive ν_C mode in calculated and experimental Raman spectra of **L** and coordination polymers with M=Zn, Hg, Cu, and ($\mathbf{L}^{\cdot+}$-$CdCl_2$ I_3^-), with M=Cd, Zn. [a] Theory level: B3LYP/6-31++G(d,p), scaled with a 0.9614 factor. 83
Table 3- 7. Experimental polyiodide frequencies in cm^{-1} observed in Raman spectra of $\mathbf{L}^{\bullet+}(CdCl_2)(I_3)^-$ 84
Table 3- 8. Crystallographic data of **L**-$[CuCl_2]_2$. 86

Table 3- 9. Selected bond distances and angles for **L**-$[CuCl_2]_2$. i and o correspond to the S atoms located on the inner rings and outer rings of **L**, respectively. 88
Table 3- 10. $\boldsymbol{EOx}$ and $\boldsymbol{ERed}$ of BVDT-TTF-Py_4 and **L**-$[CuCl_2]_2$ at 20 mV·s^{-1}. 91
Table 3- 11. Experimental polyiodide frequencies in cm^{-1} observed in Raman spectra of $\mathbf{L}^{\bullet+}$-$[CuCl_2]_2$ I_3^-.93
Table 3- 12. Crystallographic data of **L**-$(CuCl_2)_2(CH_3OH)_2$. 94
Table 3- 13. Potential oxidation, $\boldsymbol{EOx}$ and reduction, $\boldsymbol{ERed}$ potentials and $\boldsymbol{E1/2}$ of H_8TTFOC vs SCE at different scan rates. 98
Table 3- 14. Metals and conditions used for solvothermal synthesis. 99
Table 3- 15. Crystal data of Ni_3-TTFOC. 101
Table 3- 16. Crystal data of Cu_3-TTFOC. 103

Figure 4- 1. BVDT-TTF and EVT-TTF donors. 109
Figure 4- 2. Selected C–C and C–S internal bond distances for (BVDT-TTF)(TaF_6). 110
Figure 4- 3. X-ray crystal structure of (BVDT-TTF)(TaF_6) (Carbon: grey ; Sulfur : yellow ; Tantalum : blue ; Fluorine : green ; Hydrogen : white). 111
Figure 4- 4. Band structure for the (a) metallic and (b) antiferromagnetic (along *a*), states of (BVDT-TTF)(TaF_6) using a double cell along *a*. The energy zero refers to the highest occupied state in both cases and Γ = (0, 0, 0), X = (*a**/2, 0, 0), Y = (0, *b**/2, 0), Z = (0, 0, *c**/2), M= (*a**/2, *b**/2, 0) and N= (*a**/2, 0, *c**/2). In (b) the spin-up and spin-down bands are shown in blue and red, respectively. However, since the spin-up and spin-down bands are identical, although located in spatially different but equivalent sites, they superpose and only the blue bands are visible. 112
Figure 4- 5. Selected C–C and C–S internal bond distances for $(BVDT\text{-}TTF)_{2.5}(I_3)$. 113
Figure 4- 6. X-ray crystal structure of $(BVDT\text{-}TTF)_{2.5}(I_3)$ (Carbon: grey ; Sulfur : yellow ; Iodine : purple ; Hydrogen : white). 114
Figure 4- 7. Temperature dependent resistivity measurement on single crystal for $(BVDT\text{-}TTF)_{2.5}(I_3)$, plotted as ρ versus temperature. 115
Figure 4- 8. a) Band structure for the hypothetical metallic state of $(BVDT\text{-}TTF)_{2.5}(I_3)$ where Γ = (0, 0, 0), X = (*a**/2, 0, 0), Y = (0, *b**/2, 0), Z = (0, 0, *c**/2), M= (*a**/2, *b**/2, 0) and N= (*a**/2, 0, *c**/2). Discrete $(donor_m)^{n+}$ (b) and $(donor_5)^{2+}$ (c) units discussed in the text. 116
Figure 4- 9. X-ray crystal structure of $(BVDT\text{-}TTF)_2(ReO_4)$ (Carbon: grey ; Sulfur : yellow ; Rhenium : blue ; Oxygen : red ; Hydrogen : white). 118
Figure 4- 10. Temperature dependent resistivity measurement on single crystal for $(BVDT\text{-}TTF)_2(ReO_4)$. 119
Figure 4- 11. Synthesis of EVT-TTF, **25** 120
Figure 4- 12. Cyclic voltammetry of a **25** solution 10^{-3} M, $TBAPF_6$ 0.1M in THF. Platinum electrode as WE, platinum wire as CE and an Ag/AgCl/Saturated KCl electrode as RE at scan rate 20/50/100 mV·cm^{-1}. Values were converted with respect to the standard calomel electrode (SCE). 121
Figure 4- 13. Selected C–C and C–S internal bond distances for (EVT-TTF)(ClO_4). The carbon atom from DCM molecule is disordered over two positions with refined partial occupancy factors (0.5/0.5). One

molecule appears grey, the other white, while the shared chlorine atoms are depicted in green for clarity. Only one out of the two disordered positions of the perchlorate anion is displayed for the sake of clarity. 123
Figure 4- 14. X-ray crystal structure of (EVT-TTF)(ClO_4) (Carbon: grey ; Sulfur : yellow ; Chlorine : green ; Oxygen : red ; Hydrogen : white). Solvent molecules and anions have been omitted for the sake of clarity on (a). Disordered solvent molecules and anions have been omitted for the sake of clarity on (b). 124
Figure 4- 15. Temperature dependent resistivity measurement on single crystal for (EVT-TTF)(ClO_4) in two and four contact measurements. 125
Figure 4- 16. Band structure for (EVT-TTF)(ClO_4) where Γ = (0, 0, 0), X = (a*/2, 0, 0), Y = (0, b*/2, 0), Z = (0, 0, c*/2), M= (a*/2, b*/2, 0), N= (a*/2, 0, c*/2) and R = (a*/2, b*/2, c*/2). Because of disorder, only donor molecules were included explicitly in the calculation while anions and solvent molecules were replaced by a uniform background charge. 126
Figure 4- 17. Frontier molecular orbitals: HOMO (Highest Occupied Molecular Orbital) of the neutral BVDT-TTF (left), and α-SOMO (Single Occupied MO) of the BVDT-TTF^{*+} radical cation (right), calculated by DFT methods.....127
Figure 4- 18. Frontier molecular orbitals: HOMO (Highest Occupied Molecular Orbital) of the neutral EVT-TTF (left), and α-SOMO (Single Occupied MO) of the EVT-TTF^{*+} radical cation (right), calculated by DFT methods.....127
Figure 4- 19. The schematic patterns of the charge-sensitive C=C stretching ν_C mode (upper panels) and the out-of-plane C-S stretching ν_S mode (lower panels) of the BVDT-TTF^{*+} cation (left) and the EVT-TTF^{*+} cation (right), based on the DFT calculations. 128
Figure 4- 20. (a) Raman spectra of (BVDT-TTF)(TaF_6), (BVDT-TTF)$_2$(ReO_4), (BVDT-TTF)$_{2.5}$(I_3), and (EVT-TTF)(ClO_4) measured at room temperature, in the frequency range of the C=C stretching vibrations; the spectra show the presence of the ν_C modes associated with the donor molecules of charge +1e and +0.5e; (b) theoretical Raman spectra of the isolated BVDT-TTF and EVT-TTF donor molecules, both the neutral and the cation, calculated at the B3LYP/6-31+ +G(d,p) level of theory; 129
Figure 4- 21. (a) Raman spectra of (BVDT-TTF)(TaF_6), (BVDT-TTF)$_2$(ReO_4), (BVDT-TTF)$_{2.5}$(I_3), and (EVT-TTF)(ClO_4) measured at room temperature with the 632.8 nm excitation line, in the frequency range of the C=S stretching vibrations; (b) theoretical Raman spectra of the isolated BVDT-TTF and EVT-TTF donor molecules, both the neutral and the cation, calculated at the B3LYP/6-31+ +G(d,p) level of theory. ...130
Figure 4- 22. Raman spectrum of (BVDT-TTF)$_{2.5}$(I_3) measured at room temperature in the frequency range of the polyiodide stretching vibrations. 131

Abbreviations and Symbols

TTF	Tetrathiafulvalene
TCNQ	Tetracyanoquinodimethane
TCNQF4	Tetracyanotetrafluoroquinodimethane
NLO	Nonlinear optical materials
OPVs	Organic Field-Effect Transistor
DB-TTF	Dibenzotetrathiafulvalene
I_4-TTF	Tetraiodo- Tetrathiafulvalene
TMT-TTF	Tetrakis(methylthio)tetrathiafulvalene
BEDT	Bis-ethylenedithio-tetrathiafulvalene
BVDT-TTF	Bis(Vinylenedithio)-Tetrathiafulvalene
EVT-TTF	Ethylene-vinylenedithiotetrathiafulvalene
Tc	Critical Temperature
MOF	Metal organic framework
SBU	Secondary Building Unit
TGA	Thermogravimetric Analysis
RT	Room Temperature
THF	Tetrahydrofuran
DMSO	Dimethylsulfoxide
DCM	Dichloromethane
TBAP	Tetrabutylammonium Terchlorate
ACN	Acetonitrile
TCE	Trichloroethane
SCE	Standard calomel electrode
HOMO	Highest occupied molecular orbital
LUMO	Lowest Unoccupied Molecular Orbital
SOMO	Singly Occupied Molecular Orbital
D	Donor
L	Ligand
E_a	Activation energy
σ	Conductivity
μ	High Mobility
h	Holes
e	Electrons
Å	Angstrom
ρ	Resistivity
H_4TTFTB	Tetrathiafulvalene-Tetrabenzoate
DFT	Density Functional Theory
CV	Cyclic Voltammetry
GCP	Glassy Carbon Plate
GCE	Glassy Carbon Electrode
E_{Red}	Reduction Potential
E_{Ox}	Oxidation Potential
$E_{1/2}$	Half-Wave Potential
I_4-BVDT-TTF	Tetraiodo-Bis(Vinylenedithio)-Tetrathiafulvalene
VDT	Vinylenedithio-1,3-dithiol-2-thione
I-VDT	Iodo Vinylenedithio-1,3-dithiol-2-thione
BVDT-TTF (Dipicolinic acid)$_4$	Bis(Vinylenedithio)-Tetrathiafulvalene tetradipicolinc acid
BVDT-TTF-Py$_4$	Tetrapyridine Bis(Vinylenedithio)-Tetrathiafulvalene
H_8TTFOC	TTF (isophthalic acid)$_4$
SCXRD	Single Crystal X-ray Diffraction
PXRD	Powder X-ray Diffraction

General Introduction

This work focuses on exploring the electronic properties of materials based on the scaffold of tetrathiafulvalene (TTF), one of the most prominent electroactive molecules. The research is centred on two main domains:

- Porous conductive materials, particularly Metal-organic frameworks (MOFs) and the understanding of the relationship between their structural characteristics and their electronic properties, highlighting the crucial role of π-stacking interactions in charge carrier mobility.
- Charge transfer salts featuring unsaturated variants of the ubiquitous bis(ethylenedithio)-tetrathiafulvalene (BEDT-TTF), namely BVDT-TTF (Bis(Vinylenedithio)-Tetrathiafulvalene) and EVT-TTF (Ethylene-vinylenedithiotetrathiafulvalene).

In the opening chapter, the physicochemical properties of the TTF compound and its alkylthio derivatives will be discussed. The methodology of electrocrystallization and the resulting packing arrangements of BEDT-TTF salts will be described. Furthermore, an introduction into the realm of conductive MOFs will be given, with a particular emphasis on the exploitation of TTF-based ligands.

The second chapter will discuss the synthetic strategies employed in the production of functionalized BVDT-TTF derivatives. The challenges and difficulties encountered during the synthesis will be explained and discussed.

The third chapter will focus on the synthesis and characterization of metal-organic frameworks (MOFs) utilizing a tetrapyridine functionalized BVDT-TTF and a TTF-tetraisophthalic acid. The thorough characterization using techniques such as SCRXD, PXRD, TGA, and solid-state cyclic voltammetry of the obtained coordination networks BVDT-TTF-Py_4-MCl_2 and BVDT-TTF-Py_4-$[CuCl_2]_2$ will be described and discussed. In the case of BVDT-TTF-Py_4-MCl_2, the band structure calculations reveal the presence of a 2D conducting path. If defaults do exist in the conduction pathway, the charge transport will not be too impacted. Furthermore, post-synthetic oxidation of these networks lead to an increase of the electrical conductivity. The structures of the networks obtained by combining TTF(isophthalic acid)$_4$ ligand with Zn, Cu, and Ni metals will be also described.

In the final chapter, the charge transfer salts using BVDT-TTF and EVT-TTF as donors will be described. While these donors share structural similarities with the well-studied BEDT-TTF structure, there is a noticeable dearth of comprehensive structural data for these organic components. This motivated us to investigate their compatibility to form various salts. We will present the successful synthesis and analyses for four novel structures, namely (BVDT-TTF)(TaF_6), (BVDT-TTF)$_2$(ReO_4), (BVDT-TTF)$_{2.5}$(I_3), and (EVT-TTF)(ClO_4), employing a combination of X-ray crystallography on single crystals, conductivity measurements, band structure calculations and Raman spectroscopy.

CHAPTER I

Tetrathiafulvalene: donor and ligand

CHAPTER I: Tetrathiafulvalene: donor and ligand

1. Tetrathiafulvalene: structure, properties, applications

1.1. Structure, generalities and properties

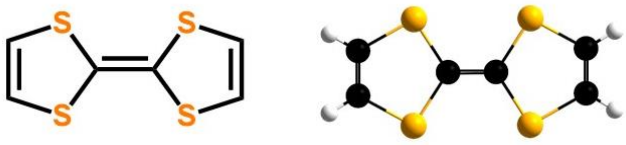


Figure 1- 1. TTF structure

Tetrathiafulvalene (TTF) (Figure 1- 1), also named 2,2'-bis(1,3-dithiole), is a non-aromatic sulfur-containing heterocyclic compound well known as an excellent organic π-electron donor. Its first synthesis goes back to 1926 by Hurley and Smiles.[1] In the 1970's, Wudl and Smith[2] proved the high electrical conductivity achieved from TTF's radical cation. TTF and its derivatives have attracted enormous attention in the fields of organic metals and organic superconductors[3,4] in the following years.

TTF presents an electroactive system in which oxidation to the radical cation ($TTF^{+\cdot}$) and dication (TTF^{2+}) states occurs sequentially and reversibly at relatively low oxidation potential values, resulting in the formation of aromaticity on the dithiolium rings and the release of two electrons. This gives to TTF an excellent electron-donating capacity. The three states – neutral, radical-cation and dication – possess different geometries. There is therefore a direct relationship between the redox properties of the TTF and its geometry. According to density functional theory (DFT) studies, neutral TTF has a boat C_{2V} structures as the most stable conformers[5] with a bridging C=C bond at a length of 1.34 Å. The radical cation ($TTF^{+\cdot}$) presents a planar D_{2h} structure,[6] while the dication (TTF^{2+}) shows a twisted D_2 structure bearing the two dithiolium rings.[7] The central carbon-carbon bond length rises as the oxidation state increases.[8]

---

[1] Hurtley, W. R. H.; Smiles, S. *J. Chem. Soc.* **1926,** *129*, 2263.
[2] Wudl, F.; Smith, G. M.; Hufnagel, E. J. *J. Chem. Soc. D* **1970**, *21*, 1453.
[3] Ferraris, J.; Cowan, D. O.; Walatka, V.; Perlstein, J. H. *J. Am. Chem. Soc.* **1973**, *95* (3), 948–949.
[4] Martín, N. *Chem. Commun.* **2013**, *49* (63), 7025.
[5] Viruela, R.; Viruela, P. M.; Pou-Amérigo, R.; Ortí, E. *Synth. Met*. **1999**, *103* (1–3), 1991–1992.
[6] Pou-Amérigo, R.; Ortí, E.; Merchán, M.; Rubio, M.; Viruela, P. M. *J. Phys. Chem. A* **2002**, *106* (4), 631–640.
[7] Ashton, P. R.; Balzani, V.; Becher, J.; Credi, A.; Fyfe, M. C. T.; Mattersteig, G.; Menzer, S.; Nielsen, M. B.; Raymo, F. M.; Stoddart, J. F.; Venturi, M.; Williams, D. J. *J. Am. Chem. Soc.* **1999**, *121* (16), 3951–3957.
[8] Yakushi, K.; Nishimura, S.; Sugano, T.; Kuroda, H.; Ikemoto, I. *Acta Cryst*, **1980**, *36*, 358-363.

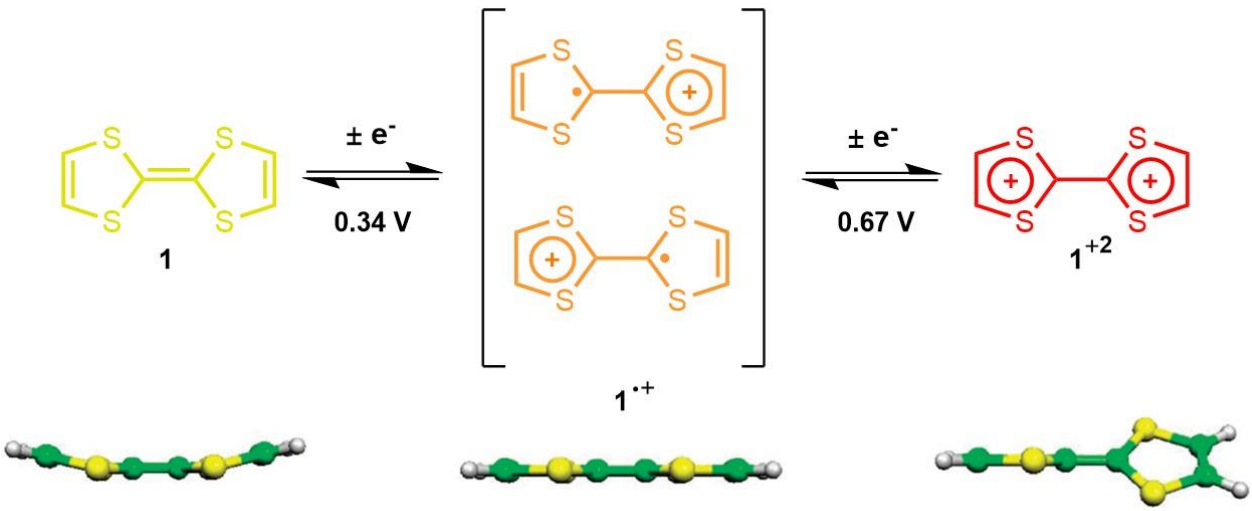


Figure 1- 2. TTF, radical cation and dication species and their geometries

The first oxidation-reduction relative to the TTF ring system to form the cation radical occurs at $E^1_{1/2}$ 0.34 V while the second wave producing the dication species appears at $E^2_{1/2}$ 0.67 V (vs. Ag/AgCl in acetonitrile) and both processes are reversible (Figure 1- 2). In addition to possessing an excellent electron donating ability, TTF presents several interesting features:

- A fine tuning of the redox potentials through functionalization, thanks to the multiple synthetic strategies of functionalization available.
- Radical cations of TTF and derivatives are well-known for their high stability. The formation of stable aromatic dithiolium ions delocalises the unpaired electron.
- Distinctive spectral absorption realized upon formation of $TTF^{+\cdot}$ or TTF^{2+}. While the neutral form of TTF exhibits two absorption bands with absorption maxima (λ_{max}) at 302 and 317 nm, λ_{max} of $TTF^{+\cdot}$ are at 335, 430 and 579 nm, and at 355 nm and 273 nm for TTF^{2+}.
- Radical cations of TTF derivatives readily form dimers in the solid state which are stabilised by orbital overlap, intermolecular π-π interactions and non-bonding S··S interactions.[9]

TTF, thanks to its electron-donating properties, is able to form charge transfer CT complexes with a variety of electron-accepting compounds. The electrochemical properties and the packing mode in the radical cation salts afford insulating, semiconducting, metallic or superconducting materials. Wudl *et al.*[10] were the first to synthetize and demonstrate that the salt $[TTF]^+Cl^-$ has semiconducting properties. This salt exhibits a room temperature conductivity of 0.27 $S{\cdot}cm^{-1}$ and an activation energy of 0.19 eV. In 1973, TTF

[9] Bryce, M. R. *J. Mater. Chem.* **2000**, *10* (3), 589–598.
[10] Wudl, F.; Smith, G. M.; Hufnagel, E. J. *J. Chem. Soc. D* **1970**, 21, 1453.

combined with the tetracyanoquinodimethane (TCNQ) as electron acceptor gave spontaneously a charge transfer complex TTF-TCNQ that is considered to be the first organic metal.[11]

1.2. Applications

The rich redox activity of TTF has made it a very popular molecular building block for many applications (Figure 1- 3):

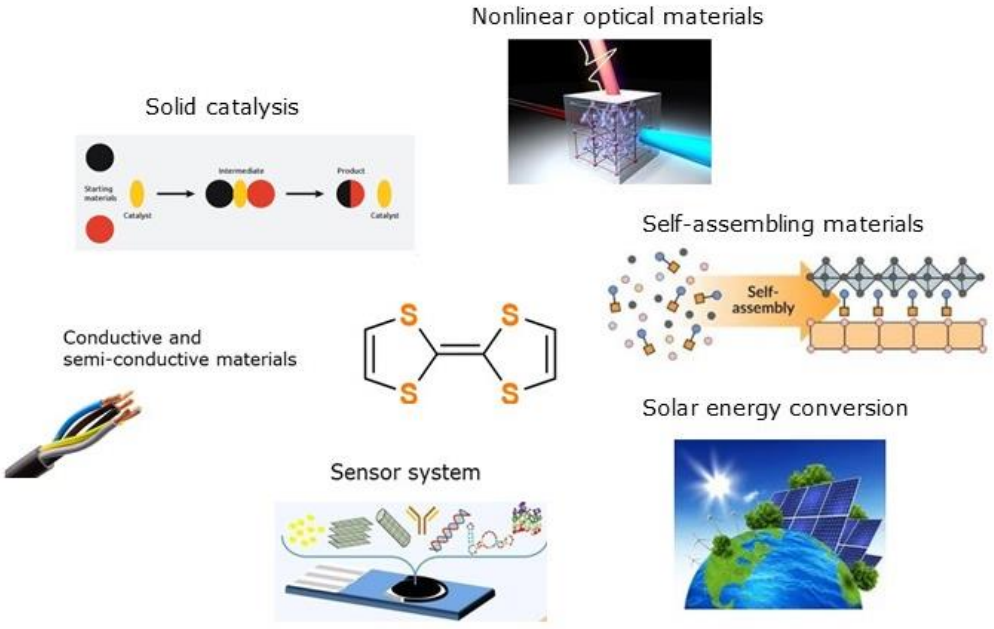
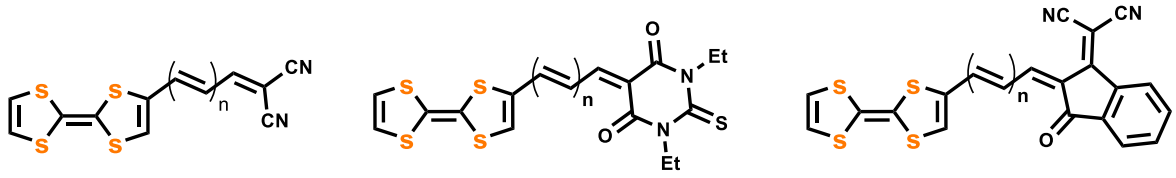


Figure 1- 3. Applications of TTFs.

- Nonlinear optical materials (NLO): tetrathiafulvalenes are well known for their strong electron donating properties. Due to that, functionalized TTF moieties have been covalently linked to electron acceptors in order to provide D-A systems. In these compounds, the electron-donating TTF moiety and the electron-accepting group form a conjugated framework that facilitates intermolecular charge transfer (ICT) upon excitation by light.[12] In this context, several push–pull chromophores based on TTF were studied to determine their NLO properties.[13] Push-pull chromophores are based on an electron donor and an electron acceptor linked by a saturated or a conjugated spacer such as in Figure 1- 4. The best value, $\mu\beta = 1350 \times 10^{-48}$ esu, is observed on the TTF linked to the strong acceptor 3-

[11] Ferraris, John.; Cowan, D. O.; Walatka, V.; Perlstein, J. H. *J. Am. Chem. Soc.* **1973**, *95* (3), 948–949.
[12] Fuks-Janczarek, I.; Luc, J.; Sahraoui, B.; Dumur, F.; Hudhomme, P.; Berdowski, J.; Kityk, I. V.*J. Phys. Chem. B* **2005**, *109* (20), 10179–10183.
[13] Insuasty, B.; Atienza, C.; Seoane, C.; Martín, N.; Garín, J.; Orduna, J.; Alcalá, R.; Villacampa, B. *J. Org. Chem.* **2004**, *69* (21), 6986–6995.

(dicyanomethylidene) indan-1-one. The UV/Vis spectra of all these derivatives showed a low-intensity charge-transfer band in the visible region, which is a prerequisite for the attainment of high β values.



n=1 μβ=**470**
n=2 μβ=**630**

n=1 μβ=760
n=2 μβ=**960**

n=1 μβ=**700**
n=2 μβ=**1350**

Figure 1- 4. Push-pull chromophores based on TTF.

- Solar cell system: TTF-based materials have been explored as electron-donor components in organic photovoltaic devices (OPVs). TTF derivatives can act as electron-donating materials and used in combination with electron-accepting materials to form bulk heterojunction structures. When light is absorbed, TTF releases electrons thus acting as a donor of electrons in the photoactive layer. By chemical modification, HOMO energy level of TTF can be adjusted, enabling better energy level matching with the electron acceptor material and facilitating efficient charge separation. An example is π-extended tetrathiafulvalene-wire-fullerene. The extended-TTF-C60 dyads combine extended-TTF (ex-TTF) as an electron-donating unit with fullerene C60 as an electron-accepting unit. This combination allows for efficient charge separation and transfer in the active layer of OPVs.[14] The power conversion efficiency is 0.02% under solar simulated light with 80 $mW \cdot cm^{-2}$.

- TTF-based self-assembled material: Self-assembly refers to the spontaneous organization of molecules into well-defined structures or patterns driven by non-covalent interactions or coordination bonds. The planarity and π-conjugated structure of TTF allow for π-π stacking interactions and other non-covalent interactions. These interactions play a significant role in the self-assembly of TTF-based materials, leading to the formation of various supramolecular architectures. For example, Bis(pyrrolo)tetrathiafulvalene (BPTTF) is a tetrathiafulvalene where two pyrrole groups are attached to the TTF core. It can be functionalized by four pyridine units and can self-assemble with Pt (II) complexes, forming three-dimensional cages.[15] As result, the 3D cage formed by the electron-rich TTF framework binds electron acceptors, such as $TCNQF_4$ (7,7,8,8-tetracyano-p-quinodimethane).

- Sensor systems based on TTF: they involve the use of TTF as a recognition element or an electroactive probe to detect and analyze target analytes such as small molecules, metal ions, organic compounds,

[14] Martín, N.; Sánchez, L.; Herranz, M. Á.; Illescas, B.; Guldi, D. M. *Acc. Chem. Res.* **2007**, *40* (10), 1015–1024.
[15] Bivaud, S.; Goeb, S.; Balandier, J.-Y.; Chas, M.; Allain, M.; Sallé M. *Eur. J. Inorg. Chem*. **2014**, *2014*(14), 2440–2448.

gases, or biomolecules. Electrochemical or spectroscopic devices monitor changes in TTF's behaviour triggered by the presence of the analyte.[16] For example, incorporating TTF into a calix[4]pyrrole framework provides tetrakis-TTF-calix[4]pyrrole, adding rigidity and electron-donating character to the building block (Figure 1- 5, a).[17] The pyrrole moieties provide NH-anion hydrogen-bonding interactions that create affinity toward anions while the peripheral TTF subunits are inherently electron-rich. This results in a building block that recognizes and embraces several anions guests, with exciting chemical and photophysical features. It has the ability to adopt two different limiting conformations (Figure 1- 5, b). In the absence of anions, the 1,3-alternate form is energetically favourable and the system acts as an effective receptor for neutral electron acceptors. In the presence of coordinating anions such as Cl^-, these systems adopt the corresponding cone conformation. This happens thanks to strong hydrogen bonding interactions between the pyrrolic NH protons and the bound anionic guest. This led to the release of the electron-deficient guest.

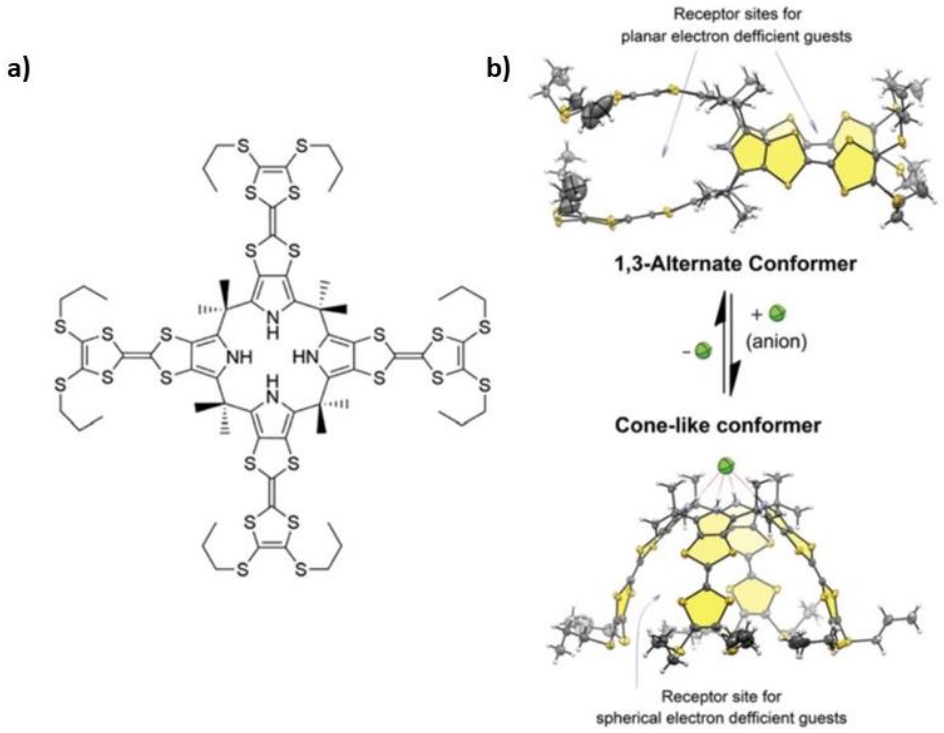


Figure 1- 5. Tetrakis-TTF-calix[4]pyrrole and the two distinct conformers assuming in the presence and absence of an anion.[18]

[16] Jørgensen, T.; Hansen, T. K.; Becher, J. *Chem. Soc. Rev.* **1994**, *23* (1), 41–51.
[17] Nielsen, K. A., Cho, W.-S., Jeppesen, J. O., Lynch, V. M., Becher, J., & Sessler, J. L. J. *Am. Chem. Soc.* **2004**, *126,* 16296–16297.
[18] Jana, A.; Bähring, S.; Ishida, M.; Goeb, S.; Canevet, D.; Sallé, M.; Jeppesen, J. O.; Sessler, J. L. *Chem. Soc. Rev.* **2018**, *47* (15), 5614–5645.

- Conductive polymers: These polymers are formed by linking multiple TTF units together through σ-bonds, conjugated π-systems, chalcogen atoms or alkyl chains. The combination of through-bond and through-space interactions leads to a multistage redox behaviour each corresponding to the transfer of electrons between TTF units. By carefully designing the polymer structure and TTF interactions, the conductivity and electrochemical properties of these materials can be controlled, making them attractive for several application such as electrochromic devices, energy storage systems, and molecular electronics.[19] For example, a famous class of materials are the mixed-valence tetrathiafulvalene (TTF)/poly(methyl methacrylate) (PMMA) composites where TTF cation radicals and neutral heterogeneous TTF derivatives are incorporated into a PMMA matrix. The relationship between the conductivities of the composite films and the differences in oxidation potentials between the heterogeneous TTF pairs has been observed. The conductivities of the PMMA composites were found to be in the order of 10^2 S cm^{-1} when the TTF cation radical and heterogeneous TTF derivatives had similar oxidation potentials. In contrast, when there were larger gaps in the oxidation potentials between the coexisting TTF derivatives, the conductivities of the PMMA composites increased significantly to the order of 10^4 S cm^{-1}. This indicates that the TTF derivatives with larger oxidation potentials act as energy barriers within the composite material.[20]

2. Alkylthio-tetrathiafulvalenes (RS)nTTF

2.1. Synthesis of functionalized TTF and $(RS)_nTTF$

For decades, interest in the use of organic conductive materials has led to the development and investigation of various TTF derivatives. Stabilized charge-transfer salts are obtained thanks to the decreased charge repulsion. Additionally, the extended π-conjugation allows controlling the energies of the HOMO-LUMO gap.[21] The TTF scaffold has been modified by several strategies.

The oldest method consists in a double condensation of dichalcogenolate entities with tetrachloroethylene (Figure 1- 6).[22] This road suffers of the very low yields, non-selectivity and low availability of ethylenic 1,2-dithiolates's variety.

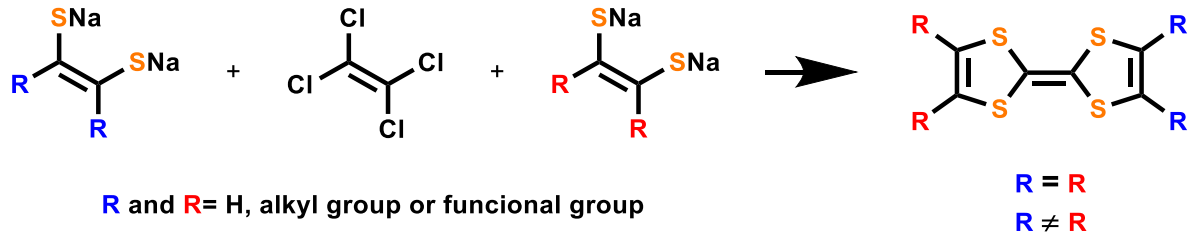


Figure 1- 6. Biscondensation of 1,2-Dichalcogenolates with Tetrachloroethylene

[19] Iyoda, M.; Hasegawa, M.; Miyake, Y. *Chem. Rev.* **2004**, *104* (11), 5085–5114.
[20] Tanaka, K.; Matsumoto, T.; Ishiguro, F.; Chujo, Y. *J. Mater. Chem.* **2011**, *21* (26), 9603.
[21] Bendikov, M.; Wudl, F.; Perepichka, D. F. *Chem. Rev.* **2004**, *104* (11), 4891–4946.
[22] Fabre, J. M. *Chem. Rev.* **2004**, *104* (11), 5133–5150.

The second strategy consists in a monocondensation of two 1,3-dichalcogenole rings and different approaches are summarised in Figure 1- 7. The first method (II a) is used to synthesise symmetric (TTF-(**R**)$_4$) and asymmetric (TTF-(**R**)$_2$(**R**)$_2$) derivatives. The mechanism consists in the deprotonation of a dithiolium salt by trimethylamine, thus generating a carbene. The carbene reacts by dimerisation with another carbene or with a dithiolium salt. The second route (II b) involves a phosphonium salt deprotonated by *n*-BuLi. Then, it reacts by nucleophilic addition to the dithiolium salt giving an adduct deprotonated by trimethylamine. This pathway is highly selective, almost excluding the formation of symmetrical TTF. To limit or even eliminate the formation of homo coupling products, Lerstrup *et al*.[23] found a new pathway involving the reaction of a phosphonate and an iminium salt (II c). The first step is to extract the proton from the phosphonate by *t*-BuOK. Subsequently, a nucleophilic addition of the carbanion phosphonate to the piperidinium salt produces an adduct. This intermediate is protonated by anhydrous AcOH and followed by elimination of piperidine and the formation of an oxaphosphetane-type intermediate. Then, via the nucleophilic addition of the acetate anion, it collapses to produce the final TTF. In addition to good selectivity, this method works very well to design TTFs carrying donor groups, which was one of the limiting points of previous couplings. Yamada *et al*.[24] developed a pathway (II d) based on a coupling between a dithiolate protected by $SnBu_2$ group and a dithiolate ester in the presence of $Al(Me)_3$.

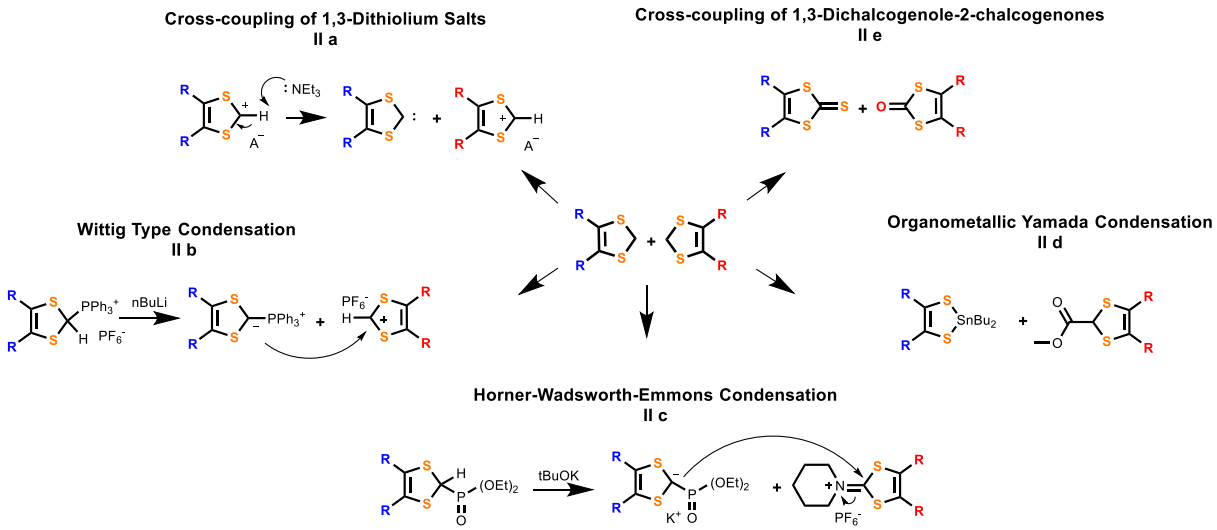


Figure 1- 7. Second strategy for substituted TTFs

The last route (II e), first used in 1970 by Hartzler[25] is based on the dechalcogenation of chalcogenones by the action of triethyl/methyl phosphite. It is among the most widely used methods for the synthesis of

[23] Lerstrup, K.; Johannsen, I.; Jørgensen, M. *Synth. Met.* **1988**, *27* (3–4), 9–13.
[24] Yamada, J.; Satoki, S.; Mishima, S.; Akashi, N.; Takahashi, K.; Masuda, N.; Nishimoto, Y.; Takasaki, S.; Anzai, H. *J. Org. Chem.* **1996**, *61* (12), 3987–3995.
[25] Hartzler, D. *J. Am. Chem. Soc.* **1970**, *92*, 1412

asymmetrical and symmetric TTFs. It has been shown that the temperature, the concentration and the nature of the phosphorus reagent play a crucial role in optimizing the reaction. For example, a thione substituted with electron withdrawing ester groups CO_2Me was most reactive with the triethyl phosphite reagent.[26] The main advantage of this strategy is the easy access to a very large variety of 1,3-dichalcogenole-2-chalcogenones used as reagents.[27]

The mechanism, as shown in Figure 1- 8, is based on a thiophilic attack of triethyl/methyl phosphite on the C=X bond forming a carbanion intermediate. Follows a carbophilic attack of the carbanion on the C=X bond of the other 1,3-dithiol-2-one/ 1,3-dithiole-2-thione generating the first adduct. The unstable adduct, by loss of $X=P(OEt)_3$ or $X=P(OMe)_3$, forms a thiirane intermediate. As a consequence of a new nucleophilic attack by triethyl/methyl phosphite on one C of the thiirane ring, a second adduct is generated. Again, by the loss of $X=P(OEt)_3$ or $X=P(OMe)_3$ the target TTF is obtained.

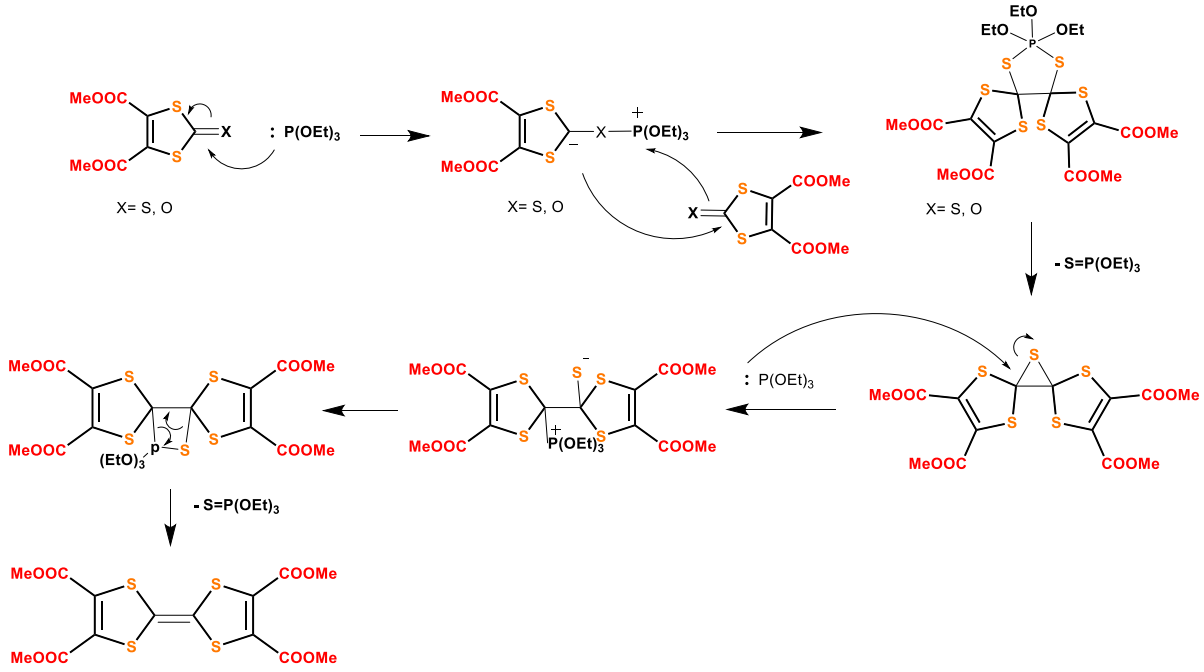


Figure 1- 8. Mechanism of phosphite coupling (II e)

The disadvantage of this strategy is the low selectivity in the case of an asymmetric TTF target, because the homo-coupling TTF-(**R**)$_4$ or TTF-(**R**)$_4$ will be obtained as well. Despite that, the choice of substituents **R**, **R** of the chalcogenone with an electron-withdrawing group such as COOMe or thioproprionitrile (S-CH_2CH_2CN) increases the yield of the asymmetric TTF.

There are no clear rules to the prediction of which combination of chalcogenones (X=O/O, X=S/O X=S/S) will give the highest yield of the desired asymmetric TTF. However, it is often observed that better results are obtained when the dithiolone (X=O) is coupled with a dithiole-thione (X=S). This is explained by the

[26] Parg, R. P.; Kilburn, J. D.; Ryan, T. G. *Synth.* **1994**, *1994 (2)*, 195–198.
[27] Nishinaga, T. **2015**. *Organic redox systems: Synthesis, Properties, and applications*. John Wiley & Sons.

predisposition of the dithiole-thiones (X=S) to form carbanion intermediate and to the greater facility of the dithiole-ones (X=O) to suffer nucleophilic attack on the carbon of the C=O bond.

The third strategy to obtain a functionalized TTF is the direct functionalization of an unsubstituted TTF. As the previous case, this strategy has several possible ways of approach:

- Method a) lithiation of the TTF molecule followed by reaction with electrophilic agents.[28]

Taking advantage of the slightly acidic character of TTF's hydrogen atom, this can be substituted by lithium in a metallic reaction using LDA. The organolithium obtained reacts immediately at low temperature with various electrophiles to give the corresponding functionalized TTF by nucleophilic substitution as observed in the Figure 1- 9.

In this way, a wide variety of functions is reachable. The main disadvantage of this strategy is, when targeting a monolithiation on the simple TTF, even using only one equivalent of LDA, di-, tri- and tetra substituted product are formed, depending on the reaction conditions.

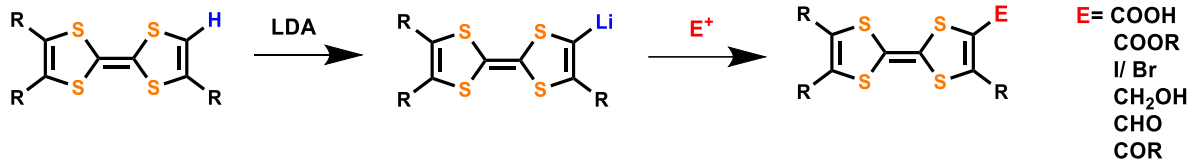


Figure 1- 9. Lithiation of the TTF molecule followed by reaction with electrophilic agents

- Method b) synthesis and deprotection of 2,3,6,7-Tetrakis(2'-cyanoethylthio)tetrathiafulvalene, followed by alkylation of the resulting thiolate (Figure 1- 10).[29] This route is widely used in the case of the synthesis of alkylthio substituents on tetrathiafulvalene $(RS)_nTTF$ such as bis(ethylenedithio)tetrathiafulvalene, BEDT-TTF or the tetrakis(methylthio)tetrathiafulvalene, TMT-TTF.

  The 2,3,6,7-Tetrakis(2'cyanoethylthio)tetrathiafulvalene is synthetized in three steps starting from the Bis(tetraethylammonium)bis(1,3-dithiole-2-thione-4,5-dithiolato) zincate by alkylation with 3-bromoproprionitrile in acetonitrile (ACN) under reflux. After transchalcogenation by mercury (II) acetate and a phosphite homo-coupling, the skeleton of TTF is formed. The propionitrile groups are removed by a base such as NaOH or CsOH and finally alkylated with an alkyl halide.

[28] Garín, J. *Adv. Heterocycl. Chem.* **1995**, *62*, 249–304

[29] Svenstrup, N.; Rasmussen, M. K.; Hansen, T. K.; Becher J. *Synth.* **1994**, *8*, 809-812.

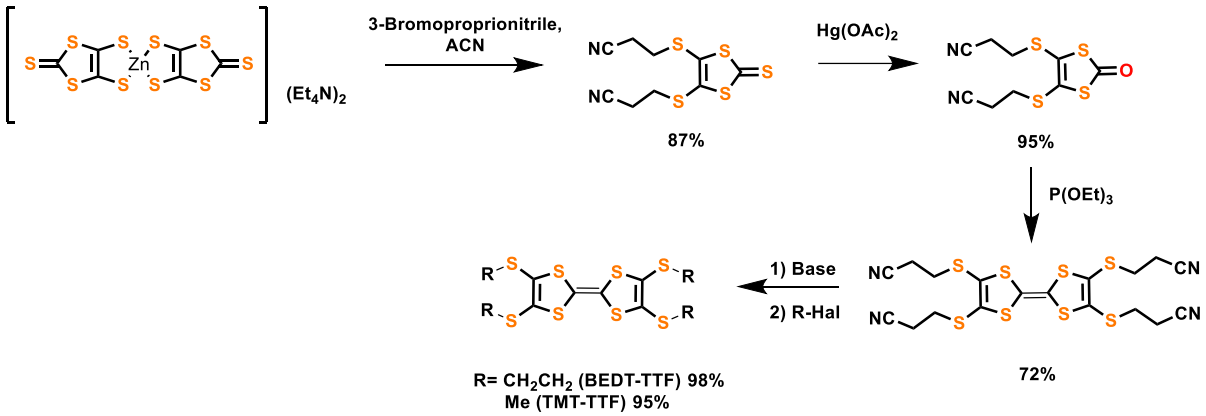


Figure 1- 10. Synthesis of 2,3,6,7-Tetrakis(2'-cyanoethylthio)tetrathiafulvalene followed by deprotection and alkylation to afford on $(RS)_nTTF$

2.2. Synthesis of Substituted BEDT-TTF

A prominent TTF derivative in the field of organic crystalline conductors is BEDT-TTF, along with its derivatives. They provided hundreds of different conducting materials ranging between semiconductors, metals and superconductors.[30] The most common synthetic pathway of derivatives BEDT-TTF is described on the Figure 1- 11. The first step consists in an oxidation of the zincate salt by iodine to form the trithione oligomer.[31] A Diels-Alder reaction between alkene and trithione is performed to afford the dithiole-thione compound. After a transchalcogenation of the remaining thione group by mercuric acetate, the final step consists in a triethyl or trimethyl phosphite-mediated self-coupling.[32]

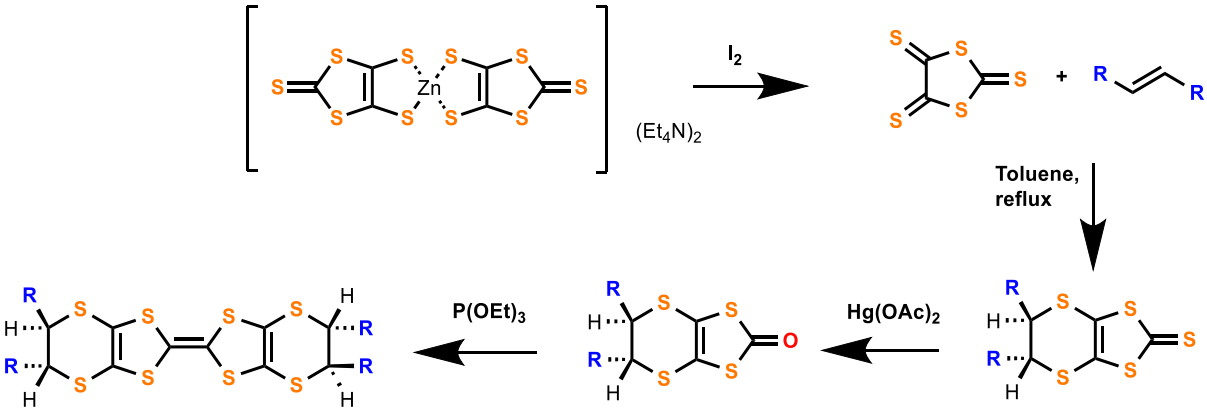


Figure 1- 11. Synthesis pathway of substituted BEDT- TTF

[30] Mroweh, N.; Mézière, C.; Pop, F.; Auban-Senzier, P.; Alemany, P.; Canadell, E.; Avarvari, N. *Adv. Mater.* **2020**, 2002811.
[31] Svenstrup, N.; Becher, J. *Synth.* **1995**, *3*, 215-235.
[32] Kini, A. M.; Parakka, J. P.; Geiser, U.; Wang, H.-H.; Rivas, F.; DiNino, E.; Thomas, S.; Dudek, J. D.; Williams, J. M. *J. Mater. Chem.* **1999**, *9* (4), 883–892.

2.3. Properties of electron-withdrawing substituents on TTF

By the attachment of electron-donating or electron-withdrawing substituents on TTF, it is possible to modulate its oxidation potentials. For example, adding arenes to the dithiole rings as in the case of 2-(1,3-Benzodithiol-2-ylidene)-1,3-benzodithiole, BD-TTF, the oxidation potential is higher ($E^1_{1/2}$0.6 V, $E^2_{1/2}$ 0.92 V) than the classic TTF ($E^1_{1/2}$ 0.34, $E^2_{1/2}$ 0.67 V). This happens for the electron-withdrawing effect engendered by the annulation of benzene ring.[33] Additionally, the fused aromatic increases intermolecular π-π interactions, leading to a large transfer integral between molecules, which is crucial for high carrier mobility.[34]

As a result, Dibenzotetrathiafulvalene (DB-TTF) shows high performance organic field effect transistors (OFETs).[35] In order to observe the consequences of π-expansion on the molecular arrangement of acenes in the solid state, as these are strongly dependent on π-π stacking and C-H···π interaction, dinaphthoTTF (DN-TTF), dianthracenoTTF (DA-TTF) and ditetracenoTTF (DTet-TTF) were studied.[36] Molecular orbital, MO, calculations of them were also performed (Figure 1- 12). HOMOs of DN-TTF (HOMO-1) and DA-TTF (HOMO-2) are localized on the TTF unit while in the DTet-TTF, it is localized on the tetracene units. Increasing the number of fused benzene rings makes the degenerated occupied MOs more localised on the acene parts.

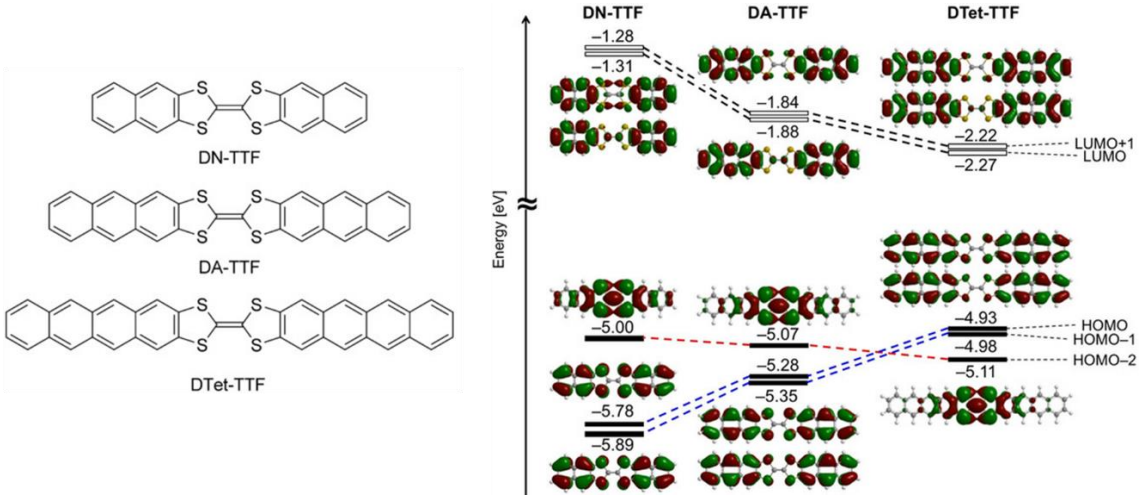


Figure 1- 12. MOs of DN-TTF, DA-TTF, and DTet-TTF.[36]

The addition of electron-withdrawing substituents such as halogens introduces significant changes in TTF properties. For example, the tetraiodo-TTF (I_4-TTF) is considered more electron-deficient compared to regular TTF due to the presence of iodine atoms. This electron deficiency arises from the electronegativity

[33] Mas-Torrent, M.; Hadley, P.; Bromley, S. T.; Crivillers, N.; Veciana, J.; Rovira, C. *Appl. Phys. Lett.* **2005**, *86* (1), 012110.
[34] Naraso; Nishida, J.; Ando, S.; Yamaguchi, J.; Itaka, K.; Koinuma, H.; Tada, H.; Tokito, S.; Yamashita, Y. *J. Am. Chem. Soc*. **2005**, *127* (29), 10142–10143.
[35] Mori, T. *Chem. Lett.* **2011**, *40* (5), 428–434.
[36] Yamashita, M.; Kuzuhara, D.; Yamada; H. *Chem. Eur. J.* **2014**, *20*, 6309 – 6314.

of iodine, which withdraws electron density from the TTF core.[37] The electron-deficient nature of I_4-TTF makes it more favorable to engage in charge acceptance or electron-accepting interactions rather than charge donation or electron-donating interactions. The presence of electron-withdrawing substituent raises the oxidation potential of the TTF molecule causing a higher energy input to remove an electron and undergo oxidation. The introduction of halogen substituents into donor molecules enables the formation of intermolecular donor-acceptor interactions, which can significantly impact the crystal structure and properties of organic conductors and charge-transfer complexes. Halogen atoms have been known to form intermolecular donor-acceptor bonds with various donor atoms, including oxygen, nitrogen and π-aromatic systems. The conductivity measured by compressed pellets of the complex I_4-TTF F_4TCNQ amounts to 0.2 $S{\cdot}cm^{-1}$.

2.4. Properties of Alkylthio tetrathiafulvalenes $(RS)_nTTF$

Since the early studies of TTF-TCNQ by Wudl *et al.*[2] and Ferraris *et coll.*[3], several TTF derivatives were synthesized in order to design new molecular-based organic conductors and superconductors. Through alkylthio substitution on TTF, it was shown that an increase of electronic polarizability along with a decrease of band occupancy increases electrical transport since it reduces the energy cost of electron-electron correlations.[38]

The π-donor abilities of alkylthio substituted are smaller than TTF as seen from comparing the $E_{1/2}$values (Table 1- 1). This leads to smaller charge-transfer with TCNQ and hence should decrease the band occupancy in the crystalline state. On the other hand, the double-occupancy fluctuations in the conducting state are easily accessible thanks to low difference between $E^1_{1/2}$ and $E^2_{1/2}$. Electrical conductivity of BEDT-TTF TCNQ salt is 0.02 $S{\cdot}cm^{-1}$ at room temperature. According the band theory, this is due to the use of strong π-donor which allow the polarizability and band occupancy condition.[39] The charge transfer is 0.3 e- par molecule indicating indicates that around 30% of an electron is transferred from the BEDT-TTF donor molecule to the TCNQ acceptor molecule in the complex. This charge transfer process leads to the creation of partially filled bands, allowing for the movement of charge carriers within the material. In TTF-TCNQ, there is a significant charge transfer from TTF to TCNQ. Approximately 0.6 e- per molecule are transferred from the TTF donor molecule to the TCNQ acceptor molecule in the complex. This substantial charge transfer leads to high electrical conductivity of 10^2 $S{\cdot}cm^{-1}$. The 2:1 complex of $(TMT\text{-}TTF)_2$TCNQ is described by Mori *et al*. [40] where the charge for each donor is estimated to be 0.3-0.4 e- and conductivity has value

[37] Batsanov, A. S.; Bryce, M. R.; Chesney, A.; Howard, J. A. K.; John, D. E.; Moore, A. J.; Wood, C. L.; Gershtenman, H.; Becker, J. Y.; Khodorkovsky, V. Y.; Ellern, A.; Bernstein, J.; Perepichka, I. F.; Rotello, V.; Gray, M.; Cuello, A. O. *J. Mater. Chem.* **2001**, *11* (9), 2181–2191.
[38] Garito, A. F.; Heeger, A. J. *Acc. Chem. Res.* **1974**, *7*, 232–240.
[39] Mizuno, M.; Garito, A. F.; Cava, M. P. *J. Chem. Soc., Chem. Commun*. **1978**, *1*, 18–19.
[40] Mori, T.; Wu, P.; Imaeda, K.; Enoki, T.; Inokuchi, H.; Saito, G. *Synth. Met*. **1987**, *19* (1–3), 545–550.

$1.8x10^{-5}$ S·cm^{-1}. In the case of BEDT-TTF TCNQ salt the TCNQ molecules are stacked face to face, whereas the BEDT-TTF molecules are arranged side by side promoting strong intermolecular interactions.[41] The crystal structure of $(TTM\text{-}TTF)_2(TCNQ)$ has a DDADDA stacking sequence. The slipping arrangement of the donors along both the molecular long axis and the molecular short axis disrupts the regular overlap of π-orbitals along the stacking direction. This disruption in π-conjugation reduces the extent of charge delocalization and the overall electronic coupling between neighboring molecules. As a result, the crystal structure of the $(TMT\text{-}TTF)_2TCNQ$ complex has a less favorable arrangement for efficient charge transport compared to BEDT-TTF TCNQ which explains the low conductivity.

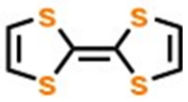
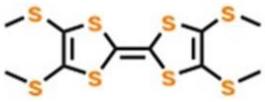
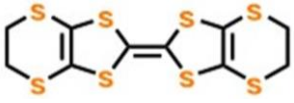
			
$E^1_{1/2}$ [V]	0.34	0.49	0.53
$E^2_{1/2}$ [V]	0.67	0.67	0.58
TCNQ salt conductivity [S·cm^{-1}]	10^2	$1.8x10^{-5}$	0.02
TCNQ salt charge transfer [e]	0.6	0.3-0.4	0.3

Table 1- 1. $E_{1/2}$ of TTF, Tetrakis(methylthio)tetrathiafulvalene TMT-TTF and BEDT-TTF, conductivity and charge transfer values in TCNQ salts.

3. Electrocrystallization

3.1. Definition, principles

The electrocrystallization technique is based on nucleation and growth of crystals occurring on electrodes in electrochemical systems under the influence of an electric field (Figure 1- 13).

[41] Mori, T.; Inokuchi, H. *Solid State Commun.* **1986**, *59* (6), 355–359.

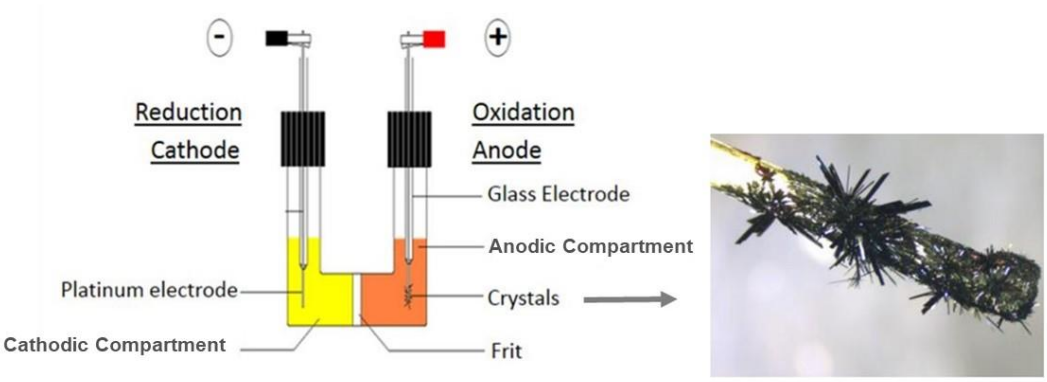


Figure 1- 13. Configuration of an electrocrystallization cell and the crystals of radical cation salts obtained on the electrode.

The mechanism consists in the formation of a stable radical originated from an electroactive species, neutral or charged, and a counterion. Ion transport and charge transfer across the electrode/electrolyte interface have fundamental roles. During the process, electroactive species undergo oxidation or reduction at the electrode interface, subsequently combining with the counteranions already present in the solution to form crystalline structures. The electrode potential and the current control the driving force and the rate of crystallization.[42] The anions play a very important role as they can tune the oxidation state of donors and influence the solid state architecture through the establishment of a complex set of intermolecular interactions. Other parameters affecting the electrocrystallization are: the concentration and purity of starting materials, the dryness of the solvents, the polarity of the solvents and the temperature.[43]
Oxidation of a neutral donor molecule can provide salts with a 1:1 stoichiometry (1) or other stoichiometries (2) such as 2:1 or 3:2 (donor: anion) (Figure 1- 14). This formation of mixed valence salts, where the donor presents more than one oxidation state, often provides conducting materials. This happens because neutral molecules and radical ionic species of electron-donor and/or electron-acceptor molecules co-exist within a π-stacking column. The mixed valence generates a partially filled band structure that is granting conductivity to the material.[44]

$$D \xrightarrow{-\,è} D^{+\cdot} \xrightarrow{X^-} (D^{+\cdot}, X^-) \qquad (1)$$

$$n(D^{+\cdot}, X^-) + D^\circ \longrightarrow (nD^{+\cdot}, mD^\circ, nX^-) \qquad (2)$$

Figure 1- 14. Salts stoichiometry.

[42] Batail, P.; Boubekeur, K.; Fourmigué, M.; Gabriel, J.C. P. *Chem. Mater*. **1998**, *10*, 3005–3015.
[43] Anzai, H.; Tokumoto, M.; Saito, G. *Mol. Cryst. Liq. Cryst*. **2011**, *125*, 385–392.
[44] Murata, T.; Yamada, C.; Furukawa, K.; Morita, Y. *Commun Chem* **2018**, *1* (1), 47.

3.2. Electrocrystallization of $(RS)_nTTFs$

Due to the small geometrical difference between planar and boat-like conformations, TTF radical cation ($TTF^{+\cdot}$) is very flexible and can appear in various conformations, depending on the donor-acceptor interactions in the crystals. S···S interactions as well as the π-π and CH-π interactions influence the packing structure of TTF molecules in the crystals. The conductive properties of the crystal are directed by the packing.[45] As showed in Figure 1- 15, the main types of packing relevant for TTF derivatives are: herringbone-like structure (a and b), 1D-π-stacking (c) and 2D- π-staking (d).

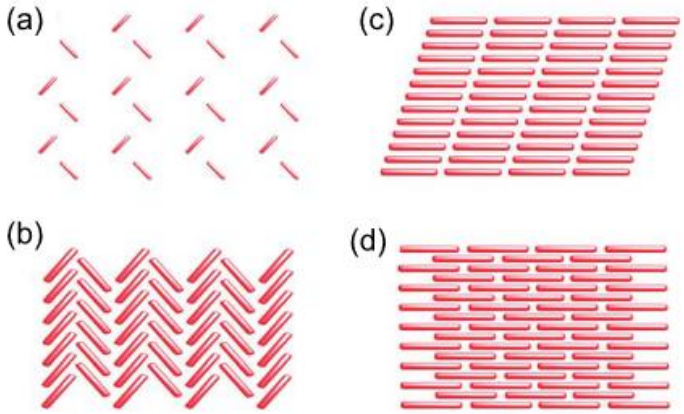


Figure 1- 15. Main packing modes.[45]

To form stabilized charge-transfer salts, several TTF derivatives with an extended π-conjugated core were used to decrease the charge repulsion and increase the polarizability.[46] In particular, the extension of the TTF skeleton with alkylthio groups capped, such as BEDT-TTF, or uncapped, such TMT-TTF, are investigated. The uncapped alkylthio group compounds compared to capped alkylthio group compounds present the disadvantage to be even less planar because of the unrestricted rotation of the outer substituents. However, depending on the size, shape, and nature of the substituents, the uncapped alkylthio group compounds may give interesting packing depending to the nature of the substituents and the interactions between donors and anions.[47]

Peiji et al.[48] synthesised and characterized $(TMT\text{-}TTF)I_3$ salt. The non-planar donor TMT-TTF becomes flat upon the formation of the radical salt. The structure displays regular segregated columns of TMT-TTF along the b axis. The S···S distance are between 3.75 and 3.98 Å along a axis (Figure 1- 16, b). The intercolumnar

[45] Frère, P.; Skabara, P. J. *Chem. Soc. Rev.* **2005**, *34* (1), 69–98.
[46] Wang, C.; Dong, H.; Jiang, L.; Hu, W. *Chem. Soc. Rev.* **2018**, *47* (2), 422–500.
[47] Saito, G.; Kumagai, H.; Katayama, C.; Tanaka, C.; Tanaka, J.; Wu, P.; Mori, T.; Imaeda, K.; Enoki, T.; Inokuchi, H.; Higuchi, Y.; Yasuoka, N. *Isr. J. Chem.* **1986**, *27* (4), 319–325.
[48] Peiji, W.; Takehiko, M.; Toshiaki, E.; Kenichi, I.; Gunzi, S.; Hiroo, I. *Bull. Chem. Soc. Jpn.* **1986**, *59*, 127-132.

sulphur-sulphur contact between the outer sulphur atoms is 3.92 Å (Figure 1- 16, a). At room temperature, the conductivity is 142.85 $S \cdot cm^{-1}$ with a metal-insulator transition around 100 K.

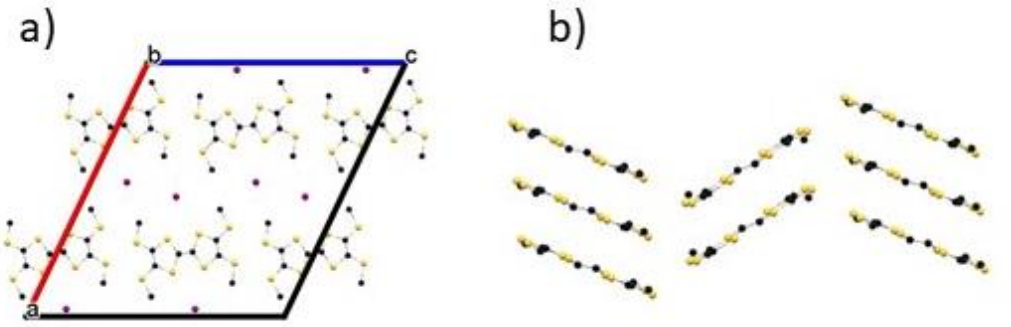


Figure 1- 16. $(TMT\text{-}TTF)I_3$ packing diagram.

3.3. Electrocrystallization of BEDT-TTF

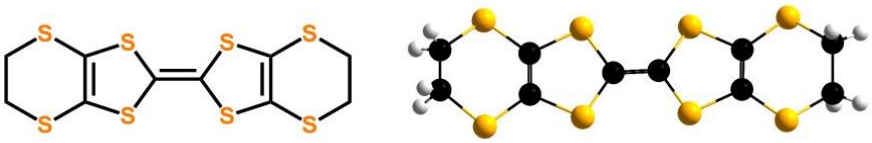


Figure 1- 17. BEDT-TTF structure.

Bis(ethylenedithio)tetrathiafulvalene BEDT-TTF, (Figure 1- 17) contains four extra sulphur atoms compared to TTF and a saturated non planar CH_2CH_2 group, thus favouring the formation of S···S multiple side intermolecular interaction in the layers of the radical cations, while the ethylene groups establish weak hydrogen bonds with the anions. The charged BEDT-TTF, due to its dimensionality and planar geometry, possesses strong interactions as face-to-face stacking and side-by-side interactions in the organic layer. According to that, a variety of possible packing arrangements are expected.

BEDT-TTF salts show five main packing motifs: α-, β-, κ-, θ-, λ- (Figure 1- 18).[49]

In the α-type packing the molecules are stacked in a herringbone pattern with S···S contacts shorter than van der Waals radius (3.60 Å). The θ-type shows same packing of α-type but with a difference in the number of molecules in the unit cell. The β-type packing has almost linear stacks which is close to the packing in the Bechgaard salts.[50]

The BEDT-TTF molecules form dimers through intermolecular interactions. These dimers are composed of two BEDT-TTF molecules that are stacked on top of each other in a head-to-tail fashion. The small interstack distances led to two-dimensional electronic structure. In the β and β'-phases of BEDT-TTF

[49] Toyota, N.; Lang, M.; Müller, J. **2007**. *Low-Dimensional Molecular Metals*; Springer.
[50] Jérome, D.; Mazaud, A.; Ribault, M.; Bechgaard, K. *J. Phys*. **1980**, *41*, 95.

compounds, the molecules pair up to form dimers that run parallel to each other. In the β-phase, the dimers are aligned in a straight, linear fashion, while in the β'-phase, the dimers are slightly tilted or skewed. Because of this difference in arrangement, it is commonly understood that β'-type salts exhibit stronger dimerization compared to β-type salts.[51]

A particular case is the κ-phase, which consists of interacting dimers that are almost orthogonal to each other and having inter- and intra-dimer interactions. As result, the κ-phase shows a quasi-2D electronic structure with a small in-plane anisotropy.

A series of BEDT-TTF salts were synthesised to investigate the structure-property relationships of conducting solids by controlling molecular structure and intermolecular interactions.

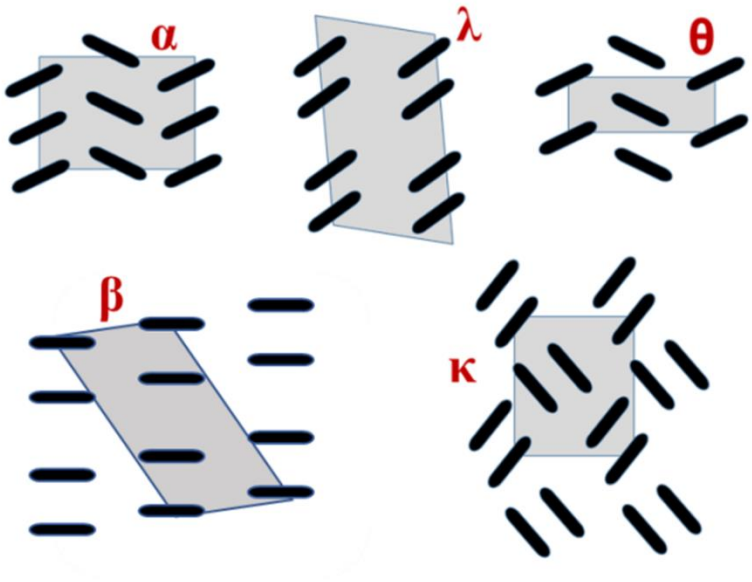


Figure 1- 18. Different packing types of BEDT-TTF salts.

The first reported BEDT-TTF conductor was [(BEDT-TTF)$_2$(ClO_4) $TCE_{0.5}$] in 1982.[52] The donor molecules are stacked along the c-axis. The overlap of the neighbouring molecules along this axis is relatively small. Conversely, along the *a*-axis, which is close to the elongated direction of the crystal, the donor molecules are arranged with each other giving short sulphur-sulphur distances (3.3-3.45 Å) resulting in a high conductivity (Figure 1- 19). Resistivity measurements showed that the conductivity increases from (26.31 $S{\cdot}cm^{-1}$) to a maximum at 16 K (1000 $S{\cdot}cm^{-1}$). At 1.4 K a slight decrease of conductivity to (666.66 $S{\cdot}cm^{-1}$) was observed indicating a metallic-insulator transition.

[51] Eto, Y.; Kawamoto, A. *Phys. Rev. B* **2010**, *81* (2), 020512.
[52] Saito, G.; Enoki, T.; Toriumi, K.; Inokuchi, H. *Solid State Commun.* **1982**, *42* (8), 557–560.

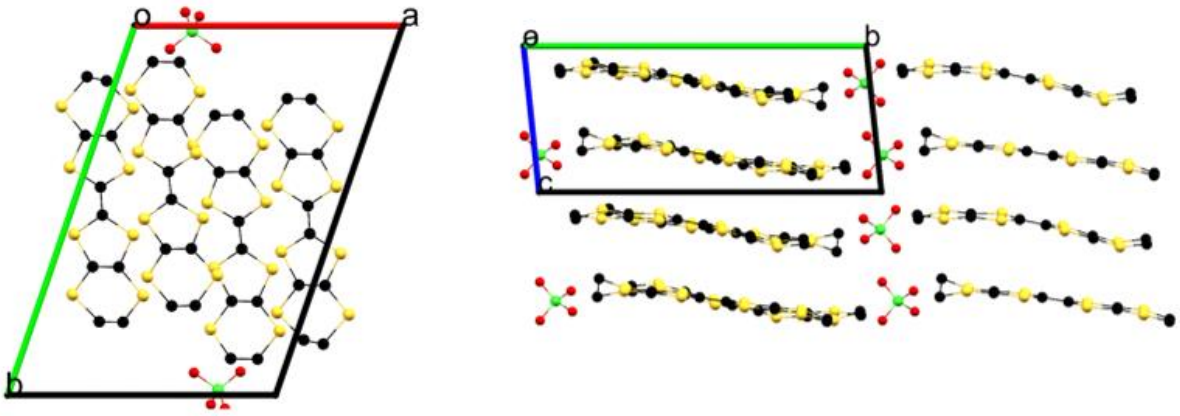


Figure 1- 19. $(BEDT\text{-}TTF)_2(ClO_4)$ packing diagram.

In 1983, the salt $(BEDT\text{-}TTF)_2(ReO_4)$ was synthesized and characterised by Parkin et al.[53] Along the *a*-axis, BEDT-TTF molecules are "zig-zagged" stacked providing cages in which the ReO_4^- anions sit. Along the *b* direction, strong S···S interactions between BEDT-TTF molecules can be observed in the Figure 1- 20. The 2:1 salt at 4 kbar and below 2 K gave a superconducting state.

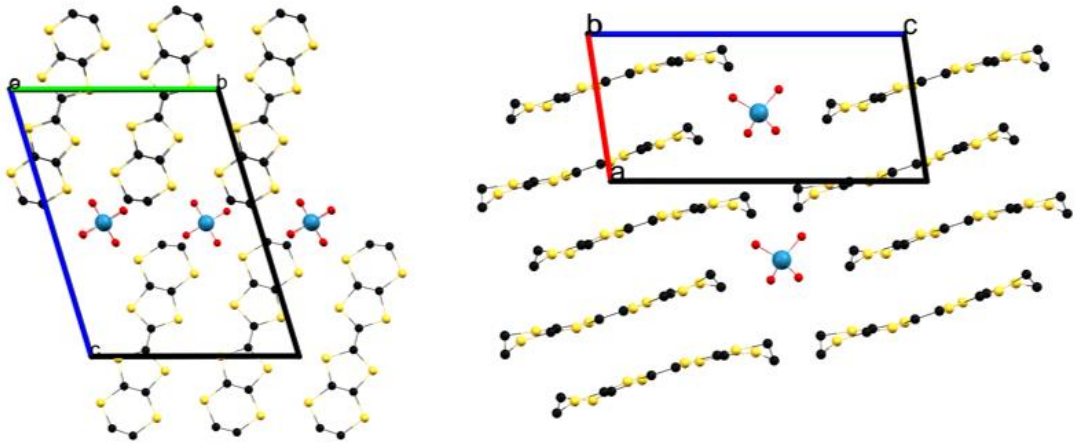


Figure 1- 20. $(BEDT\text{-}TTF)_2(ReO_4)$ packing diagram.

BEDT-TTF salts were synthesised using trihalogenated anions (such as IBr_2, BrI_2, ICl_2). These efforts led to the discovery a new ambient pressure superconductor, $\beta\text{-}(BEDT\text{-}TTF)_2IBr_2$ which exhibited a Tc of 2.8 K.[54] In contrast, no superconductivity was observed in the isostructural compound $\beta\text{-}(BEDT\text{-}TTF)_2I_2Br$.[55]

[53] Parkin, S. S. P.; Engler, E. M.; Schumaker, R. R. *Phys. Rev. Lett.* **1983**, *50* (4), 270–273.
[54] Williams, J. M.; Wang, H. H.; Beno, M. A.; Emge, T. J.; Sowa, L. M.; Copps, P. T.; Behroozi, F.; Hall, L. N.; Carlson, K. D.; Crabtree, G. W. *Inorg. Chem.* **1984**, *23*, 3839–3841.
[55] Emge, T. J.; Wang, H. H.; Leung, P. C. W.; Rust, P. R.; Cook, J. D.; Jackson, P. L.; Carlson, K. D.; Williams, J. M.; Whangbo, M. H. *J. Am. Chem. Soc.* **1986**, *108*, 695–702.

Another noteworthy compound, β'-(BEDT-TTF)$_2$ICl$_2$, behaves as a one-dimensional metal at room temperature and undergoes a metal-insulator transition at 22 K.[56]

In the case of the linear anion trisiodide, α-, β-, κ-, θ- polymorphic phases (BEDT-TTF)$_2$I$_3$ were found with metallic, isolating or superconducting properties.[57,58]

The β-(BEDT-TTF)$_2$I$_3$[59] phase was the first S-based organic salt to show superconductivity at ambient-pressure. Below the critical temperature, β-(BEDT-TTF)$_2$I$_3$ exhibits near-zero electrical resistance, meaning that the conductivity becomes extremely high. This region represents the superconducting state, where electric current can flow without any loss of energy due to resistance (Figure 1- 21. "Corrugated sheet" network of β-(BEDT-TTF)$_2$I$_3$ and the interstack S···S contacts and temperature dependence of the conductivity of β-(BEDT-TTF)$_2$I$_3$.). This property is relative to a "corrugated sheet" network packing featured by short interstack S···S contacts (<3.60 Å) between sheets of linear-symmetric I_3^- anions (Figure 1- 21).

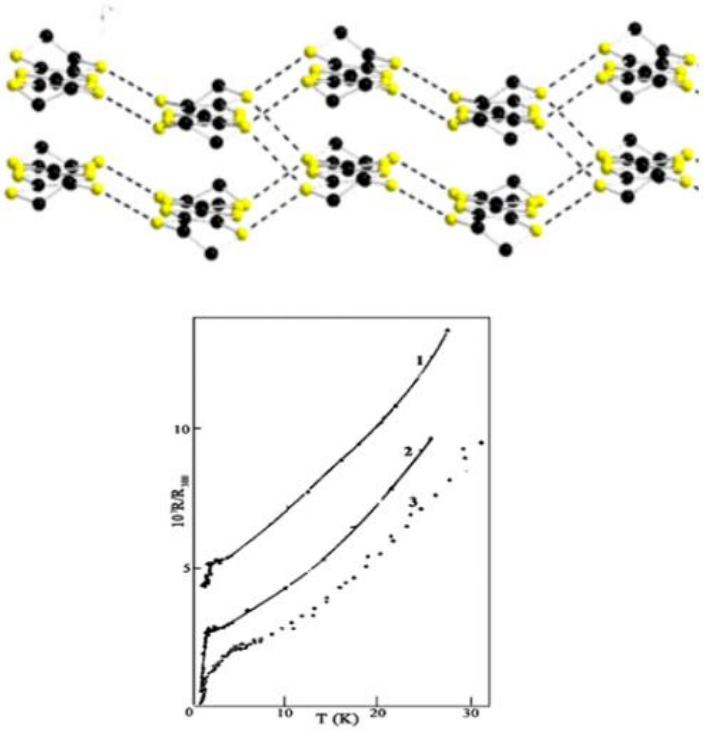


Figure 1- 21. "Corrugated sheet" network of β-(BEDT-TTF)$_2$I$_3$ and the interstack S···S contacts and temperature dependence of the conductivity of β-(BEDT-TTF)$_2$I$_3$.

[56] Leung, P. C. W.; Emge, T. J.; Schultz, A. J.; Beno, M. A.; Carlson, K. D.; Wang, H. H.; Firestone, M. A.; Williams, J. M. *Solid State Commun.* **1986**, *57*, 93–97.
[57] Montgomery, L. K.; Geiser, U.; Wang, H. H.; Beno, M. A.; Schultz, A. J.; Kini, A. M.; Carlson, K. D.; Williams, J. M.; Whitworth, J. R.; Gates, B. D.; Cariss, C. S.; Pipan, C. M.; Donega, K. M.; Wenz, C.; Kwok, W. K.; Crabtree, G. W. *Synth. Met.* **1988**, *27,* A195 -A207.
[58] Mori, H. *J. Phys. Soc. Jpn.* **2006**, *75* (5), 051003.
[59] Williams, J. M.; Emge, T. J.; Wang, H. H.; Beno, M. A.; Copps, P. T.; Hall, L. N.; Carlson, K. D.; Crabtree, G. W. *Inorg. Chem.* **1984**, *23* (17), 2558–2560.

The compound $(BEDT\text{-}TTF)_2Cu(NCS)_2$[60] has been identified as the first ambient pressure organic superconductor with a critical temperature (Tc) higher than 10 K. It exhibits a layered structure composed of donor and anion sheets. The packing pattern of the donor molecules BEDT-TTF is reported to be similar to that in κ-$(BEDT\text{-}TTF)_2I_3$. The donor molecules form a nearly analogous arrangement in both compounds (Figure 1- 22).

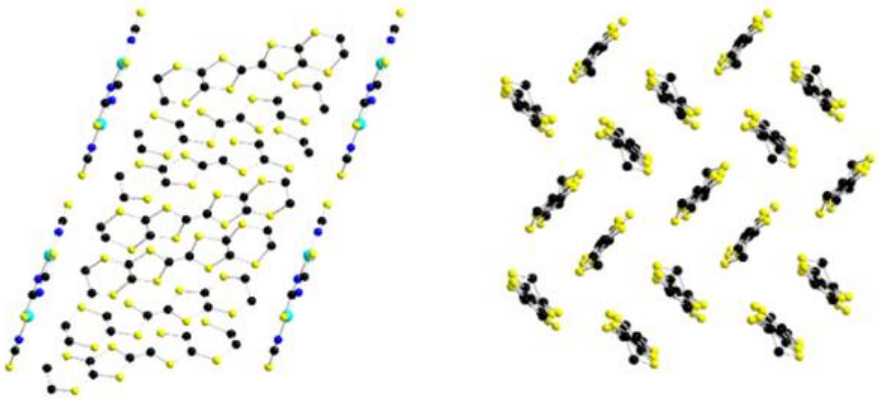


Figure 1- 22. $(BEDT\text{-}TTF)_2Cu(SCN)_2$ showing donor stacking and a view of the κ-phase.

[60] Urayama, H.; Yamochi, H.; Saito, G.; Sato, S.; Sugano, T.; Kinoshita, M.; Kawamoto, A.; Tanaka, J.; Inabe, T.; Mori, T.; Maruyama, Y.; Inokuchi, H. *Synth. Met*. **1988**, *27*, A393–A400.

A series of $(BEDT\text{-}TTF)_2MF_6$ salts were prepared to evaluate the dependence of anion volume on the donor packing and consequently on the physical properties.

Regarding the PF_6^- anion, two phases were found: α-$(BEDT\text{-}TTF)_2PF_6$[61] and β-$(BEDT\text{-}TTF)_2PF_6$[62]. The latter shows higher conductivity along the c axis thanks to short intermolecular S···S contact between neighbouring stacks (3.44-3.49 Å) (Figure 1- 23) and gives a sharp metal-insulator transition at 297 K.

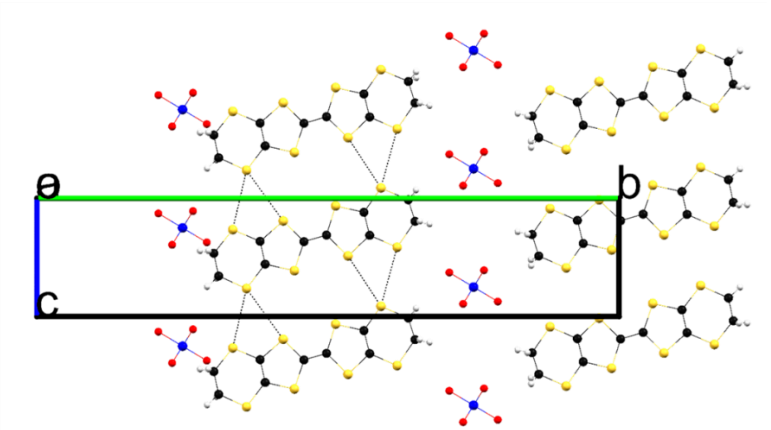


Figure 1- 23. Intermolecular S···S contact between neighbouring stacks of β-$(BEDT\text{-}TTF)_2PF_6$.

In the case of β-$(BEDT\text{-}TTF)_2SbF_6$ and AsF_6[63] the highest conductivity was measured along the b axis and have been observed a metal-insulator phase transition at 273 and 264 K respectively.

Kawamoto *et al.*[64] investigated about two δ-type polymorphs of $(BEDT\text{-}TTF)_2TaF_6$, respectively monoclinic and orthorhombic phases. While in the monoclinic phase, along the a-axis the BEDT-TTF molecular planes are almost parallel to each other, in the orthorhombic phase, donor planes are inclined alternately (Figure 1- 24).

[61] Kobayashi, H.; Kobayashi, A.; Saito, G.; Enoki, T.; Inokuchi, H. *J. Am. Chem. Soc.* **1983**, *105* (2), 297–298.
[62] Kobayashi, H.; Mori, T.; Kato, R.; Kobayashi, A.; Sasaki, Y.; Saito G.; Inokuchi, H. *Chem. Lett*. **1983**, *12*, 581–584
[63] Laversanne, R.; Amiell, J.; Delhaes, P.; Chasseau, D.; Hauw, C. *Solid State Commun.* **1984**, *52* (2), 177–181.
[64] Kawamoto, T.; Kurata, K.; Mori, T.; Kumai, R. *Magnetochemistry.* **2017**, *3* (1), 14.

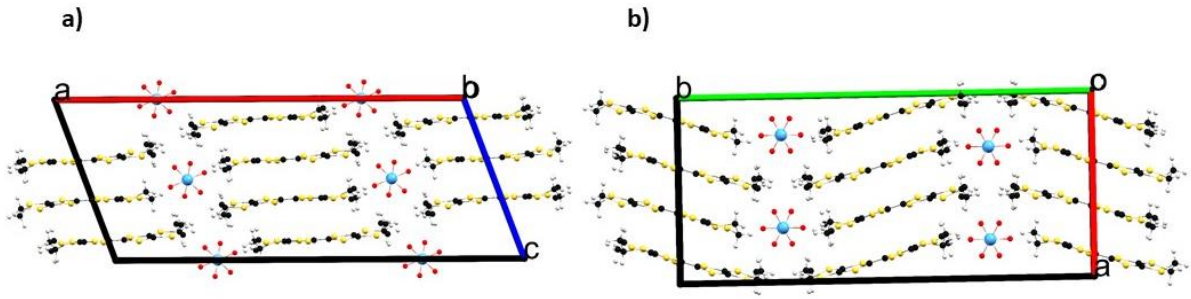


Figure 1- 24. δ-m $(BEDT\text{-}TTF)_2TaF_6$ (**a**) and the δ-o $(BEDT\text{-}TTF)_2TaF_6$ phase (**b**).

The phase transition is observed at 276 K for δ-m and 300 K for δ-o phases. Both can be classified as a dimer Mott insulator[65] as they maintain an insulating behaviour up to 350 K, suggesting that the electron-electron interactions and correlations within the dimers are responsible for the insulating behavior where the charge localization within the dimers hinders electron mobility and leads to an insulating state, despite the presence of partially filled energy bands.

A new 1:1 phase of $(BEDT\text{-}TTF)_2(TaF_6)_2\,CH_2Cl_2$ was prepared by Avarvari *et coll*.[66] In the packing, the donors formed isolated dimers of a bond-over-ring type with intermolecular S···S distances in the range 3.66–3.92 Å (Figure 1- 25). δ-$(BEDT\text{-}TTF)_2TaF_6$ is a semiconductor with a room temperature conductivity value of 0.001 to 0.0025 $S.cm^{-1}$, in agreement with the +1 oxidation state and strong dimerization of the donors.

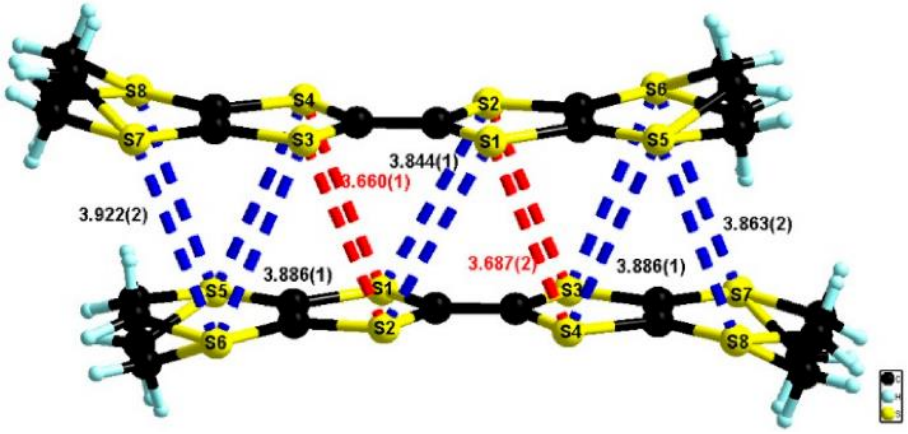


Figure 1- 25. Intermolecular S···S distances of $(BEDT\text{-}TTF)_2(TaF_6)_2\,CH_2Cl_2$.[66] **Error! Bookmark not defined.**

[65] Abdel-Jawad, M.; Terasaki, I.; Sasaki, T.; Yoneyama, N.; Kobayashi, N.; Uesu, Y.; Hotta, *Phys. Rev. B* **2010**, *82* (12), 125119.
[66] Allain, M.; Mézière, C.; Auban-Senzier, P.; Avarvari, N. *Crystals* **2021**, *11* (4), 386.

3.4. Synthesis and electrocrystallization of BVDT-TTF

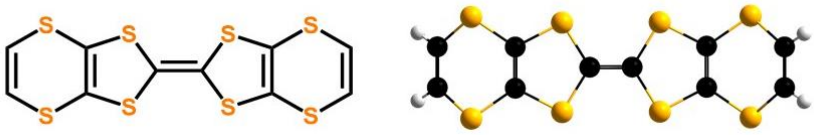


Figure 1- 26. BVDT-TTF structure.

An unsaturated version of BEDT-TTF as electroactive building blocks is the Bis(Vinylenedithio)-Tetrathiafulvalene (BVDT-TTF) (Figure 1- 26**Error! Reference source not found.**). It possesses an extended conjugated core and two additional double bonds regarding to BEDT-TTF. The resulting scaffold will maximize the orbital overlap.[67] These characteristics make BVDT-TTF an interesting building block for conductive materials.

Nakamura *et al*.[68] were the first to describe a pathway to synthesise the BVDT-TTF which is divided in four reaction steps (Figure 1- 27a). It starts by the zincate salt and 1,2-dichloroethyl ethyl ether under refluxing in acetone to get the 5-ethoxy-5,6-dihydro-[1,3]dithiolo[4,5-b][1,4]dithiine-2-thione. It follows an elimination of ethanol made by refluxing with anhydrous *p*-toluenesulfonic acid in benzene to give vinylenedithio-1,3-dithiol-2-thione, VDT with a 24% yield. Considering the drastic conditions, an easier alternative was found (Figure 1- 27b). The synthesis consists in an oxidation of the zincate salt by iodine to form the trithione. A Diels-Alder reaction between the Trithione and Phenyl vinyl sulfoxide forms VDT with a 25% yield. Garin *et al*.[69] already reported this reaction without a detailed description of the synthetic procedure. For both pathways, the next step is the transchalcogenation of the remaining thione group by mercuric acetate. Finally a homo-coupling in triethyl phosphite affords the target BVDT-TTF.

[67] Nakamura, T.; Iwasaka, S.; Nakano, H.; Inoue, K.; Nogami, T.; Mikawa, H. *Bull. Chem. Soc. Jpn.* **1987**, *60,* 365-368.
[68] Nogami, T.; Inoue, K.; Nakamura, T.; Iwasaka, S.-I.; Nakano, H.; Mikawa, H. *Synth. Met.* **1987**, *19* (1–3), 539–544.
[69] Garin, J; Andreu, R; Orduna, J; Royo, J, *Synth. Met.* **2001**, *120*, 749-750.

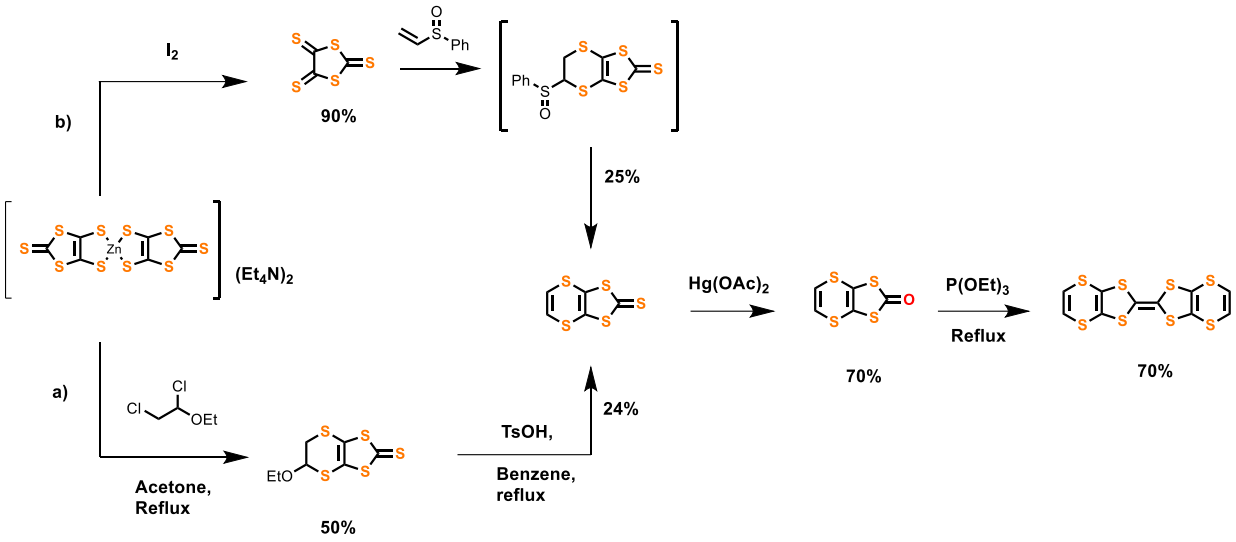


Figure 1- 27. Pathways for the synthesis of BVDT-TTF.

Kobayashi *et al*. [70] were the first to use BVDT-TTF as a donor molecule for conductive salts to get BVDT-TTF_2PF_6 crystals. BVDT-TTF molecules are stacked face-to-face to form a column along the c axis and PF_6^- anion stands on an inversion center (Figure 1- 28). The shortest S···S distance along the *c* axis is 3.43 Å, similar to the shortest S···S distances in BEDT-TTF structures. At room temperature BVDT-TTF_2PF_6 has a conductivity of 20 $S{\cdot}cm^{-1}$ similar to room temperature conductivity of β-$(BEDT\text{-}TTF)_2I_3$.

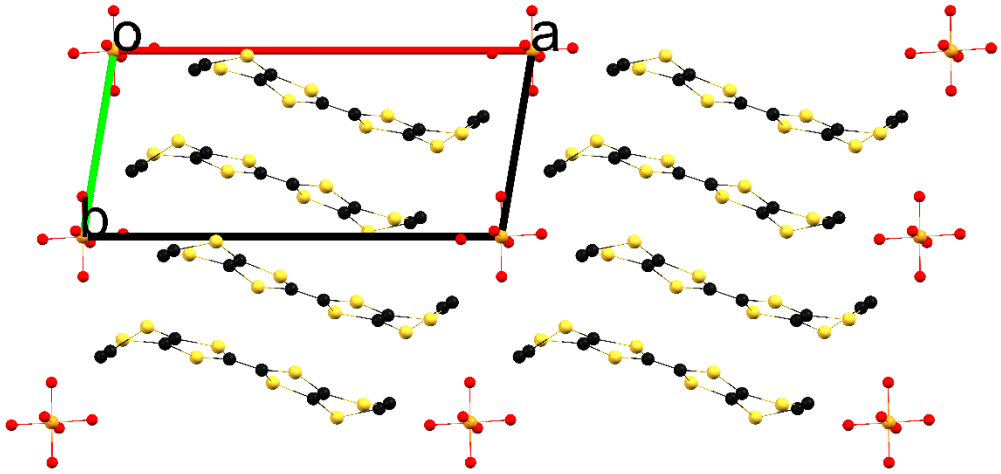


Figure 1- 28. BVDT-TTF_2PF_6 along c axis.

To the best of our knowledge, this is the only BVDT-TTF salt crystal structure already reported in the literature. Despite this, a few studies on BVDT-TTF salts were conducted in the 1980s, in which X-ray

[70] Kobayashi, H.; Kobayashi, A.; Nakamura, T.; Nogami, A.; Shirota, Y. *Chem. Lett.* **1987**, 559-562.

analysis was not yet accessible to all or the crystals were too small for measurements.[71, 72,73] Except for the case of $(BVDT\text{-}TTF)_2PF_6$, the stoichiometry of charge transfer complexes was determined by elementary analysis. As observable in Table 1- 2. Charge transfer complexes., most of the charge transfer complexes show semi-conductive values, except for BVDT-TTF-TCNQ. This is probably due to the small amount of charge transfer from the donor molecule to TCNQ.

Charge Transfer Complexes	Stoichiometry	Conductivity ($S{\cdot}cm^{-1}$)
$(BVDT\text{-}TTF)_xClO_4$	unknown	0.033
$(BVDT\text{-}TTF)_xAsF_6$	unknown	0.014
$(BVDT\text{-}TTF)_2PF_6$	2:1	20
BVDT-TTF TCNQ	1:1	insulator
$(BVDT\text{-}TTF)_2(F_4TCNQ)$	2:1	6.3
$(BVDT\text{-}TTF)_3(DDQ)_2$	3:2	0.2
$(BVDT\text{-}TTF)_3I_3$	3:1	5
BVDT-TTF Br_3	unknown	unknown

Table 1- 2. Charge transfer complexes.

The lack of knowledge on the reported salts sparked our interest in investigating the properties of other BVDT-TTF salts, which we will explore in more detail in Chapter 4.

4. Metal Organic Framework, MOFs

4.1. Definition, properties

Metal organic framework (MOFs) are a class of crystalline hybrid porous materials constructed from metal ions or cluster and organic linkers, which are linked through coordination bonds. The directionality imposed by the ligand and the coordination geometry give the overall geometry of the framework as observed in the Figure 1- 29. They form networks in one, two or three dimensions. High surface area, low densities, high porosity, thermal stability make these materials increasingly attractive.[74]

[71] Iwasaka, S.; Nogami, T.; Shirota, Y. *Synth. Met.,* **1988**, *26* (2), 177–184.
[72] Schumaker, R. R.; Lee, V. Y.; Engler, E. M. *J. Phys. Colloques* **1983**, *44* (C3), 1139-1145.
[73] Swietlik, R.; Garrigou-Lagrange, C. *Synth. Met.* **1993**, *55-57*, 2217-2221.
[74] Chae, H. K.; Siberio-Pérez, D. Y.; Kim, J.; Go, Y.; Eddaoudi, M.; Matzger, A. J.; O'Keeffe, M.; Yaghi, O. M. *Nature* **2004**, *427* (6974), 523–527.

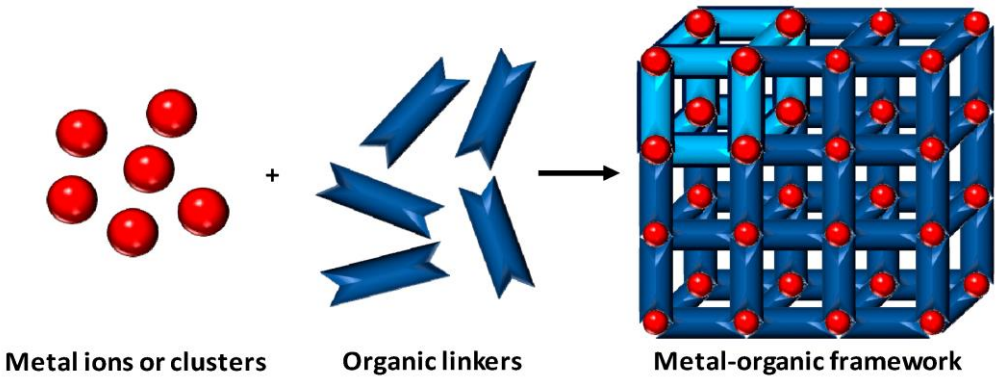


Figure 1- 29. Synthesis of MOFs.[75]

To facilitate the description of structures, MOFs can be divided in four levels (Figure 1- 30):

- The first level is the identification of the chemical constituents (metal ion and coordinating ligand) used to construct the MOF. The most common coordinating moieties used in MOF synthesis are carboxylate groups, or N- based ligands (pyridines or triazoles).
- The second level of structure involves the secondary building unit (SBU), which is the coordination site of multiple ligands with a metal ion into a relatively rigid and predictable geometry. SBUs are the structuring unit of the framework.
- The linking of multiple SBUs by bridging ligands, ligands linking two metal nodes, defines the internal framework, the third level of MOF structure. This third level encompasses the pores and cages of MOFs.
- The last level concerns the morphology such as size, shape, orientation of crystallites.[76]

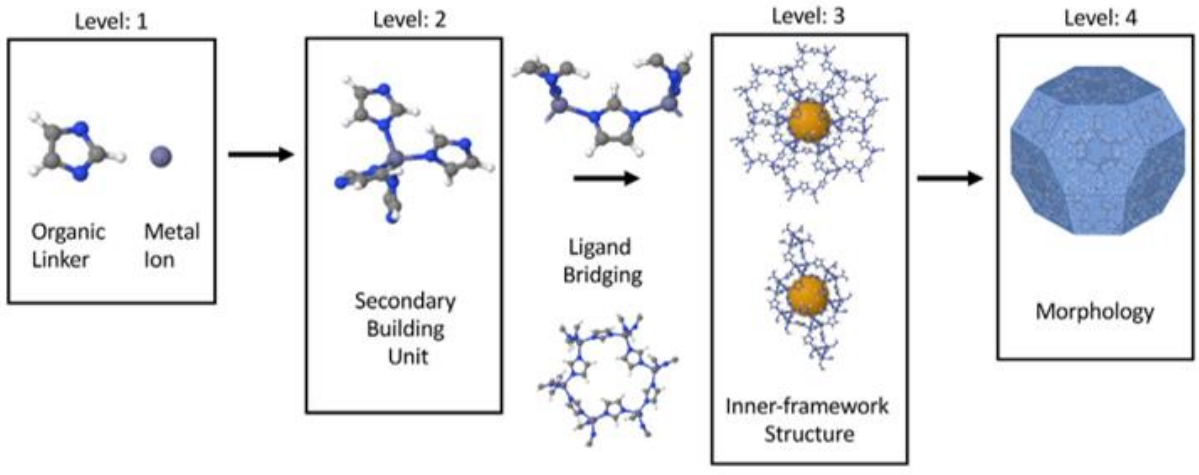


Figure 1- 30. Levels of construction in MOFs.[77]

[75] Carrasco, S. *Biosensors* **2018**, *8* (4), 92.
[76] Kalmutzki, M. J.; Hanikel, N.; Yaghi, O. M. *Sci. Adv.* **2018**, *4* (10), 2375-2548.
[77] Lawson, H. D.; Walton, S. P.; Chan, C. *ACS Appl. Mater. Interfaces* **2021**, *13* (6), 7004–7020.

Early examples of extended inorganic coordination compound can be traced back to the Prussian Blue, Fe^{III}_4 $[Fe^{II}(CN)_6]_3 \cdot H_2O$.[78] It was discovered in Berlin in the beginning of the 18th century. At that time only little was known about their structure and composition and no theory existed to rationalize the behaviour of these materials. In the following decades coordination chemistry started to be conceptualized by Werner *et al*.[79] They observed that complexes of formula $[M(NH_3)_4Cl_2]$ gave three distinct geometries: hexagonal planar, trigonal prismatic or octahedral. It follows then another Werner family of complexes, β-$[M(4\text{-}MePy)_4(NCS)_2]$ with M= Ni^{II}, Co^{II} , NCS=thiocyanate and 4-MePy= 4-Methylpyridine.[80] The crystal structure showed open spaces between the complexes. It was subsequently demonstrated that gases, such as nitrogen, oxygen, noble gases, or hydrocarbons were adsorbed in a reversible manner. The Werner complexes adopt a zeolite-like sorption behavior.[81] In 1897 Hofmann *et al*.[82] synthetized a network of formula $[Ni(CN)_2(NH_3)] \cdot C_6H_6$. The clear structure of the network was determined only 60 years later by Powell *et al*.[83] when the structural characterization by X-ray analysis on single-crystal became accessible. In Figure 1- 31, the structure shows two-dimensional layers of alternating octahedral and square planar Ni^{II} linearly connected through four CN^- moieties. The terminal NH_3 ligand is axially bound and points towards the adjacent layer, thus forming a cavity encapsulating benzene molecules.

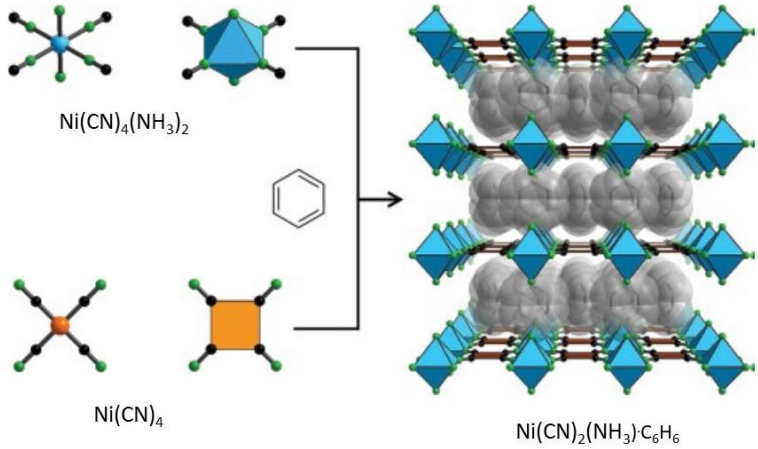


Figure 1- 31. Hofmann network: $Ni(CN)_2(NH_3) \cdot C_6H_6$.[84]

[78] Constable, E. C.; Housecroft, C. E. *Chem. Soc. Rev.* **2013**, *42* (4), 1429–1439.
[79] Werner, A. *Z. Anorg. Chem.* **1893**, *3* (1), 267–330.
[80] Soldatov, D. V.; Enright, G. D.; Ripmeester, J. A. *Cryst. Growth Des.* **2004**, *4* (6), 1185–1194.
[81] Allison, S.A.; Barrer, R.M. *J. Chem. Soc. A* **1969**, 1717–1723.
[82] Hofmann, K.A.; Küspert, F. *ZAAC* **1897**, *15,* 204–207.
[83] Rayner, J.H.; Powell, H.M. *J. Chem. Soc.*, **1952**, *67*, 319–328.
[84] Schoedel, A.; Yaghi, O. M. **2016,** 200–219. Macrocyclic and Supramolecular Chemistry. John Wiley & Sons.

Later, Iwamoto *et al*.[85] used two charged components to build a series of networks, with general formula $[M^{I}(NH_3)_2M^{II}(CN)_4]\cdot G$ (G = guest molecule). Guest molecules such as benzene, aniline, pyrrole or thiophene were enclathrated. Subsequently, ammonia ligands was replaced by α,ω-diaminoalkanes (HMDA = hexamethylene-1,6-diamine) that links adjacent layers and creates space for encapsulation of guests such as o-Toluidine (Figure 1- 32).[86] Mathey *et al*.[87] demonstrated that the variation of the linker length allows a selective encapsulation of aromatic guests.

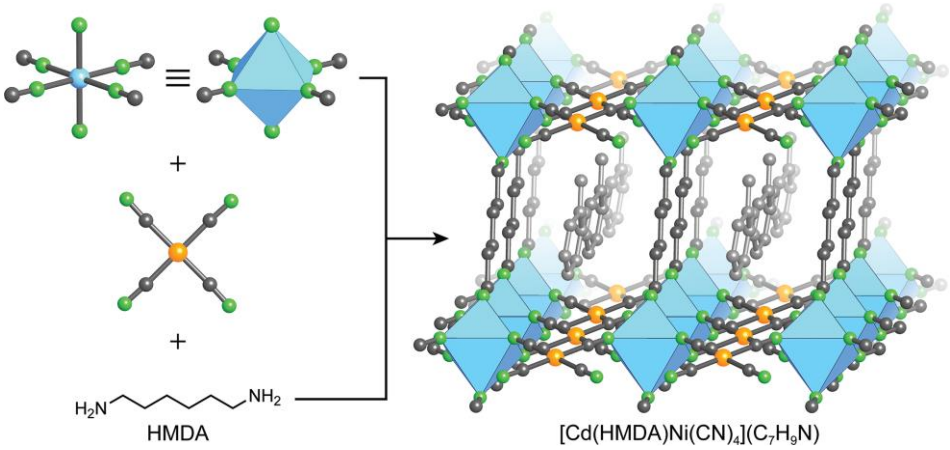


Figure 1- 32. $Cd(HMDA)Ni(CN)_4(C_7H_9N)$.[88]

The modern history of MOFs starts in the 90's. Robson *et al.*[89] utilized tetrahedral Cu(I) as single-metal building unit along with the tetrahedral organic linker 4,4',4'',4'''-tetracyanotetraphenylmethane (TCTPM) to create an infinite, non-interpenetrated, cationic framework. The resulting framework had the formula $[Cu(TCTPM)]^+$ and contained BF_4^- as counter anions into the pore. The high structural integrity of the framework was confirmed by the exchange of the previous counter anion with PF_6^-. In 1998, the MOF-2 network was synthesized from Zinc nitrate hexahydrate and 1,4-dicarboxylic acid (H_2BDC).[90] The structure is composed of $Zn_2(-COO)_4(H_2O)_2$ paddlewheel-like secondary building units (SBUs) that are in turn connected by BDC linkers. The resulting two-dimensional grid network is held together by strong hydrogen-bonding interactions among the axial water molecules as well as carboxylate moieties on the paddlewheel units.

Thanks to the high stability imparted by the SBUs it is possible to remove all solvent molecules from the pores without collapsing the structure of MOF-2, leading to permanent microporosity as evidenced by reversible nitrogen gas adsorption at 77 K. These experiments enabled the estimation of Langmuir apparent

[85] Iwamoto, T.; Nakano, T.; Morita, M.; Miyoshi, T.; Miyamoto T.; Sasaki, Y. *Inorg. Chim. Acta*, **1968**, *2*, 313–316.
[86] Nishikiori, S.-I.; Hasegawa, T.; Iwamoto, T. *J. Incl. Phenom. Macrocycl. Chem.*, **1991**, *11* (2), 137–152.
[87] Mathey, Y., Mazieres, C., Setton, R. *Inorg. Nucl. Chem. Lett.*, **1977**, *13*, 1–3.
[88] Yaghi, O. M.; Kalmutzki, M. J.; Diercks, M. J.; Diercks, C. S. **2019**. *Introduction to Reticular Chemistry: Metal-Organic Frameworks and Covalent Organic Frameworks.*
[89] Hoskins, B. F.; Robson, R. *J. Am. Chem. Soc.* **1989**, *111* (15), 5962–5964.
[90] Li, H., Eddaoudi, M.; Groy, T.L.; Yaghi, O.M. *J. Am. Chem. Soc.* **1998**, *120,* 8571–8572.

surface areas between 270 and 310 $m^2 \cdot g^{-1}$, as well as micropore volumes between 0.094 and 0.086 $cm^3 \cdot g^{-1}$.

Yaghi *et al*.[91] synthesized and characterized the well-known MOF-5 in 1999. The enormous popularity of this structure is related to a simple network accessible through rational design principles, a facile route of preparation, a very high porosity and stability.

This network (Figure 1- 33) is synthesized from zinc acetate and benzene-1,4-dicarboxylic acid. The SBU of MOF-5 is composed of a tetrahedral central oxide surrounded by four tetrahedrally coordinated Zn^{2+} ions which are in turn coordinated by a total of six bridging carboxylate groups (–COO). The large size (8.9 Å) and high connectivity of the SBUs in combination with the long BDC linker (6.9 Å) provides a three-dimensional structure with regular internal pore size (15.1 and 11.0 Å in diameter, and a pore aperture of 8.0 Å) containing DMF and chlorobenzene guests.

It possesses a BET surface area of 3800 $m^2.g^{-1}$ and pore volume of 1.55 $cm^3 \cdot g^{-1}$ and thermal stability up to 400° C. MOF-5 is used in several applications such as catalysis,[92] gas storage[93] and sensors.[94]

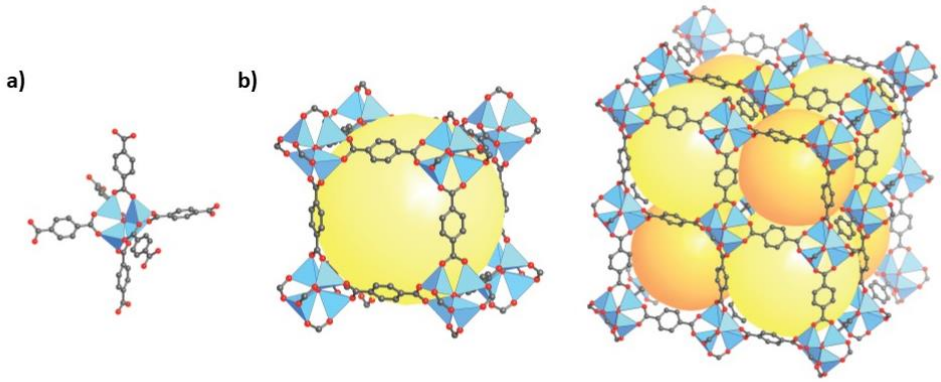


Figure 1- 33. a) coordination ligand-metal cluster b) cavities in the MOF-5 framework.

MOFs are considered chemically stable when they do not undergo a structural change after a chemical treatment. This can be evaluated by subjecting a material to different liquid or gaseous chemicals, followed by X-ray diffraction analysis to verify that the structure of the material has not been altered or degraded. Thermal stability is the ability of MOFs to withstand thermal treatment without any significant change in its structure. This can often be assessed by thermogravimetric analysis (TGA) where the mass loss is related to the temperature, indicating decomposition and/or changes in the structure. MOFs are also characterized by an architectural stability which is the ability of a framework material to retain its structural

[91] Li, H.; Eddaoudi, M.; O'Keeffe, M.; Yaghi, O. M. *Nature* **1999**, *402* (6759), 276–279.
[92] Kleist, W.; Maciejewski, M.; Baiker, A. *Thermochim. Acta* **2010**, *499* (1–2), 71–78.
[93] Aghajanloo, M.; Rashidi, A. M. *J. Chem. Eng. Process Technol*. **2014**, *05*, 1000203.
[94] Hou, C.; Peng, J.; Xu, Q.; Ji, Z.; Hu, X. *RSC Adv.* **2012**, *2* (33), 12696.

integrity in the absence of guest molecules. It can be proven by evacuating the solvent from the pores of a MOF and subsequent confirmation of its crystal structure and porosity.

Pores of MOF can vary in size from angstroms to several nanometers, bridging the gap between microporous (pore sizes of <2 nm) and mesoporous (pore sizes of 2–50 nm) materials. The pore volume and surface area of MOFs are controlled by the elongation and shape of the ligand, the SBUs, or through the presence of additives during the networks' synthesis.[95]

The high degree of structural predictability, the control of pores apertures size and shape, the flexibility, the high sorption capacities and complex sorption behaviour make MOFs a strong rival for zeolites.[96]

The performance of certain aspects of MOFs is often improved by a post-synthetic modification technique. It is a chemical modulation which includes a number of strategies shown in Figure 1- 34. The resulting MOF presents new physical/chemistry properties compared to its precursor.[97] The first strategy is the metal exchange, a), where the inorganic part is replaced, totally or partially, by new metal ions breaking the coordination bonds between the organic struts and the previous metal ion.

The metal incorporation, b), is a metal doping inside the pores of the MOF. The added metal, at this point, coordinates functional groups not yet involved in any link and thus modifies the structure.

By performing a ligand exchange, c), the functional groups can act as adsorption sites for various target molecules, mainly when achieved without changing the parent framework structure.

The ligand installation, d), has been developed to construct multivariate MOFs with functional groups precisely positioned which would otherwise be difficult to achieve.

The approach e) consists to remove some ligands to form defective MOFs. The defect engineering can excavate hidden active sites in MOFs, which can lead to better performance in many fields such as catalysis, gas adsorption, decontamination, or detoxification. While the decontamination provides to remove contaminants, the detoxification involves the chemical transformation or conversion of toxic substances into non-toxic forms.[98]

The last strategy, used in this thesis, is the guest replacement, f). It is common for MOFs to incorporate solvents, ions or molecules generated during the synthesis into the pores. In order to increase the accessible pore volume, the solvent molecules are removed. The replacement of the guest molecules introduces new properties in the MOF structure. These properties result from the ability of the guest molecule to interact with the framework in a highly specific fashion, creating, for example, new pathways for energy and charge transfer.

The final strategy, g), entails the post-synthesis incorporation of functional groups into the ligands of the MOF framework. This innovative approach results in the development of new MOFs endowed with multiple functionalities, a feat that may pose challenges or prove impractical through conventional direct synthetic

---

[95] Ahmadi, M.; Ayyoubzadeh, S. M.; Ghorbani-Bidkorbeh, F.; Shahhosseini, S.; Dadashzadeh, S.; Asadian, E.; Mosayebnia, M.; Siavashy, S. *Heliyon* **2021**, *7* (4), e06914.
[96] James, S. L. *Chem. Soc. Rev.* **2003**, *32* (5), 276.
[97] Mandal, S.; Natarajan, S.; Mani, P.; Pankajakshan, A. *Adv. Funct. Mater*. **2021**, *31*, 2006291
[98] Dissegna, S.; Epp, K.; Heinz, W. R.; Kieslich, G.; Fischer, R. A. *Adv. Mater*. **2018**, *30*, 1704501.

methods. Moreover, this process introduces novel interactions, thereby creating catalytic sites within the MOF structure, enhancing its potential for catalytic applications.[99]

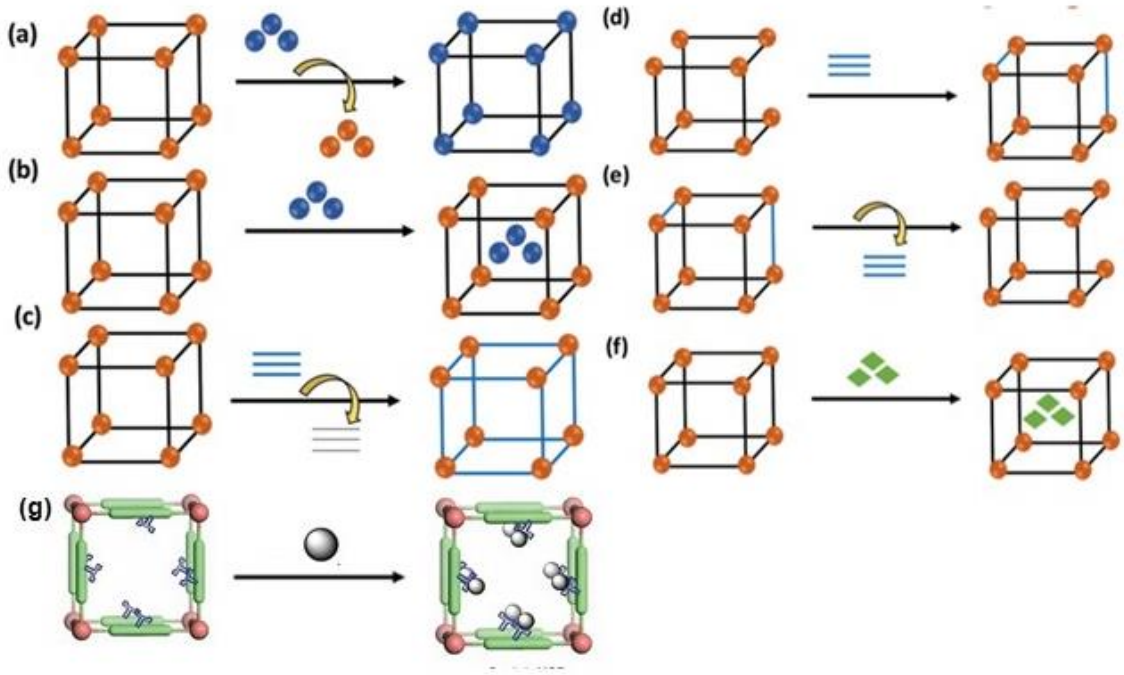


Figure 1- 34. a) metal exchange b) metal incorporation c) ligand exchange d) ligand installation e) ligand removal f) guest inclusion within the pores.[97]

4.2. Applications

The versatility of the design of MOFs makes them suitable for several application:

- Gas Storage: Many MOFs have been synthesized for CO_2, CH_4, H_2 capture from flue gas through guest–framework interactions directly into the pores of MOFs. Surface areas and specific site of adsorption are tuned to reach high effective capacities and selectivities.[100]

  The MOF NU-100, containing different size of pores, has a surface area of 6.143 $m^2 \cdot g^{-1}$. This is one of the highest surface area reported among porous materials. For NU-100, high-pressure hydrogen and carbon dioxide storage capacities were measured and with promising results: 164 $mg \cdot g^{-1}$ for hydrogen at 77 K and 2.315 $mg \cdot g^{-1}$ for carbon dioxide at 298 K. [101]

- Biomedical/Drug Delivery: MOFs have been explored in drug delivery applications due to the precise tunability, high surface areas, high loading capacities and the biocompatibility of its

[99] Yin, Z.; Wan, S.; Yang, J.; Kurmoo, M.; Zeng, M.-H. *Coord. Chem. Rev.* **2019**, *378*, 500–512.
[100] Heymans, N.; Bourrelly, S.; Normand, P.; Bloch, E.; Mkhadder, H.; Cooper, L.; Gorman, M.; Bouzidi, I.; Guillou, N.; De Weireld, G.; Devic, T. *J. Phys. Chem. C* **2020**, *124* (5), 3188–3195.
[101] Farha, O. K.; Özgür Yazaydın, A.; Eryazici, I.; Malliakas, C. D.; Hauser, B. G.; Kanatzidis, M. G.; Nguyen, S. T.; Snurr, R. Q.; Hupp, J. T. *Nature Chem* **2010**, *2* (11), 944–948.

separated components after the drug is released. MOFs can encapsulate a wide variety of small molecules and macromolecules and release them under an external stimuli such as pH or adenosine triphosphate ATP.[102]

A problem that is still relevant today concerns the fast kinetics of delivery of up to 3 days from several drug–MOF complexes. The performance of a serie of Zr-based MOF with different functionalized (bromo, nitro and amino) and extended linkers were analysed, in particular concern the drug loading experiments, amorphization process and the efficiency of the delivery. For an efficient release a balance between the pore size of the materials and the size of the guest molecules are indeed necessary, which is not provided by an amorphous material with collapsed pores.[103]

- Asymmetric Catalysis: enantiopure building blocks form chiral MOFs containing catalytic centres. The catalytic activities and stereoselectivities of MOFs are determined by the substrate diffusion through the channels, which are influenced by the sizes of the open channels.[104]

  Wang *et al.*[105] synthesized chiral Lewis acid catalysts starting by homochiral MOF, with formula $LCu_2(solvent)_2$ where L is chiral tetracarboxylate ligand derived from 1,1′-bi-2-naphthol. It is followed by a post-synthetic modification with $Ti(O'Pr)_4$ which organic substrates have access through the open channels or cavities (Figure 1- 35). In particular, organic substrates such as aromatic aldehydes are converted into chiral secondary alcohols in the presence of diethylzinc.

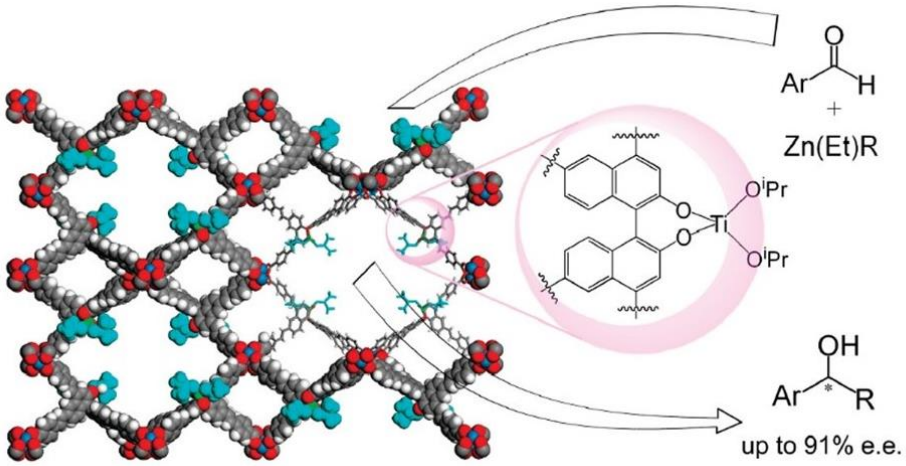


Figure 1- 35. Asymmetric alkyl- and alkynylzinc additions catalyzed by the CMOF/Ti-BINOLate catalyst within large open channels.[105]

[102] Lawson, H. D.; Walton, S. P.; Chan, C. *ACS Appl. Mater. Interfaces* **2021**, *13* (6), 7004–7020.
[103] Orellana-Tavra, C.; Marshall, R. J.; Baxter, E. F.; Lázaro, I. A.; Tao, A.; Cheetham, A. K.; Forgan, R. S.; Fairen-Jimenez, D. *J. Mater. Chem. B* **2016**, *4* (47), 7697–7707.
[104] Wang, C.; Zheng, M.; Lin, W. *J. Phys. Chem. Lett.* **2011**, *2* (14), 1701–1709.
[105] Ma, L.; Falkowski, J. M.; Abney, C.; Lin, W. *Nature Chem.* **2010**, *2* (10), 838–846.

4.3. Conductivity in MOFs

The electrical conductivity (σ) is determined by the high density (n) and high mobility (μ) of charge carriers. The charge carriers are electrons (e) and holes (h) which can have different effective concentrations and mobilities contributing to the overall conductivity according to the relation. The equation linking these factors is the following:[106]

$$\sigma = e(\mu_e n_e + \mu_h n_h)$$

μ and n depend on several factors related to the electronic structure of a material like crystal structure, bonding, valence electron counts, impurity concentrations and disorder.

According to the band theory, semiconducting materials are characterised by a delocalised valence band and a conduction band through which charge carriers are mobile. The energy difference separating the two levels (band gap, E_g) defines the properties of the material (Figure 1- 36):[107]

- Insulator characterized by low conductivity, $\sigma < 10^{-10}$ S.cm^{-1}, large $E_g > 4$ eV, which results in a very low population of the conduction band
- Metal characterized by high conductivity, $\sigma > 10^{2}$ S.cm^{-1}, where at least one band crosses the Fermi level (E_F), resulting in a continuum of allowed electronic states
- Semi-conductor characterized by an intermediate E_g that allows promotion of free charge carriers to the conduction band by thermal or photophysical excitation

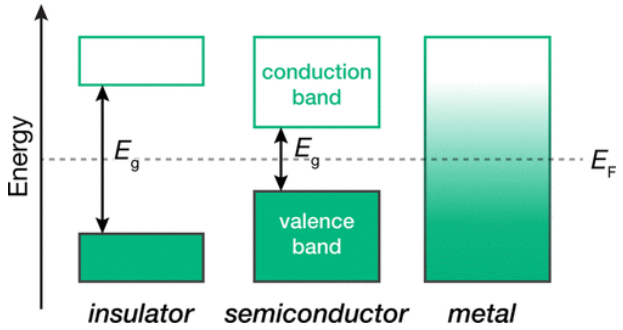


Figure 1- 36. Electronic structures of a generic insulator, semiconductor, and metal.

MOFs are generally poor electrical conductors because of the insulating character of organic ligands and the unfavourable orbital overlap between the metal d-orbital with the ligand p-orbital. Charge-carriers are localized and the electronic band structures display low dispersion and large energy gaps between their

[106] Sun, L.; Campbell, M. G.; Dincă, M. *Angew. Chem. Int. Ed.* **2016**, *55* (11), 3566–3579.
[107] Nasalevich, M. A.; van der Veen, M.; Kapteijn, F.; Gascon. *Cryst Eng Comm* **2014**, *16* (23), 4919–4926.

frontier orbitals. A classic example is MOF-5 that shows a band gap of 4.6 eV (Figure 1- 37).[108] The vast majority of band structures for MOFs are computed using density functional theory (DFT) calculations. The accuracy of a computed electronic band structure is determinate by the quality of the input crystal structure and the functional used. Significant structural disorder and large unit cells in many MOFs can introduce considerable challenges for band structure calculations and preclude the use of more accurate but more computationally intensive functionals. The relevance of computed band structures to the real transport properties of a MOF should be considered in relation to the structural integrity of the model and practical constraints on computational resources.[109]

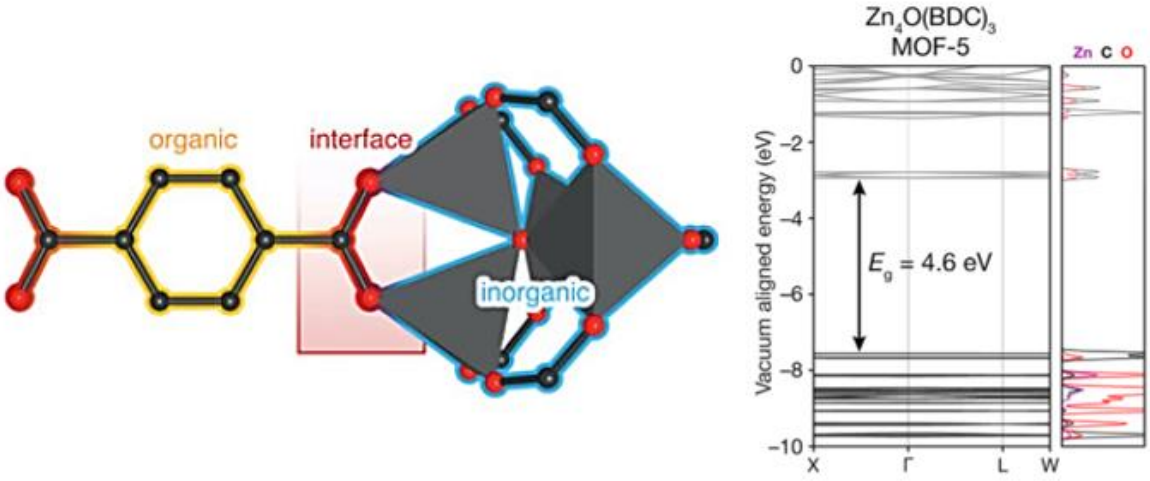


Figure 1- 37. Poor electronic communication between the interface of the inorganic and organic regions and the resulting electronic band structure.[108]

In the past 10 years, several studies have focused on the development of electrically conductive MOFs as a promising class of porous conductors. Thanks to a facile charge transport and a high surface area, conductive MOFs can be exploited in various applications such as:

- Supercapacitors: MOFs are a promising area of research for energy storage because the high surface area, porosity, and tunable properties make them attractive for storing and releasing electrical charge.[110] For example, $Ni_3(HITP)_2$ (HITP = 2,3,6,7,10,11-hexaiminotriphenylene) is well-know to have one of the highest recorded conductivities for MOFs, amounting to 150 $S \cdot cm^{-1}$.[111] Sheberla *et al.*[112] used $Ni_3(HITP)_2$ as supercapacitor electrode material showing an excellent electrical double-layer

[108] Walsh, A.; Butler, K. T.; Hendon, C. H. *MRS Bull.* **2016**, *41* (11), 870–876.
[109] Butler, K. T.; Hendon, C. H.; Walsh, A. *J. Am. Chem. Soc.* **2014**, *136*, 2703-2706.
[110] Niu, L.; Wu, T.; Chen, M.; Yang, L.; Yang, J.; Wang, Z.; Kornyshev, A. A.; Jiang, H.; Bi, S.; Feng, G. *Adv. Mater.* **2022**, *34* (52), 2200999.
[111] Day, R. W.; Bediako, D. K.; Rezaee, M.; Parent, L. R.; Skorupskii, G.; Arguilla, M. Q.; Hendon, C. H.; Stassen, I.; Gianneschi, N.; Kim, P. *ACS Cent. Sci*. **2019**, *5,* 1959–1964.
[112] Sheberla, D.; Bachman, J. C.: Elias, J. S.; Sun, C. J.; Shao-Horn, Y.;Dincă, M. *Nat. Mater.* **2017**, *16*, 220.

capacitance, EDLC performance. At a current density of 0.05 $A \cdot g^{-1}$ and a voltage of 1 V, it demonstrated a specific capacitance of 111 $F \cdot g^{-1}$, which is a measure of the amount of charge it can store per unit mass of the electrode material. The specific area capacitance was found to be approximately 18 $\mu F \cdot cm^{-2}$. This value indicates the ability of $Ni_3(HITP)_2$ to store a significant amount of charge within its porous structure.

- Batteries: ion diffusion is possible through the porous structure of MOFs. The incorporation of electroactive sites offers infinite possibilities for the search of candidate electrode materials in battery systems.[113] In particular, Fe-based MOFs are investigated as electrode materials for Lithium-Ion Batteries (LIBs) thanks to the capacity to store lithium ions exploiting the Fe^{III}/Fe^{II} redox couple.[114]
- Chemiresistive sensing: MOF-based chemical sensors are used to transduce sensing signals. The low band gap or high electrical conductivity of some MOFs allow the transport of electrical signals. In addition, the storage property of MOFs and the selection of guest molecules make them a promising devise for selective chemical sensors. A non-enzymatic Glucose sensors based on the direct electrocatalysis of electrode materials was designed by Zhou *et al*.[115] Mn_2(Ni-bis(dithiolene-dibenzoic acid) MOFs oxidizes glucose to glucolactone thanks to the highly oxidizing power of NiS_4 center. The electrode was prepared in a one-step hydrothermal method, in which the MOF were coated on copper foam (CF). The electrode shows high sensitivity of 27.9 $A.M^{-1} \cdot cm^{-2}$. The limit of detectability is 1.0×10^{-7} M and the range of a wide linear detection goes from 2.0×10^{-6} to 2.0×10^{-3} M that appears to be extensive for glucose detection in the blood, considering the normal range of 3.9-4.4 mmol/L.

Forming conductive MOFs is possible through the choice of metal ions possessing high-energy electrons or holes and/or organic ligands that contain stable radicals that can provide unpaired electrons and therefore facilitate charge transport.

According to the hopping theory,[116] the charge carrier transport mechanism occurs by hopping between localized states, while in the band theory,[117] the electrons jump up to the delocalized levels where they can move without resistance. Both modes are capable of reflecting charge transport in conductive MOFs and thanks to them, it is possible to identify several strategies for the construction of conductive MOFs[118,119]

---

[113] Weng, Y.-G.; Ren, Z.-H.; Zhang, Z.-R.; Shao, J.; Zhu, Q.-Y.; Dai, J. *Inorg. Chem.* **2021**, *60* (22), 17074–17082.
[114] Férey, G.; Millange, F.; Morcrette, M.; Serre, C.; Doublet, M.-L.; Grenèche, J.-M., Tarascon, J.-M. *Angew. Chem. Int. Ed*. **2007**, *46* (18), 3259–3263.
[115] Zhou, Y.; Hu, Q.; Yu, F.; Ran, G.-Y.; Wang, H.-Y.; Shepherd, N. D.; D'Alessandro, D. M.; Kurmoo, M.; Zuo, J.-L. *J. Am. Chem. Soc*. **2020**, *142* (48), 20313–20317.
[116] Movaghar, B.; Schirmacher, W. *J. Phys. C: Solid State Phys.* **1981**, *14* (6), 859–880.
[117] Parravicini, G. P.; Grosso, G. **2014**, 577-608 *Solid State Phys*.
[118] Shen, Y.; Liang, L.; Zhang, S.; Huang, D.; Zhang, J.; Xu, S.; Liang, C.; Xu, W. *Nanoscale* **2018**, *10* (4), 1622–1630.
[119] Xie, L. S.; Skorupskii, G.; Dincă, M. *Chem. Rev.* **2020**, *120* (16), 8536–8580.

by exploiting the metal-ligand coordination (Figure 1- 38, a and b), ligand-ligand π··π stacking (Figure 1- 38, c) and post-synthetic modification (Figure 1- 38, d).

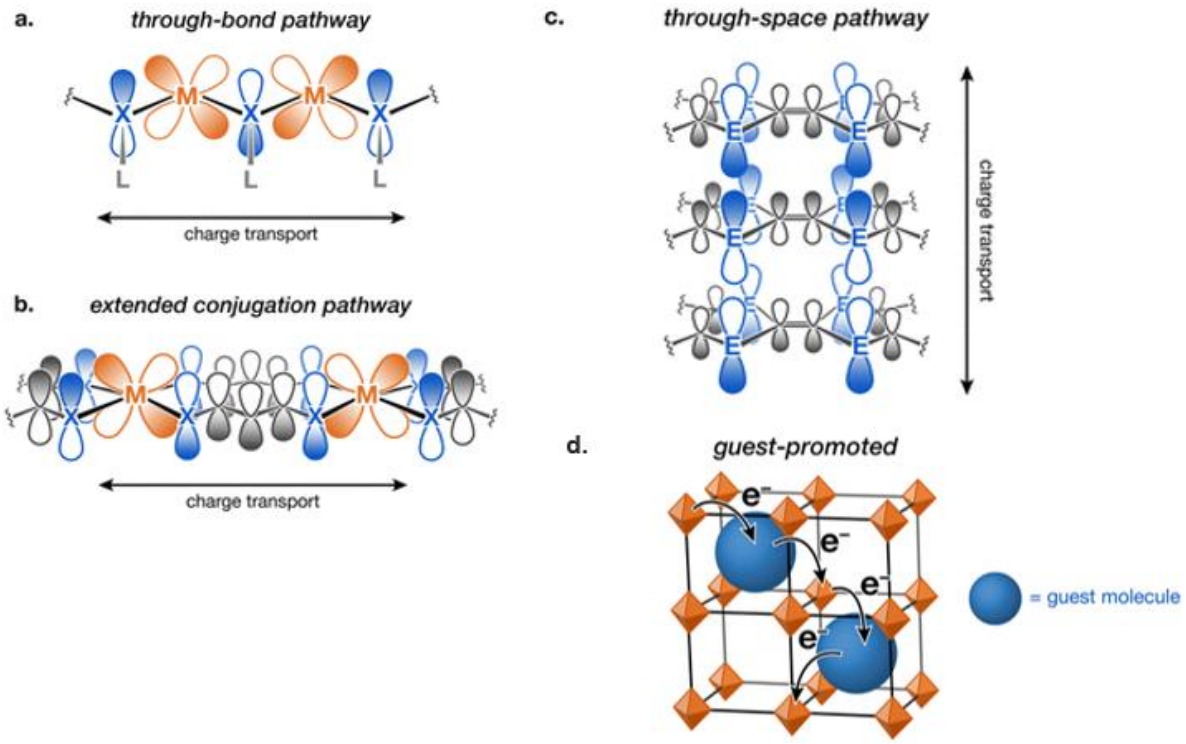


Figure 1- 38. Pathways for conductive MOFs.[119]

The through-bond pathway (Figure 1- 38, a) is relying on a good orbital overlap (π–d) between the metal and the ligand, with sulphur or nitrogen coordinating to the metals in most cases. The extended conjugation pathway (Figure 1- 38, b) also involves π–d conjugation. Using ligands containing chelating functional groups such as dithiols is possible to obtain an extended conjugation encompassing both the organic and inorganic components. The charge carriers are delocalized within the plane resulting in a small band gap. Ligands such as dihydroxybenzoquinone increases the conductivity according to their intrinsic redox active nature. During the synthesis or by post-synthesis modification ligands can be partially oxidized, thus introducing charge carriers into the frameworks.

The through-space pathway (Figure 1- 38, c) is found when ligands with a strong propensity for intermolecular interaction are used. In general, conjugated ligands with large planar surfaces create structures containing π···π stacking between organic ligands. The orbital overlap constructs an extended charge-transport pathway. The result is a structure with a close packing and sufficient orbital overlap between the neighbouring ligands. As is the case for the other approaches, partial oxidation of organic ligands provides charge carriers generating mixed-valence MOFs.

The guest-promoted pathway (Figure 1- 38, d) consists in the insertion of electroactive guest molecules into the pores of framework. These guests form charge transport pathways throughout the material through guest–guest or guest–framework interactions. Redox-active guest molecules have been widely

used to improve the conductivity of isolated structures. The downside of this strategy is that the accessible pore volume is reduced at the cost of electrical conductivity. In some cases, the guest is itself conductive, and simply provides a viable channel for charge transport to go through, while in others the guest induces a generation of charge carriers within the framework or structural transformations resulting in new conductive pathways that make the previously insulating framework conductive. The most widely used dopant is iodine and the first example was reported by Kobayashi *et al*.[120] Similarly, incorporation of TCNQ guest moieties into the pores leads to enhancement of the electrical conductivity.[121]

4.4. TTF as ligand for conductive MOFs

TTF is one of the most used scaffold in semi-conductive MOFs due to its electroactive nature and π···π stacking propensity. A series of isostructural MOFs containing tetrathiafulvalene-tetrabenzoate (H_4TTFTB) were synthesised by Park *et al*.[122] using Mn(II), Co(II), Zn(II), and Cd(II) as metals. The correlation of conductivity with the S···S distance and ionic radius of metals was deduced from these results. By using a metal cation with a larger ionic radius, an extension of the length of the metal-carboxylate chains was observed. The TTF stacks are squeezed, leading to a reduction in the S···S distance between the π-cores. According to that, Cd_2(TTFTB), which presents the largest cation radius (Cd^{2+}), has the shortest S···S distance (3.65 Å) while Co_2(TTFTB), with a small cation radius, shows an S···S distance of 3.77 Å. The short S···S distance implies a better p_z orbitals overlap between S and C atoms of the TTF stacks, thus ensuring a better conductivity according to principle of through-space mechanism. Cd_2(TTFTB) presents the highest conductivity of the series at 2.86 × 10^{-4} S·cm^{-1}.

	Ionic radius of M(II) (pm)	**S···S distance (Å)**	**Conductivity (S.cm^{-1})**
Co_2(TTFTB)	88.5	3.7732(26)	1.49 x 10^{-5}
Zn_2(TTFTB)	88	3.7568(13)	3.95 x 10^{-6}
Mn_2(TTFTB)	97	3.6929(6)	8.64 x 10^{-5}
Cd_2(TTFTB)	109	3.6538(23)	2.86 × 10^{-4}

Table 1- 3. Correlation between ionic radius of metals and S···S distance of TTF filaments.

[120] Kobayashi, Y.; Jacobs, B.; Allendorf, M. D.; Long, J. R. *Chem. Mater.* **2010**, *22* (14), 4120–4122.
[121] Usov, P. M.; Jiang, H.; Chevreau, H.; Peterson, V. K.; Leong, C. F.; D'Alessandro, D. M. *J. Phys. Chem. C* **2017**, *121* (47), 26330–26339.
[122] Park, S. S.; Hontz, E. R.; Sun, L.; Hendon, C. H.; Walsh, A.; Van Voorhis, T.; Dincă, M. *J. Am. Chem. Soc.* **2015**, *137* (5), 1774–1777.

As observed in the Figure 1- 39, the frameworks contain infinite 1D helical stacks of TTF. It possesses a BET surface area between 559 and 665 $m^2 \cdot g^{-1}$.

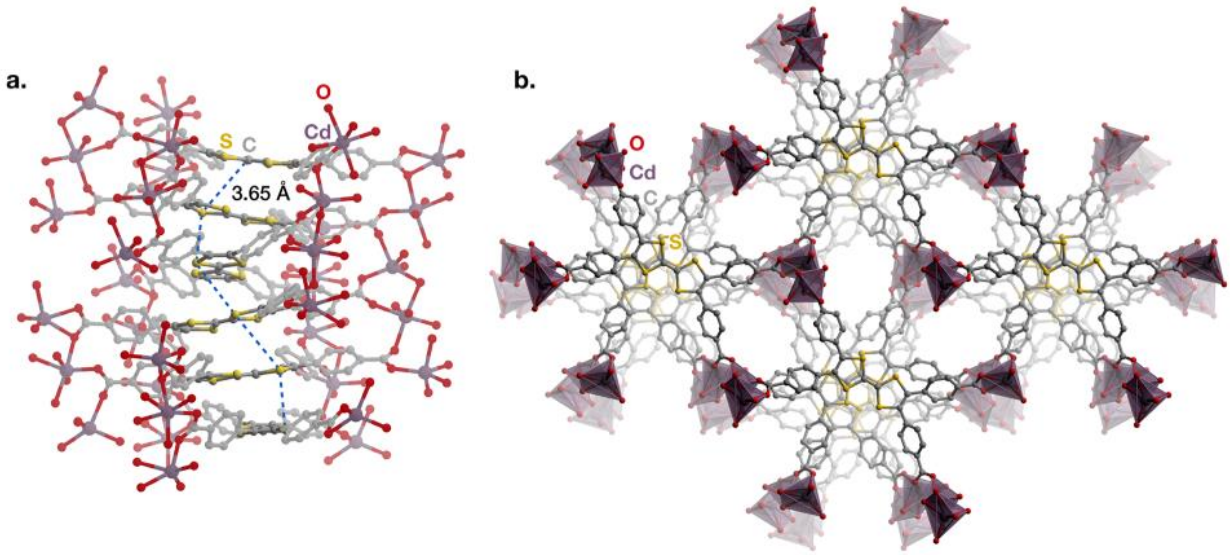


Figure 1- 39. a) Helical stacking of TTF cores with S···S distances contact, b) 1D channels parallel to the stacking direction.

The band structure of Zn_2TTFTB using density functional theory (DFT) was calculated (Figure 1- 40). The valence band is considerably wider than the conduction band, which can be expected from a hole conductor based on electron-donating TTF units. The valence band is defined by the p orbitals of the sulphur and the central carbon atoms of the TTF. This suggests that the charge transport involves these orbitals and that the band dispersion of a TTF stack would be dramatically varied as the overlap of these p orbitals changes.

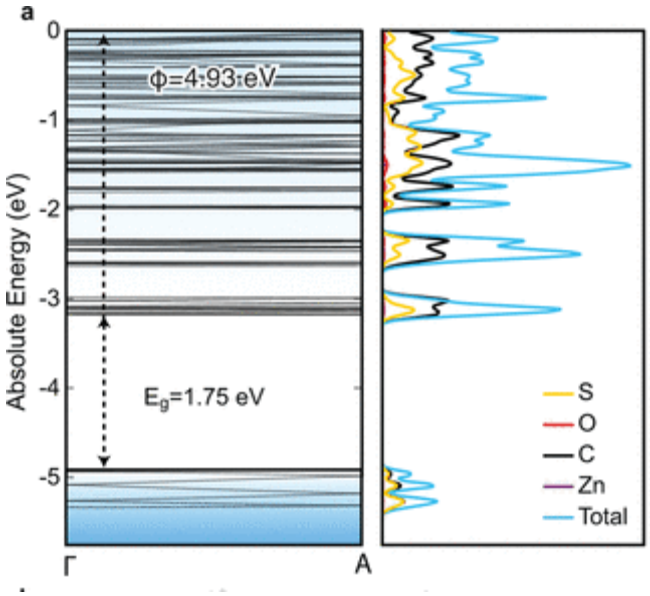


Figure 1- 40. Calculated band structure and projected density of states of Zn_2(TTFTB).[122]

3D Fe^{II}-based MOF, $Fe(dca)[TTF(py)_4](ClO_4)$ (dca = dicyanamide and TTF-$(py)_4$ = (4-pyridyl)$_4$tetrathiafulvalene), was synthesised by Wang *et al*.[123] (Figure 1- 41). The absence of continuous $\pi\cdots\pi$ stacking pathways between TTF molecules indicates that charge transport occurs through a hopping mechanism rather than band conduction. In fact, the additional space constraints and disrupts the formation of extended π-orbital networks and the charge carriers cannot delocalize over extended energy bands. Instead, charge carriers are localized on individual TTF molecules and move by hopping between neighbouring sites. As result, the conductivity is around 10^{-9} $S.cm^{-1}$, lower compared to materials with strong π-stacking interaction. To increase the conductivity a partial oxidation of the framework by I_2 was performed, which provides unpaired electrons as effective charge carriers. After the post-synthetic oxidation, the conductivity increased to 7.6×10^{-5} $S{\cdot}cm^{-1}$ thanks to the formation of TTF radical cation. This is evidenced by the lengthening of central C=C bond distance (1.41(2) Å) which is sensitive to the level of insertion in the stacks.[124]

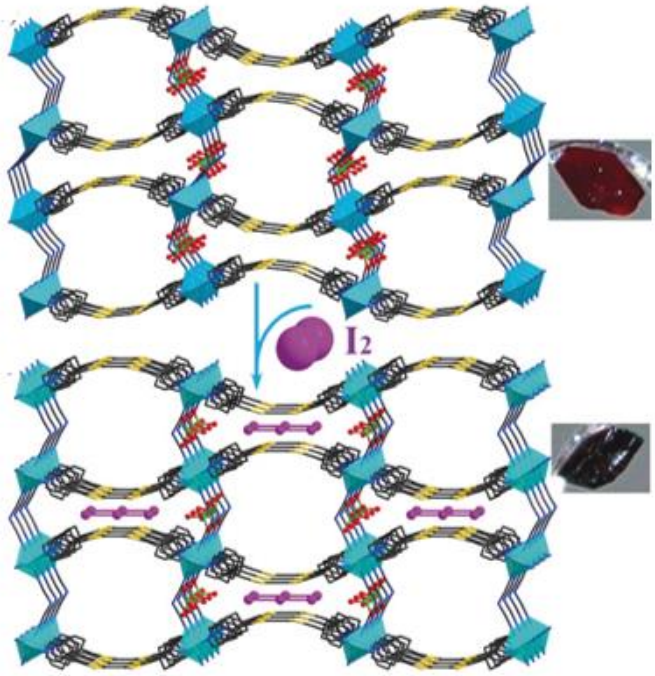


Figure 1- 41. 3D network of $Fe(dca)[TTF(py)_4](ClO_4)$ before and after insertion.[123]

[123] Wang, H.; Ge, J.; Hua, C.; Jiao, C.; Wu, Y.; Leong, C. F.;D 'Alessandro, D.M.; Liu, T.; Zuo, J. *Angew. Chem. Int. Ed.* **2017**, *56*, 5465–5470.
[124] Pop, F.; Auban-Senzier, P.; Frąckowiak, A.; Ptaszyński, K.; Olejniczak, I.; Wallis, J. D.; Canadell, E.; Avarvari, N. *J. Am. Chem. Soc.* **2013**, *135* (45), 17176–17186.

4.5. BVDT-TT as ligand for electro-active MOFs

Electrically conductive MOFs are a promising class of porous conductors. In the last few years, the use of TTF-based ligands as molecular building blocks for constructing conductive MOFs has been increasingly explored.

A key point for the growth of MOFs is the formation of strong metal–ligand bonds, carboxylate linkers being known to afford numerous stable coordination networks. Likewise, pyridyl groups have the characteristic of forming coordination with metals. Both have been used as functionalized groups for TTF-based ligands. These building blocks tend to form π-π interactions in extended structures, indeed, short S···S contacts causing higher conductivities. [100,125] However, the search for new building blocks of organic molecular conductors to use as ligand has been challenging. The BVDT-TTF turns out to be one of them. In fact, while the already described electro-active properties of TTF are preserved, the non-covalent interactions between organic ligands to construct an extended charge-transport pathway are amplified. This effect appears due to the addition of the two 1,4-dithiine rings. The addition of double bond replacing the ethylene group of BEDT-TTF avoids the problem of separating chiral components. This makes it an outstanding candidate for the conception of coordination networks with conducting properties (Figure 1- 42**Error! Reference source not found.**). Such extended π-architectures have never been incorporated in self-assembled structures despite their outstanding electrochemical properties: excellent charge carrier properties, extended delocalization, and several accessible and stable redox states. For this reason, the thesis project focused on the synthesis of new BVDT-TTF-based ligands and strategies for the realisation of MOFs dealt with in Chapters 2 and 3.

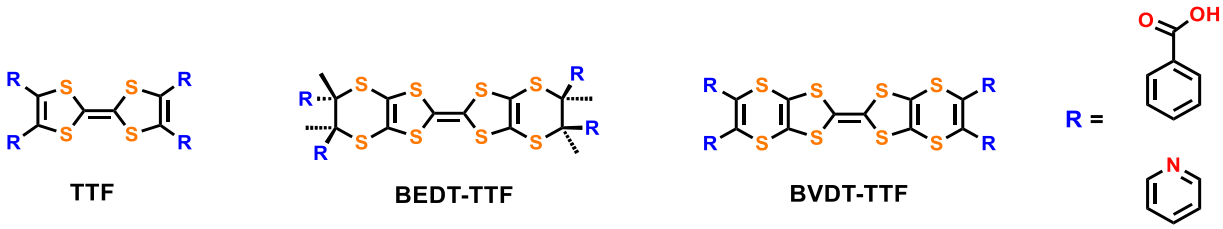


Figure 1- 42. Overview of TTF, BEDT-TTF and BVDT-TTF as building blocks.

[125] Castells-Gil, J.; Mañas-Valero, S.; Vitórica-Yrezábal, I. J.; Ananias, D.; Rocha, J.; Santiago, R.; Bromley, S. T.; Baldoví, J. J.; Coronado, E.; l Souto, M.; Mínguez Espallargas, G. *Chem. Eur. J.* **2019**, *25*, 12636 – 12643

CHAPTER II

Synthesis of functionalized BVDT-TTF

CHAPTER II: Synthesis of functionalized BVDT-TTF

1. Electro-active MOFs : ligand design

Achieving high electrical conductivity in Metal-Organic Frameworks (MOFs) is a persistent challenge. This is due to the intricate relationships that exist amongst the MOF's structure, connectivity, and electrical properties. MOFs, composed of metal ions or clusters coordinated with organic ligands, exhibit diverse and tuneable structures.[1,2] However, the translation of this structural diversity into electrical conductivity is not straightforward. Factors such as the presence of accessible pathways for charge transport, efficient electron delocalization, and the suitable energy levels of the molecular orbitals play vital roles in determining the electrical properties of MOFs. By systematically studying the relationships between the structure, connectivity and electrical behaviour of MOFs, it is possible to design and synthesise MOFs with improved electrical conductivity for applications in areas such as energy storage and electronics.[3,4]

The occurrence of high electrical conductivity in MOFs is still scarcely reported in the literature. The tendency of TTF to form $\pi\cdots\pi$ stacked columns with relatively short S···S interactions creates a favourable environment for electron mobility, promoting efficient charge transfer and facilitating high electrical conductivity. The transport properties of TTF-based systems are directly correlated with the stacking motifs observed within the structure. In particular, when adjacent ligands exhibit longer S···S contact distances, the resulting materials tend to exhibit lower electrical conductivities and higher activation energies. This highlights the critical role of intermolecular interactions and structural arrangements in governing the electrical properties of TTF-based systems. In addition, as redox-active building blocks, TTF exhibits the remarkable ability to undergo partial oxidation. When integrated into a PCP (Porous Coordination Polymer) structure, this could lead to the formation of mixed-valence MOFs. This partial oxidation facilitates the charge delocalization within the MOF structure, resulting in an enhanced electronic conductivity.[5,6]

Taking into account these principles, BVDT-TTF-based ligand were designed to be used as building blocks (Figure 2- 1). BVDT-TTF is a TTF fused to two 1,4-dithiin rings. The incorporation of four additional sulphur

---

[1] Medina, D. D.; Mähringer, A.; Bein, T. *Isr. J. Chem.* **2018**, *58* (9–10), 1089–1101.
[2] Ko, M.; Mendecki, L.; Mirica, K. A. *Chem. Commun.* **2018**, *54* (57), 7873–7891.
[3] Campbell, M. G.; Sheberla, D.; Liu, S. F.; Swager, T. M.; Dincă, M. *Angew. Chem. Int. Ed*. **2015**, *54*, 4349–4352.
[4] Feng, D.; Lei, T.; Lukatskaya, M. R.; Park, J.; Huang, Z.; Lee, M.; Shaw, L.; Chen, S.; Yakovenko, A. A.; Kulkarni, A.; Xiao, J.; Fredrickson, K.; Tok, J. B.; Zou, X.; Cui, Y.; Bao, Z. *Nat Energy* **2018**, *3* (1), 30–36.
[5] Park, S. S.; Hontz, E. R.; Sun, L.; Hendon, C. H.; Walsh, A.; Van Voorhis, T.; Dincă, M. *J. Am. Chem. Soc.* **2015**, *137* (5), 1774–1777.
[6] Castells-Gil, J.; Mañas-Valero, S.; Vitórica-Yrezábal, I. J.; Ananias, D.; Rocha, J.; Santiago, R.; Bromley, S. T.; Baldoví, J. J.; Coronado, E.; l Souto, M.; Mínguez Espallargas, G. *Chem. Eur. J.* **2019**, *25*, 12636 – 12643.

atoms in the ligand backbone enhances the π···π stacking propensity. This will provide an optimal overlap along the ligand stacks and therefore will increase the band dispersion.

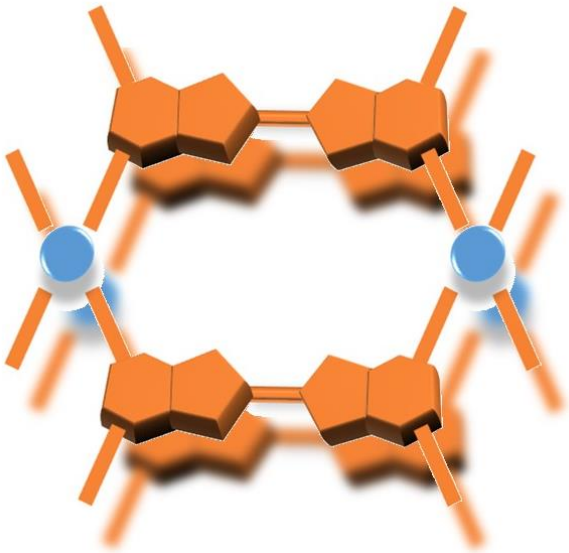


Figure 2- 1. Construction of MOFs based on BVDT-TTF building block.

While the synthesis of functionalized TTF is well-established, [7,8,9] the knowledge about BVDT-TTF and derivatives is relatively limited.

Various attempts have been made to functionalize the BVDT-TTF with coordinating moieties, as reported in the subsequent chapter. The first target molecule of the study was on the BVDT-TTF tetrabenzoic acid (Figure 2- 2). The benzoic group is ubiquitous in MOF synthesis and is reported to coordinate with a broad variety of transition metals and SBUs. The phenyl rings are organic spacers between the electroactive core and the coordination parts to regulate their orientation and number. The carboxylate linkers are well-known to form strong coordination bonds with various metal ions affording numerous stable, neutral and often highly porous 3D coordination networks.[10,11]

[7] Mitamura, Y.; Yorimitsu, H.; Oshima, K.; Osuka, A. *Chem. Sci.* **2011**, *2* (10), 2017.
[8] Batsanov, A. S.; Bryce, M. R.; Chesney, A.; Howard, J. A. K.; John, D. E.; Moore, A. J.; Wood, C. L.; Gershtenman, H.; Becker, J. Y.; Khodorkovsky, V. Y.; Ellern, A.; Bernstein, J.; Perepichka, I. F.; Rotello, V.; Gray, M.; Cuello, A. O. *J. Mater. Chem.* **2001**, *11* (9), 2181–2191.
[9] Giacalone, F.; Herranz, M.; Grüter, L.; González, M. T.; Calame, M.; Schönenberger, C.; Arroyo, C. R.; Rubio-Bollinger, G.; Vélez, M.; Agraït, N.; Martín, N. *Chem. Commun.* **2007**, No. 46, 4854.
[10] De, S.; Devic, T.; Fateeva, A. *Dalton Trans.* **2021**, *50* (4), 1166–1188.
[11] Guillerm, V.; Ragon, F.; Dan-Hardi, M.; Devic, T.; Vishnuvarthan, M.; Campo, B.; Vimont, A.; Clet, G.; Yang, Q.; Maurin, G.; Férey, G.; Vittadini, A.; Gross, S.; Serre, C. *Angew. Chem. Int. Ed.* **2012**, *51* (37), 9267–9271.

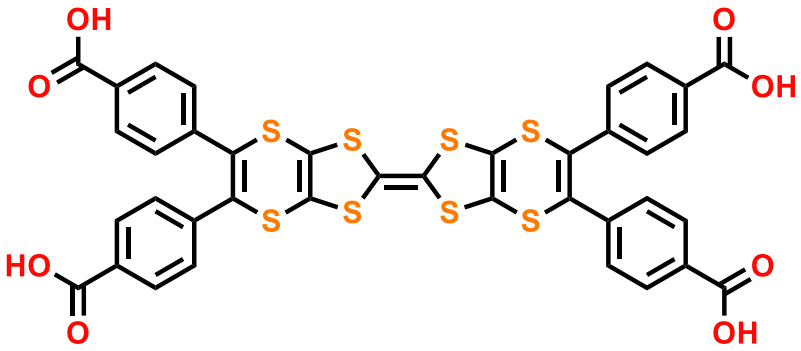


Figure 2- 2. Target BVDT-TTF tetrabenzoic acid.

2. Synthetic strategy for a direct functionalization of the BVDT-TTF

2.1. Synthesis of BVDT-TTF and functionalized BVDT-TTF in prior studies

Although the synthesis of functionalized BVDT-TTF derivatives is an area of interest, the number of prior studies exploring this topic is relatively limited. In chapter 3, the synthesis and self-assembly of tetrapyridine BVDT-TTF (BVDT-TTF-Py_4) compound, reported in 2009 by Almeida *et al*.[12] will be discussed. This compound bears four pyridine functional groups that able to form coordination bonds with metal ions. This enhanced connectivity in the MOF structure facilitates the formation of extended structures, leading to the creation of MOFs with well-defined and easily accessible pores.

In early studies, the synthesis of functionalized BVDT-TTF has been achieved through a reaction involving a 1,8-diketone and Lawesson's reagent (LR)[13] or phosphorus pentasulfide (P_4S_{10}).[14] The synthesis of TTF molecules with fused thiophene and 1,4-dithiin rings, along with thien-2-yl substituents was accomplished through the following steps (Figure 2- 3). First, the zincate salt was reacted with 2-(2-bromoacetyl)thiophene, resulting in the formation of a diketone derivative. The reaction continues with a cyclization[15] of the 1,8-diketone with phosphorus pentasulfide under basic conditions to afford the dithiin derivate and an undesirable thiophene-1,3-dithiole-2-thione product. After a transchalcogenation reaction followed by phosphite coupling, the final compound was obtained.[16]

---

[12] Brooks, A. C.; Day, P.; Dias, S. I. G.; Rabaça, S.; Santos, I. C.; Henriques, R. T.; Wallis, J. D.; Almeida, M. *Eur. J. Inorg. Chem.* **2009**, *10*, 3084–3093.
[13] Ozturk, T.; Ertas, E.; Mert, O. *Chem. Rev.* **2007**, *107*, 5210–5278.
[14] Ozturk, T. *Tetrahedron Letters* **1996**, *37* (16), 2821–2824.
[15] Cinar, M. E. *Comput Theor Chem.* **2019**, *1170*, 112641.
[16] Ertas, E.; Bildirir, H.; Sahin, O.; Oksen, I. *Phosphorus Sulfur Silicon Relat. Elem.* **2013**, *188* (12), 1835–1844.

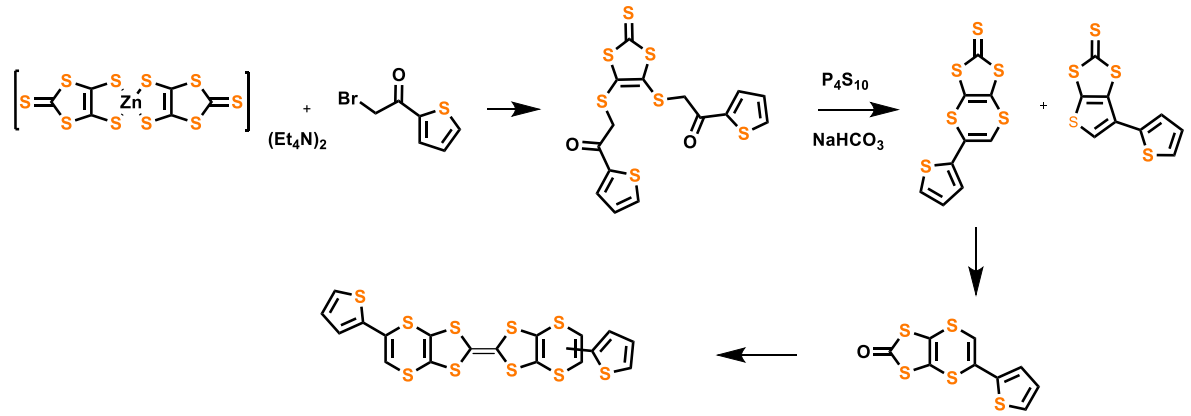


Figure 2- 3. Synthesis of BVDT-TTF molecules with fused thiophene and 1,4-dithiin rings.

Ertas *et al*.[17] reported another example of cyclization involving a 1,8-diketone and P_4S_{10} (Figure 2- 4). The synthesis of the 1,8-diketone was achieved by reacting sodium dithiolene with desyl chloride. When this 1,8-diketone reacted with P_4S_{10}, it formed the 1,4-dithiin ring under relatively short reaction times and dark conditions. Interestingly, upon increasing the reaction time, a rearrangement process occurred, leading to the formation of diphenyl-thieno-dithiole.

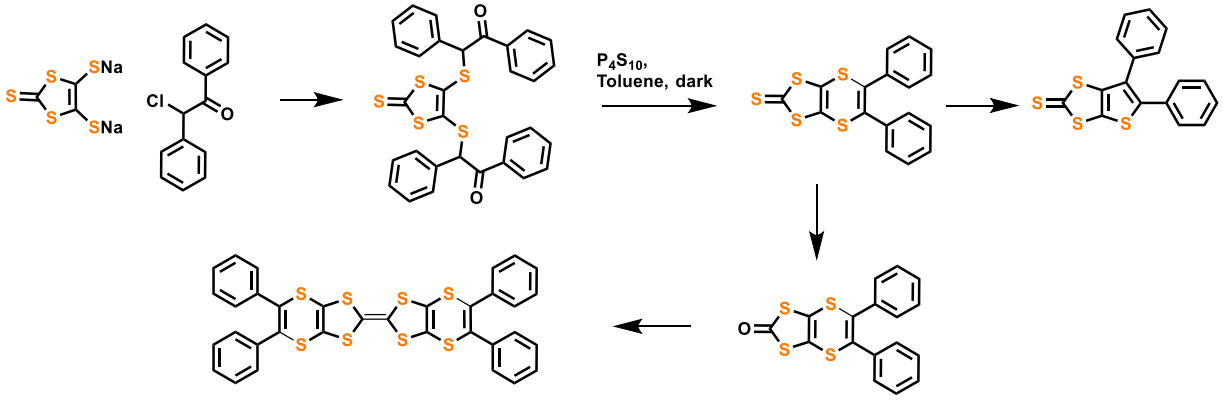


Figure 2- 4. Synthesis of tetraphenyl-BVDT-TTF.

Our first tentative approach to synthesise a functionalized BVDT-TTF was through the direct catalytic C-H activation on the vinylene moieties. The synthesis of BVDT-TTF and its precursor vinylenedithio-1,3-dithiol-2-thione (VDT) are already reported. The reactivity of both compounds is on the other hand not well established, and several reaction conditions, reactants, and catalysts were tried to understand their reactivity.

The synthesis of BVDT-TTF was already described in the first chapter and is represented on Figure 2- 5. The zincate salt **1** is oxidised by iodine to form the trithione **2**. A Diels-Alder reaction is performed between trithione and phenyl (Ph) vinyl sulfoxide with the formation of the cycloadduct and the elimination of the

[17] Ertas, E.; Ozturk, T. *Chem. Commun.* **2000**, *20*, 2039–2040.

group PhSOH to form VDT **3**. Garin *et al.*[18] already reported this step without any detailed description of the synthetic procedure. The next step is the transchalcogenation of the remaining thione group by mercuric acetate to afford the ketone **4**. The final step consists in a triethyl phosphite mediated coupling to give BVDT-TTF **5**.

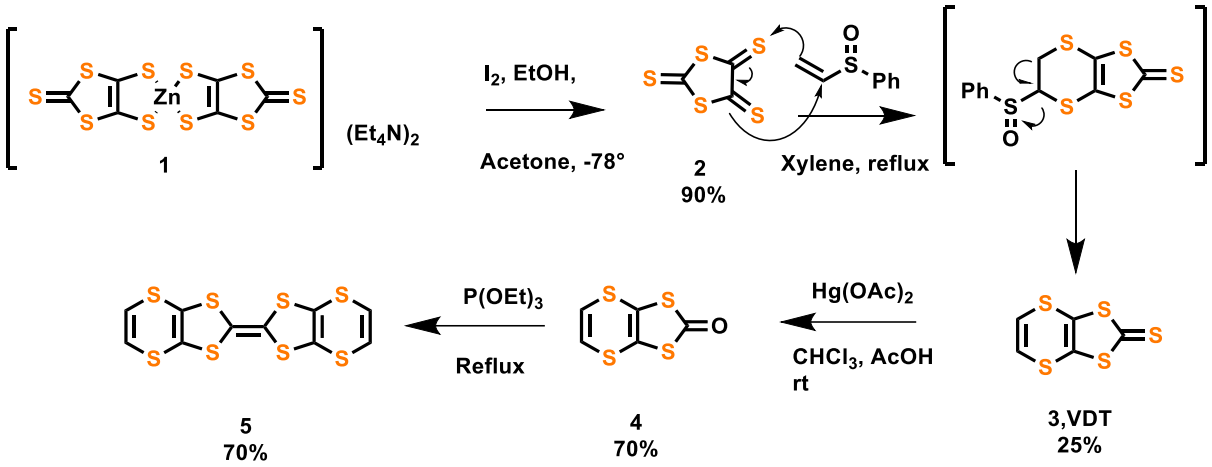


Figure 2- 5. Synthesis of BVDT-TTF.

The cyclic voltammogram of compound **5** was measured at different scan rates (Figure 2- 6) and oxidation (E_{Ox}) and reduction (E_{Red}) potentials and $E_{1/2}$ are reported in the Table 2- 1. The value of the first oxidation potential, related to the formation of the radical cation is higher compared to the TTF ($E^1_{1/2}$ 0.34 V vs. SCE) and falls within a similar range as of BEDT-TTF ($E^1_{1/2}$ 0.53 vs.SCE). While the first oxido-reduction wave is reversible, maintaining a constant $E^1_{1/2}$ at different scan rates, the second oxido-reduction shows a slow electronic transfer.

[18] Garin, J; Andreu, R; Orduna, J; Royo, J. *Synth. Met.* **2001**, *120*, 749-750.

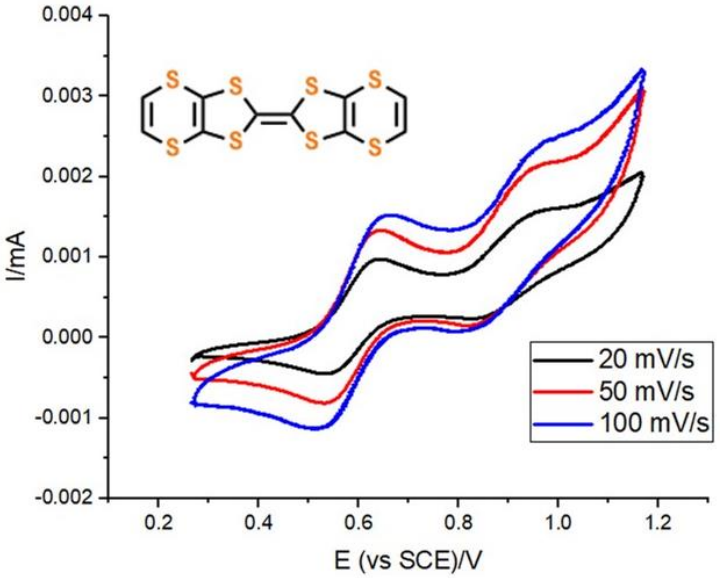


Figure 2- 6. Cyclic voltammetry of a **5** solution (10^{-3} M, $TBAPF_6$ 0.1M in DCM). Platinum electrode as WE, platinum wire as CE and an Ag/AgCl/Saturated KCl electrode as RE at scan rate 20/50/100 $mV \cdot cm^{-1}$. Values were converted with respect to the standard calomel electrode (SCE).[19]

Scan rate [$mV.s^{-1}$]	E^1_{Ox}	E^1_{Red}	$E^1_{1/2}$	E^2_{Ox}	E^2_{Red}	$E^2_{1/2}$
20	0.639	0.544	0.591	0.95	0.85	0.9
50	0.641	0.533	0.586	0.95	0.86	
100	0.653	0.531	0.592	0.97	0.83	

Table 2- 1. Potential oxidation, E_{Ox} and reduction, E_{Red} potentials and $E_{1/2}$ of **5** vs SCE at different scan rates.

2.2. Transition-metal-catalyzed direct C–H arylation of BVDT-TTF with aryl halides

Mitamura *et al.*[20] reported the straightforward synthesis of aryl TTFs by palladium-catalyzed direct C–H arylation.[21] The exact reaction mechanism is not described, although a metal-assisted deprotonation is

[19] Pavlishchuk, V. V.; Addison, A. W. *Inorganica Chim.* **2000**, *298* (1), 97–102.
[20] Mitamura, Y.; Yorimitsu, H.; Oshima, K.; Osuka, A. *Chem. Sci.* **2011**, *2* (10), 2017.
[21] Lyons, T. W.; Sanford, M. S. *Chem. Rev.* **2010**, *110* (2), 1147–1169.

probably the key step.[22] The palladium catalyst coordinates to the substrate, facilitating the simultaneous transfer of an electron to the carbon atom (metalation) and the abstraction of a proton by the basic cesium carbonate (deprotonation), leading to an efficient C-H bond activation. This protocol allowed the synthesis of several arylated TTFs, including TTF tetra(methyl benzoate) as observed on Figure 2- 7, with high yields and in a one-step protocol.[23]

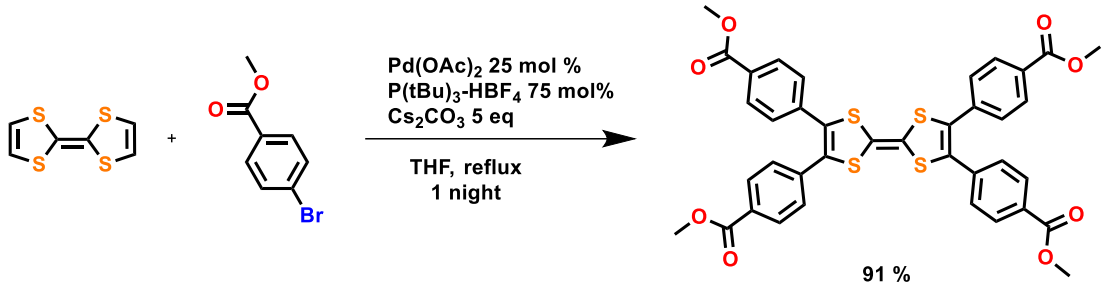


Figure 2- 7. Protocol for direct C–H arylation on TTF.

Similar experimental protocols[20] were attempted for BVDT-TTF as described on Figure 2- 8. Different conditions were tested such as microwave heating or the replacement of $Pd(OAc)_2$ by $Pd_2(dba)_3$. In all of these experiments, the formation of dimethyl 4,4'-thiodibenzoate as main product was observed. Isolated yield up to 30% of 4,4'-thiodibenzoate was observed using $Pd(OAc)_2$ (25 mol%). This undesired side product was characterized by SCXRD (Figure 2- 9). This indicates that the BVDT-TTF underwent a degradation leading to undesired products and is unstable under the given reaction conditions. None of these trials gave the desired tetrasubstituted target compound or a valuable mono-, di- or tri-substituted BVDT-TTF.

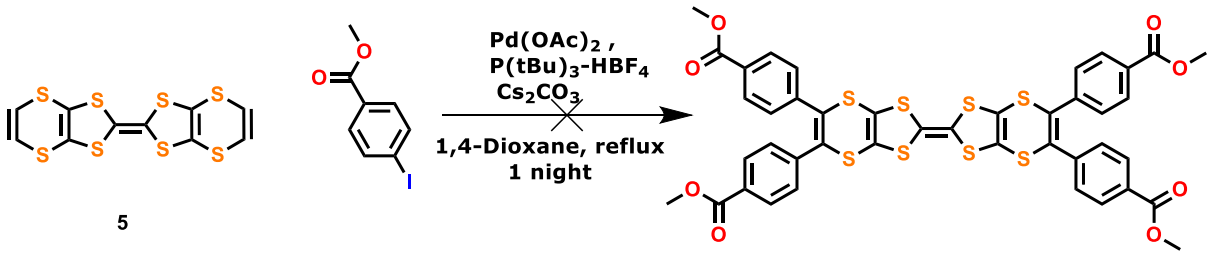


Figure 2- 8. Protocol for direct C–H arylation on BVDT-TTF.

[22] Moore, A. J.; Bryce, M. R.; Cooke, G.; Marshallsay, G. J.; Skabara, P. J.; Batsanov, A. S.; Howard, J. A. K.; Daley, S. T. A. K. *J. Chem. Soc., Perkin Trans.* **1993**, *1*(13), 1403.
[23] Batsanov, A. S.; Bryce, M. R.; Chesney, A.; Howard, J. A. K.; John, D. E.; Moore, A. J.; Wood, C. L.; Gershtenman, H.; Becker, J. Y.; Khodorkovsky, V. Y.; Ellern, A.; Bernstein, J.; Perepichka, I. F.; Rotello, V.; Gray, M.; Cuello, A. O. *J. Mater. Chem.* **2001**, *11* (9), 2181–2191.

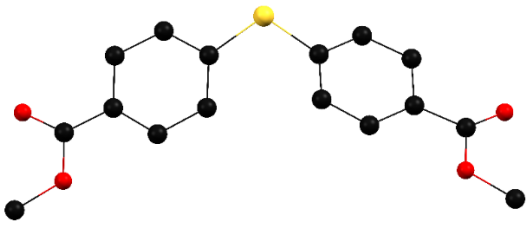


Figure 2- 9. X-ray structure of the undesired product: dimethyl 4,4'-thiodibenzoate.

Althoug the reaction mechanism is unknown, one can hypothesize that an opening of 1,4-dithiin ring is possible as observed by Turksoy *et al.*[24] (Figure 2- 10), thus generating sulfide that would further react with *p*-iodo(methylbenzoate).

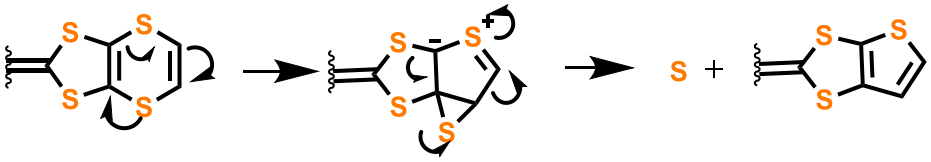


Figure 2- 10. Possible mechanism for 1,4-dithiin ring rearrangement.

2.3. Lithiation/Iodination of VDT

Since a direct arylation of the BVDT-TTF was not feasible, an alternative approach was employed. In order to introduce the desired functional groups, a lithiation-iodination was performed to generate the tetra-halogenated compound Tetraiodo-Bis(Vinylenedithio)-Tetrathiafulvalene (I_4-BVDT-TTF). The (I_4-BVDT-TTF) would be an accessible halogenated substrate that can undergo Pd-catalyzed cross-coupling reactions to introduce the desired methyl benzoate group (Figure 2- 11).

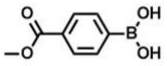
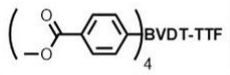
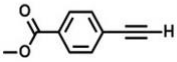
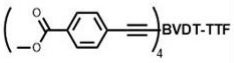
SUBSTRATE A	COUPLING	SUBSTRATE B	PRODUCT
I_4–BVDT-TTF	Suzuki		
	Sonogashira		

Figure 2- 11. Pd-catalyzed cross-coupling reactions.

[24] Turksoy, F.; Wallis, J. D.; Tunca, U.; Ozturk, T. *Tetrahedron* **2003**, *59* (41), 8107–8116.

The lithiation reactions are abundantly reported on the TTF.[25] Typically, a non-nucleophilic strong base such as LDA is used to obtain a tetra-lithiated TTF. The organolithium intermediate reacts even at low temperatures with the perfluorohexyl iodide to give the tetraiodotetrathiafulvalene with an 84% yield. Since the BVDT-TTF is poorly soluble in THF and diethyl ether, the lithiation-iodination was tested on the VDT **3**. The best conditions for this reaction are described Figure 2- 12. The monoiodo-VDT (I-VDT) **6** was synthesized with a 15% yield. The disubstituted VDT was not obtained using this method. Upon extension of the reaction time of lithiation step or addition of equivalents of LDA (until 3.2 equiv.), a lower yield (5%) of **6** was observed. This is indicative of the instability of the obtained compounds.

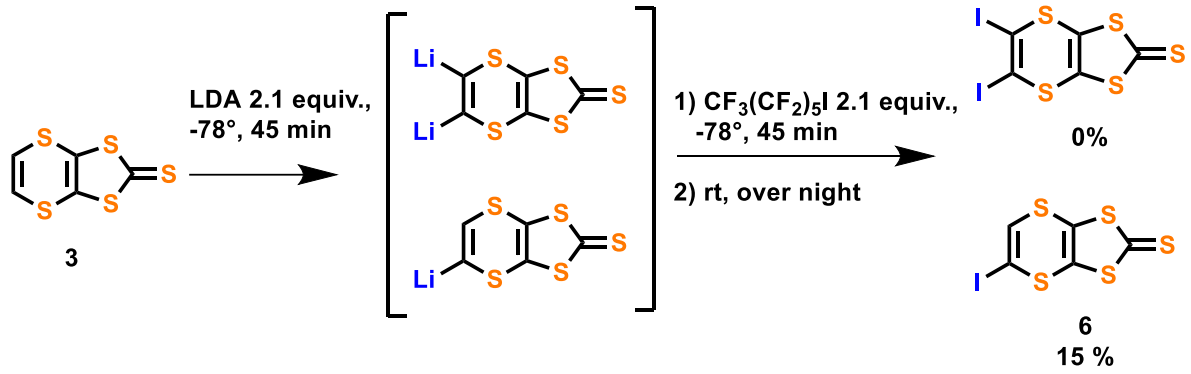


Figure 2- 12. Lithiation-iodination of compound **3**.

2.4. Synthesis of methyl 4-((2-thioxo-[1,3]dithiolo[4,5-b][1,4]dithiin-5-yl)ethynyl)benzoate

In order to introduce a methyl benzoate group on BVDT-TTF, Suzuki-Miyaura and Sonogashira coupling conditions were tested on I-VDT **6**. Several Pd catalysts, bases and ligands were used to afford the VDT methyl benzoate (Figure 2- 13 and Figure 2- 14). No target compounds were detected in any of the tested conditions. The degradation of the compound **6** was observed in every case and can be attributed to several factors. As already hypothesised, 1,4-dithiin rings are prone to chemical transformations under prolonged heating.[24] The formation of reactive intermediates, such as aryl-palladium species, can potentially interact with the 1,4-dithiin rings and lead to the cleavage of sulfur-containing bonds.

[25]Batsanov, A. S.; Bryce, M. R.; Chesney, A.; Howard, J. A. K.; John, D. E.; Moore, A. J.; Wood, C. L.; Gershtenman, H.; Becker, J. Y.; Khodorkovsky, V. Y.; Ellern, A.; Bernstein, J.; Perepichka, I. F.; Rotello, V.; Gray, M.; Cuello, A. O. *J. Mater. Chem.* **2001**, *11* (9), 2181–2191.

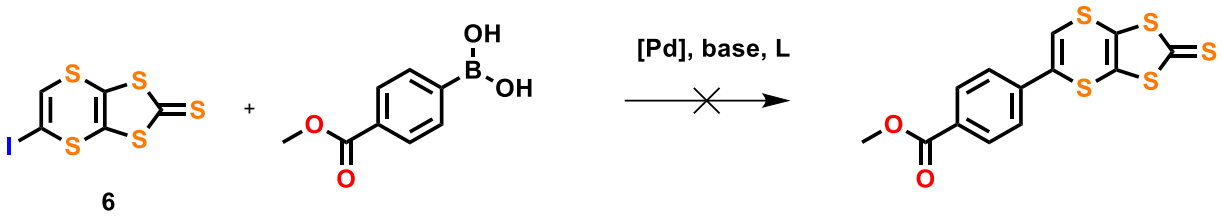


Figure 2- 13. Suzuki-Miyaura coupling between **6** and (4-(methoxycarbonyl)phenyl)boronic acid.

[Pd]	base	Ligand, L
$Pd(PPh_3)_4$ 10 mol%	Na_2CO_3 3 equiv.	-
$Pd(OAc)_2$ 10 mol%	K_3PO_4 2 equiv.	Sphos 20 mol%
$Pd(OAc)_2$ 10 mol%	K_3PO_4 2 equiv.	Xphos 20 mol%
$Pd_2(dba)_3$ 5mol%	K_3PO_4 2 equiv.	Sphos 10 mol%
$Pd_2(dba)_3$ 5mol%	K_3PO_4 2 equiv.	Xphos 10 mol%

Figure 2- 14. Main condition used for Suzuki-Miyaura coupling.

On the other hand, the Sonogashira cross-coupling between I-VDT and methyl 4-ethynylbenzoate afforded **7** with a 30% yield (Figure 2- 15).

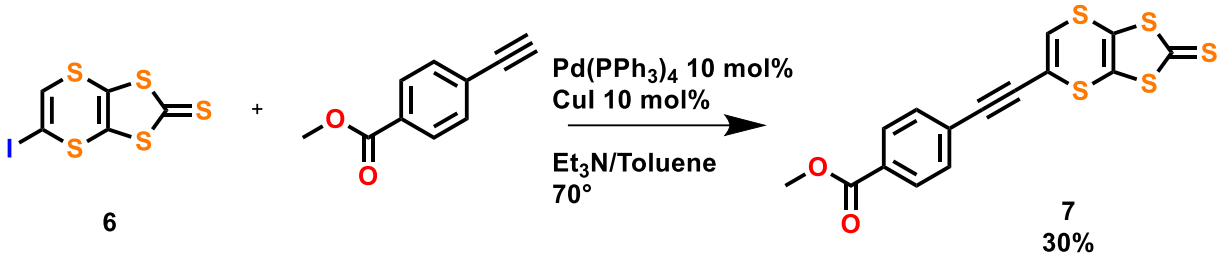


Figure 2- 15. Sonogashira cross-coupling reaction.

A second lithiation on the compound **7** was attempted without success using the same conditions as reported above (paragraphe 2.3). The fact that the phosphite mediated coupling of **7** would lead to a mixture of *cis/trans* isomers, along with the poor reaction yields, discouraged the continuation on this pathway.

2.5. Synthesis of BVDT-TTF (Dipicolinic acid)$_4$

Dipicolinic acid has a well-know coordination chemistry thanks to its unique structural characteristics and versatile coordination behavior. The rigid 120° angle between the central pyridine ring and the two carboxylate groups creates a chelating environment that allows to serve as a bidentate ligand, coordinating to metal ions. [26,27]

It is an organic tridentate ligand used to form lanthanide-based complexes and MOFs (Ln-MOFs).[28,29] Choosing lanthanides as metal gives several advantages:

- a high coordination number, often ranging from 6 to 12, due to the presence of multiple empty f-orbitals.
- a wide range of coordination geometries leading to intricated highly porous MOFs architectures. [30,31]
- luminescence features such as a high luminescence quantum yield, a long-lived emission with sharp lines.[32] The luminescence properties of MOFs are influenced by multiple factors, including the presence of Ln ions, the choice of the organic linker, and the overall structure of the MOF. The organic linker, via the antenna effect[33], stimulates Ln^{3+} ion luminescence and ensures an effective transfer of absorbed energy to the Ln^{3+} ions.[34]

Predicting the structure of Ln-MOFs is complicated because of the high coordination flexibility and the lack of preferential geometries of Ln^{3+} ions.[35] Ln^{3+} ions have high affinities with oxygen from carboxylic groups and their delocalized π-electric system that provide a strongly absorbing chromophore. This

---

[26] Shahryari, T.; Vahidipour, F.; Chauhan N. P. S.; Sargazi G. *Polym Eng Sci*. **2020**, *60*, 2793–2803
[27] Demir, S.; Çepni, H. M.; Hołyńska, M.; Kavanoz, M.; Yilmaz, F.; Zorlu, Y. *J. Coord.* **2017**, *70* (19), 3422–3433.
[28] Shen, L.; Yang, L.; Fan, Y.; Wang, L.; Xu, J. *CrystEngComm* **2015**, *17* (48), 9363–9369.
[29] Gao, H.-L.; Yi, L.; Zhao, B.; Zhao, X.-Q.; Cheng, P.; Liao, D.-Z.; Yan, S.-P. *Inorg. Chem.* **2006**, *45* (15), 5980–5988.
[30] Li, X.-Z.; Tian, C.-B.; Sun, Q.-F. *Chem. Rev.* **2022**, *122* (6), 6374–6458.
[31] Liu, K.; Zhang, X.; Meng, X.; Shi, W.; Cheng, P.; Powell, A. K. *Chem. Soc. Rev.* **2016**, *45* (9), 2423–2439.
[32] Zhang, D.; Lu, Y.; Zhu, D.; Xu, Y. *Inorg. Chem.* **2013**, *52* (6), 3253–3258.
[33] Cui, Y.; Chen, B.; Qian, G. *Coord. Chem. Rev.* **2014**, *273–274*, 76–86.
[34] Xu, H.; Cao, C.-S.; Kang, X.-M.; Zhao, B. *Dalton Trans.* **2016**, *45* (45), 18003–18017.
[35] Horcajada, P.; Gref, R.; Baati, T.; Allan, P. K.; Maurin, G.; Couvreur, P.; Férey, G.; Morris R. E.; Serre, C. *Chem. Rev.,* **2011**, *112*, 1232.

effect can be amplified by the use of aromatic multidentate ligands with oxygen or hybrid oxygen–nitrogen atoms. Several different TTFTB MOFs based on lanthanides were prepared over the past few years as multifunctional materials in which porosity combined with electronic properties such as electrical conductivity, redox activity, luminescence and magnetism.[36,37] This is because TTF-based ligands can act both as structural agent and organic chromophore isolating the magnetic centres and sensitising the lanthanide luminescence.[38] For example, Castells-Gil *et al*.[39] reported a series of $Ln_3(TTFTB)_2(OAc)(OH)$ networks which Ln = Gd^{3+}, Tb^{3+}, Dy^{3+}, Ho^{3+}, and Er^{3+} and OAc = acetate, abbreviated MUV-5. TTF units are characterized by a continuous parallel π···π stacking with 3.61 and 3.86 Å S···S distances (Figure 2- 16). TTF units are partially oxidised without the need of any doping process. The highest electrical conductivity founded is 1.5 × 10^{-5} S·cm^{-1} measured in a pellet of the Tb^{3+}-MUV-5. $Yb_{0.76}$ $Er_{0.24}$-MUV-5, Er-MUV-5 and Gd-MUV-5 were analysed to observe a possible increase of photoluminescence through energy transfer among different lanthanide ions. While for Er-MUV-5 and Gd-MUV-5 the organic linker cover most of the ultraviolet and visible spectral range, the spectra of $Yb_{0.76}$ $Er_{0.24}$-MUV-5 shows an intense signal in the 920–980 nm range assigned to the $^2F_{7/2}\rightarrow{}^2F_{5/2}$ transition of Yb^{3+}, thanks to the antenna effect of TTFTB ligand more sensible at Yb^{3+}ion.

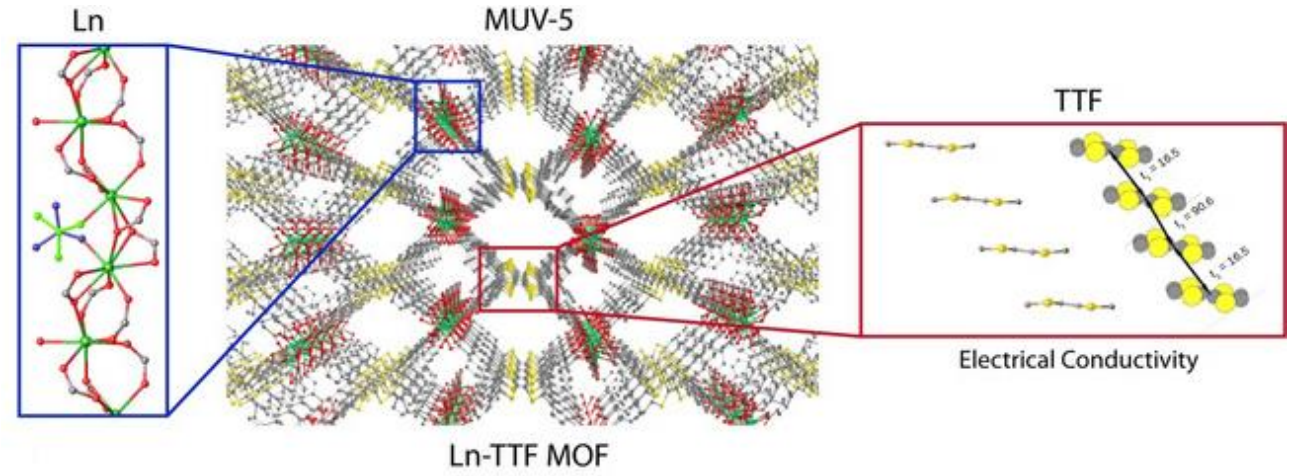


Figure 2- 16. MUV-5 networks.[39]

[36] Su, J.; Hu, T.-H.; Murase, R.; Wang, H.-Y.; D'Alessandro, D. M.; Kurmoo, M.; Zuo, J.-L. *Inorg. Chem.* **2019**, *58*, 3698–3706.
[37] Xie, L. S.; Dincă, M. *Isr. J. Chem.* **2018**, *58,* 1119–1122.
[38] Pointillart, F.; Le Guennic, B.; Cador, O.; Maury, O.; Ouahab, L. *Acc. Chem. Res.* **2015**, *48* (11), 2834–2842.
[39] Castells-Gil, J.; Mañas-Valero, S.; Vitórica-Yrezábal, I. J.; Ananias, D.; Rocha, J.; Santiago, R.; Bromley, S. T.; Baldoví, J. J.; Coronado, E.; Souto, M. *Chem. Eur. J.* **2019**, *25*, 12636–12643.

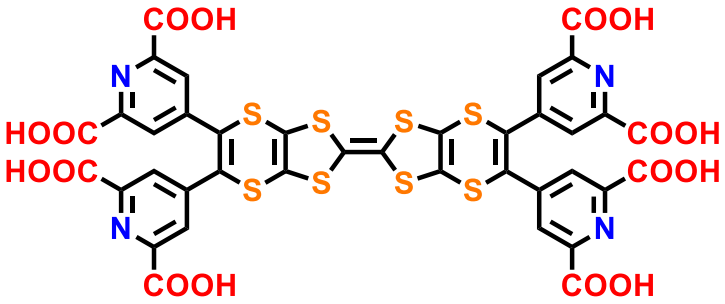


Figure 2- 17. BVDT-TTF (Dipicolinic acid)$_4$, **13**.

A promising ligand for synthesizing Ln-based MOFs is therefore the Bis(Vinylenedithio)-Tetrathiafulvalene tetradipicolinc acid (BVDT-TTF(Dipicolinic acid)$_4$, Figure 2- 17. Since the BVDT-TTF(pyridine)$_4$ was already reported by Almeida *et al.*, we assumed that a similar protocol was viable using a substituted bis(*p*-pyridyl)alkyne in a Diels-Alder reaction with a trithione as our key synthetic step.

The synthesis of BVDT-TTF(Dipicolinic acid)$_4$ starts from the chelidamic acid efficiently converted to the 4-brominated diethyl ester **8**. The symmetric alkyne **9** was obtained by Sonogashira coupling and subsequently reacted with trithione through a hetero Diels-Alder reaction to afford the thione **10**. A transchalcogenation reaction to obtain the ketone **11** was done with mercuric acetate. A homo-coupling phosphite mediated reaction of the ketone **11** was performed with a low 15 % yield. The starting material was consumed according to TLC monitoring, and several products formed. These unwanted side products are probably phosphonate intermediates which do not react further in the phosphite mediated coupling. The final step consists in the saponification of the octa-ester **12** using LiOH as a base to obtain the BVDT-TTF (Dipicolinic acid)$_4$, **13** (Figure 2- 18).

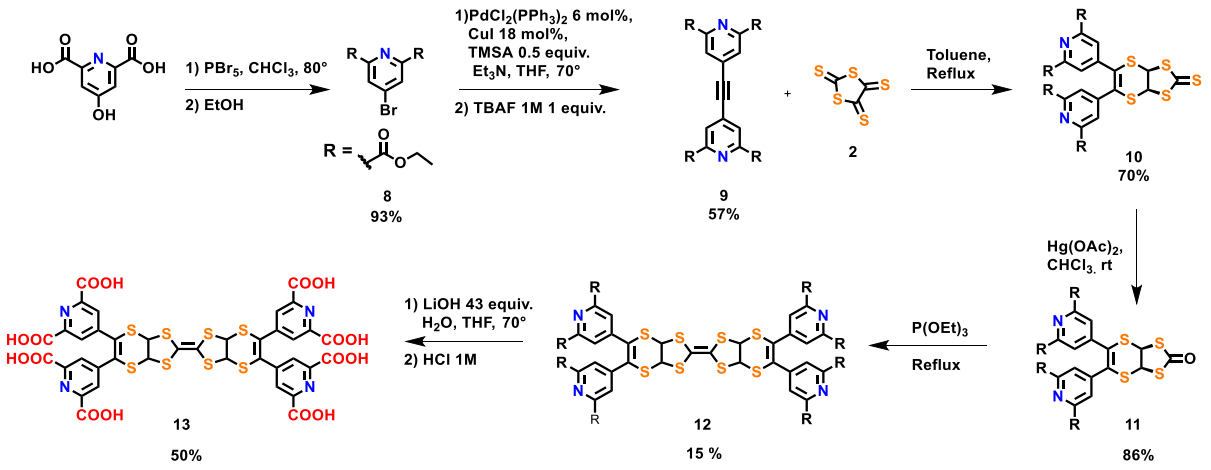


Figure 2- 18. Synthesis of BVDT-TTF (Dipicolinic acid)$_4$ **13**.

The cyclic voltammetry of compound **12** was measured in two distinct solvents, acetonitrile (ACN) and dichloromethane (DCM) to compare its behaviour with that of TTF and BVDT-TTF. The E_{Ox} , E_{Red}, and $E_{1/2}$values of compound **12** were determined and are provided in Table 2- 2. The Figure 2- 19 is relative to the cyclic voltammetry of compound **12** in DCM.

The value of the first oxidation potential in ACN, related to the formation of the radical cation is higher compared to the TTF ($E^1_{1/2}$ 0.34 V vs SCE) in accordance with the presence of electron-withdrawing groups. While the first oxido-reduction wave is reversible, maintaining a constant $E^1_{1/2}$ at different scan rates, the second oxido-reduction shows a slow electronic transfer and the anodic peak E^2_{Ox} tends to disappear at higher scan rates. The analysis of the compound **12** in DCM has $E^1_{1/2}$ at 0.72 V is also higher compare to BVDT-TTF. This is attributed to the presence of the dipicolinate functional group. The dipicolinate group acts as an electron-withdrawing moiety, resulting in a decrease in electron density within the molecule. As a result, the energy barrier for the oxidation process is higher.

The low solubility of the compound **13** made it impossible to characterise it via cyclic voltammetry.

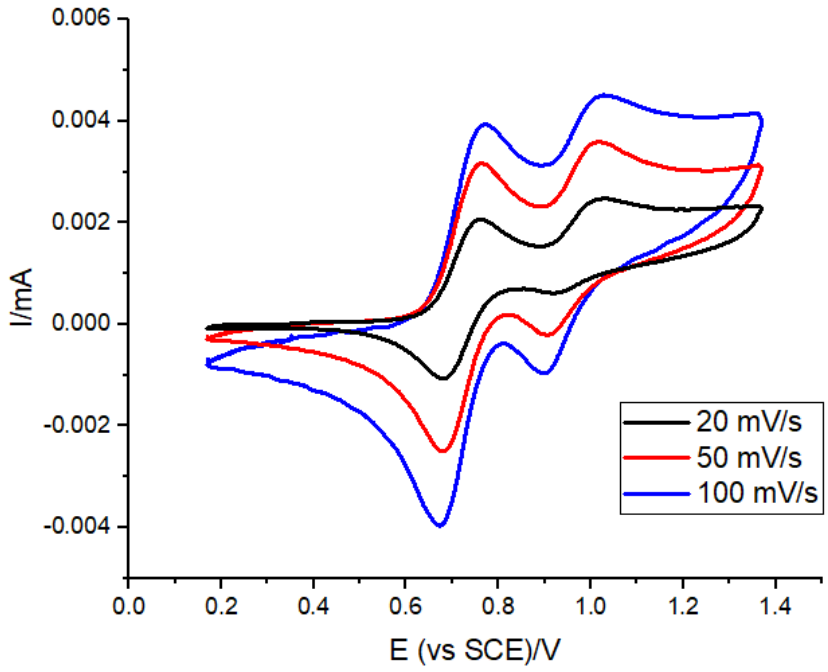


Figure 2- 19. Cyclic voltammetry of a solution of **12** (10^{-3} M, $TBAPF_6$ 0.1M in DCM). Platinum electrode as WE, platinum wire as CE and an Ag/AgCl/Saturated KCl electrode as RE at scan rate 20/50/100 $mV{\cdot}cm^{-1}$. Values were converted with respect to SCE electrode.

Scan rate [$mV.s^{-1}$]	DCM						ACN				
	E^1_{Ox}	E^1_{Red}	$E^1_{1/2}$	E^2_{Ox}	E^2_{Red}	$E^2_{1/2}$	E^1_{Ox}	E^1_{Red}	$E^1_{1/2}$	E^2_{Ox}	E^2_{Red}
20	0.758	0.682	0.720	1.018	0.931	0.974	0.639	0.492	0.565	0.84	0.77
50	0.762	0.681	0.721	1.018	0.907	0.962	0.648	0.488	0.568	0.85	0.76
100	0.768	0.675	0.721	1.027	0.903	0.965	0.640	0.480	0.56	0.82	0.75

Table 2- 2. Potential oxidation, E_{Ox} and reduction, E_{Red} potentials and $E_{1/2}$ of **12** at different scan rates in DCM and ACN vs SCE.

Several solvo-thermal reactions were conducted using the ligand **13** in combination with diverse metals (Figure 2- 20). None of these led to the formation of single crystals and the amount of powder obtained was not high enough to determine a possible crystallinity through Powder X-ray Diffraction. The formation of single crystals requires a precise control over reaction conditions, such as solvent choice, temperature, and concentration, which can be challenging to achieve consistently. Furthermore, a rapid MOF synthesis reaction promotes the formation of powders. Solvo-thermal method was used because reaching elevated temperatures and pressures increase the collision frequency and promote the formation of coordination bonds between metal ions and benzoate ligands. On the other hand, the elevated temperatures and pressures promote the reversibility of the bond formation process. HCl is often used as additive in solvo-thermal method. This increase of acidity impacts the reaction kinetics by favouring the presence of protonated, non-coordinated ligand in the reaction medium. The extended reaction time allows a better control over nucleation and crystal growth processes. On the other side, the addition of a strong base facilitates the deprotonation of the carboxylic acid groups, which favours the formation of coordination bonds between the ligands and metal ions.[40]

Metals	Solvents	Temp., time	Additives
• **Zn(II)** • **Co(II)** • **Cu(II)** • **Tb(III)** • **Eu(III)** • **Er(III)**	• DMF/EtOH • DMF/EtOH/H_2O • DMAc/EtOH • DMAc/EtOH/H_2O	• 120 °C, 24 h • 120 °C, 48 h • 160 °C, 24 h	• HCl • NaOH

Figure 2- 20. Metals and reaction conditions to synthetize MOFs using BVDT-TTF (Dipicolinic acid)$_4$ **13** as ligand.

The BVDT-TTF (Dipicolinic acid)$_4$ contains multiple coordinating moieties that can adopt several binding motives. This favours the possibility of creating amorphous MOF structures rather than single crystals. It can link multiple metal ions through nitrogen and oxygen donor atoms, leading to the formation of extended polymeric structures or amorphous networks.

[40] Furukawa, H.; Cordova, K. E.; O'Keeffe, M.; Yaghi, O. M. *Science* **2013**, *341* (6149), 1230444.

2.6. Tetrabromo(dibenzodithio)tetrathiafulvalene

The influence of aryls connected via the C-C bond on TTF can have a significant impact on its electronic nature due to the extension of π-conjugation. By connecting aryl groups to TTF through C-C bonds, the conjugation of π-electrons can be extended, leading to enhanced electronic delocalization along the molecule. This enhanced electron delocalization can contribute to the stabilization of charge carriers and facilitate the movement of electrons within the molecule. The extension of π-conjugation can affect the energy levels and spatial distribution of the frontier molecular orbitals of TTF. This, in turn, can influence the molecule's electronic properties, such as its ionization potential, electron affinity, and conductivity as already described on Chapter 1, paragraph 2.1.

Sun et al.[41] describe a facile method to synthesise aryl-substituted BVDT-TTF via Cu_2O-catalyzed C–S coupling between aryl iodides and zincate salt (Figure 2- 21). It is a straightforward method to obtain aryl-substituted 1,3-dithiole-2-thiones with ortho-substituent bearing electron-donating group.

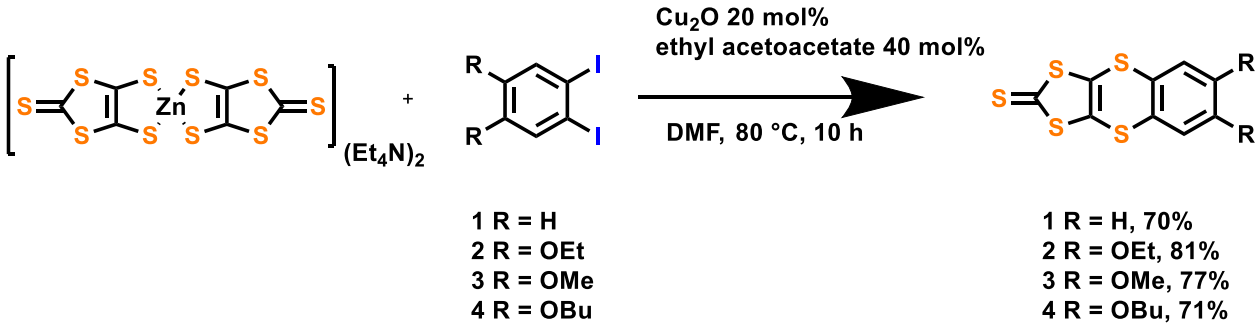


Figure 2- 21. Cu_2O-catalyzed C–S coupling between aryl iodides and zincate salt as reported by Sun et al.

The target ligand was the BVDT-TTF bisphenyl-tetrabenzoic acid (Figure 2- 22). The presence of aryl directly connected to the BVDT-TTF amplifies the π-scaffold and should increase the ligands overlap if coordination polymers are obtained.

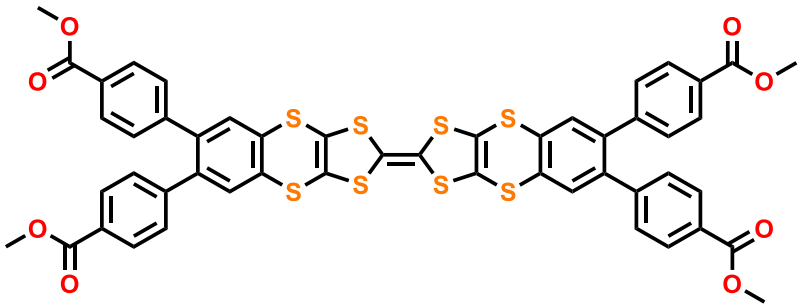


Figure 2- 22. BVDT-TTF bisphenyl-tetrabenzoic acid.

[41] Sun, J.; Lu, X.; Shao, J.; Cui, Z.; Shao, Y.; Jiang, G.; Yu, W.; Shao, X. *RSC Adv.* **2013**, *3* (26), 10193.

The failed attempt of Cu_2O-catalyzed C–S coupling reaction between the zincate salt and dibromo-terphenyl dicarboxylate **14** (Figure 2- 23) encouraged us to find new pathways to reach the BVDT-TTF bisphenyl-tetrabenzoic acid. The absence of reaction originates in the use of aryl bromide instead of aryl iodide. Copper catalysts typically exhibit a lower reactivity towards aryl bromide. The oxidative addition of aryl bromides to the Cu catalyst is less favourable.[42] It should be noted that a test reaction with bromobenzene did not afford any compound, as already described in the literature.[41]

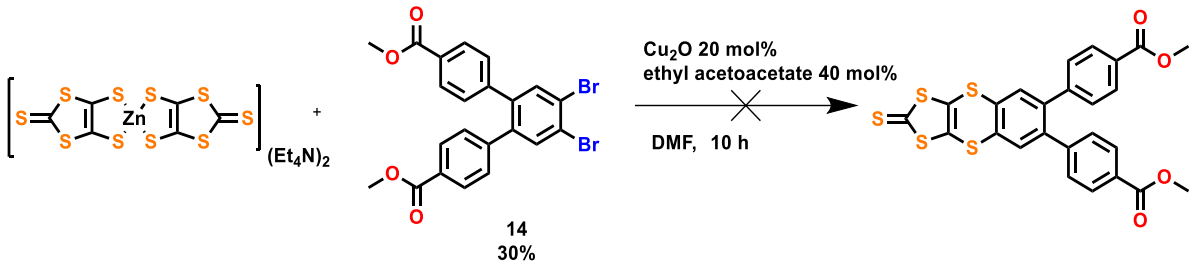


Figure 2- 23. Cu_2O-catalyzed C–S coupling between aryl bromide and zincate salt.

In order to use Pd-Catalyzed cross-coupling reactions the tetrabromo(dibenzodithio)tetrathiafulvalene **18** was synthesized.

The first step consists in a Cu_2O-catalyzed C–S coupling reaction between the zincate salt **1** and **15** with 20% yield. Then mercuric acetate converts carbon-sulfur bond (C=S) of the thione **16** to ketone **17** with 80% yield. In the final step of the reaction, a homo-coupling process is carried out to generate the desired compound **18**. The final step is a homo-coupling to afford the insoluble compound **18** with a low 17% yield attributed to the presence of phosphonate intermediate that does not readily react in the desired homo-coupling process.

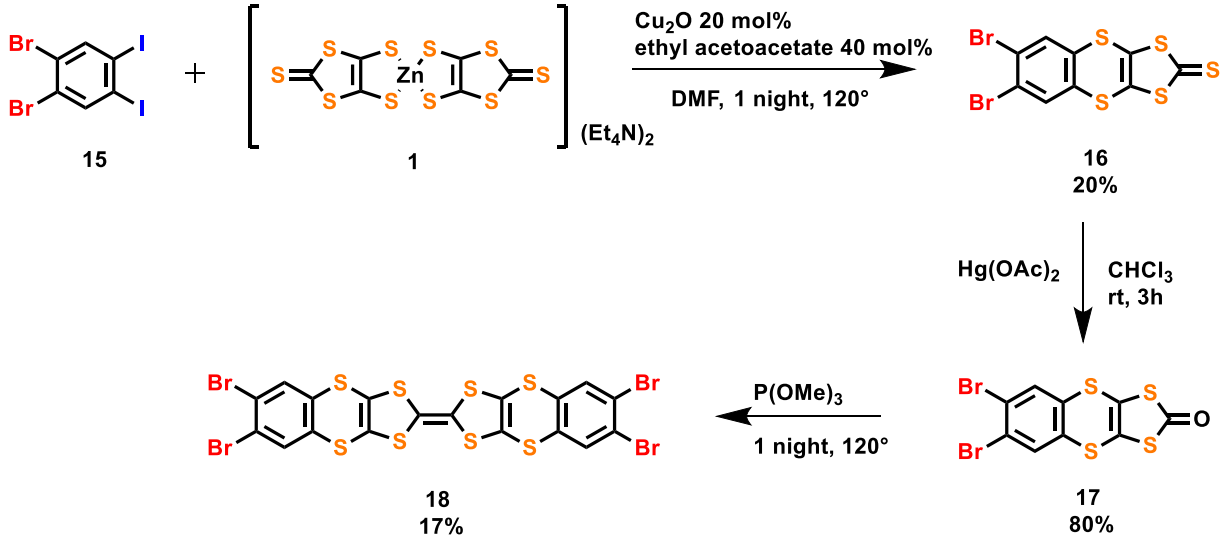


Figure 2- 24. Pathway for the synthesis of tetrabromo(dibenzodithio)tetrathiafulvalene **18**.

[42] Sujatha, A.; Thomas, A. M.; Thankachan, A. P.; Anilkumar, G. *Arkivoc* **2014**, *2015* (1), 1–28.

The compound **18** is insoluble in common organic solvents. The insolubility can be attributed to the highly planar unfunctionalized structure, which prevents its interaction with solvent molecules and promotes self-aggregation.

Despite our attempts to perform Pd-catalyzed cross-coupling reaction, its limited solubility hindered the reaction's progress. To address this challenge, we employed a solid-state reaction in a ball-milling utilizing $Pd(OAc)_2$ and $KFAl_2O_3$.[43] However, we only observed the degradation of both starting materials.

An investigation into the reactivity of **16** was therefore conducted. Suzuki-Miyaura and Sonogashira coupling on the substrate **16** were tested using different Pd catalysts such as palladium acetate $Pd(OAc)_2$, tetrakis (triphenylphosphine) palladium $Pd(PPh_3)_4$, tris(dibenzylideneacetone)dipalladium $Pd_2(dba)_3$ and ligands such as triphenylphosphine PPh_3, 2-Dicyclohexylphosphino-2′,4′,6′-triisopropylbiphenyl XPhos, and 2-Dicyclohexylphosphino-2′,6′-dimethoxybiphenyl SPhos. The degradation of dibromo 1,3-dithiole-2-thiones was observed in the case of Suzuki-Miyaura reaction while no reaction was observed in Sonogashira cross-coupling.

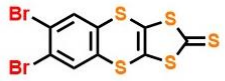
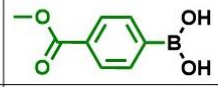
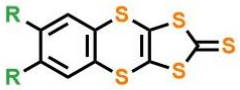
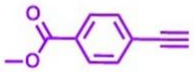
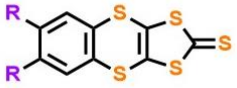
SUBSTRATE A	COUPLING	SUBSTRATE B	PRODUCT
	Suzuki		
	Sonogashira		

Figure 2- 25. Catalyst and substrates for Suzuki-Miyaura and Sonogashira coupling on the compound **16**.

2.7. Diiododibenzoate(dibenzodithio)tetrathiafulvalene

In response to the challenges encountered during the attempted coupling reactions for compounds **16** and **18**, an alternative approach was devised aiming at the key precursor **20** for the subsequent C-S coupling with the zincate salt **1** (Figure 2- 27). Initially, the Suzuki-Miyaura coupling reaction was anticipated to directly produce the fully di-substituted compound, 4,5-dimethyl benzoate 1,2-diiodobenzene. During the experiment, the expected product, 4,5-dimethylbenzoate 1,2-diiodobenzene, was not obtained. Instead, the major product was 4,6-dimethylbenzoate 1,3-diiodobenzene, which was obtained in 40% yield. Additionally, compound **20** was produced in 10% yield, and 20% of the starting material **19** remained unreacted (Figure 2- 26, red line).

[43] Bernhardt, F.; Trotzki, R.; Szuppa, T.; Stolle, A.; Ondruschka, B. *Beilstein J. Org. Chem.* **2010**, *6*.

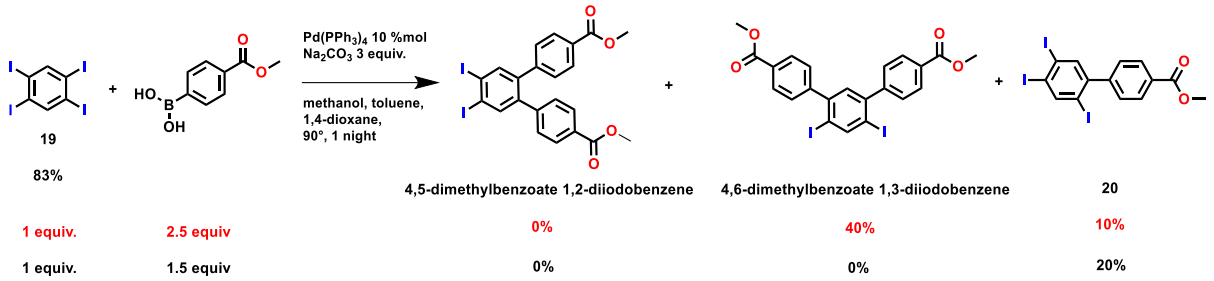


Figure 2- 26. Suzuki-Miyaura coupling to obtain 4,5-dimethylbenzoate 1,2-diiodobenzene.

After obtaining 4,6-dimethylbenzoate 1,3-diiodobenzene as a major product in the initial Suzuki-Miyaura coupling reaction, we decided to optimize the reaction conditions to increase the yield of compound **20**. By adjusting the stoichiometry of the reaction from 2.5 equivalents of (4-(methoxycarbonyl)phenyl)boronic acid to 1.5 equivalents (Figure 2- 26), compound **20** with a yield of 20% was obtained. The synthesis proceeds by a Cu_2O-catalyzed C–S coupling reaction between the compound **20** and **1** in DMF gave compound **21**. A transchalcogenation reaction converts the compound **21** in compound **22**. Finally, compound **22** was submitted to phosphite homo-coupling. The compound **23** was detected as traces by MS, along with a phosphonate intermediate as the major compound (Figure 2- 27). The compound **23** could not be isolated. The reactivity limitations of the phosphonate intermediate made herein the phosphite-mediated coupling reaction unsuitable.

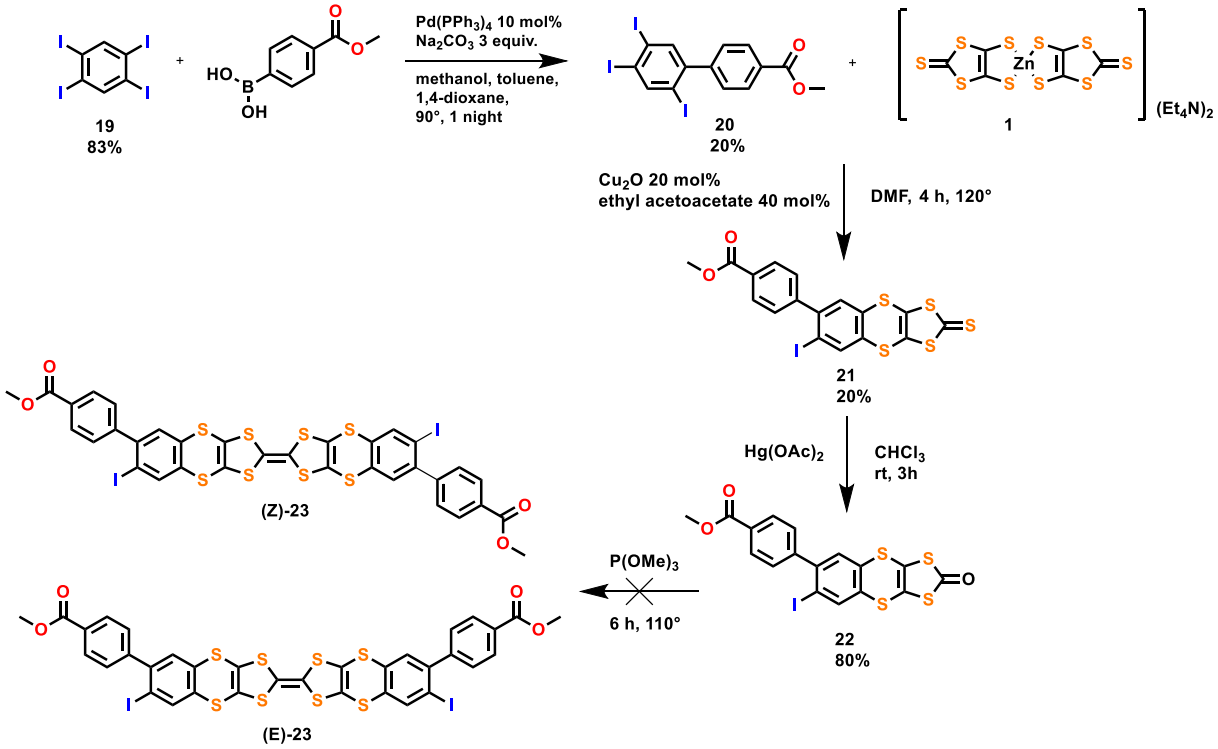


Figure 2- 27. Diiodo, dibenzoate(dibenzodithio)tetrathiafulvalene synthesis.

3. Conclusions

The synthesis of new ligands based on the BVDT-TTF scaffold was tried through several strategies. One particular interest lies in the synthesis of BVDT-TTF-tetrabenzoate derivatives. This scaffold should be redox active, a π···π stacking propensity, an extended π-conjugated system and coordinating divergent moieties. However, the synthesis of BVDT-TTF tetrasubstituted with coordinating moieties was challenging due to several factors. One of the main obstacles encountered is the lack of reactivity or decomposition of several intermediates, along with the low solubility of large planar molecules. These limitations and the low reaction yields complicated the synthesis.

In comparison, the synthesis of TTF-tetrabenzoate ligand (H_4TTFTB) is easier and can be performed on a large scale. This accessibility allows for screening experiments where various parameters such as ligand-to-metal ratios, solvents, temperature, and additives are systematically varied to optimize the formation of coordination networks. On the other hand, the poor reaction yield of BVDT-TTF (Dipicolinic acid)$_4$ poses a significant challenge. The low yields limit the amount of material available for further exploration and hinder the ability to conduct extensive screening experiments. As a result, the opportunities to investigate and optimize the reaction conditions for the formation of BVDT-TTF(Dipicolinic acid)$_4$-based MOFs are restricted.

CHAPTER III

Synthesis and studies of coordination networks based on electroactive ligands

CHAPTER III : Synthesis and studies of coordination networks based on electroactive ligands

1. Electroactive MOFs based on TTF

Porous conductive materials, like metal-organic frameworks (MOFs), are highly desirable for applications such as battery electrodes, fuel cell electrodes, and supercapacitors.[1,2,3] Recently, electroactive MOFs have emerged, combining porosity and conductivity. Different mechanisms describe conductivity in MOFs such as through-bond, through-space, redox-hopping or guest-promoted redox hopping. The "through-space" approach involves orbital overlap between adjacent organic moieties, especially for ligands that arrange themselves in $\pi\cdots\pi$ stacks. Examples include naphthalenediimide[4] and triphenylene,[5] which can yield conductive or even metallic MOFs.[6] Tetrathiafulvalenes (TTFs) have been used to enhance charge mobility and conductivity in MOFs, with TTF-tetrabenzoate (TTFTB) being a notable example.[7,8,9] Dincă *et al*.[10] demonstrated the high charge mobility of the TTFTB-based networks, and the dependency of the electrical properties to the cation diameter. They have been extensively studied and have found applications in various fields, including the reduction of CO_2,[11] electrocatalysis,[12] and energy storage.[13] Our research is dedicated to the exploration of innovative architectural possibilities using derivatives of TTF as the basis for PCPs. This aimed to gain insights into the connection between MOF architectures and their resultant electronic properties, thereby contributing to an enhanced understanding of this crucial area of research. Two distinct networks based on BVDT-TTF-Py_4 ligand have been investigated, **L**-MCl_2 (M= Cu, Zn, Hg, Cd) and **L**-$[CuCl_2]_2$. DFT calculation on **L**-MCl_2 networks revealed a 2D conducting pathway along charge

---

[1] Liu, L.; Zhou, Y.; Liu, S.; Xu, M. *ChemElectroChem.* **2018**, *5*, 6–19
[2] Ren, Y.; Chia, G. H.; Gao Z. *Nano Today* **2013**, *8*, 577–597.
[3] Erickson, K. J.; Léonard, F.; Stavila, V.; Foster, M. E.; Spataru, C. D.; Jones, R. E.; Foley, B. M.; Hopkins, P. E.; Allendorf, M. D.; Talin, A. A. *Adv. Mater.* **2015**, *27*, 3453–3459
[4] Castner, A. T.; Su, H.; Svensson Grape, E.; Inge, A. K.; Johnson, B. A.; Ahlquist, M. S. G.; Ott, S. *J. Am. Chem. Soc.* **2022**, *144* (13), 5910–5920.
[5] Huang, J.; He, Y.; Yao, M.-S.; He, J.; Xu, G.; Zeller, M.; Xu, Z. *J. Mater. Chem. A* **2017**, *5* (31), 16139–16143.
[6] Skorupskii, G.; Le, K. N.; Cordova, D. L. M.; Yang, L.; Chen, T.; Hendon, C. H.; Arguilla, M. Q.; Dincă, M. *PNAS* **2022**, *119*, e2205127119.
[7] Xie, L. S.; Alexandrov, E. V.; Skorupskii, G.; Proserpio, D. M.; Dincă, M. *Chem. Sci.* **2019**, *10* (37), 8558–8565.
[8] Ukaj, D.; Bunzen, H.; Berger, J.; Kieslich, G.; Fischer, R. A. *Chem. Mater.* **2021**, *33* (7), 2532–2542.
[9] Leong, C. F.; Wang, C.-H.; Ling, C. D.; D'Alessandro, D. M. *Polyhedron* **2018**, *154*, 334–342.
[10] Narayan, T. C.; Miyakai, T.; Seki, S.; Dincă, M. *J. Am. Chem. Soc.* **2012**, *134* (31), 12932–12935.
[11] Dey, A.; Rahimi, F. A.; Verma, P.; Suresh, S.; Maji, T. K. *ACS Appl. Energy Mater.* **2023**, acsaem.3c00244.
[12] Liu, L.; Xu, Q.; Zhu, Q. *Adv. Energy Sustain. Res.* **2021**, *2* (11), 2100100.
[13] Hong, C. N.; Crom, A.; Feldblyum, J. I., Lukatskaya M. R. *Chem* **2023**, *9*(4), 798 – 822.

carriers. **L**-$[CuCl_2]_2$ structure suggests a 1D charge carrier pathway, with a 50% solvent-accessible volume. Oxidation of BVDT-TTF-Py_4 by iodine exposition was supported by Raman spectroscopy along with conductivity measurements. Carboxylates-based networks have been also explored with TTF(isophthalic acid)$_4$ (H_8TTFOC) as a ligand. Three distinct networks were successfully synthesized using Zn, Cu, and Ni with H_8TTFOC. However, all of these networks displayed a notable instability.

The results presented in the Paragraph 3 of this manuscript concerning **L**-MCl_2 (M= Cu, Zn, Hg, Cd) networks have been already reported in a paper.[14]

2. BVDT-TTF-Py_4 as a ligand for electroactive MOFs

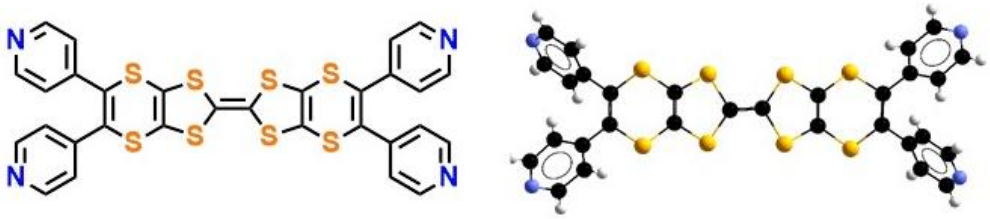


Figure 3- 1. BVDT-TTF-Py_4.

TTF and its derivatives have been widely investigated for their impressive electron-donating abilities and for their reversible oxidation to the radical cation ($TTF^{+\cdot}$) and dication (TTF^{2+}) forms.[15,16] The possibility of obtaining an open-shell band within a MOF structure paves the way towards highly conductive materials. Moreover, extended scaffolds such as BEDT-TTF contain four extra sulphur atoms and saturated non-planar CH_2CH_2 groups, thus favouring the formation of S···S multiple side intermolecular interaction in the layers of the radical cations to generate superconducting states at low temperatures for BEDT-TTF based organic conductors.[17]

Herein, BVDT-TTF-Py_4 is used (Figure 3- 1), an unsaturated version of BEDT-TTF functionalized by four pyridines.[18] Replacement of the ethylene bridge of BEDT-TTF by a vinylene one creates a more rigid structure and avoids the formation of stereogenic centres upon substitution of the ethylene bridge of BEDT-TTF.

[14]Solano, F.; Auban-Senzier, P.; Olejniczak, I.; Barszcz, B.; Runka, T.; Alemany, P.; Canadell, E.; Avarvari, N.; Zigon, N. *Chem. Eur.J.* **2023**, *29*, e202203138.
[15] M. Bendikov, F. Wudl, D. F. Perepichka, *Chem. Rev*. **2004**, *104*, 4891–4946
[16] N. Martin, *Chem. Commun.* **2013**, *49,* 7025–7027
[17] N. Avarvari, J. D. Wallis, *J. Mater. Chem.* **2009**, *19,* 4061.
[18] Nogami, T.; Inoue, K.; Nakamura, T.; Iwasaka, S.-I.; Nakano, H.; Mikawa, H. *Synth. Met*. **1987**, *19* (1–3), 539–544.

Pyridine stands as an ubiquitous coordinating moiety for MOF synthesis. They have been also widely applied to functionalize TTF as a redox active ligand in coordination chemistry.[19,20] The TTF-tetrapyridyl ligand was extensively explored for MOFs synthesis and was combined with Fe^{II} to yield spin-crossover materials.[21] The vast coordination chemistry of the pyridyl ligand afforded networks with various topologies,[22] where a strong influence of the counterion was noted.[23] The expansion of the TTF scaffold to a flexible tetrathiopyridyl-TTF provided polymers whose structural properties depended on the conformation adopted by the ligand.[24] Alternative design with an ethylenedithio-capped TTF-bis(thiopyridyl) supplied 1-D coordination polymers where the redox active cores overlapped in an interdigitated fashion, thus enhancing the conduction properties.[25]

2.1. Synthesis of BVDT-TTF-Py_4

BVDT-TTF-Py_4 was prepared according to the literature procedure.[26] The synthesis of BVDT-TTF-Py_4 begins with the preparation of Bis(4-pyridyl)acetylene[27] through the reaction of iodopyridine with 4-Ethynylpyridin. This intermediate compound undergoes a Diels-Alder reaction with the trithione. Subsequently, trans-chalcogenation with mercury acetate was performed, followed by a phosphite-mediated coupling step. BVDT-TTF-Py_4 is synthetized with an overall yield of 31% (Figure 3- 2).

[19] Devic, T.; Rondeau, D.; Şahin, Y.; Levillain, E.; Clérac, R.; Batail, P.; Avarvari, N. *Dalton Trans*. **2006**, 1331–1337.
[20] Lorcy, D.; Bellec, N.; Fourmigué, M.; Avarvari, N. *Coord. Chem. Rev*. **2009**, *253*, 1398–1438
[21] Wang, H.-Y.; Ge, J.-Y.; Hua, C.; Jiao, C.-Q.; Wu, Y.; Leong, C. F.; D'Alessandro, D. M.; Liu, T.; Zuo, J.-L. *Angew. Chem*. **2017**, *129*, 5557–5562.
[22] Wang, H.-Y.; Wu, Y.; Leong, C. F.; D'Alessandro, D. M.; Zuo, J.-L. *Inorg. Chem*. **2015**, *54*, 10766–10775.
[23] Yu, Q.; Su, J.; Ma, J.-P.; Leong, C. F.; D'Alessandro, D. M.; Wang, H.-Y.; Kurmoo, M.; Zuo, J.-L. *Cryst. Growth Des.* **2019**, *19*, 3012–3018.
[24] Bechu, D.; Rogez, G.; Hosseini, M. W.; Baudron, S. A. *New J. Chem.* **2019**, *43*, 14291–14298.
[25] Bechu, D.; Xie, L. S.; Breton, N. L.; Choua, S.; Dincă, M.; Hosseini, M. W.; Baudron, S. A. *Chem. Commun*. **2020**, *56*, 2407–2410.
[26] Brooks, A. C.; Day, P.; Dias, S. I. G.; Rabaça, S.; Santos, I. C.; Henriques, R. T.; Wallis, J. D.; Almeida, M. *Eur. J. Inorg. Chem.* **2009**, *10*, 3084–3093.
[27] Schmidt, B.; Berger, R.; Kelling, A.; Schilde, U. *Chem. Eur. J.* **2011**, *17*, 7032–7040.

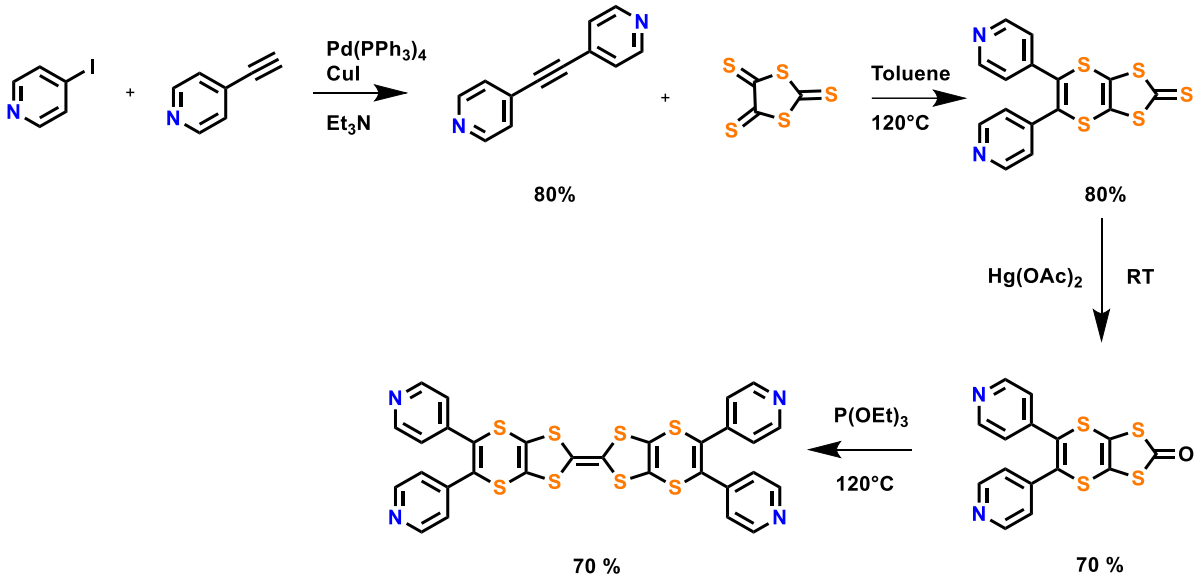


Figure 3- 2. Synthesis of BVDT-TTF-Py$_4$.

The cyclic voltammetry of BVDT-TTF-Py$_4$ ligand (**L**) was measured in DCM as shown in Figure 3- 3. The results revealed a single reversible wave corresponding to the formation of the radical cation. Various scan rates were employed to assess the reversibility of the process. The values of E_{Ox} , E_{Red}, and $E_{1/2}$ were converted vs SCE (Table 3- 1). The value of the half-wave potential, related to the formation of the radical cation is higher compared to the BVDT-TTF ($E^1_{1/2}$ 0.59 V vs SCE). On the other hand, the second oxidation $E^2_{1/2}$ was not observed, as already reported by Brooks *et al*.[26]

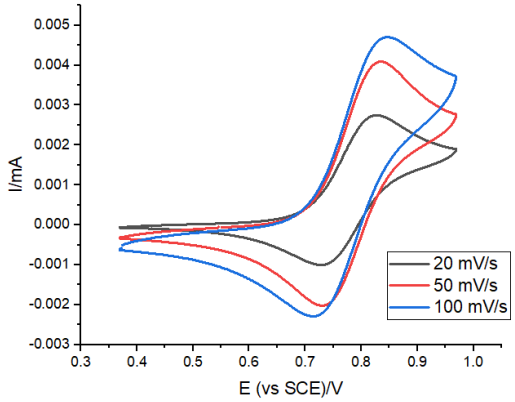


Figure 3- 3. Cyclic voltammetry of a solution of **L** 10^{-3} M, $TBAPF_6$ 0.1M in DCM. Platinum electrode as WE, platinum wire as CE and an Ag/AgCl/Saturated KCl electrode as RE at scan rate 20/50/100 mV·cm^{-1}. Values were converted with respect to the standard calomel electrode (SCE).

Scan rate [mV.s^{-1}]	E^1_{Ox}	E^1_{Red}	$E^1_{1/2}$
20	0.827	0.730	0.778
50	0.830	0.736	0.783
100	0.842	0.717	0.779

Table 3- 1. Potential oxidation, E_{Ox} and reduction, E_{Red} potentials and $E_{1/2}$ of **L** vs SCE at different scan rates.

3. Isostructural MOFs containing Hg(II), Cu(II), Cd(II), Zn(II) and BVDT-TTF-Py$_4$

3.1. Synthesis and structure of MOFs

The slow diffusion method is a commonly employed technique for the formation of MOFs. In this process, two solutions are prepared: one containing the metal ion and the other containing the organic ligand. These solutions are carefully layered in a tube, along with a buffer layer at the interface. A slow and controlled diffusion of one solution within the other is occurring, which promotes the growth of crystals. The formation of coordination bonds leads to the formation of extended networks, as the metal ions bind with the ligands to create a framework structure.[28]

The crystalline MOFs based on BVDT-TTF-Py$_4$ ligand (**L**) were synthesized by slow diffusion at RT during five days: a solution of ligand in DCM (1 mg/mL) was placed in a tube, a buffer solution of DCM/MeOH 1/1 and a solution (1 mg/mL) of metal ($CdCl_2$, $HgCl_2$, $ZnCl_2$) in MeOH were successively layered. The same procedure was used for the synthesis of BVDT-TTF-Py$_4$-$CuCl_2$ with the ligand dissolved in $CHCl_3$.

Single crystals suitable for SCXRD were obtained with the four different metals. The four networks were all isostructural and adopted the monoclinic $P2_1/c$ crystallographic space group. Crystallographic data are presented in Table 3- 2. The structure of **L**-$ZnCl_2$ network is presented in Figure 3- 4. These four materials all have the same formula **L**-MCl_2 (M = Cu, Zn, Cd or Hg). The asymmetric unit contains half of a ligand and half of a metal centre. Additional non-coordinated solvent molecules are also observed in the structures. Elemental analysis of the isostructural MOFs revealed the presence of specific guest molecules incorporated within their porous structures, two molecules of DCM, one molecule of DCM, one molecule of $CHCl_3$, three molecules of DCM for **L**-$CdCl_2$, **L**- $HgCl_2$, **L**-$CuCl_2$, **L**-$ZnCl_2$ respectively.

[28] Gangu, K. K.; Maddila, S.; Mukkamala, S. B.; Jonnalagadda, S. B. *Inorg. Chim. Acta* **2016**, *446*, 61–74.

	L-$CuCl_2$	**L-$ZnCl_2$**	**L-$CdCl_2$**	**L-$HgCl_2$**
Crystal system	monoclinic	monoclinic	monoclinic	monoclinic
Space group	$P2_1/c$	$P2_1/c$	$P2_1/c$	$P2_1/c$
V/Å^3	2020.43(17)	1962.91(6)	2016.7(3)	2041.59(7)
a/Å	12.7692(6)	12.8519(2)	13.1301(15)	13.0601(3)
b/Å	9.5235(5)	9.6095(2)	9.5611(10)	9.7826(2)
c/Å	16.6155(8)	15.9424(3)	16.1205(12)	16.0640(3)
α/°	90	90	90	90
β/°	90.673(4)	94.469(2)	94.781(8)	95.873(2)
γ/°	90	90	90	90
R_1,wR_2 (all data)	0.0631/0.1240	0.0486/0.1188	0.1647/0.3488	0.0391/0.0985
Completeness (%)	98.5	99.9	96.7	99.9

Table 3- 2. Crystallographic data **L** -MCl_2 (M=Cu, Zn, Cd or Hg).

The metal atoms stand in an octahedral environment, with four pyridyl moieties forming the square base while two chlorine atoms are located in apical positions, with L–M–L angles in the 83 to 96° range (Table 3- 3). The four pyridyl groups around one metal centre come from four different ligands. The metal-ligand distances are reported in Table 3- 3. The longest M–Cl distance of 2.891 Å is observed for **L**-$CuCl_2$. The central C=C bonds are in the 1.34 Å range for **L**-$CuCl_2$, **L**-$ZnCl_2$ and **L**-$HgCl_2$, which is in the expected range for a non-oxidized TTF. The distance is slightly longer at 1.36(2) Å for **L**-$CdCl_2$, which is probably due to the lower quality of the data collection affording a high uncertainty on the bond measurement. The ligands are organized through coordination bonds in 2-D layers (Figure 3- 4 b) where metals are separated by 9.5–9.8 Å along the *b* axis, and 20.8–21.7 Å in the perpendicular direction. The layers are superimposed in a shifted fashion, the central C=C bond of the ligand in a 2-D layer standing below the metal centre of the following layer (Figure 3- 4 a and c). Between two ligands of different layers, the smallest S–S distance is in the 3.21–3.24 Å range in the four structures. 1-D channels are formed within the packing and are occupied by solvent molecules, representing ca. 30 % of the overall crystal volume with pore size of 4.3×4.7 Å.

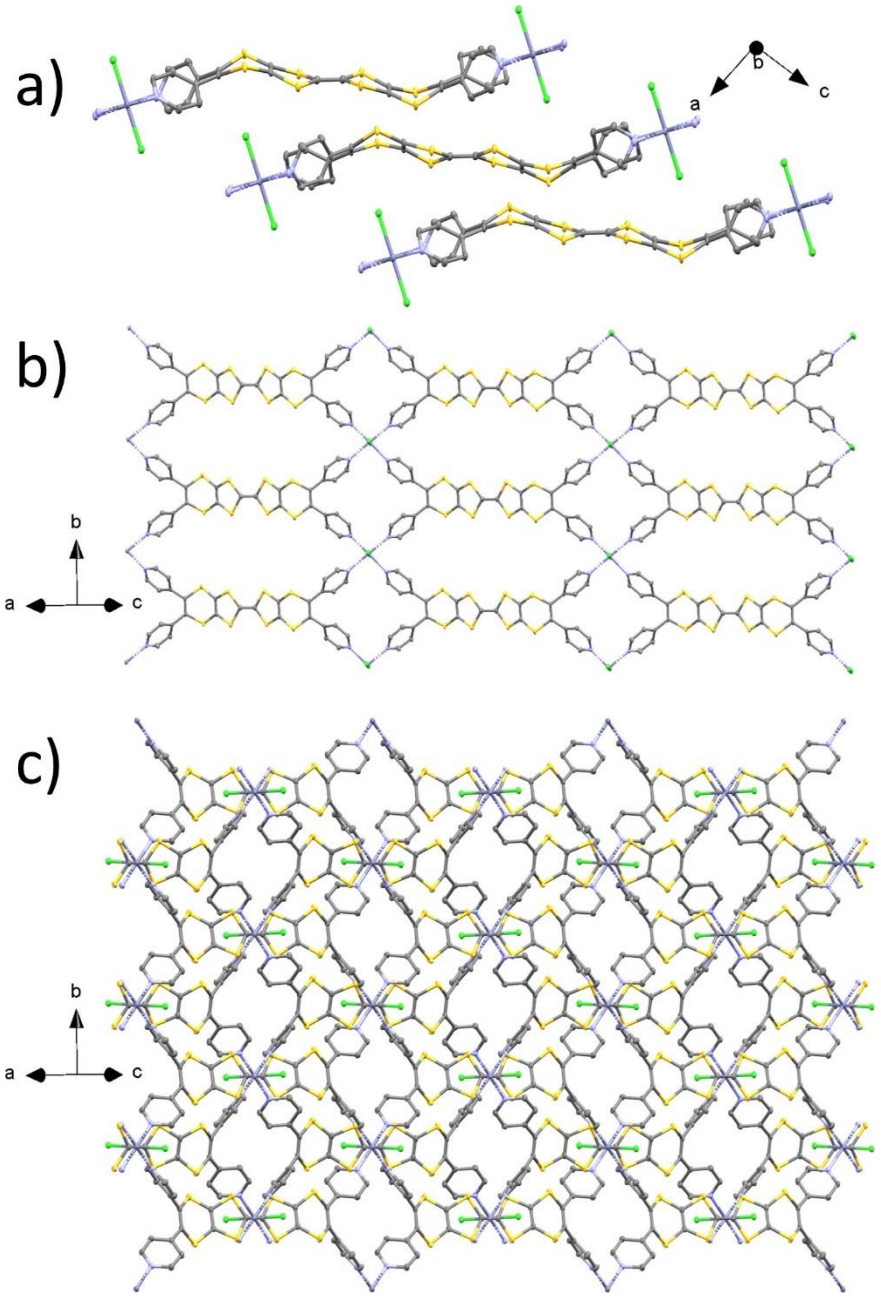


Figure 3- 4. Single crystal X-ray structure for BVDT-TTF-Py_4-$ZnCl_2$. a) Side view of the BVDT-TTF stacking, b) view of a single 2D layer and c) packing (solvent molecules and H atoms have been omitted for the sake of clarity. C: grey; S: yellow; N: blue; Cl: green and Zn: dark blue).

	Central C=C [Å]	M–N distance [Å]	M–Cl distance [Å]	N–M–N angle [°]	N–M–Cl angle [°]	Interligand S–S distance [Å]		
						o-o	i-o	i-o
L-$CuCl_2$	1.338(5)	2.062(3)–2.085(3)	2.8907(9)	88.4–91.7	89.6–90.3	3.215(1)	3.759(1)	3.713(1)
L-$ZnCl_2$	1.350(5)	2.193(3)–2.290(3)	2.4466(7)	85.2–94.8	90.0–90.4	3.249(1)	3.504(1)	3.707(1)
L-$CdCl_2$	1.36(2)	2.374(12)–2.443(10)	2.563(3)	84.8–95.2	89.6–90.6	3.217(6)	3.556(5)	3.721(6)
L-$HgCl_2$	1.340(7)	2.437(3)–2.547(3)	2.5286(10)	83.3–96.6	89.4–90.6	3.217(1)	3.516(1)	3.738(1)

Table 3- 3. Selected bond distances and angles for **L**-MCl_2. i and o correspond to the S atoms located on the inner rings and outer rings of **L**, respectively.

3.2. Solid state voltammetry

Electrochemical-based cyclic voltammetry measurements were performed to analyze the redox processes of the MOFs. A peculiar setup was adapted in the case of MOFs since they are not soluble in any solvent. The approach is based on a solid-state electrochemical configuration. The system is described in Figure 3-5. It consists in a cylindrical Teflon cell featuring a hole (0.4 cm diameter) in the bottom. A glassy carbon plate (GCP) as working electrode, WE, was tightened from below. The cell was tightened on a copper plate as the electrical contact. A Pt and Ag wire were used as counter (CE) and reference electrode (RE) respectively and placed at the top of the cylinder in contact with the electrolytic solution (0.1 M $TBAPF_6$ in AN). The MOFs were placed over the WE and covered with a Nafion membrane. After a 5-minute drying period the electrolytic solution was added. A similar configuration was previously used by Fontanesi *et al*.[29] The Nafion membrane acts as a physical barrier, preventing a direct contact between the solid and the electrolytic solution. Nafion is a perfluorosulfonic acid polymer with a unique structure that provides them with high ionic conductivity. This conductivity arises from the presence of sulfonic acid groups ($-SO_3H$) within the polymer matrix. These groups can dissociate and form mobile H^+ cations and negatively charged counterions within the membrane. The protons (H^+) and the other ions move through the polymer matrix

[29] Solano, F.; Inaudi, P.; Chiesa, M.; Kociok-Köhn, G.; Salvadori, E.; Da Como, E.; Vanossi, D.; Malandrino, M.; Carmieli, R.; Giacomino, A.; Fontanesi, C. *J. Phys. Chem. C* **2021**, *125* (16), 8677–8683.

by hopping between adjacent sulfonic acid groups within the membrane.[30,31] When a potential is applied to the electrochemical cell, the Nafion membrane allows the transfer of ions between the solid-state material and the electrolyte. This ion conduction occurs through the channels within the Nafion membrane enabling the transfer of ions between the solid-state material and the electrolyte. This efficient ion transport allows for rapid exchange of charge and promotes desirable electrochemical processes, such as redox reactions, at the electrode-electrolyte interface.

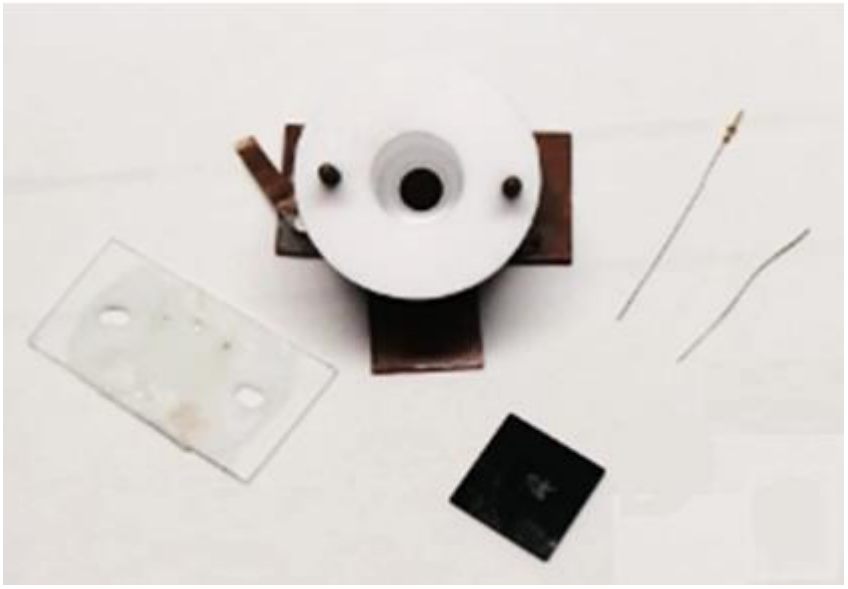


Figure 3- 5. Solid-state electrochemical configuration.

Cyclic voltammetry of the ligand was performed in solution and in a solid-state configuration. In solution, the redox reactions of BVDT-TTF-Py_4 tend to be more reversible compared to solid-state voltammetry, a characteristic attributed to the heightened diffusion dynamics near the electrode surface. This dynamic environment promotes more efficient interaction between the electroactive species and the electrode interface. As observed in Figure 3- 6, BVDT-TTF-Py_4 shows a pair of reversible redox waves centred at $E_{1/2}$=0.620 V in a CH_2Cl_2 solution. The anodic peak of the ligand in solid state is at a higher voltage compared to those recorded in solution because of a slower diffusion process. It is indeed necessary to consider that the transport of electrons is probably limited to the region of the solid particles in contact with the electrode and the solid-electrolyte or solid-electrode interface. This can introduce additional solid-state effects such as adsorption phenomena and charge transfer processes at these interfaces. Interfacial reactions or charge transfer resistances cause deviations from the reversible behaviour observed in solution

[30] Hosseini, M. G.; Rasouli, H.; Shahryari, E.; Naji L. *J. Appl. Polym. Sci*. **2017**, *134*, 44926.
[31] Lufrano, F.; Staiti, P. *Electrochim. Acta* **2004**, *49* (16), 2683–2689.

and result in shifts or asymmetry in the redox potentials. The values of the ligand are higher when compared with those of the related BEDT-TTF donor (whose first oxidation potential is $E_{1/2}$=0.49 V).

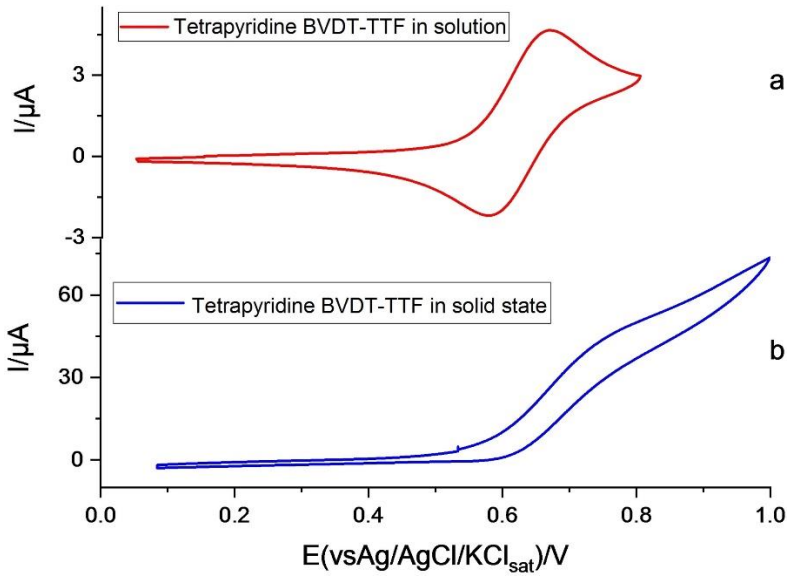


Figure 3- 6. CV curves of a) 1 mM ligand in solution in 0.1 M $TBAPF_6$ DCM solution and (b) ligand powder with Nafion. WE/GCE for a) and GCP for b). RE: Ag wire, CE: Pt wire. CV profiles were obtained at 20 mV s^{-1} scan rate.

The CV curve of **L**-$HgCl_2$, **L**-$CdCl_2$, **L**-$ZnCl_2$, **L**-$CuCl_2$ describe a one quasi-reversible redox process corresponding to the formation of the BVDT-TTF radical cation at 0.74 V, 0.73 V, 0.77 V, 0.66 V respectively (Figure 3- 7, Table 3- 4). The redox properties of the ligand are therefore maintained in the structure of the four networks. In the solid-state voltammetry of MOFs, the presence of pores within the MOF structure plays a crucial role in facilitating the redox conductivity and extending the oxidation process throughout the entire solid particle.[32] In fact, pores provide pathways for the entry and transport of the electrolyte species, such as mobile cations and anions. The connectivity of the pores ensures that the electrolyte can deeply penetrate into the MOFs structure, allowing for the efficient transfer of charge carriers resulting in enhanced redox conductivity. Indeed, the size of the pores in the MOFs is a critical factor influencing redox conductivity. Larger pores allow for the efficient diffusion and movement of electrolyte species, promoting rapid ion transport and facilitating extended redox processes. Smaller pores may restrict the mobility of ions and limit the extent of the redox reactions.[33] This elucidation would plausibly account for the relatively subdued visibility of the redox activity in the **L**-MCl_2.

[32] Domenech, A.; Garcıa, H.; Domenech-Carbo, M. T.; Llabres-i-Xamena, F. *J. Phys. Chem. C* **2007**, *111*, 13701-13711.
[33] Cai, M.; Loague, Q.; Morris, A. J. *J. Phys. Chem. Lett.* **2020**, *11* (3), 702–709.

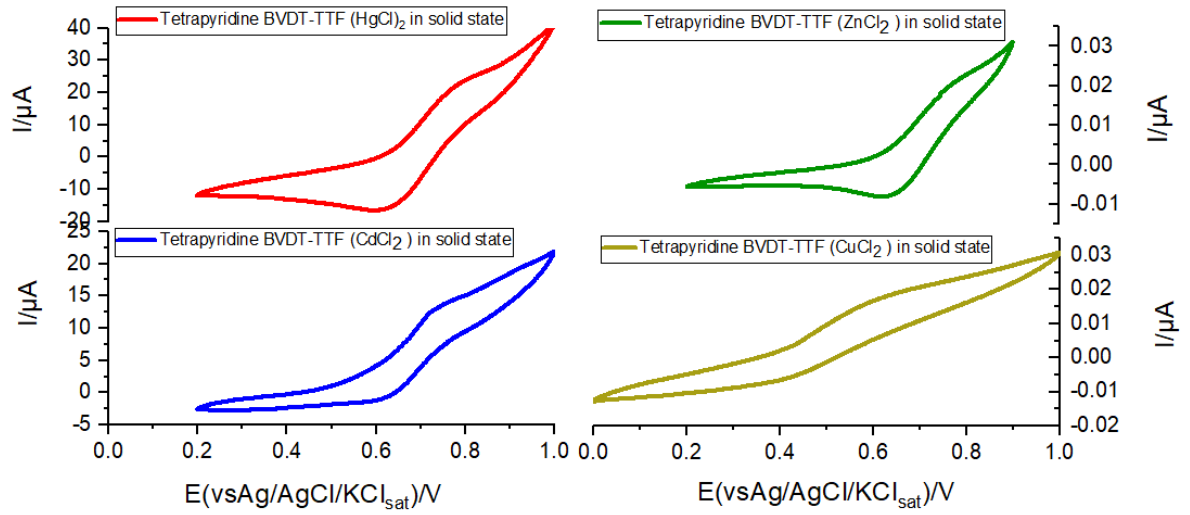


Figure 3- 7. CV curve of **L**-$HgCl_2$, **L**-$CdCl_2$, **L**-$ZnCl_2$, **L**-$CuCl_2$ crystalline powder with Nafion. WE/GCP, RE: Ag wire. CE: Pt wire. CV profiles were obtained at a 20 mV s^{-1} scan rate.

	E_{pa} [V]	E_{pc} [V]
BVDT-TTF-Py_4 in solution	0.665	0.575
BVDT-TTF-Py_4 in solid state	0.75	0.61
L-$HgCl_2$ in solid state	0.74	0.62
L-$CdCl_2$ in solid state	0.73	0.62
L-$ZnCl_2$ in solid state	0.77	0.63
L-$CuCl_2$ in solid state	0.66	0.40

Table 3- 4. Oxidation potential, E_{Ox}, and reduction potential, E_{Red} of BVDT-TTF-Py_4, **L**-$HgCl_2$, **L**-$CdCl_2$, **L**-$ZnCl_2$, **L**-$CuCl_2$ WE/GCE for a) and GCP for b). RE: Ag wire CE: Pt wire.

3.3. Post-synthetic Oxidation

In an attempt to improve the electrical conductivity through post-synthetic modifications, incorporation of iodine as an electron acceptor molecule within MOFs has emerged as an important approach.[34,35] This methodology has shown considerable success for increasing the conductivity of the frameworks based on TTF.[36] This oxidation process results in the formation of positively charged TTF radical cations ($TTF^{\bullet+}$), which are stabilized within the MOF structure leading to an increase in the overall electrical conductivity of the material. The conductive pathways within the MOF are enhanced as the $TTF^{\bullet+}$ species facilitate the movement of electrons through the framework.

The reaction of iodine with MOFs was achieved via adsorption from solution[37] or vapour diffusion.[38] For solution-based methods, iodine is dissolved in a nonpolar organic solvent such as cyclohexane and the desolvated MOFs are placed into the solution to allow the absorption of iodine in competition with solvent molecules. In the vapour-phase deposition method, solid iodine crystals or pellets are placed into a chamber. A vial containing the MOF is then positioned within the chamber. Iodine vapor is released from the source and comes into contact with the MOF substrate. The iodine molecules are adsorbed onto the surface of the MOF and promote its oxidation.

The vapour-phase deposition method was used for the obtained isostructural MOFs. 10 mg of **L**-MCl_2 were deposited in a 2 mL vial and placed in a larger vial containing I_2 (ca. 50 mg). The vial was closed and left overnight at room temperature. A colour change from red to dark purple is observed in every case, indicating the oxidation of BVDT-TTF (Figure 3- 8). A loss of crystal quality is visually observed during the oxidation process and confirmed by SCXRD.



Figure 3- 8. Crystal of **L**-$HgCl_2$ before and after oxidation.

[34] Zhang, X.; Maddock, J.; Nenoff, T. M.; Denecke, M. A.; Yang, S.; Schröder, M. *Chem. Soc. Rev.* **2022**, *51* (8), 3243–3262.
[35] Murase, R.; Leong, C. F.; D'Alessandro, D. M. *Inorg. Chem.* **2017**, *56* (23), 14373–14382.
[36] Zhang, Z.-R.; Ren, Z.-H.; Luo, C.-Y.; Ma, L.-J.; Dai, J.; Zhu, Q.-Y. *Inorg. Chem.* **2023**, *62* (11), 4672–4679.
[37] Hashemi L.; Morsali, A. *CrystEngComm*. **2014**, *16*, 4955–4958
[38] Sava, D. F.; Rodriguez, M. A.; Chapman, K. W.; Chupas, P. J.; Greathouse, J. A.; Crozier P. S.; Nenoff, T. M. *J. Am. Chem. Soc.* **2011**, *133*, 12398–12401

3.4. Structure of BVDT-TTF-$Py_4$$^{\bullet+}CdCl_2$ I_3^-

To our delight, crystals of **L**$^{\bullet+}CdCl_2$ I_3^- have been formed in a single-crystal to single-crystal fashion and have been characterized by SCXRD despite a loss of data quality due to a decrease of the overall crystallinity. The network is in the *C*2/m space group, with cell parameters close to the parent **L**-$CdCl_2$ cell as observe in Table 3- 5.

	L-$CdCl_2$	**L$^{\bullet+}CdCl_2$ I_3^-**
Crystal system	monoclinic	monoclinic
Space group	$P2_1/c$	$C2/m$
V/Å^3	2016.7(3)	2024.9(13)
a/Å	13.1301(15)	16.216(6)
b/Å	9.5611(10)	9.725(3)
c/Å	16.1205(12)	12.885(5)
α/°	90	90
β/°	94.781(8)	94.80(3)
γ/°	90	90
R_1,wR_2 (all data)	0.1647/0.3488	0.2265/0.5198
Completeness (%)	96.7	97.3

Table 3- 5. Crystal data of **L**-$CdCl_2$ and **L**$^{\bullet+}CdCl_2$ I_3^-.

A molecule of I_3^- has now replaced the solvent molecules within the pores, making the structure densely packed (Figure 3- 9). Due to the lack of precision on the bond length, no characteristic lengthening of the central C=C bond is observed. Despite a change of the space group from $P2_1/c$ to $C2/m$, the overall structural arrangement of the ligands and metal is preserved between **L**-$CdCl_2$ and **L**$^{\bullet+}CdCl_2$ I_3^-, both networks being practically superimposable. The unit cell parameters are similar (+/-2% in length and angles). The S···S interligand bond distances remain in the 3.2–3.7 Å range. The dihedral angles between the pyridyl and vinyl moieties change from 51–57° to 88° between **L**-$CdCl_2$ and **L**$^{\bullet+}CdCl_2$ I_3^-.

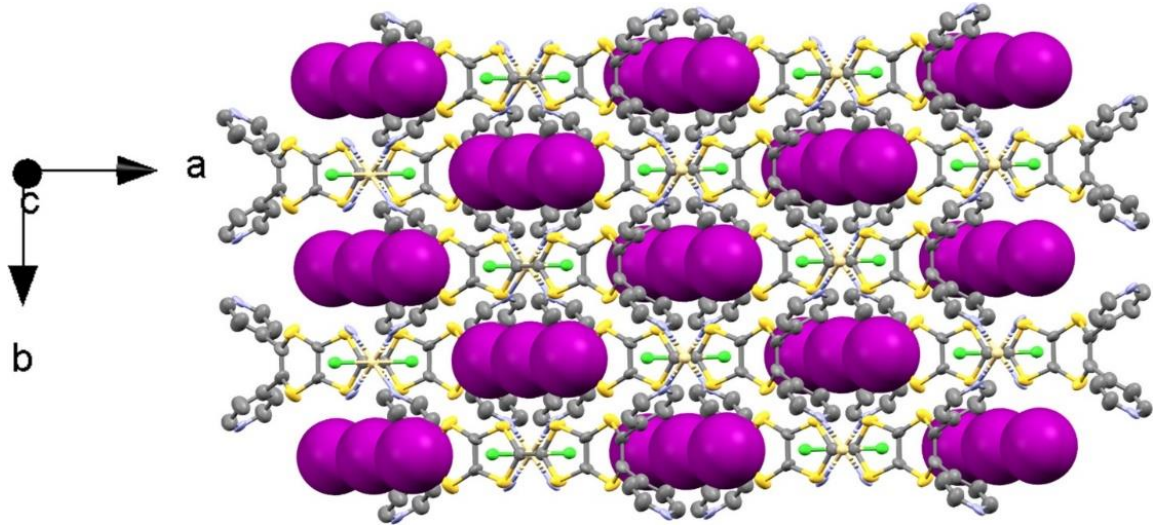


Figure 3- 9. Single crystal X-ray structure for **L**$^{\bullet+}CdCl_2$ I_3^- along the c axis.

3.5. Band structure calculations

Band structure calculations were conducted in collaboration with Dr. E. Canadell from ICMAB, Spain, and Dr. P. Alemany from the University of Barcelona, Spain.

The electronic delocalization in the present coordination networks occurs essentially via direct through-space S···S contacts within the (BVDT-TTF-Py_4) sublattice. As shown in Figure 3- 10 a) where the short S···S contacts are shown as dotted red lines, the conductive path is confined within the ab layers well separated by $CdCl_2$ and the pyridine ligands (and solvent molecules, not shown). These layers (Figure 3-10b) result from the superposition of two layers as those in Figure 3- 4c. These layers are in fact step-layers (Figure 3- 10d) where every step is made of a series of equivalent donors along b. As schematically shown in Figure 3- 10d, the molecules of successive steps turn around opposite directions. When molecules in step-layers are arranged in an alternating fashion, it leads to the formation of unique electronic energy levels within the material. This effect allow charge carriers to hop or tunnel between molecules more

efficiently increasing the material's electrical conductivity.[39] Although the a- and c-directions are interchanged, the same description applies for **L**$^{\bullet+}$-$CdCl_2$-I_3^-. These step-layers ensure a 2D continuous path of S···S interactions through the overlap mode displayed in Figure 3- 10c and should make the present networks relatively immune to defects.

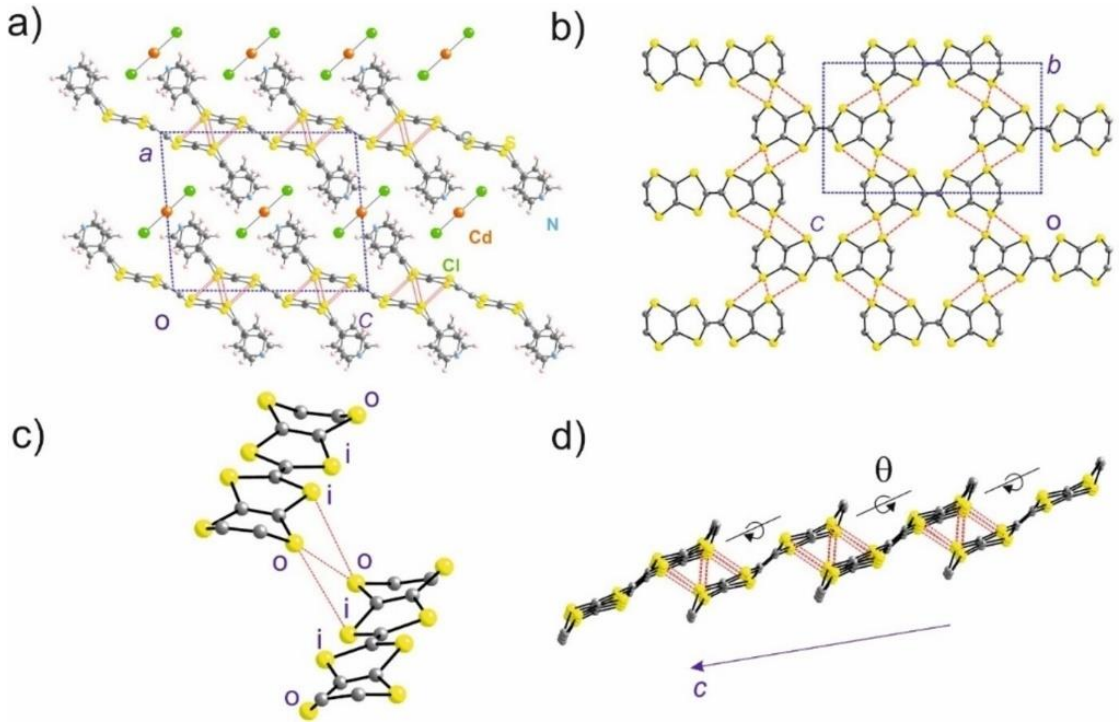


Figure 3- 10. Crystal structure of **L**-$CdCl_2$ where the short S···S contacts are shown as red dotted lines; for clarity solvent molecules are not displayed and the pyridine ligands have been omitted in b), c) and d). a) Projection view along the b-direction, b) top view of a double layer, c) overlap mode between pairs of **L** donors where the inner (i) and outer (o) types of S atoms are noted, and d) schematic lateral view showing that the double layers are step-layers with successive steps built from donors turning in opposite senses.

The calculated DFT band structure for **L**-$CdCl_2$ is shown in Figure 3- 11a where the energy zero refers to the highest occupied level of the HOMO band. It is the typical band structure of a slightly direct band gap semiconductor with hole type conductivity. The HOMO band is folded along the b*- and c*-directions because there are two equivalent molecules in the repeat unit. It exhibits similar dispersion along both the c* (Γ-Z) and b* (Γ-Y) directions, i. e. it is a typical 2D band. The total dispersion is ~0.3 eV which is not far from that of some of the most studied conducting metal-organic frameworks like Zn_2(TTFTB) [H_4TTFTB=tetrathiafulvalene tetrabenzoic acid], ~0.4 eV.[40] The band gaps of the two systems are also quite comparable, 1.47 eV for **L**-$CdCl_2$ and 1.75 eV for Zn_2(TTFTB). It is interesting to compare the results for the two frameworks even if the first is electronically 2D whereas the second is 1D. The shortest S···S

[39] Pouget, J.-P.; Alemany, P.; Canadell, E. *Mater. Horiz.* **2018**, *5* (4), 590–640.
[40] Park, S. S.; Hontz, E. R.; Sun, L.; Hendon, C. H.; Walsh, A.; Van Voorhis, T.; Dincă, M. *J. Am. Chem. Soc.* **2015**, *137* (5), 1774–1777.

contact in the present compound is 3.217 Å which is considerably shorter than in Zn_2(TTFTB), 3.757 Å. It is therefore surprising that the band dispersion is somewhat smaller for **L**-$CdCl_2$. Despite intrinsic orbital orientation aspects fixed by the coordination network there is another important aspect worth of notice. In the extended BVDT-TTF donor there are two types of S atoms: those of the inner TTF core and those which are out of this core (noted "i" and "o" respectively in Figure 3- 10c). It is well known for similar ligands like BEDT-TTF that the participation of the outer S p_z orbitals into the HOMO is noticeably smaller than that of the inner S ones (for BEDT-TTF the relation is around 1/3).[39,41] In the case of Zn_2(TTFTB) the contacts are of the i···i type but in the present case the 3.217 Å contact is of the o···o type and the two other contacts, 3.546 and 3.721 Å are of the i···o type. Thus, the S···S contacts are less effective than in Zn_2(TTFTB) because they all implicate S atoms of the o type but they are more numerous and finally the band dispersion is only a bit smaller. These contacts can be tuned for instance varying the angle θ (Figure 3- 10d) or the nature of the transition metal. Using more extended donors, it is possible to achieve step-layers with band dispersion comparable to those in the M_2(TTFTB) family and other frameworks where the conducting path is mostly 1D. Additionally, the presence of a 2D conducting path is expected to enhance conductivity stability and immunity to defects. This because a 2D network can provide multiple pathways for charge carriers to move through the material, reducing the chance of encountering obstacles or bottlenecks that could hinder the flow of charge.

[41] Whangbo, M. H.; Williams, J. M.; Leung, P. C. W.; Beno, M. A.; Emge, T. J.; Wang, H. H. *Inorg. Chem.* **1985**, *24* (22), 3500–3502.

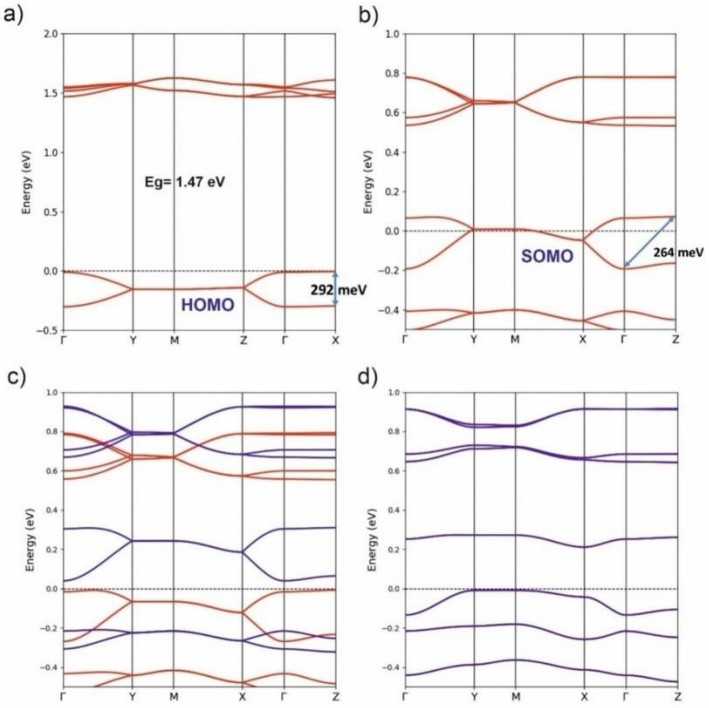


Figure 3- 11. DFT band structure for **L**-$CdCl_2$ (a). DFT band structure for the metallic (b), ferromagnetic (FM) (c) and fully antiferromagnetic states (AF) (d) of $\mathbf{L}^{\bullet+}$-$CdCl_2$-I_3^-. Γ=(0, 0, 0), X=(a*/2, 0, 0), Y=(0, b*/2, 0) and Z=(0, 0, c*/2); M=(0, b*/2, c*/2) in a) but (a*/2, b*/2, 0) in b), c) and d). The dashed line refers to the highest occupied level in all cases. All levels up to the energy zero are doubly filled in a) and b). Spin-up and spin-down bands are shown in red and blue, respectively in (c) and (d). The spin-up and spin-down bands are identical although located in spatially different but equivalent sites in (d) so that they superpose and only the blue bands are visible. Note the larger energy scale in a).

The calculated DFT band structure for $\mathbf{L}^{\bullet+}$-$CdCl_2$-I_3^- assuming double occupation of the levels (i. e., a metallic state) is shown in Figure 3- 11b. Now the HOMO band is half-filled and the Fermi level lies inside the band. The important feature is that the topology of this SOMO band is similar to that of the HOMO band for the non-oxidized donor lattice and the total dispersion is also comparable (264 meV in Figure 3- 11b and 292 meV in Figure 3- 11a. Consequently, the nature of the S···S interactions already discussed has not experienced a major disturbance upon the oxidation of the donor lattice. The major change concerns the energy separation between the SOMO and the lower fully empty bands but this does not play any important physical role for $\mathbf{L}^{\bullet+}$-$CdCl_2$-I_3^-. Since the band is half-filled and given the stoichiometry, the electronic structure for situations where every donor accommodates a single localized electron must be considered. In Figure 3- 11c and Figure 3- 11d are shown the DFT band structures for localized states where all donors have an electron with the same spin i. e. a ferromagnetic state (FM), or where all adjacent donors have opposite spins, i. e. a fully antiferromagnetic state (AF). The metallic state was found to be higher in energy (in meV/formula unit) than both the FM and full AF states: Metallic (0), FM (−23.8) and full AF (−34.0), thus confirming the electronically localized nature of $\mathbf{L}^{\bullet+}$-$CdCl_2$-I_3^-. This system should therefore exhibit an antiferromagnetic ground state.

In a comparison between metallic (Figure 3- 11b) and ferromagnetic (FM) (Figure 3- 11c) states, the effect of electron repulsions is evident. The FM state shows spin-up (red) and spin-down (blue) bands that shift together and have similar shapes as those in the metallic state. Because of the electron repulsions, a gap develops separating the filled and empty bands so that the conductivity is activated.

In the fully AF state (Figure 3- 11d), the gap is distinctly different from **L**-$CdCl_2$ (Figure 3- 11a) because it is mainly dominated by electron-electron repulsions within the SOMO of the donors, which outweigh the effect of the direct S···S overlap. The bands for the more stable full AF state (Figure 3- 11d) are really the superposition of two bands (one mostly associated with spin up and more localized in the donors of one out of every two steps of the layer while the other, with spin down, is more localized in the donors of the other step). The more favorable electron-electron repulsions in the fully AF state lead to the opening of a very noticeable gap between flatter bands as a result of the spatial confinement of electrons with different spins into different steps of the layer

Despite checking various spin configurations, the fully AF state remains the most stable, and we have not observed significant magnetic order between layers. Consequently, the conducting and magnetic properties are unlikely to be seriously affected by the presence of a small number of non-oxidized donors due to the intercrossed nature of the 2D interactions.

In summary, the use of extended TTF-based donors such as **L** may lead to interesting new conducting coordination networks mostly because of two features: (i) they favor 2D conducting paths which will make these systems considerably less sensitive to defaults, and (ii) the extended nature of the sulfur-containing fragment of the donor decreases the U intra-site electron repulsion term (i. e. the U_{SOMO}) which dominates the activation energy. Further engineering of the conductivity can also be anticipated by controlling the S···S contacts, as noted above, that will play on the overlap component of the hopping.

3.6. Powder X-ray Diffraction (PXRD)

PXRD is a non-destructive technique widely used for characterizing the stability, purity, and structural changes in MOFs. By collecting a single-crystal X-ray diffraction pattern of the MOF, the positions and intensities of the diffraction peaks on PXRD can be simulated. These diffraction patterns serve as unique fingerprints of the MOF's crystal structure, enabling the determination of its stability and purity by comparing the diffraction patterns against the reference.[42,43]

The powdered crystals of **L**-$CuCl_2$, **L**-$CdCl_2$ and **L**-$HgCl_2$ preserve their crystallinity after drying in the air at room temperature for 1 day as observed in Figure 3- 12, confirming also that the products are phase-pure.

---

[42] Bunzen, H. *ChemNanoMat* **2021**, *7*, 998–1007.
[43] Li, Z.-J.; Yue, Z.; Ju, Y.; Wu, X.; Ren, Y.; Wang, S.; Li, Y.; Zhang, Z.-H.; Guo, X.; Lin, J.; Wang, J.-Q. *Inorg. Chem.* **2020**, *59* (7), 4435–4442.

On the other hand, the crystals of **L**-$ZnCl_2$ lose their crystalline character and only broad bands were observed by PXRD. Nevertheless, non-grinded single crystals for all the networks are kept in the air for several days without significant loss of diffraction intensity for all the materials.

The introduction of iodine into a MOF structure can be reflected in the PXRD analysis, for example in the positions and intensities of the diffraction peaks. These shifts indicate changes in the interatomic distances and lattice parameters due to the presence of iodine. Upon obtaining single-crystal X-ray data for the neutral and doped MOF **L**-$CdCl_2$, it was possible to simulate the PXRD pattern. Despite a change in the space group from $P2_1/c$ to $C2/m$, the overall structural arrangement of the ligands and metal ions remains highly similar between the neutral MOF (BVDT-TTF$(py)_4$-$CdCl_2$) and the doped MOF (**L**$^{\bullet+}$-$CdCl_2$-I_3^-). In fact, the networks of both structures can be practically superimposed. The PXRD simulation yields very similar results, as the observed changes in lattice symmetry are subtle. This study provides compelling evidence for the chemical stability of at least three out of the four isostructural MOFs investigated.

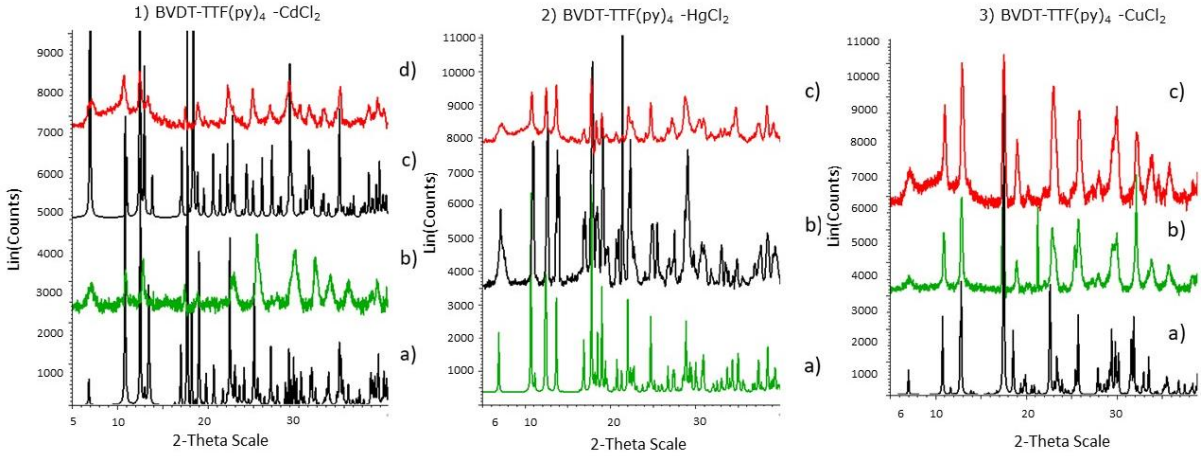


Figure 3- 12. 1) Theoretical PXRD pattern of (a) **L**-$CdCl_2$ and (c) **L**$^{\bullet+}$-$CdCl_2$-I_3^- ; Experimental PXRD pattern of (b) **L**-$CdCl_2$ and (d) **L**$^{\bullet+}$-$CdCl_2$-I_3^-. 2) (a) Theoretical PXRD pattern of **L**-$HgCl_2$, (b) experimental PXRD pattern of **L**-$HgCl_2$ and (c) of **L**$^{\bullet+}$-$HgCl_2$-I_3^-. 3) (a) Theoretical PXRD pattern of **L**-$CuCl_2$, (b) experimental PXRD pattern of **L**-$CuCl_2$ and (c) of **L**$^{\bullet+}$-$CuCl_2$-I_3^-.

3.7. Raman measurements: comparison between neutral and oxidised MOFs

Raman spectroscopy experiments and theoretical calculations were conducted in collaboration with our colleagues at the Institute of Molecular Physics, Polish Academy of Sciences, specifically with Iwona Olejniczak, Arkadiusz Frąckowiak, and Bolesław Barszcz. This part of project was made possible through the support of the POLONIUM 2022 project, during which I had the privilege to work two weeks at their institute.

Raman spectroscopy experiments and theoretical calculations were performed to assess the oxidation state of BVDT-TTF in the non-oxidized and oxidized species of MOFs. The ligand BVDT-TTF-Py_4 is characterized

by a strong σ-donating and π-accepting character and the coordination bond between the pyridine and the metal is responsible for the notable cooperative electronic properties of the resulting material. The C=C stretching modes of TTF derivate usually observed in Raman spectra stand in the frequency range 1300–1700 cm^{-1}. These modes are known to display a strong dependence of frequency on charge and have been widely used in the characterization of charge states in BEDT-TTF-based salts.[44, 45] DFT calculations of vibrational modes for both the neutral and the radical cation BVDT-TTF-Py_4 have been performed in order to estimate the charge localized on ligand in the selected coordination networks. Charge-sensitive vibrations can be used to determine the charge state. The tetrapyridine-substituted BVDT-TTF molecule is not flat but assumes an approximately orthogonal orientation

with respect to the main molecular plane. This is clearly seen in Figure 3- 13 that displays comparison of the frontier molecular orbitals in the neutral and the cationic forms. As a consequence of this steric arrangement, molecular dynamics of **L** significantly differ between the neutral and the cationic species. The charge-sensitive vibration mode labelled ν_C (Figure 3- 14) displays the strongest frequency dependence on charge. In case of neutral **L**, the ν_C mode features in-phase stretching of the three inner double C=C bonds, but the vibration is confined to the central C=C bond for the cation. The theoretical frequency of ν_C is 1500 cm^{-1} for the neutral and 1382 cm^{-1} for the cation, therefore we observe a similar frequency shift of the charge-sensitive mode due to oxidation of the donor molecule as the value characteristic for charge sensitive modes of BEDT-TTF. Figure 3- 15 shows Raman experimental spectra measured at room temperature for selected coordination networks based on neutral BVDT-TTF-Py_4 and cation BVDT-TTF-Py_4 dot+, respectively, together with theoretical Raman spectra; experimental Raman spectrum of the neutral BVDT-TTF-py_4 is included in Figure 3- 15 (a). The characteristic

vibrational structure in the frequency range of the stretching C=C modes is clearly seen in all experimental spectra, in close agreement with the theoretical spectrum. We assign the strong band centred at 1500 cm^{-1} in the theoretical spectrum of neutral BVDT-TTF-Py_4 (Figure 3- 15 (b)), and in the range 1503–1514 cm^{-1} in experimental spectra (Figure 3- 15 (a)), as the charge-sensitive ν_C mode characteristic for the neutral species (Table 3- 6). The presence of a broad feature at 1410 cm^{-1} in BVDT-TTF-py_4-$HgCl_2$ and at 1414 cm^{-1} in BVDT-TTF-py_4-$ZnCl_2$, that we attribute to ν_C of the cation, suggests that a minute amount of BVDT-TTF-$Py_4^{\bullet+}$ radicals is present in these materials. Note that in theoretical spectra, the Raman intensity at the frequency of ν_C is two orders of magnitude higher in the case of the cation than in the case of the neutral donor.

In the theoretical spectrum of BVDT-TTF-$Py_4^{\bullet+}$ (Figure 3- 15 (d)) the charge-sensitive ν_C mode, identified as a signature of the cation, appears as a strong band centred at 1382 cm^{-1}. In the experimental Raman spectra (Figure 3- 15 (c)), this mode is located at 1402 cm^{-1} in BVDT-TTF-$Py_4^{\bullet+}CdCl_2$-I_3^- (Table 3- 6). On

[44] Yamamoto, T.; Uruichi, M.; Yamamoto, K.; Yakushi, K.; Kawamoto, A.; Taniguchi, H. *J. Phys. Chem. B* **2005**, *109*, 15226–1523.
[45] Girlando, A. *J. Phys. Chem. C* **2011**, *115*, 19371–19378.

the other hand, the relatively weak feature centred at 1503 cm^{-1}, BVDT-TTF-Py_4 is suggestive of remaining neutral BVDT-TTF-Py_4 molecules in the structure (Table 3- 6).

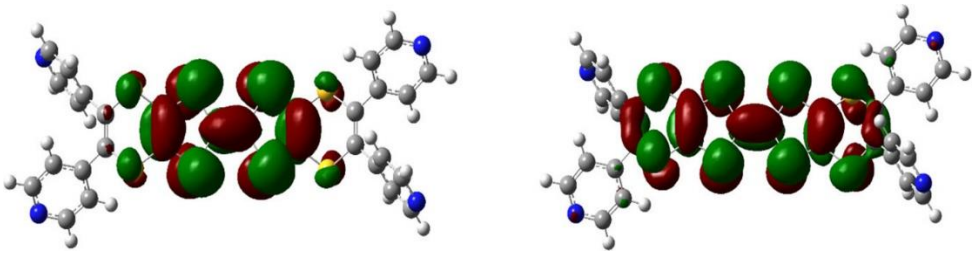


Figure 3- 13. Frontier molecular orbitals: HOMO (Highest Occupied Molecular Orbital) of neutral BVDT-TTF-Py_4 (left), and α-SOMO (Single Occupied MO) of the BVDT-TTF-$Py_4^{\bullet+}$ cation (right), calculated using DFT methods

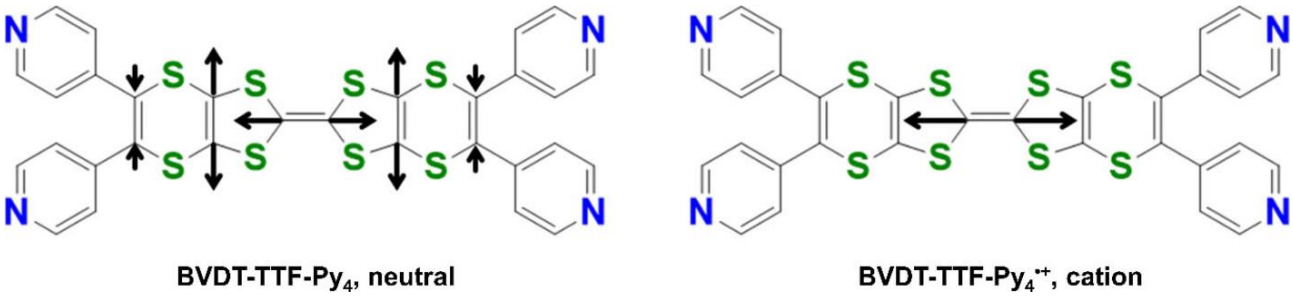


Figure 3- 14. Schematic view of the symmetric C=C stretching ν_C mode of the neutral BVDT-TTF-Py_4 molecule (left) and BVDT-TTF-$Py_4^{\bullet+}$ radical cation (right), as it results from DFT calculations.

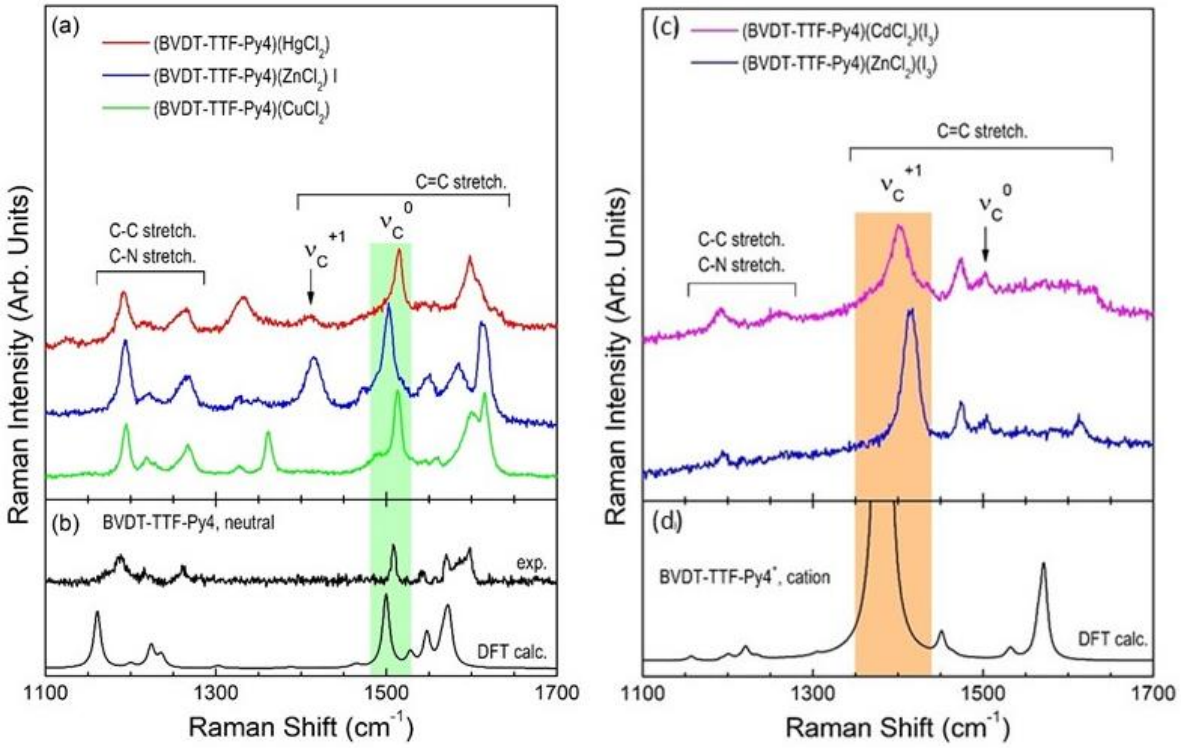


Figure 3- 15. (a) Raman spectra of selected BVDT-TTF-Py$_4$ coordination networks; (b) Raman spectrum of neutral BVDT-TTF-Py$_4$, together with the respective theoretical Raman spectrum calculated at the B3LYP/6-31+ +G(d,p) level of theory. (c) Raman spectra of **L**$^{\bullet+}$CdCl$_2$ I$_3^-$ and **L**$^{\bullet+}$ZnCl$_2$ I$_3^{-\cdot}$ (d) Theoretical Raman spectrum of BVDT-TTF-Py$_4^{\bullet+}$ calculated at the B3LYP/6-31+ +G(d,p) level of theory. The charge-sensitive v_C mode is labelled as v_C^{+1} for the cation. (a), (b) and (c) are measured at room temperature with the 785 nm excitation line at room temperature.

	DFT calc[a]/Neutral exp.	**L-ZnCl$_2$**	**L-HgCl$_2$**	**L-CuCl$_2$**	**L-CdCl$_2$-I$_3^-$**
ν_C^0	1500/1509	1503	1515	1513	1503
ν_C^{+1}	1382/–	1414	1410	–	1402

Table 3- 6. The positions in cm^{-1} of the charge-sensitive ν_C mode in calculated and experimental Raman spectra of **L** and coordination polymers with M=Zn, Hg, Cu, and (**L**$^{\cdot+}$-CdCl$_2$ I$_3^-$), with M=Cd, Zn. [a] Theory level: B3LYP/6-31++G(d,p), scaled with a 0.9614 factor.

Figure 3- 16 displays Raman spectra of coordination network that contain triiodide ions, **L**$^{\cdot+}$-CdCl$_2$ I$_3^-$ in the frequency range of the stretching polyiodide modes. The spectra are characterized by three distinct features (Table 3- 7). The band centred at 111 cm^{-1} is attributed to the Raman-active symmetric stretching v_s (I$_3^-$) mode of the centrosymmetric triiodide anion with the symmetry *Dih*. The middle feature at ~144

cm^{-1} assigned to asymmetric stretch ν_a (I_3^-) mode, reveals the presence of the asymmetric triiodide with the symmetry lower than *Dih*. On the other hand, the highest-frequency band at 167 cm^{-1}, is most probably related with the presence of iodine I_2 weakly coordinated to triiodide, resulting in an appearance of L-shaped pentaiodide in the structure. Therefore, we attribute the 167 cm^{-1} band to a symmetric stretching ν_s (I_5^-) mode of pentaiodide.[46,47]

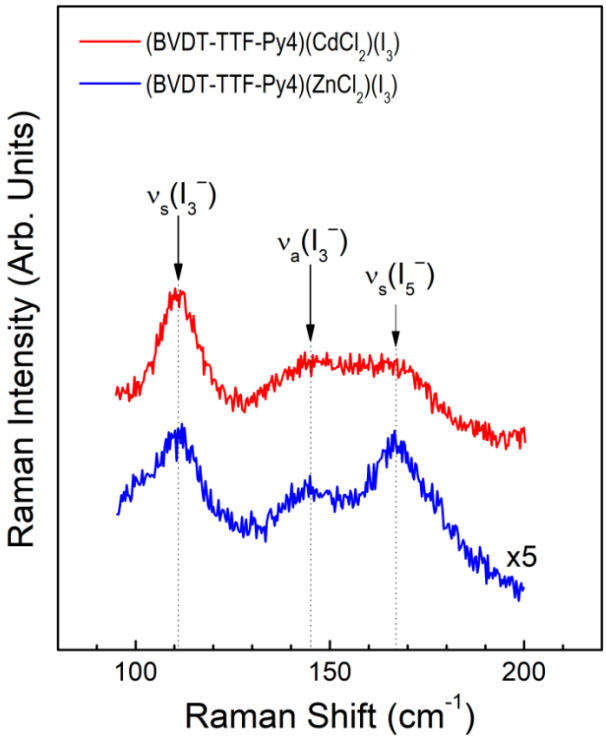


Figure 3- 16. Raman spectra of **L**$^{\bullet+}$-$CdCl_2$-I_3^- measured at room temperature with the 632.8 nm excitation line, in the frequency range of the stretching polyiodide modes; the spectra are offset for clarity.

	$L^{\bullet+}$ $(CdCl_2)(I_3)^-$
$\nu_s(I_3^-)$	111
$\nu_a(I_3^-)$	~144
$\nu_s(I_3^-)$	~167

Table 3- 7. Experimental polyiodide frequencies in cm^{-1} observed in Raman spectra of **L** $^{\bullet+}(CdCl_2)(I_3)^-$.

[46] Svensson, P. H.; Kloo, L. *Chem. Rev.* **2003**, *103* (5), 1649–1684.
[47] Jerman, I.; Jovanovski, V.; ŠurcaVuk, A.; Hočevar, S. B.; Gaberšček, M.; Jesih, A.; Orel, B. *Electrochim. Acta* **2008**, *53* (5), 2281–2288

3.8. Conductivity measurements: comparison between neutral and oxidised MOFs

Conductivity measurements were conducted in collaboration with Dr. Pascale Auban-Senzier at Université Paris-Saclay.

Conductivity measurements were performed with a two-contact method on single crystals.[48] Single-crystal measurements are highly preferred when investigating the intrinsic conductivity of a material. They offer several advantages, such as eliminating contributions from grain boundary resistances and providing insights into transport along specific crystallographic directions, particularly in anisotropic structures. The two-contact configuration involves making contact with a material using two wires, typically placed at opposite ends of a crystal. In this setup, a known voltage is applied across the sample, and the resulting current is measured. Through Ohm's law ($V = I \times R$), the resistance (R) or its reciprocal, conductance (G), are determined. This configuration enables the measurement of electrical properties by applying a voltage and measuring the resulting current. Two-contact configuration does not compensate for contact resistance. If the connections between the sample and wires are poor (like non-ohmic), the measured conductivity might be lower than the real conductivity of the material. Four-contact devices – where two wires impose a current and two others measure the potential – are therefore more accurate because the contact resistance is suppressed. .

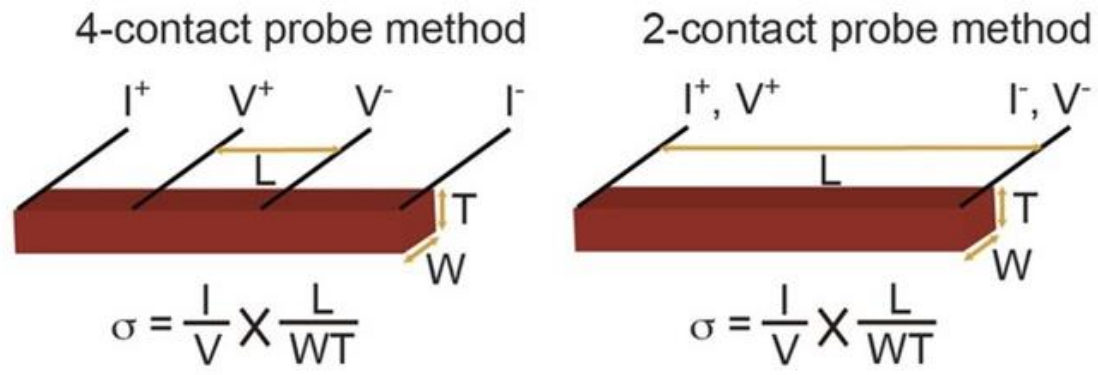


Figure 2- 28. Four and Two-contact method commonly used for measuring electrical conductivity of MOFs. I and V denote current and voltage, respectively, and L, w, and t denote the length, width, and thickness of the samples, respectively.[49]

Compounds **L**-$CdCl_2$ and **L**-$HgCl_2$ before and after oxidation were analysed. **L**-$CuCl_2$ and **L**-$ZnCl_2$ crystals were too small for connection with the electrodes. For **L**-$HgCl_2$ the conductivity goes from $2–2.5 \cdot 10^{-9}$

[48] Givaja, G.; Amo-Ochoa, P.; Gómez-García, C. J.; Zamora, F. *Chem. Soc. Rev.* **2012**, *41* (1), 115–147.
[49] Sun, L.; Campbell, M. G.; Dincă, M. *Angew. Chem. Int. Ed.* **2016**, *55* (11), 3566–3579.

$S \cdot cm^{-1}$ to $1.2–2 \cdot 10^{-8}$ $S \cdot cm^{-1}$ upon oxidation and for **L**-$CdCl_2$ from $7–9 \cdot 10^{-10}$ $S \cdot cm^{-1}$ to $4–6 \cdot 10^{-9}$ $S \cdot cm^{-1}$ (2 crystals measured for each compound). This *ca*. 8-fold enhancement of the conductivity for both compounds is directly related to the oxidation of the ligands, yielding an open-shell structure, and may be partly counter-balanced by the loss of crystallinity observed in X-ray.

4. BVDT-TTF-Py_4-$[CuCl_2]_2$

4.1. Synthesis and structure

A new MOF was synthesized by the slow diffusion method using a solution of BVDT-TTF-Py_4 (**L**) in $CHCl_3$ placed in a tube, a buffer of DMSO layered, and finally a solution of $CuCl_2$ in MeOH. DMSO lowers the diffusion rate of species compared to $CHCl_3$ or MeOH thanks to its higher viscosity (*ca*. 2 mPa.s for DMSO *vs*. 0.5 mPa.s for $CHCl_3$ and MeOH). This slower diffusion leads to the formation of a novel MOF structure. The application of identical conditions with $CdCl_2$, $ZnCl_2$, and $HgCl_2$ led to the crystallization of the ligand. The structure of BVDT-TTF-Py_4-$[CuCl_2]_2$ was analysed using SCXRD. The crystallographic data are given in Table 3- 8. The structure of **L**-$[CuCl_2]_2$ network is presented in Figure 3- 17. The asymmetric unit contains half of a ligand and a metal centre. Additional non-coordinated solvent molecules are not observed in the structure and the residual electronic density was removed using the Solvent Mask function of the Olex2 software.

Crystal system	monoclinic
Space group	*I*2/a
V/Å^3	6042.4(9)
a/Å	8.9751(7)
b/Å	17.3241(15)
c/Å	38.861(3)
α/°	90
β/°	90.014(7)
γ/°	90
R_1,wR_2 (all data)	0.0669/0.1907
Completeness (%)	97.2

Table 3- 8. Crystallographic data of **L**-$[CuCl_2]_2$.

As observed in Figure 3- 17 the metal is pentacoordinated, approximating a distorted trigonal bipyramid, surrounded by two N atoms of the ligands and three chloride atoms. The $(N\cdots M\cdots N)_{trans}$ bond angles is 171.7(3)° and the axial M···N distances are 2.013(6) Å and 2.015(6) Å.

The central C=C bond is 1.346(14) Å, supporting the neutral charge of the BVDT-TTF moiety. The ligand shows a torsion of 126.2° about the S···S vector of the dithiin ring and a much lower torsion about the S···S vector in the dithiole ring of 168.2°. The donors and metals form 2-D layers that are further interconnected by bridging Cl atoms in equatorial positions with Cu-Cl bond length of 2.354(2) Å and 2.626(2) Å. The other equatorial position is occupied by non-bridging Cl-Cu bond length of 2.251(2) Å. Between two ligands of different layers, the smallest S···S distance is 3.58 Å , and this distance pertains to the S atom on the inner ring and the S atom on the outer ring (i-o) (Figure 3- 17 c). 1-D channels are formed within the packing and are occupied by solvent molecules. These solvent molecules are disordered and therefore not crystallographically observed. They represent approximately 50 % of the overall crystal volume, as determined through PLATON calculations. The channels have a measured pore size of 11 x 16 Å.

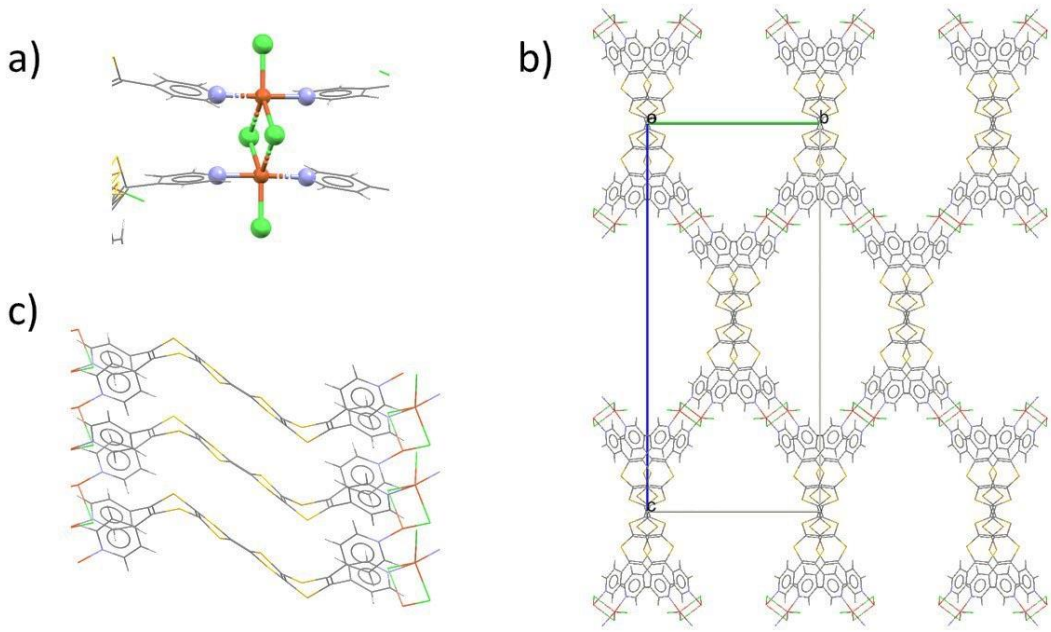


Figure 3- 17. Single crystal X-ray structure for **L**-$[CuCl_2]_2$. a) Secondary building unit b) packing c) side view of the BVDT-TTF-Py_4 stacking sequences along b-axis (C: grey; N: blue; Cl: green; Cu: orange).

Central C=C [Å]	M–N distance [Å]	M–Cl distance [Å]	M–Cl distance [Å] bridge	N–M–N angle [°]	N–M–Cl angle [°]	Interligand S–S distance [Å]		
						i-i	i-i	i-o
1.346(14)	2.013(6)–2.015(6)	2.251(2)	2.626(2) - 3.354(2)	171.7(3)	87.18(19)	3.707(1)	3.810(3)	3.588(3)

Table 3- 9. Selected bond distances and angles for **L**-$[CuCl_2]_2$. i and o correspond to the S atoms located on the inner rings and outer rings of **L**, respectively.

4.2 Post-synthetic Oxidation

To improve the electrical conductivity of **L**-$[CuCl_2]_2$, the incorporation of iodine through a post-synthetic modification approach was explored. However, this method presented a synthetic challenge due to the limited stability of the **L**-$[CuCl_2]_2$ under these conditions. After one day of exposure to iodine vapour or to an iodine solution in cyclohexane, a noticeable colour change was observed (Figure 3- 18). This provides valuable insights into the reactivity of BVDT-TTF and its sensitivity to oxidation by iodine.

Nevertheless, the resulting product exhibited a poor crystallinity, making it difficult to perform structural analysis using SCXRD. This chemical instability may be attributed to the interaction between the introduced iodine species and the MOF framework, leading to structural distortions or decomposition of the MOF structure.



Figure 3- 18. Crystal before and after oxidation.

4.3 Powder X-ray Diffraction (PXRD)

PXRD analysis were conducted on a powdered sample of **L**-$[CuCl_2]_2$ before and after oxidation. Figure 3-19 demonstrates a proper correlation between the experimental diffraction pattern of **L**-$[CuCl_2]_2$ and its

theoretical counterpart. The experimental peaks are broad and lack intensity, which is indicative of a loss of long-range order.

Moreover, one peak highlighted in yellow at 7° matches with a peak of the crystalline phase of **L**-$CuCl_2$ discussed in paragraph 3 (Figure 3- 19). Apart from the highlighted peak, we do not observe additional distinct peaks that can be attributed to **L**-$CuCl_2$ without ambiguity. We indeed observed a similar weak and broad peak at 7° in the background of multiple low-diffracting samples from other batches (different ligands and metals sources), which might therefore be a background signal inherent to the machine.[50]

The exposure of the sample to iodine promoted a substantial decrease in crystallinity. This indicates that the crystalline nature of the material was significantly compromised because of the interaction with iodine (Figure 3- 19 a) b) and e)).

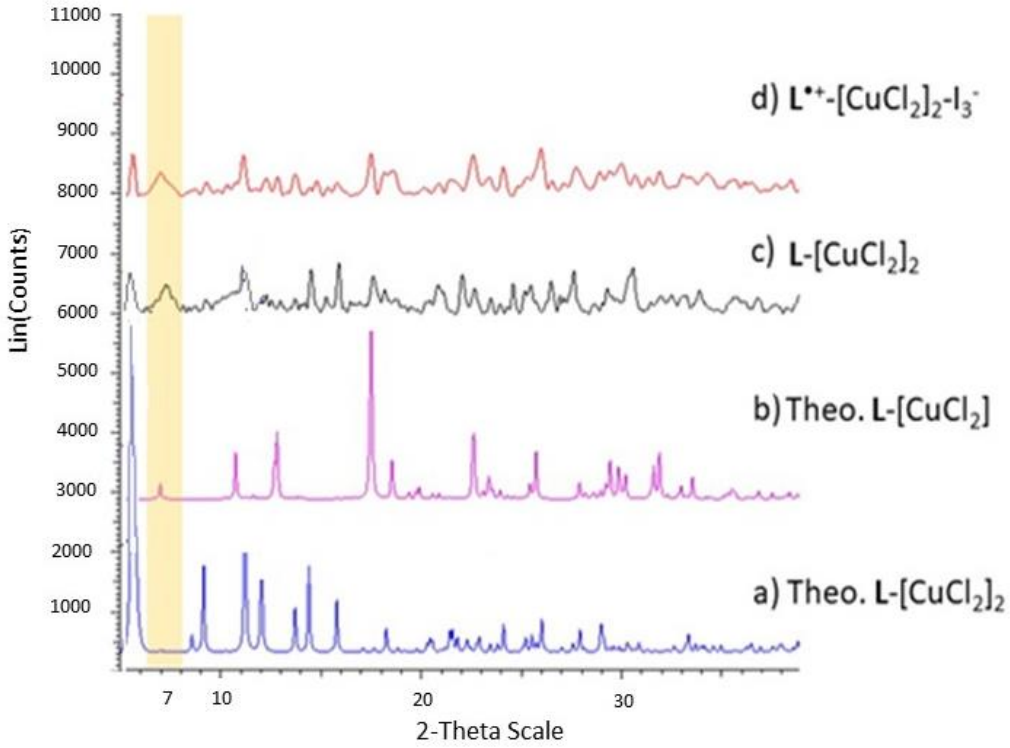


Figure 3- 19. a) theoretical pattern of **L**-$[CuCl_2]_2$ b) pattern of **L**-$[CuCl_2]_2$ c) theoretical pattern of **L**-$[CuCl_2]$ and d) pattern of **L**-$CuCl_2$ d) PXRD pattern of **L**$^{\bullet+}$-$[CuCl_2]_2$-I_3^-.

4.4 Thermogravimetric analysis (TGA)

Thermogravimetric Analysis (TGA) was conducted to determine the thermal stability of **L**-$[CuCl_2]_2$ (Figure 3- 20). During the analysis, several mass losses were observed, which were attributed to the removal of

[50] Chang, Z.; Zhu, M.; Sun, Y.; He, F.; Li, Y.; Ye, C.; Jin, Y.; Li, Z.; Xu, W. *Adv. Funct. Materials* **2023**, *33* (32), 2301513.

solvent molecules incorporated within the pores followed by decomposition. The initial weight loss occurred up to 50°C and amounted to 8.2% of the total mass, corresponding to the removal of approximately two molecules of methanol per MOF. Subsequently, at 250°C, there was a further weight loss corresponding to the removal of two molecules of DMSO. Finally, a gradual decomposition process continued until 1000°C, suggesting the breakdown of the structure and its organic components.

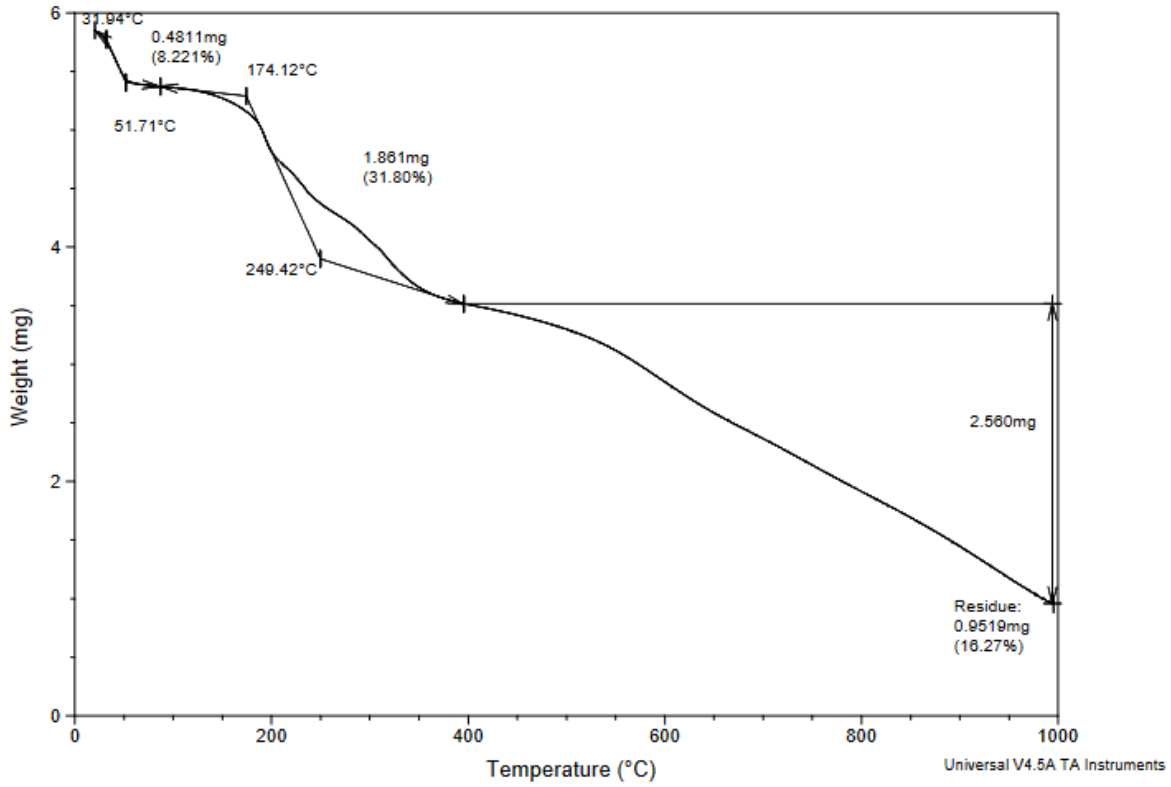


Figure 3- 20. Thermogravimetric analysis (TGA) data for **L**-$[CuCl_2]_2$.

4.5 Solid state voltammetry

The solid-state voltammetry of **L**-$[CuCl_2]_2$ was performed using the configuration described on Chapter 3 section 3.2. The CV curve of **L**-$[CuCl_2]_2$ displays one quasi-reversible redox process corresponding to the formation of the BVDT-TTF radical cation at 0.652 V (Figure 3- 21). This result is noteworthy, especially considering the inherent challenges of solid-state electrochemistry, where diffusion dynamics are constrained. The effective observation of this quasi-reversible redox process further highlights the experimental setup's ability to accommodate the specific conditions of the solid-state environment. The redox activity in MOFs is significantly influenced by the presence of pores within their structures. The four isostructural MOFs with smaller pore sizes tend to exhibit lower redox activity, as these smaller pores restrict the diffusion of ions and limit the extent of redox reactions. On the other hand, **L**-$[CuCl_2]_2$ with its larger pores demonstrates an enhanced redox activity due to the efficient diffusion and movement of electrolyte species facilitated by these spacious pathways. The presence of larger pores allows for the entry

and transport of electrolyte species, enabling the efficient transfer of charge carriers and promoting a rapid ionic transport.

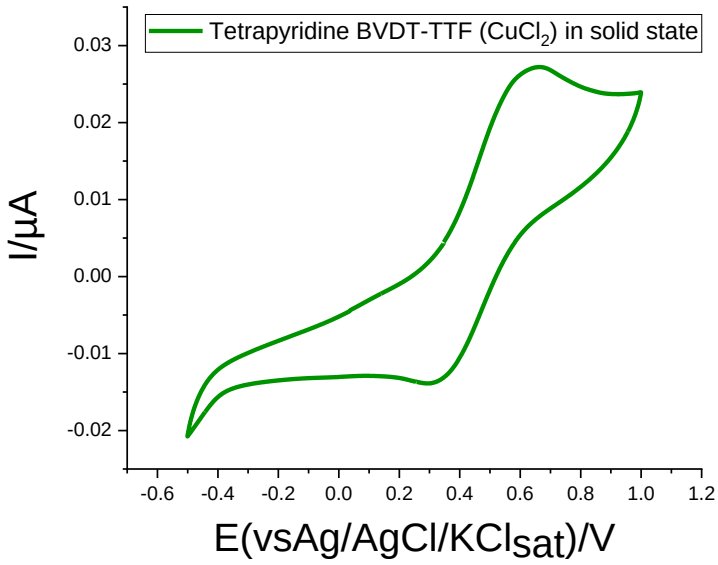


Figure 3- 21. CV curve of **L**-$[CuCl_2]_2$ crystalline powder with Nafion. WE/GCP, RE: Ag wire. CE: Pt wire. CV profile was obtained at 20 mV s^{-1} scan rate.

	E_{Ox} **(V)**	E_{Red} **(V)**
L in solution	0.665	0.575
L-$[CuCl_2]_2$	0.652	0.331

Table 3- 10. E_{Ox} and E_{Red} of BVDT-TTF-Py_4 and **L**-$[CuCl_2]_2$ at 20 mV·s^{-1}.

4.6 Raman measurements

The loss of crystallinity hindered SCXRD analysis after oxidation, preventing the direct observation of the presence of iodine within the pores. Raman experiments proved particularly valuable for the monitoring of the charge-sensitive ν_C mode, considering the theoretical studies already described in section 3.7. This approach enabled a more precise determination of the oxidation state of BVDT-TTF. Figure 3- 22 displays the Raman spectra of the neutral **L**-$[CuCl_2]_2$, followed by an analysis after exposure to iodine. In the first spectrum, the expected ν_C mode relative to the neutral state is observed at 1501 cm^{-1}. However, intriguingly, we also detected the presence of the ν_C mode associated with the cation. This observation suggests the existence of minute quantities of BVDT-TTF$(Py)_4^{\cdot+}$ radicals within these materials. After exposure to iodine, the Raman experimental analysis reveals a notable change in the ν_C^+ mode, with a clear increase in intensity. This suggests the presence of radical cations formed by the interaction of iodine with the material. Interestingly, when examining **L**-MCl_2 MOFs described in the paragraph 3 of this chapter

(Figure 3- 15), a different behaviour is observed. In the case of the isostructural MOFs, the ν_C^0 mode completely disappears, indicating the complete oxidation of the ligand. In the present scenario, both the ν_C^+ and ν_C^0 modes coexist in the Raman spectra. This observation suggests that the oxidation process is only partial, resulting in a mixed valence state.

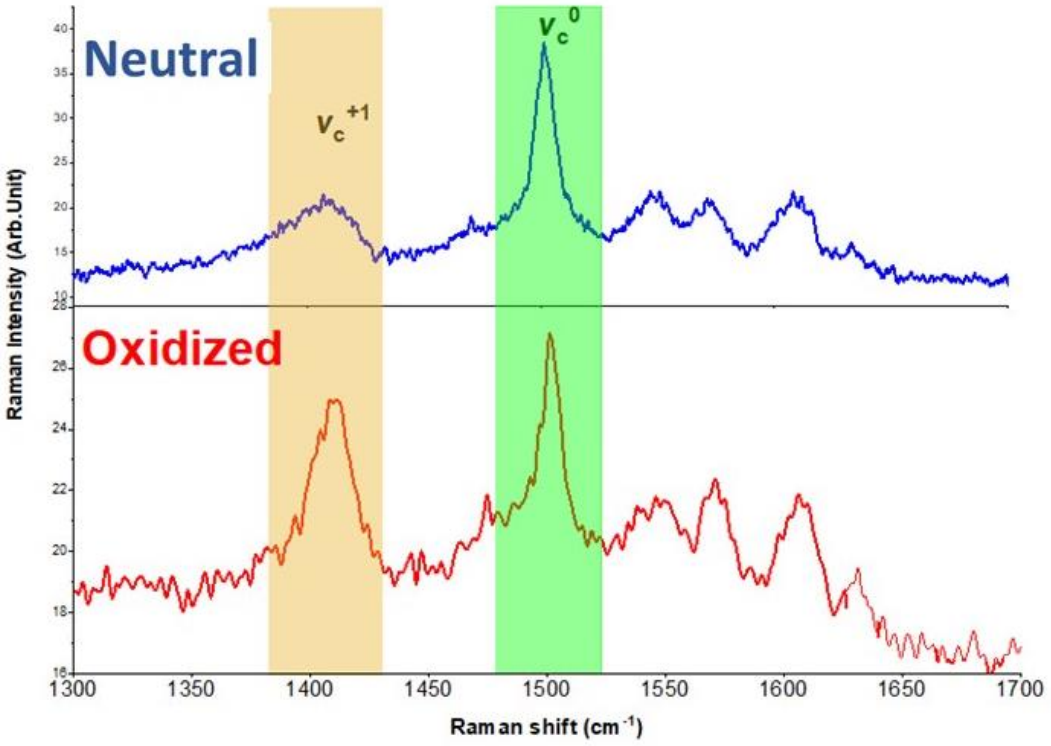


Figure 3- 22. Raman spectra of selected neutral **L**-$[CuCl_2]_2$and of oxidized **L**-$[CuCl_2]_2$. The charge-sensitive ν_C mode is labelled as ν_C^{+1} for the cation and ν_C^0 for the neutral. Both are measured at room temperature with the 785 nm excitation line at room temperature.

In **L**-$[CuCl_2]_2$, we observed similar Raman spectra in the frequency range of stretching polyiodide modes in the isostructural **L-**MCl_2 MOFs, as depicted in Figure 3- 23 and in Table 3- 11.
The presence of these modes indicates the coexistence of centrosymmetric triiodide, asymmetric triiodide, and pentaiodide species within the MOF structure.

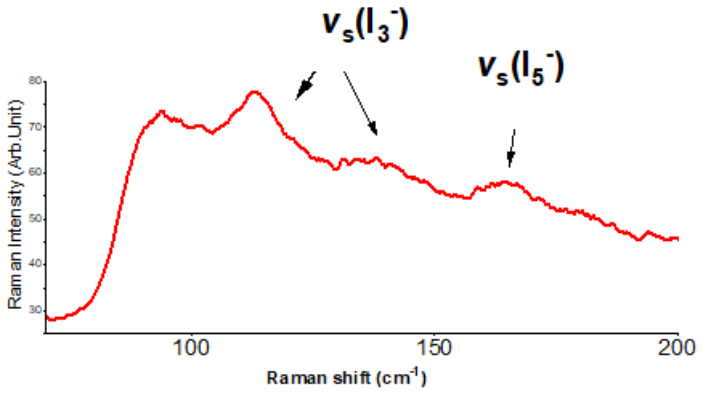


Figure 3- 23. Raman spectra of $\mathbf{L}^{\bullet+}$-$[CuCl_2]_2$-I_3^- measured at room temperature with the 632.8 nm excitation line, in the frequency range of the stretching polyiodide modes.

	$\mathbf{L}^{\bullet+}$-$[CuCl_2]_2$-I_3^-
$\nu_s(I_3^-)$	~113
$\nu_a(I_3^-)$	~140
$\nu_s(I_3^-)$	~166

Table 3- 11. Experimental polyiodide frequencies in cm^{-1} observed in Raman spectra of $\mathbf{L}^{\bullet+}$-$[CuCl_2]_2$ I_3^-.

4.7 Conductivity measurements

Conductivity measurements were conducted in collaboration with Dr. Pascale Auban-Senzier at Université Paris-Saclay.

Conductivity measurements were performed with a two-contact method on compressed pellet where electrical contacts are applied to the surface of the pellet. Compressed pellets are convenient and practical for conductivity measurements, but they do have limitations. The random orientation of crystallites within the pellet obscures any anisotropic charge transport properties. As a result, the measured conductivity represents the least conductive direction of the material, influenced by grain boundaries. These factors contribute to underestimated values for the intrinsic conductivity, which refers to the conductivity of a defect-free single crystal.[49]

The conductivity of **L**-$[CuCl_2]_2$ before insertion was measured to be 1.48x10^{-8} S·cm^{-1}. After exposing the material to an iodine solution for two days, the conductivity slightly increased to 9.66x10^{-8} S·cm^{-1}. It is important to note that the conductivity decreased again when the pellet stood for a few days without exposure to iodine, indicating that the reaction is reversible. Within one day, the storage solution becomes coloured with a violet hue likely due to iodine release.

4.8 Ligand exchange in BVDT-TTF-Py_4-$[CuCl_2]_2$

Ligand exchange is a dynamic process that occurs when a new ligand replaces an existing ligand in the coordination sphere of a metal centre. When crystals of **L**-$[CuCl_2]_2$ were kept in a solution of chloroform and methanol for four weeks, a ligand exchange reaction occurred over time. The crystal analysis performed at the synchrotron SOLEIL revealed that a methanol molecule displaced one of the bridging chloride ligands to give a new coordination polymer **L**-$(CuCl_2)_2(CH_3OH)_2$.

As a result, the arrangement of the network **L**-$(CuCl_2)_2(CH_3OH)_2$ underwent small changes, impacting the quality of the crystal data (R_{int} = 16.79% at 0.8 Å resolution) that are described in Table 3- 12. The space group is maintained as *I*2/a, and the cell parameters closely resemble those of the parent **L**-$[CuCl_2]_2$ compound.

Crystal system	monoclinic
Space group	*I*2/a
V/Å^3	5858.44
a/Å	8.6098(3)
b/Å	17.5168(6)
c/Å	38.8522(11)
α/°	90
β/°	91.111(3)
γ/°	90
R_{int}	16.79%
Completeness (%)	98.6

Table 3- 12. Crystallographic data of **L**-$(CuCl_2)_2(CH_3OH)_2$.

The asymmetric unit comprises half of a ligand and one metal. The metal is coordinated by two pyridines, two chlorides, and one methanol molecule, resulting in a five-coordinated environment. This arrangement adopts a square pyramidal geometry (Figure 3- 24a), which contrasts with the previous configuration that exhibited a distorted trigonal bipyramid geometry. The two pyridines and the two chlorines stand in a *trans* configuration and form the square basis of the pyramid. The equatorial M···N distances are 2.009(5) Å and 2.005(5) Å while the equatorial M···Cl distances are 2.275(4) Å and 2.212(4) Å. The $(Cl{\cdots}M{\cdots}N)_{equ.}$ bond angles are 92.7(2)°, 90.5(2)°, 86.4(2)° and 89.3(2)°. The axial M···OCH_3 distance is 2.315(7) Å. The central C=C bond is 1.339(8) Å, suggesting a neutral charge for the BVDT-TTF moiety. The ligands are organized

through coordination bonds in 2-D layers where metals are separated by distances in the 4.7–6.1 Å range. Notably, the layers are no longer interconnected by Cl bridges. The distances between sulphur atoms in interligand bonds are slightly longer compare to **L**-$[CuCl_2]_2$, falling within the range of 3.65-3.86 Å (Figure 3- 24c). Despite these geometric differences, both networks exhibit a superimposable structure, giving rise to 1-D channels. The solvent molecules occupy approximately 38% of the total crystal volume, with pore dimensions measuring 10×11 Å (Figure 3- 24b). In the case of **L**-$(CuCl_2)_2(CH_3OH)_2$, each unit cell accommodates 8 CH_3OH molecules, constituting approximately 5% of the crystal's total volume reducing the occupancy of larger solvent molecules such as DMSO. Notably, the coordinated methanol molecule introduces also steric hindrance effects. These factors lead to a reduction in solvent occupancy and pore dimensions.

It is worth noting that the calculated PXRD pattern of **L**-$(CuCl_2)_2(CH_3OH)_2$ does not correspond to the impurity observed in the experimental PXRD of **L**-$(CuCl_2)_2$ (refer to paragraph 4.1).

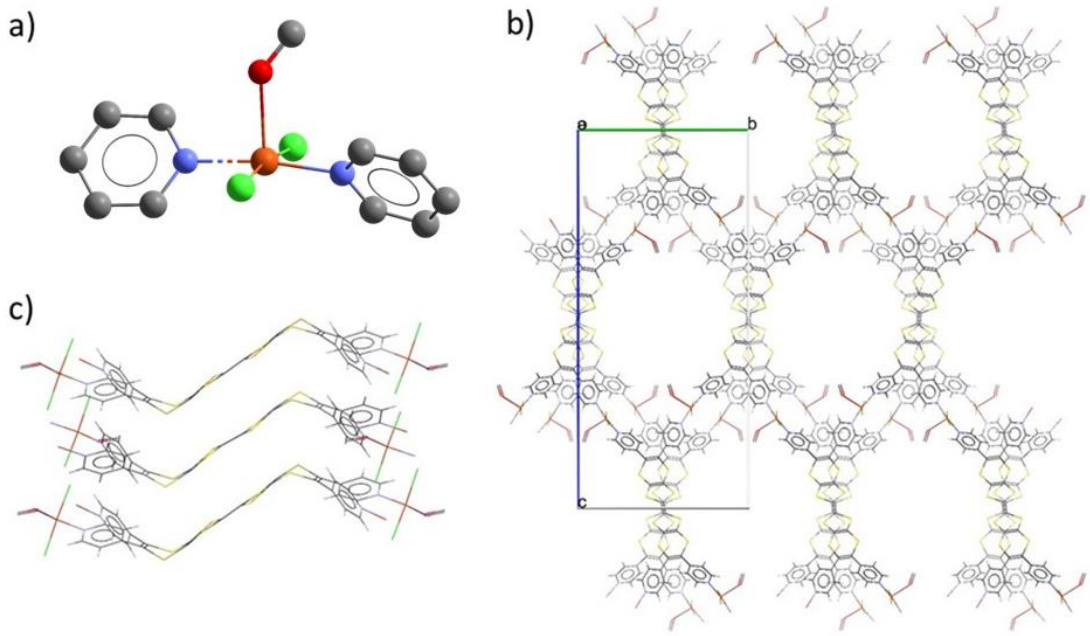


Figure 3- 24. Single crystal X-ray structure for **L**-$(CuCl_2)_2(CH_3OH)_2$. a) Secondary building unit b) packing c) side view of the BVDT-TTF-Py_4 stacking sequences (C: grey; N: blue; Cl: green; Cu: orange; O: red).

This single-crystal to single-crystal structural change underscores the inherent instability of the cluster in the air and in polar or coordinating solvents. These findings emphasize the challenges in maintaining the MOF's structural integrity and suggest that it may be prone to alterations depending on the environmental conditions.

5 TTF(isophthalic acid)$_4$ as ligand for electroactive MOF

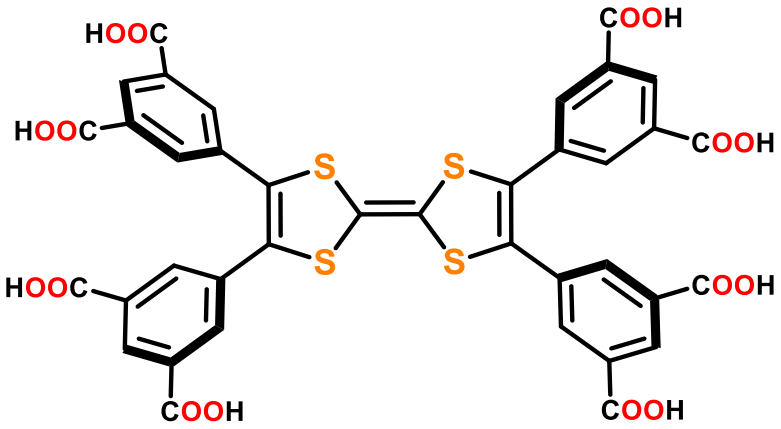


Figure 3- 25. H_8TTFOC structure.

TTF (isophthalic acid)$_4$ (H_8TTFOC) (Figure 3- 25) was also investigated as an organic linker. Chen *et al.* [51] employed H_8TTFOC as a hole-transporting material (HTM) in photovoltaic devices to facilitate the efficient transport of positively charged "holes" from the light-absorbing layer to the electrode. Their approach resulted in a remarkable power conversion efficiency of 16.7%. Isophthalic acid is an organic linker known for its ability to form robust and stable MOF structures.[52,53] MOFs featuring this ligand have been reported in the literature, highlighting their exceptional potential as highly efficient proton-conductive materials. To the best of our knowledge, the only MOF based on H_8TTFOC has been reported by Su *et al*.[54] The $[(CH_3)_2NH_2][In(TTFOC)]$ MOF has a solvent-accessible volume of 64.1%. They emphasized the high proton conductivity obtained, up to 1.30 x 10^{-2} S·cm^{-1} thanks to its non-coordinated carboxylic acid groups, which serve as sources of protons and creates H^+-conductive paths. This characteristic renders them of significant interest for electrolytes in sensors, batteries, or fuel cells. However, the S-S distances over 8 Å prevent the formation of an effective electrical conductive pathway. This is probably caused by the steric hindrance of H_8TTFOC.

Yang *et al.*[55] recently used a ligand where phthalic acid replaced isophthalic acid moieties: o-H_8TTFOB. Three isostructural MOFs $[M_4(o\text{-}TTFOB)(bpm)_2(H_2O)_2]_n$ were synthetized, where M= Mn, Zn, and Cd, and bpm= 2,2'-bipyrimidine. TTF-based ligands with four carboxylate groups typically coordinate with two,

[51] Chen, Q.; Li, X.; Jiu, T.; Ma, S.; Li, J.; Xiao, X.; Zhang, W. *Dyes Pigm.* **2017**, *147*, 113–119.

[52] Pan, Y.; Liu, W.; Liu, D.; Ding, Q.; Liu, J.; Xu, H.; Trivedi, M.; Kumar, A. *Inorg. Chem. Commun.* **2019**, *100*, 92–96.

[53] Li, G.; Wang, T.; Zhou, S.; Wang, J.; Lv, H.; Han, M.; Singh, D. P.; Kumar, A.; Jin, J. *Inorg. Chem. Commun.* **2021**, *130*, 108756.

[54] Su, J.; He, W.; Li, X.-M.; Sun, L.; Wang, H.-Y.; Lan, Y.-Q.; Ding, M.; Zuo, J.-L. *Matter* **2020**, *2* (3), 711–722.

[55] Yang, Z.M.; Zhao, S.P.; Zhang, M.H.; Zhang, Z.D.; Ma, T.R.; Yuan, S.; Su, J.; Li, C.H.; Zuo J. L. *Angew. Chem. Int. Ed*. **2023**, *62*,e202304183.

four, or eight metal atoms. The o-TTFOB$_8$ ligand is coordinated with ten metal centers. The MOFs show a notable Li^+ mobility and impressive capacities when used as anodes in lithium-ion batteries (LIBs). Specifically, Mn-o-TTFOB demonstrates reversible capacities range from 1325 mAh·g^{-1} to 836 mAh·g^{-1}. The I-V curve demonstrates a conductivity value of 5.69·10^{-8} S·m^{-1} for Mn-o-TTFOB, accompanied by S-S distances of 5.04 Å.

5.1 Synthesis and properties of H$_8$TTFOC

H$_8$TTFOC was synthesized using the well-established procedure of transition-metal-catalyzed direct C–H arylation between TTF and dimethyl 5-bromoisophthalate with a 50% yield. This step was followed by a saponification reaction mediated by KOH, resulting in the formation of a dark-red solid product (Figure 3- 26Figure 3- 27), with 89% yield.

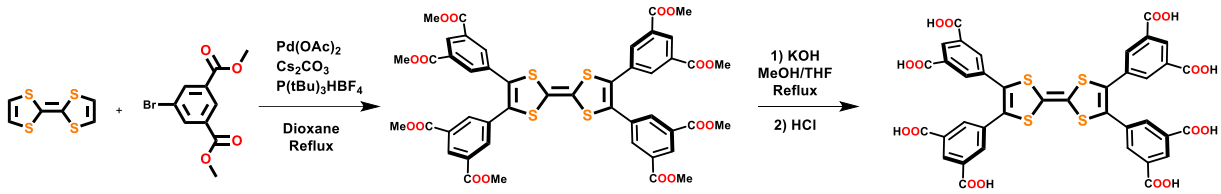


Figure 3- 26. Synthesis of H$_8$TTFOC.

The cyclic voltammogram of H$_8$TTFOC was measured at different scan rates (Figure 3- 27) and oxidation (E_{Ox}) and reduction (E_{Red}) potentials and $E_{1/2}$ are reported in the Table 3- 13. Different scan rates are employed to assess the oxido-reductive reversibility of the ligand. The value of the first oxidation potential, related to the formation of the radical cation is higher compared to the TTF ($E_{1/2}$ 0.34 V vs. SCE). While the first oxido-reduction process demonstrates a reversible behaviour, the second oxidation exhibits a quasi-reversible nature characterized by less symmetrical redox peaks and a less pronounced reduction wave. This quasi-reversible behaviour becomes more evident as the scan rate increases, highlighting the interplay of kinetics in the electrochemical response.

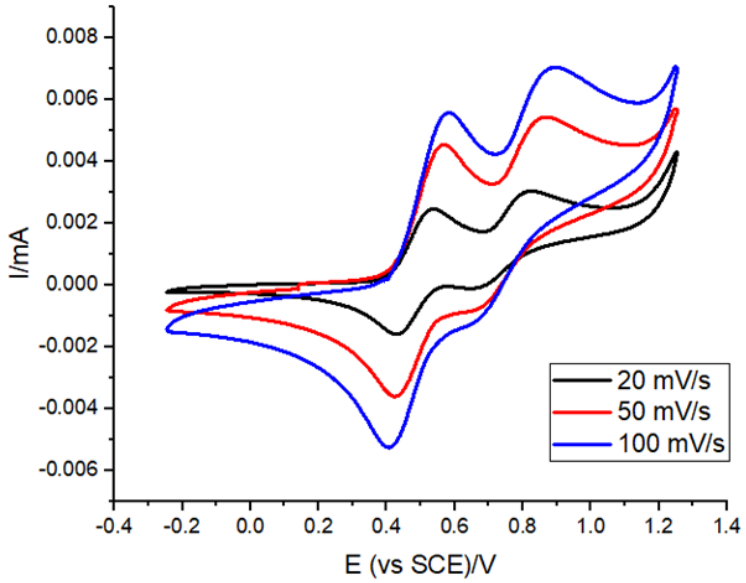


Figure 3- 27. Cyclic voltammetry of H_8TTFOC solution (10^{-3} M, $TBAPF_6$ 0.1 M in THF). Platinum electrode as WE, platinum wire as CE and an Ag/AgCl/Saturated KCl electrode as RE at scan rate 20/50/100 $mV \cdot cm^{-1}$. Values were converted with respect to the standard calomel electrode (SCE).

Scan rate [$mV.s^{-1}$]	E^1_{Ox}	E^1_{Red}	$E^1_{1/2}$	E^2_{Ox}	E^2_{Red}
20	0.538	0.440	0.489	0.82	0.67
50	0.569	0.428	0.489	0.87	0.67
100	0.581	0.405	0.493	0.89	0.67

Table 3- 13. Potential oxidation, E_{Ox} and reduction, E_{Red} potentials and $E_{1/2}$ of H_8TTFOC vs SCE at different scan rates.

Solvothermal synthesis was employed to create MOFs using this specific ligand. During the synthetic process, various parameters were systematically altered to study their impact on the MOFs' properties and characteristics such as temperature, solvents and additives (Table 3- 14).

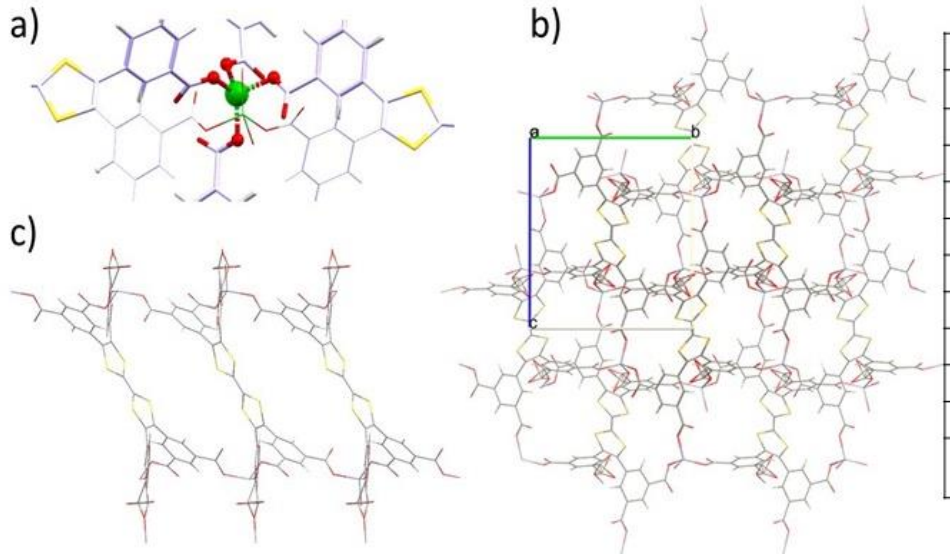
Metals	Temperature (°C)	Additives	Solvents
M(II) (M = Zn/Cu/Ni/Mn/Co)	120	HCl	DMF/H_2O
M(III) (M = Al/Eu/Tb/Er)[56]	90	NaOH	DMF/H_2O/EtOH
Zr(IV)[57]	160	Formic acid	DMAc/H_2O
	140	4,4'-bipyridine	DMAc/H_2O/EtOH

Table 3- 14. Metals and conditions used for solvothermal synthesis.

5.2 Synthesis and structure of Zn_2-TTFOC

Combining H_8TTFOC and $Zn(NO_3)_2 \cdot 6H_2O$ in DMF, EtOH, and H_2O and one drop of NaOH 12 M at 120° led to the formation of crystalline powder after 2 days. The red crystals have a six-sided, flat, plate-like shape. The structure was determined using SCXRD (Figure 3- 28). The asymmetric unit comprises half of a ligand and one metal. The structure stands in the $P2_1/c$ space group with the crystal data described on the table in Figure 3- 28. As observed in Figure 3- 28 a) the metal atoms stand in a tetrahedral environment, with four oxygen atom from four different TTF units arranged around the central zinc ion. In order to maintain a neutral charge of the network, two out of these four carboxylic acid units should be protonated. The three-dimensional resulting structure includes solvent-filled voids, constituting approximately 60% of the total volume of the crystal according to the PLATON suite. These pores have a 5 x 3 Å diameter. TTF(isophthalic acid)$_4$ align along the *b* axis with minimal S···S distances of approximately 8.7 and 9.3 Å (Figure 3- 28 c). The crystals of the MOF were not stable upon solvent removal. They quickly lost their crystallinity, leading to significant challenges in obtaining high-quality SCXRD data. The dataset quality fails indeed to reach the highest standards, and it is not possible to determine accurate distances or angles within the crystal lattice with values a maximal resolution at 1.5 Å (signal-to-noise ratio (I/σ) > 3).

[56] Castells-Gil, J.; Mañas-Valero, S.; Vitórica-Yrezábal, I. J.; Ananias, D.; Rocha, J.; Santiago, R.; Bromley, S. T.; Baldoví, J. J.; Coronado, E.; Souto, M. *Chem. Eur. J.* **2019**, *25*, 12636–12643.
[57] Su, J.; Yuan, S.; Wang, T.; Lollar, C. T.; Zuo, J.-L.; Zhang, J.; Zhou, H.-C. *Chem. Sci.* **2020**, *11* (7), 1918–1925.



	Zn_2-TTFOC
Crystal system	monoclinic
Space group	$P2_1/c$
V/Å^3	3688.88
a/Å	17.823(5)
b/Å	13.825(3)
c/Å	15.847(4)
α/°	90
β/°	109.13(3)
γ/°	90
R_{int}	11.13%
Completeness (%)	99

Figure 3- 28. Single crystal X-ray structure for Zn_2-TTFOC. a) Secondary building unit b) packing along a-axis c) side view of the Zn_2-TTFOC along b-axis (C: grey; S: yellow; O: red; Zn: green).

Because of the significant instability of the MOFs, characterization by other techniques such as PXRD, Raman spectroscopy, and solid-state electrochemistry were not possible.

Furthermore, the absence of π···π stacking interactions in the MOF suggests that conductivity may be relatively low. Souto *et al.*[58,59] synthesized MUV-2 using the TTFTB ligand and $[Fe_3O(CH_3COO)_6]ClO_4$ clusters, creating breathing MOFs that undergo structural changes in response to external stimuli. The structure reveals significant hexagonal mesoporous 1-D channels of about 3 nm, with no close contact between TTF units (9.503 Å). The MOF exhibits an anticipated high resistance, with a conductivity value of $\sigma = 3.7 \cdot 10^{-11}$ S·cm^{-1}, potentially akin to a hypothetical value for Zn_2-TTFOC.

[58] Souto, M.; Santiago-Portillo, A.; Palomino, M.; Vitórica-Yrezábal, I. J.; Vieira, B. J. C.; Waerenborgh, J. C.; Valencia, S.; Navalón, S.; Rey, F.; García, H.; Mínguez Espallargas, G. *Chem. Sci.* **2018**, *9* (9), 2413–2418.
[59] Souto, M.; Calbo, J.; Mañas-Valero, S.; Walsh, A.; Mínguez Espallargas, G. *Beilstein J. Nanotechnol.* **2019**, *10*, 1883–1893.

5.3 Synthesis and structure of Ni_3-TTFOC

By combing H_8TTFOC and $Ni(NO_3)_2 \cdot 6H_2O$ in a solution of DMF, EtOH, and H_2O, and adding two drops of NaOH 12 M at 120°C, tabular red crystals were obtained and analysed through SCXRD.

We encountered challenges with the chemical stability of the resulting network. As consequence, the quality of the dataset does not meet the highest standards. Some coordinated ligands such as water molecules were not properly refined and precise measurements of distances or angles are not possible. The maximal resolution of the data is limited to 1.6 Å, where the I/σ is > 3.

The crystals stand in a triclinic space group *P*-1 and crystal data are described in Table 3- 15.

Crystal system	triclinic
Space group	*P*-1
V/Å^3	7442.59
a/Å	18.7428(17)
b/Å	19.9818(17)
c/Å	20.6304(16)
α/°	76.768(7)
β/°	81.721(7)
γ/°	88.602(7)
R_{int} (%)	19.25
Completeness (%)	98.4

Table 3- 15. Crystal data of Ni_3-TTFOC.

The structure is presented in Figure 3- 29. In the network, two distinct SBUs are observed (Figure 3- 29a). In the first SBU, the metal is coordinated by six oxygen atoms, adopting an octahedral geometry. This coordination involves four oxygen atoms originating from separate TTF ligands in equatorial positions, while both apical positions are occupied by water molecules. The octahedral Ni center is surrounded by four non-coordinated oxygen atoms, and two hydrogen atoms are positioned on two of these oxygen atoms. This arrangement is proposed to maintain the charge balance of the system, based on the assumption that the network should ideally possess a neutral charge. The second SBU is a cluster containing four Nickel ions. This arrangement presents a distorted structure, where each of the Nickel ions adopts a tetrahedral geometry. These tetrahedral arrangements are connected by oxygen atoms derived from four different ligands. The interplay between the ligands and metals extends into a 3-D network. Pores along the *b* and

c axes, measuring approximately 8 x 6 Å, emerge as a result of a repetitive sequence between the first SBU and the second (Figure 3- 29b and c).

The isophthalic groups in the ligand are pointing towards divergent directions, instead of lying in the same plane, facilitating the S···S contact (3.9-3.8 Å) between the two columns of TTF units as observed in Figure 3- 29d. This network has theoretical solvent accessible voids accounting for 58% of the total crystal volume according to PLATON calculations.

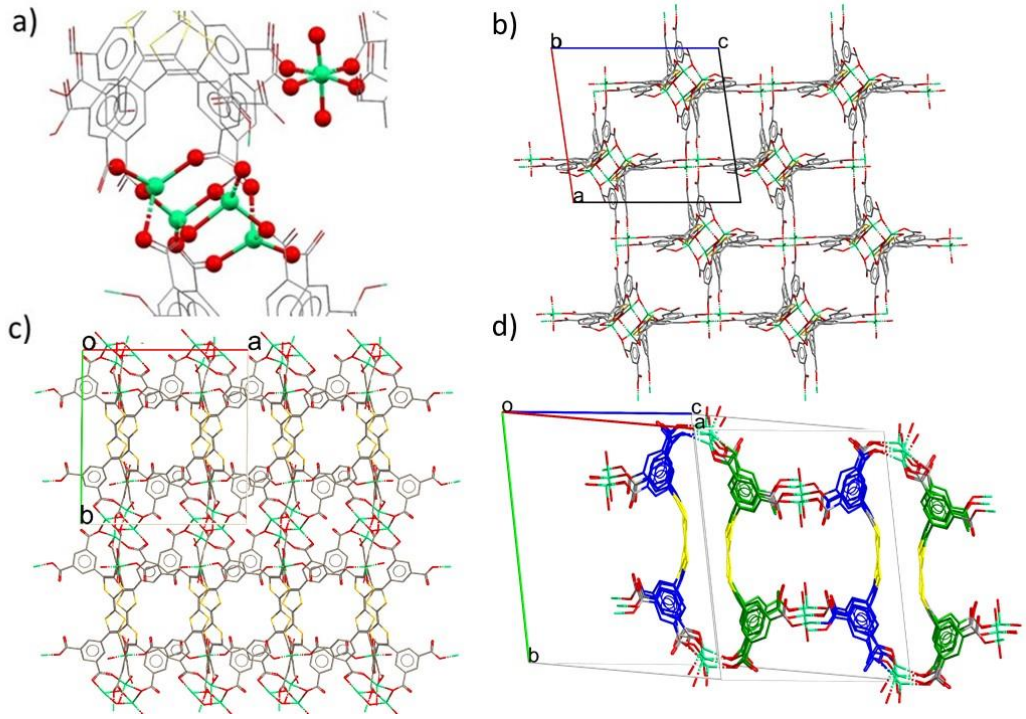


Figure 3- 29. Single crystal X-ray structure for Ni_3-TTFOC. a) Secondary building unit b) packing along b-axis c) packing along c-axis (C: grey; S: yellow; O: red; Ni: green) d) side view of the Ni_3-TTFOC stacking sequences.

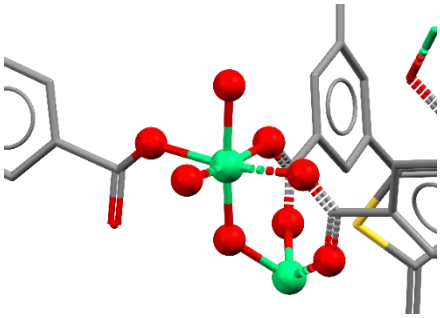


Figure 3- 30. Alternative SBU.

Another nickel atom with a low occupancy (30%) is located in the first SBU (Figure 3- 30). It is coordinated by two oxygen atoms originating from the two TTF ligands positioned in the equatorial site of the first SBU. The Nickel stands in a tetrahedral geometry. Because of the limitations in the crystal quality and the low occupancy of the second Ni centre, the direct observation of the last coordinated molecules is not possible.

5.4 Synthesis and structure of Cu_3-TTFOC

By mixing H_8TTFOC and $Cu(NO_3)_2 \cdot H_2O$ in a solution of DMF, EtOH, and H_2O, and adding one drop of NaOH 12 M at 120°C for two nights, crystals suitable for X-Ray were obtained. The structure was determined through SCXRD, as shown in Figure 3- 31. The crystals stand the space group *F*mmm, and the crystal data are described in Table 3- 16.

Crystal system	Orthorhombic
Space group	*F*mmm
V/Å^3	13307.4
a/Å	14.3486(15)
b/Å	25.669(3)
c/Å	36.130(3)
α/°	90
β/°	90
γ/°	90
R_{int}(%)	17.59
Completeness (%)	99.6

Table 3- 16. Crystal data of Cu_3-TTFOC.

The structure network is presented in Figure 3- 31. The asymmetric unit contains one fourth of the ligand and three metal centres with occupancy of 25% each. A non-coordinated water molecule is observed in the structure. In the crystal structure, the Cu centres act as SBUs, with two distinct geometries (Figure 3- 31 a). In one configuration, the copper centre exhibits a paddlewheel motif, with two copper atoms arranged in a binuclear unit. Each copper atom is coordinated by five oxygen atoms. Along the axial position, a H_2O molecule is coordinated. The remaining four oxygen atoms originate from four distinct TTF, and serve as equatorial bridging ligands. In the second arrangement, the copper centre adopts a square planar geometry. It is coordinated by four oxygen atoms of four different carboxylates coming from two different ligands (Figure 3- 31). Two out of the four carboxylates surrounding the square planar Cu center should be protonated is we assume a charge balance of the network. Ligand and metal are structured into 3D layers (Figure 3- 31 b). Solvent-occupied voids constitute around 51% of the crystal's overall volume. The pores contain unattributed electronic density arising from disordered solvent molecules, and have a maximal size of 6 x 6 Å. Sequence of TTF (isophthalic acid)$_4$ along the *b*-axis are observed where the sulphur atoms exhibit longer distances, measuring 7 Å and 7.2 Å (Figure 3- 31c).

The crystals deteriorated upon solvent removal, posing significant challenges in obtaining high-quality SCXRD data (R_{int} = 13.10% at a 1.46 Å resolution where I/σ > 3). Precise measurements of distances and angles within the crystal lattice were therefore unattainable. The rapid loss of structural integrity observed in the MOF crystals prevented us from determining its conductivity.

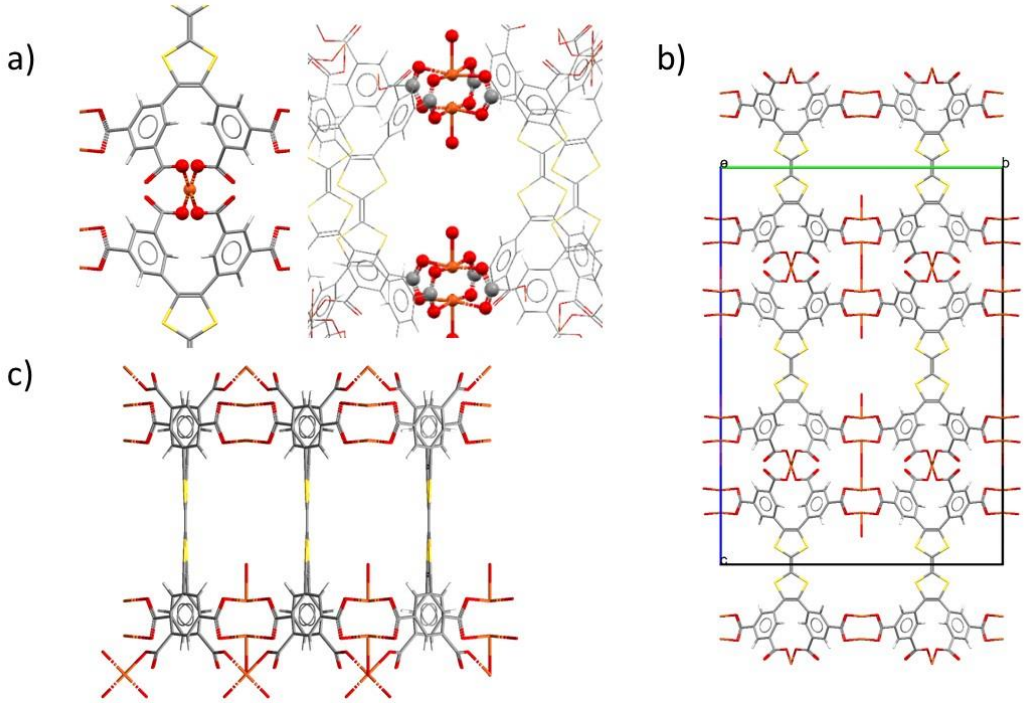


Figure 3- 31. Single crystal X-ray structure for Cu_3-TTFOC. a) Secondary building unit b) packing c) side view of the Cu_3-TTFOC (C: grey; S: yellow; O: red; Cu: orange).

In addition, a large-scale synthesis was employed under identical conditions to synthesize the MOF, resulting in the formation of a crystalline powder. The synthesized MOF was subjected to PXRD (Figure 3-32). Comparing the theoretical and experimental PXRD patterns, a proper degree of agreement was observed. However, some PXRD peaks were missing in the experimental data, especially at the lower 2θ angles, suggesting a loss of long-range crystallinity and structural integrity.

The crystalline powder was exposed to iodine vapour for 3 hours. After this treatment, the powder was subjected to PXRD analysis to assess any structural changes, but no diffraction peaks were observed. A similar outcome was observed when Cu_3-TTFOC was subjected to solvent drying. This suggests that the exposure to iodine vapour or the desolvation promoted the complete collapse of the framework.

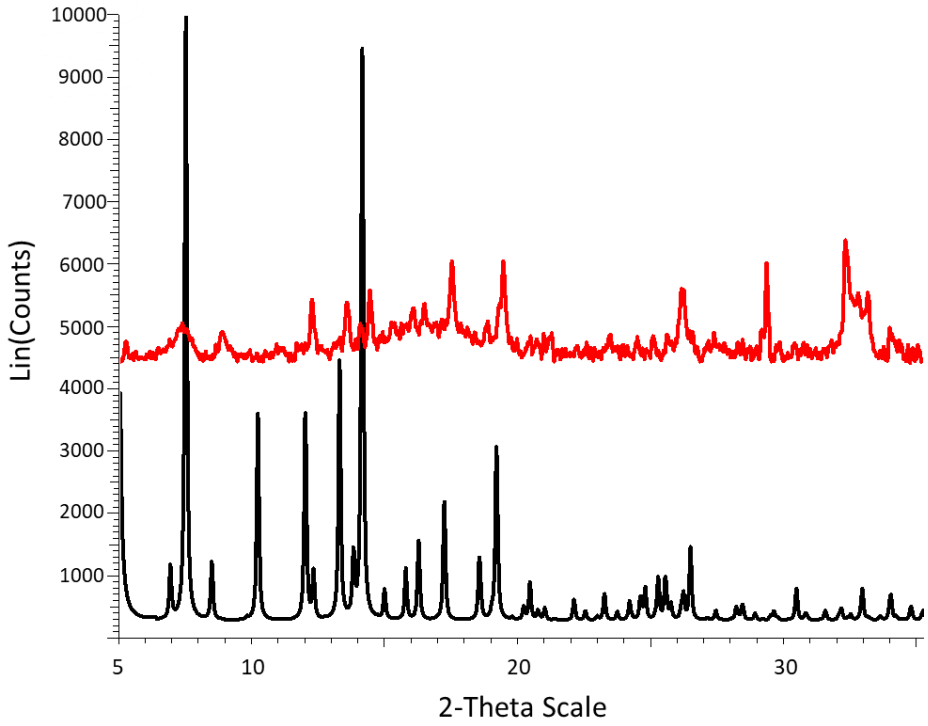


Figure 3- 32. Theoretical PXRD pattern of Cu_3-TTFOC (black) and experimental PXRD pattern (red).

2. Conclusion

In conclusion, our research aimed to investigate the correlation between the architectures of electroactive MOFs and their electronic properties, focusing on the impact of π-stacking interactions on charge carrier mobility.

In particular, BVDT-TTF-Py_4 was considered as a promising ligand and successfully formed two networks with distinct architectures and properties. We demonstrated the significance of utilizing TTF-based ligands containing additional sulphur atoms. This approach facilitated the design of conductive networks by forming 2D conductive pathways in the case of the isostructural MOFs (paragraph 3). The presence of a 2D conducting path in **L**-MCl_2 is expected to enhance its stability and make it more immune to defects. The multiple pathways for charge carriers to move through the material reduce the likelihood of encountering obstacles that could hinder the charge transport.

In the case of **L**-$[CuCl_2]_2$, the structure suggests the presence of a 1D pathway for charge carriers. The structure of **L**-$[CuCl_2]_2$ exhibits a larger pore size compared to the isostructural MOFs that contributes to a better redox activity in the solid state. Additionally, it has short interligand "i-i" S···S distances, which are similar to the values found in Zn_2(TTFTB). Raman measurements indicate that the as-synthesized **L**-$[CuCl_2]_2$ exhibits a mixed valence state, which is significantly enhanced upon oxidation without reaching a complete oxidation of the material. In comparison, the **L**-$[MCl_2]$ networks are completely oxidized after

undergoing post-synthetic oxidation. The chemical stability of the **L**-$[CuCl_2]_2$ is also reduced compared to **L**-MCl_2.

H_8TTFOC is a ligand that has an easy and high-yield synthesis. This ligand is scarcely explored in the field of MOFs. The steric effects play a crucial role in determining the spatial arrangement of ligands within the MOF. In that regard, we anticipate that the S···S distances between the TTF units could be relatively large. Furthermore, the existence of multiple coordination groups in the ligand introduces a larger degree of freedom for interactions between the metal ions and the ligands.

Three networks using TTF (isophthalic acid)$_4$ as a ligand have been obtained with Zn, Cu and Ni, but none of them exhibited the desired level of stability required for a detailed characterization. This is in contrast with our previous work based on BVDT-TTF-Py_4 MOFs. Factors such as the type of SBU, the choice of the metal ion and the presence of additional interactions like π-stacking or hydrogen bonding, play crucial roles in the stability of the MOF. Efforts to construct networks using ions with higher charges such as lanthanides, Zirconium or Aluminum did not yield successful results so far.[60]

Our research highlights the potential of implementing various electroactive structures found in organic conductors within MOF frameworks. This direction constitutes the focus of our ongoing research, seeking to integrate a wide range of electroactive structures to enhance the conductivity and electronic properties of MOFs. For example, TTF-TTP,[61] composed of two TTF units condensed and featuring an expansive π-architecture, was not yet integrated into such self-assembled structures. This offers a promising avenue for investigation, as achieving a proper band dispersion for electronic conduction requires the presence of both π-extended molecules and a significant orbital overlap, which is facilitated by the extension of the electroactive core.

By understanding and leveraging π-stacking interactions and other molecular arrangements, we aim to unlock new possibilities for MOFs in electronic applications and other areas where enhanced charge carrier mobility is desirable.

[60] Yuan, S.; Feng, L.; Wang, K.; Pang, J.; Bosch, M.; Lollar, C.; Sun, Y.; Qin, J.; Yang, X.; Zhang, P.; Wang, Q.; Zou, L.; Zhang, Y.; Zhang, L.; Fang, Y.; Li, J.; Zhou, H. *Adv. Mater.* **2018**, *30* (37), 1704303.
[61] Mori, T.; Kawamoto, T.; Yamaura, J.; Enoki, T.; Misaki, Y.; Yamabe, T.; Mori, H.; Tanaka, S. *Phys. Rev. Lett.* **1997**, *79*, 1702.

CHAPTER IV

BVDT-TTF and EVT-TTF as organic donors

CHAPTER IV: BVDT-TTF and EVT-TTF as organic donors

1. BVDT-TTF and EVT-TTF salts

A straightforward strategy to obtain TTF based highly conducting radical salts is to use derivatives containing additional sulfur atoms and/or extended π-conjugated core. One prominent example of such a donor is BEDT-TTF, where the TTF skeleton is extended with alkylthio groups. BEDT-TTF is famous for yielding metallic or superconducting salts, making it a subject of extensive research.[1,2] These salts frequently exhibit a distinctive 2-D band structure, a characteristic attributed to the multitude of lateral S-S interactions within their molecular architecture. This behaviour is often associated with Mott localization[3] or Peierls distortion,[4] depending on whether the charges are localized in the band structure or if dimerized pairs are formed within the material.[5] BEDT-TTF $Cu[N(CN)]_2X^-$ (where X = Cl, Br, I) salts have demonstrated a superconductive behaviour below 10 K,[6] which is a relatively high temperature for organic superconductors, showcasing the remarkable properties enabled by their 2-D band structure. Similarly, BEDT-TTF_2I_3 is metallic at room temperature and transits into a superconducting state below 1.4 K, further exemplifying the fascinating electronic behaviour that can be achieved.[7,8]

In our research, the focus was directed towards the investigation of two unsaturated versions of BEDT-TTF, namely BVDT-TTF and EVT-TTF (Figure 4- 1). The compounds BVDT-TTF and EVT-TTF have been clearly underexplored in the literature, with only two papers reporting X-ray structures of single-crystals of BVDT-TTF salts (PF_6^-)[9,10] and three papers of EVT-TTF salts (PF_6^-, AsF_6^-, and $Pt(CN)_4^{2-}$)[10,11] despite the fact that early reports described conductive salts without structures with anions such as ReO_4^-, ClO_4^- or I_3^-. In a comparative analysis between the α$(BEDT-TTF)_2PF_6$ and $(BVDT-TTF)_2PF_6$ systems, $(BVDT-TTF)_2PF_6$

---

[1] Day, P.; Kurmoo, M. *J. Mater. Chem.* **1997**, *7* (8), 1291–1295.
[2] Lefebvre, S.; Wzietek, P.; Brown, S.; Bourbonnais, C.; Jérome, D.; Mézière, C.; Fourmigué, M.; Batail, P. *Phys. Rev. Lett.* **2000***, 85,* 5420–5423.
[3] Faltermeier, D.; Barz, J.; Dumm, M.; Dressel, M.; Drichko, N.; Petrov, B.; Semkin, V.; Vlasova, R.; Meźière, C.; Batail, P. *Phys. Rev. B* **2007**, *76* (16), 165113.
[4] Enoki, T.; Imaeda, K.; Kobayashi, M.; Inokuchi, H.; Saito, G. *Phys. Rev. B* **1986**, *33* (3), 1553–1558.
[5] Wosnitza, J. *J. Low Temp. Phys.* **2019**, *197* (3–4), 250–271.
[6] Wang, H. H.; Carlson, K. D.; Geiser, U.; Kini, A. M.; Schultz, A. J.; Williams, J. M.; Montgomery, L. K.; Kwok, W. K.; Welp, U.; Vandervoort, K. G.; Boryschuk, S. J.; Crouch, A. V. S.; Kommers, J. M.; Watkins, D. M.; Schriber, J. E.; Overmyer, D. L.; Jung, D.; Novoa J. J.; Whangbo, M.-H. *Synth. Met.* **1991**, *42*, 1983–1990.
[7] Bender, K.; Dietz, K.; Endres, H.; Helberg, H. W.; Hennig, I.; Keller, H. J.; Schäfer, H. W.; Schweitzer, D. *Mol. Cryst. Liq. Cryst.* **1984**, *107* (1–2), 45–53.
[8] Williams, J. M.; Beno, M. A.; Wang, H. H.; Reed, P. E.; Azevedo, L. J.; Schirber, J. E. *Inorg. Chem.* **1984**, *23* (13), 1790–1792.
[9] Kobayashi, H.; Kobayashi, A.; Nakamura, T.; Nogami, A.; Shirota, Y. *Chem. Lett.* **1987**, 559-562.
[10] Nakano, H.; Miyawaki, K.; Nogami, T.; Shirota, Y.; Harada, S.; Kasai, N.; Kobayashi, A.; Kato R.; Kobayashi, H. *Bull. Chem. Soc. Jpn.* **1990**, *63,* 2281–2287.
[11] Dubrovskii, A. D.; Spitsina, N. G.; Chekhlov, A. N.; Dyachenko, O. A.; Buravov, L. I.; Lobach, A. A.; Gancedo J. V.; Rovira, C. *Synth. Met.* **2004***, 140,* 171–176.

exhibits a quasi-one-dimensional band structure, whereas its counterpart, α(BEDT-TTF)$_2$PF$_6$, have a defined two-dimensional electronic band structure.[12] (BVDT-TTF)$_2$PF$_6$ shows at room temperature a conductivity of 20 S·cm^{-1} which is similar to the conductivity of β-(BEDT-TTF)$_2$I$_3$.[13] α–(BEDT-TTF)$_2$PF$_6$ exhibits a semiconductive behavior (1 S·cm^{-1})[14] and a two-dimensional electronic band structure. α-(BEDT-TTF)$_2$PF$_6$ and (BVDT-TTF)$_2$PF$_6$ systems exhibit a similar packing arrangement. The donor molecules in both systems form stacks along the *b*-axis of the crystal structure. The shortest interplanar S-S distance are similar, 3.43 Å for (BVDT-TTF)$_2$PF$_6$ and 3.48 Å for α–(BEDT-TTF)$_2$PF$_6$. Notably, in contrast to α–(BEDT-TTF)$_2$PF$_6$, where the S-S distance between these stacked molecules along the c-axis is approximately 3.60 Å, (BVDT-TTF)$_2$PF$_6$ displays a reduced S-S distance of about 3.54 Å. This observation highlights that the planarity of the donor is not an absolute necessity to design charge transport salts. In addition, the increased π-conjugation promotes the orbital overlap within the material.[15, 16]

Ethylene-vinylenedithiotetrathiafulvalene (EVT-TTF) is an asymmetric version of BVDT-TTF, with a vinylene on one side and an ethylene on the other. The asymmetry effects on packing arrangements within the crystal lattice can lead to selective orientation during the crystallization process because of the distinct chemical environments present at each end of the asymmetric molecule. The vinylene group is more electron-poor thanks to the presence of π-electrons in the extended π-conjugated system. In contrast, the ethylene group end is relatively more electron-rich. This difference influences the interaction with acceptor molecules leading to preferred head-to-tail orientations of EVT-TTF molecules within the crystal lattice, such as for PF_6^-, AsF_6^-,[17] and $Pt(CN)_4^{2-}$.[18]

Despite the structural similarity of BVDT-TTF and EVT-TTF with the widely studied BEDT-TTF structure, there is a significant lack of detailed structural information on these organic donors. This prompted us to explore their combinations with various salts. Four new structures, (BVDT-TTF)(TaF$_6$), (BVDT-TTF)$_2$(ReO$_4$), (BVDT-TTF)$_{2.5}$(I$_3$), and (EVT-TTF)(ClO$_4$), were analysed by X-ray analysis on single-crystals, conductivity measurements, band structure calculations and Raman spectroscopy. This work is currently being processed for publication.

---

[12] Kobayashi, H.; Kato R.; Mori, T.; Kobayashi, A.; Sasaki, Y.; Saito G.; Inokuchi, H. *Chem. Lett.* **1983**, *12* (5), 759-762.
[13] Buravov, L. I.; Kartsovnik, M. V.; Kaminskii, V. F.; Kononovich, P. A.; Kostuchenko, E. E.; Laukhin, V. N.; Makova, M. K.; Pesotskii, S. I.; Topnikov, V. N.; Yagubskii, E. B. *Synth. Met*. **1985**, *11*, 207 – 212.
[14] Kobayashi, H.; Kato, R.; Mori, T.; Kobayashi, A.; Sasaki, Y.; Saito, G.; Enoki, T.; Inokuchi, H. *Mol. Cryst. Liq.* **1984**, *107* (1–2), 33–43.
[15] Ya-Rui, S.; Hui-Ling, W.; Yu-Fang, L. *RSC Adv.* **2016**, *6* (62), 57057–57068.
[16] Misaki, Y. *STAM* **2009**, *10* (2), 024301.
[17] Nakano, H., Miyawaki, K., Nogami, T., Shirota, Y., Harada, S., Kasai, N., Kobayashi, A., Kato, R., & Kobayashi, H. *Bull. Chem. Soc. Jpn.* **1990,** *63*(8), 2281-2287.
[18] Dubrovskii, A. D.; Spitsina, N. G.; Chekhlov, A. N.; Dyachenko, O. A.; Buravov, L. I.; Lobach, A. A.; Gancedo J. V.; Rovira, C. *Synth. Met.* **2004***, 140,* 171–176.

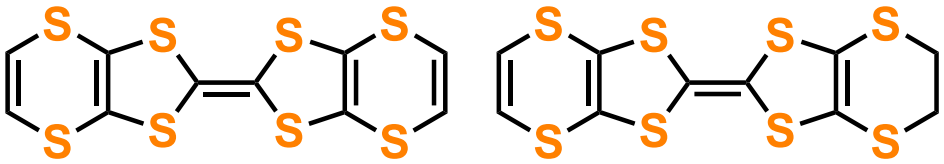


Figure 4- 1. BVDT-TTF and EVT-TTF donors.

2. (BVDT-TTF)(TaF_6)

2.1. Crystal structure description

Upon combination of BVDT-TTF (2 mg) and $TBATaF_6$ (60 mg) in $CHCl_3$ (12 mL) solvent at RT with a 1 μA current for one week into an U-shaped cell, large black blocks of (BVDT-TTF) (TaF_6) were obtained. The crystal is in the orthorhombic *P*nnm space group and the crystal data are described in Table 4- 1.

Crystal system	orthorhombic
Space group	*P*nnm
V/Å^3	879.11(8)
a/Å	4.8259(3)
b/Å	17.8935(9)
c/Å	10.1805(5)
α/°	90
β/°	90
γ/°	90
R_{int} (%)	3.21
R_1,wR_2 (all data) (%)	3.93/11.41
Completeness (%)	99.2

Table 4- 1. Crystal data of (BVDT-TTF)(TaF_6).

The asymmetric unit contains one fourth of the donor and one fourth of an anion, without any additional guest or solvent molecules. BVDT-TTF stands in its radical cationic form with a 1:1 stoichiometry. The

calculated charge of the BVDT-TTF is +1.03.[19] Central C–C and internal C–S bond distances[20, 21] are in agreement with a +I oxidation state of the TTF (Figure 4- 2).

Bond length(Å)	
Central C6–C6	1.398(15)
internal C6–S2	1.719(4)



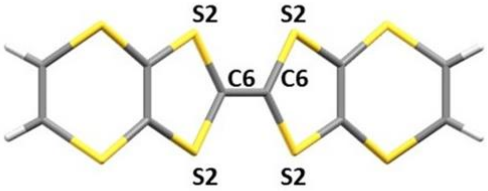


Figure 4- 2. Selected C–C and C–S internal bond distances for (BVDT-TTF)(TaF_6).

The plane defined by the bis-thiovinylene moieties of BVDT-TTF is tilted by a 131.7° angle regarding to the plane defined by the 8 sulphur atoms of the molecule, with an inversion centre lying on the central bond and a C_2 symmetry axis running along this central C=C bonds (Figure 4- 3).

The BVDT-TTF forms 1-D stacks along the *a*-axis where the planes between two molecules are distant of 3.67 Å. Within the same column, the sulphur atoms exhibit longer distances, measuring 3.678 Å and 3.700 Å (Figure 4- 3b). Adjacent 1-D stacks form a H-bonded network along the *b*-axis with the TaF_6^- anions with $d_{CH\cdots F}$ of 2.45 and 2.81 Å. Finally, lateral S-S interactions between BVDT-TTF molecules standing in two different 1-D stacks are observed with $d_{S\cdots S}$= 3.564(2) Å (Figure 4- 3a). This results in a three-dimensional anisotropic band structure, with a higher degree of energy dispersion along the *a*-axis. The comprehensive analysis of the band structure is described in section 2.3.

[19] Guionneau, P.; Kepert, C. J.; Bravic, G.; Chasseau, D.; Truter, M. R.; Kurmoo, M.; Day, P. *Synth. Met.* **1997**, *86* (1–3), 1973–1974.
[20] Clemente, D. A.; Marzotto, A. *J. Mater. Chem.* **1996**, *6* (6), 941.
[21] Kistenmacher, T. J.; Rossi, M.; Chiang, C. C.; Van Duyne, R. P.; Siedle, A. R. *Inorg. Chem*. **1980**, *19*, 12.

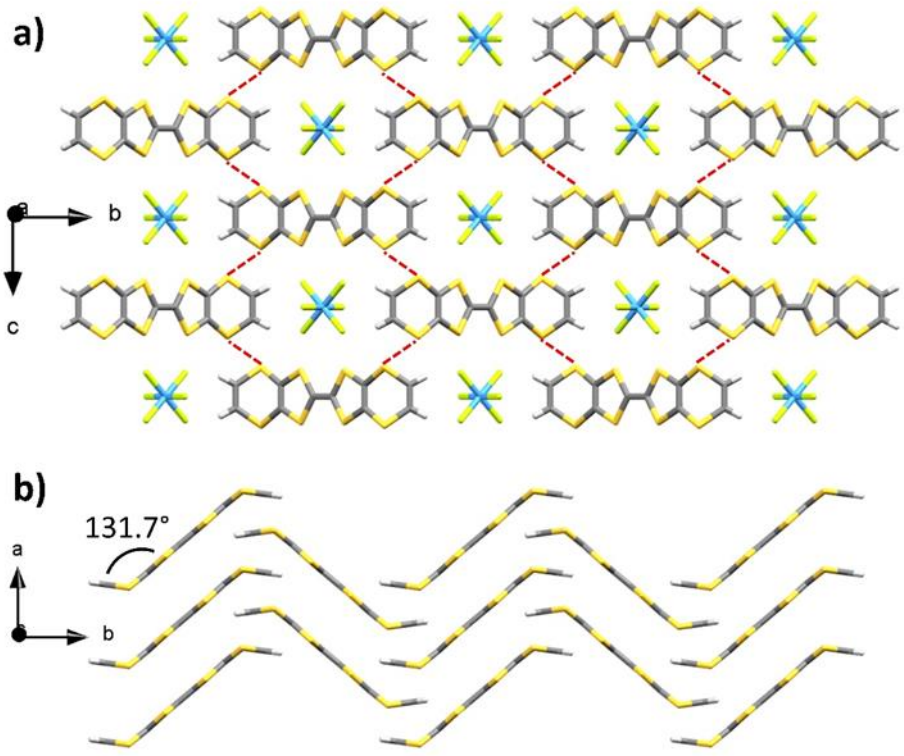


Figure 4- 3. X-ray crystal structure of (BVDT-TTF)(TaF_6) (Carbon: grey ; Sulfur : yellow ; Tantalum : blue ; Fluorine : green ; Hydrogen : white).

2.2. Conductivity measurement

Conductivity measurements were performed with a two-contact method at 290 K and ambient pressure on single crystals with silver glue contacts. BVDT-TTF TaF_6 exhibits a semiconducting behaviour with a conductivity value of $4.4 \cdot 10^{-2}$ $S \cdot cm^{-1}$.

2.3. Band structure calculations

Band structure calculations were conducted in collaboration with Dr. E. Canadell from ICMAB, Spain, and Dr. P. Alemany from the University of Barcelona, Spain.

The DFT band structure assuming a double occupation of the levels is shown in Figure 4- 4a (note that a double cell along the chain direction (*a*) has been used so that the two bands are folded in this figure). The two bands exhibit a large dispersion along the chain direction (Γ-X) but a very small one along the other directions (Γ-Y and Γ-Z). Because of the 1:1 stoichiometry only half of the levels are filled and the salt would be predicted to be a 1D metal according to these calculations. The Fermi surface is strongly 1D, i.e. contains very slightly warped parallel lines, and thus some kind of metal to insulator transition associated with a dimerization along the chains would be predicted. The fact that the 290 K conductivity measurements

indicate a semiconducting behaviour and the 1:1 stoichiometry suggest that despite the substantial band dispersion, electronic repulsions take over and localize one unpaired electron on each donor. To test this idea, we carried out spin-polarized calculations using a double unit cell along the chain direction to be able to consider an antiferromagnetic situation. The AF state was calculated to be the ground state of the system and is found to be 28.0 meV/donor more stable than the metallic state. Note the large gap opened in the band structure of the AF state (Figure 4- 4b) which is almost twice larger than in the (BVDT-TTF-Py_4)$^{\cdot+}$-$CdCl_2$-I_3^- salt described in chapter 3, for which the stabilization of the AF state with respect to the metallic state is very similar (34.0 meV/donor).[22] The width of the partially filled band in the present compound is very large (~0.8 eV, between two and three times larger than in (BVDT-TTF-Py_4)$^{\cdot+}$-$CdCl_2$-I_3^- thus providing a strong bias for electronic delocalization so that strong antiferromagnetic interactions are needed to stabilize the localized state.

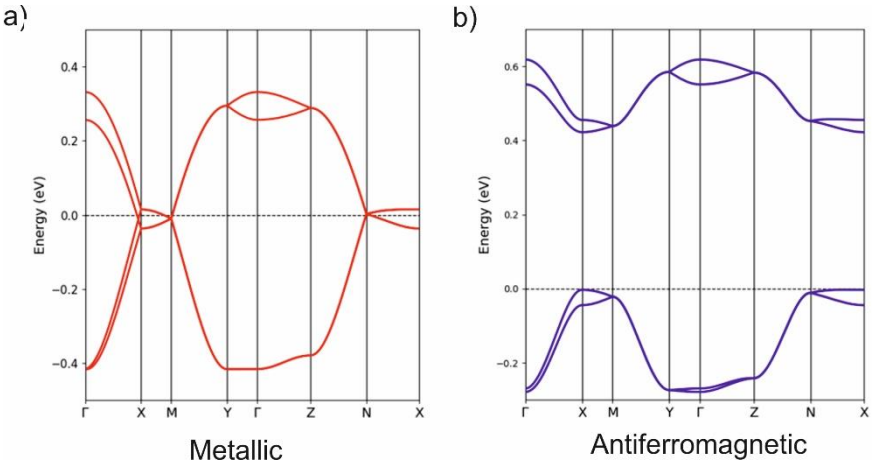


Figure 4- 4. Band structure for the (a) metallic and (b) antiferromagnetic (along *a*), states of (BVDT-TTF)(TaF_6) using a double cell along *a*. The energy zero refers to the highest occupied state in both cases and Γ = (0, 0, 0), X = (*a**/2, 0, 0), Y = (0, *b**/2, 0), Z = (0, 0, *c**/2), M= (*a**/2, *b**/2, 0) and N= (*a**/2, 0, *c**/2). In (b) the spin-up and spin-down bands are shown in blue and red, respectively. However, since the spin-up and spin-down bands are identical, although located in spatially different but equivalent sites, they superpose and only the blue bands are visible.

[22] Solano, F.; Auban-Senzier, P.; Olejniczak, I.; Barszcz, B.; Runka, T.; Alemany, P.; Canadell, E.; Avarvari, N.; Zigon, N. *Chem. Eur.J.* **2023**, *29*, e202203138.

3. $(BVDT\text{-}TTF)_{2.5}(I_3)$

3.1. Crystal structure description

Upon diffusion of I_2 vapours into a solution of BVDT-TTF (1 mg) in DCM (5 mL) for one night, large crystalline purple plates were obtained and characterized by SCXRD. The space group is orthorhombic *P*nma and the crystal data are described in Table 4- 2.

Crystal system	orthorhombic
Space group	*P*nma
V/Å^3	1523(46)
a/Å	3.777(19)
b/Å	12.18(14)
c/Å	33.1(9)
α/°	90
β/°	90
γ/°	90
R_{int} (%)	5.92
R_1,wR_2 (all data) (%)	7.95/25.40
Completeness (%)	98.1

Table 4- 2. Crystal data of $(BVDT\text{-}TTF)_{2.5}(I_3)$.

The asymmetric unit contains half of a BVDT-TTF and one fifth of a disordered I_3^- molecule. BVDT-TTF / triiodide ratio is 2.5:1. The calculated charge of the BVDT-TTF is +0.27.[19] The central C=C and internal C–S bond lengths (Figure 4- 5) are in agreement with the mixed valence oxidation state of TTF.

Bond length(Å)	
Central C–C	1.37(4)
internal C3–S2	1.75(2)
internal C4–S3	1.745(19)

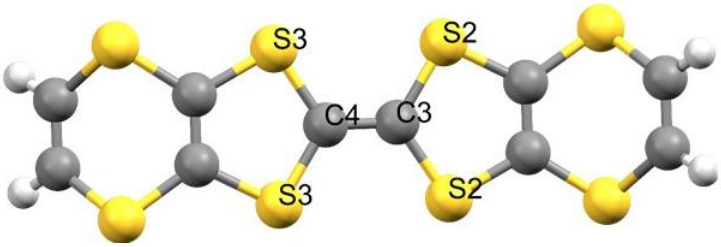


Figure 4- 5. Selected C–C and C–S internal bond distances for $(BVDT\text{-}TTF)_{2.5}(I_3)$.

The molecule of BVDT-TTF is bent with a 132.5° angle between the vinylene moiety and the plane defined by the 8 sulphur atoms (Figure 4- 6c). The molecules are stacking along the *a* axis, with an intermolecular distance of 3.46 Å (Figure 4- 6a and c). Molecules from two adjacent stacks form numerous lateral S-S interactions in the 3.45 to 3.77 Å range, thus creating a bi-dimensional band in the *ab* plane (Figure 4- 6b). The tri-iodide ions are strongly disordered along the *a* axis. On the Figure 4- 6d are represented the three disordered positions in blue, white and red colours. The occupancies are given for the red iodine atoms. If only the red atoms are considered, the distances between two iodine atoms are in the 2.84-2.85(2) Å range. Three atoms with 40-20-40% occupancies, respectively, are almost perfectly co-linear with a 179.2° angle. This represents one tri-iodide molecule with a 20% occupancy, both external atoms having a 40% occupancy shared with the next molecule in the chain (with the same colour). The next three red atoms (20-40-20% occupancies, respectively) form a 170.7° angle.

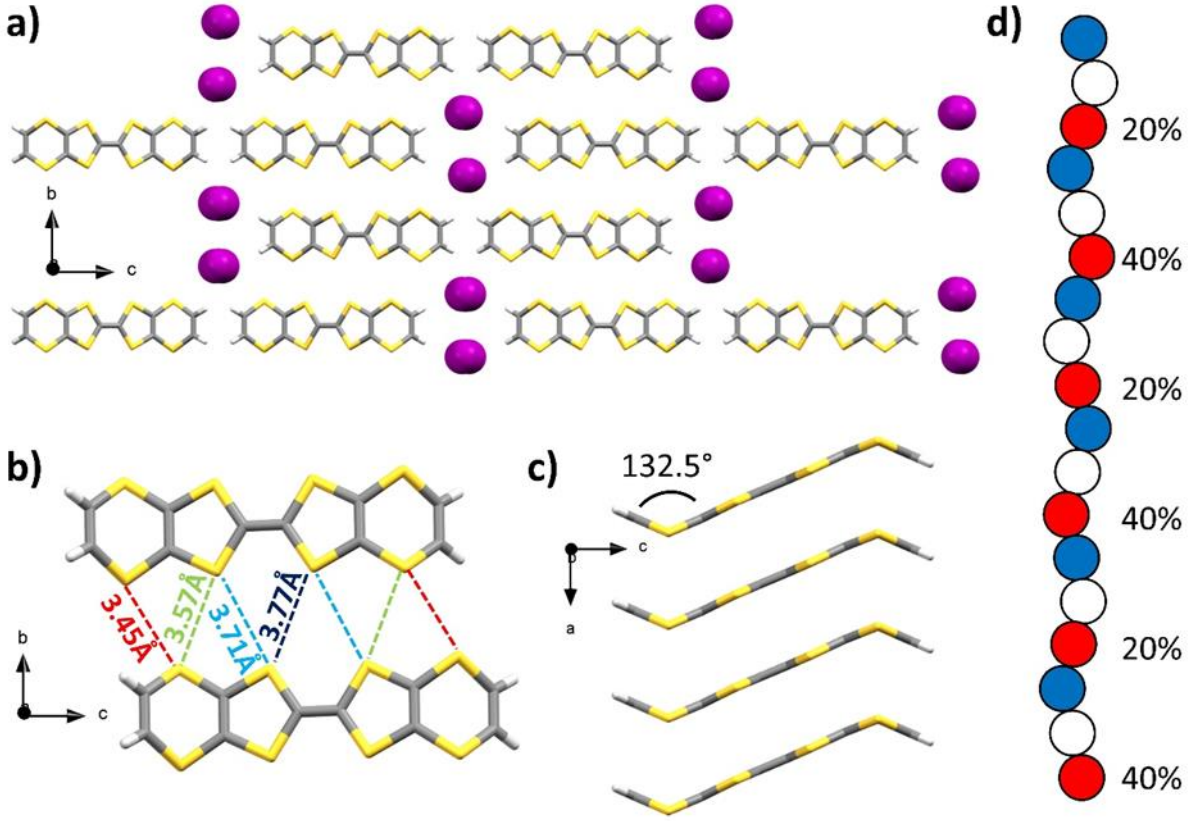


Figure 4- 6. X-ray crystal structure of $(BVDT\text{-}TTF)_{2.5}(I_3)$ (Carbon: grey ; Sulfur : yellow ; Iodine : purple ; Hydrogen : white).

3.2. Conductivity measurement

Single crystal conductivity measurement (two contact measurement) of $(BVDT\text{-}TTF)_{2.5}(I_3)$ displays a conductivity of $1.4 \cdot 10^{-1}$ S·cm^{-1} at room temperature. It is a semiconductor with an activation energy (E_a) of 34.5 meV, as deduced from the temperature-dependent resistivity data presented in Figure 4- 7. This estimation was derived employing the Arrhenius equation: $\rho = \rho_0 \, exp\frac{Ea}{kT}$, which relates resistivity (ρ) to the

temperature (T) and a reference resistivity (ρ_0) through the activation energy (E_a) and the Boltzmann constant (k).

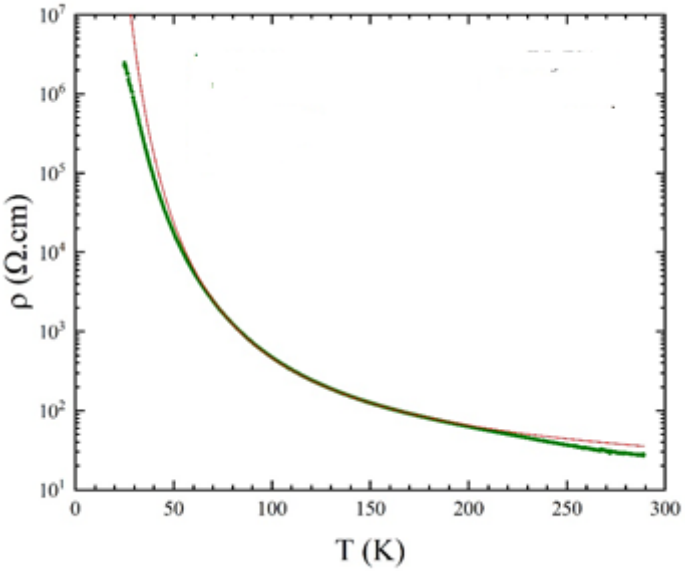


Figure 4- 7. Temperature dependent resistivity measurement on single crystal for $(BVDT\text{-}TTF)_{2.5}(I_3)$, plotted as ρ versus temperature.

3.3. Band structure calculations

Band structure calculations were conducted in collaboration with Dr. E. Canadell from ICMAB, Spain, and Dr. P. Alemany from the University of Barcelona, Spain.

The DFT band structure for the hypothetical metallic state is reported in Figure 4- 8a. The two bands along the directions parallel to chains are clearly separated by a shift of around 0.1 eV, whereas they were almost superposed in $(BVDT\text{-}TTF)(TaF_6)$. This clearly indicates a stronger interaction between the chains in $(BVDT\text{-}TTF)_{2.5}(I_3)$ and thus a more 2D behaviour. However, in contrast with the initial expectations, the band dispersion along the chains (Γ-X) is now around 28 % smaller. The reason is that the HOMO-HOMO overlap along the chain is a bit different in the two salts. Because of the different interaction with the anions, in $(BVDT\text{-}TTF)(TaF_6)$, six of the S atoms are just on top of those of the adjacent donor so that the six pairs of S p_z orbitals of the HOMO interact very strongly. In $(BVDT\text{-}TTF)_{2.5}(I_3)$ there is a sliding of one donor with respect to the adjacent one and the interaction is thus smaller, even if the inter-planar separation is shorter. A very important feature of the present salt is that there is one hole every 2.5 donors, i.e. the bands are 3/5-filled, whereas in $(BVDT\text{-}TTF)(TaF_6)$ they are half-filled. Both the larger filling of the bands and the stronger inter-chain interactions make the hypothetical metallic state associated with Figure 4- 8a less 1D. In fact, the calculated Fermi surface contains both 1D and 2D contributions.

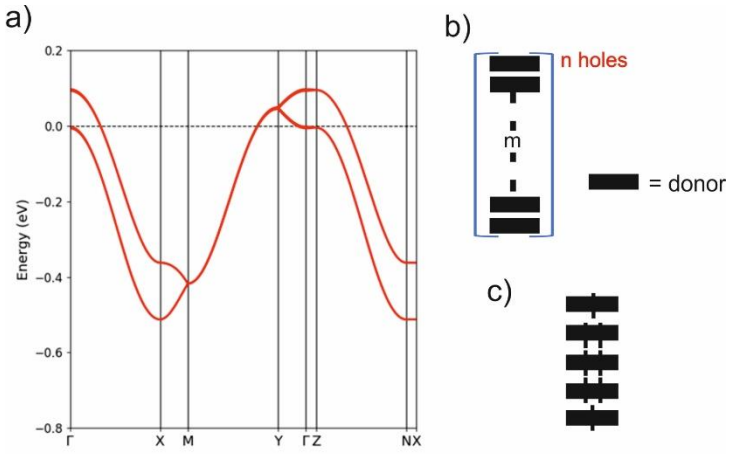


Figure 4- 8. a) Band structure for the hypothetical metallic state of $(BVDT\text{-}TTF)_{2.5}(I_3)$ where Γ = (0, 0, 0), X = (*a**/2, 0, 0), Y = (0, *b**/2, 0), Z = (0, 0, *c**/2), M= (*a**/2, *b**/2, 0) and N= (*a**/2, 0, *c**/2). Discrete $(donor_m)^{n+}$ (b) and $(donor_5)^{2+}$ (c) units discussed in the text.

With the results for $(BVDT\text{-}TTF)_{2.5}(I_3)$ in mind, the conductivity of $(BVDT\text{-}TTF)_{2.5}(I_3)$ could be attributed to the effect of the electron repulsions and this idea was tested by carrying out spin-polarized calculations. Before delving into that, we considered another feature of this salt, the strong disorder of the $(I_3)^-$ groups, which must also play a very relevant role. It is well established that the hydrogen bonding interactions between the hydrogen atoms of the donors and the two outer iodine atoms of the $(I_3)^-$ groups, which are those bearing the charge, may play a crucial role in molecular conductors.[23] For instance, these interactions are at the origin of the long debated charge-ordering transition of $\alpha(BEDT\text{-}TTF)_2I_3$.[24] The $H_{donor}\cdots I$ interactions will certainly induce small breaks in the uniformity of the chains (either through donor slidings, donor-donor separations or intra-donor changes) leading to the creation of a disordered set of $(donor_m)^{n+}$ units (Figure 4- 8b). For instance, that shown in Figure 4- 8c would be especially well adapted to an average +0.4 charge although the real chain is certainly not an ordered succession of such units. Of course, what is shown in this scheme is a fully localized picture, but some delocalization of the spin density within the *m* donor units certainly occurs. Combining units with different *n* and *m* values it is possible to come up with the average 1:2.5 stoichiometry of the average structure of $(BVDT\text{-}TTF)_{2.5}(I_3)$. The creation of these disorder-induced units will structurally localize the electrons and create relatively high conductivity of the salt.

To determine if electron repulsions play a substantial role in localising the electrons independently of disorder effects, we have carried out spin-polarized calculations using a uniform background instead of real anions and the uniform structure of the chain. We have carried out model spin-polarized calculations for an isolated chain as in $(BVDT\text{-}TTF)_{2.5}(I_3)$ with different average charges and introducing ferromagnetic or antiferromagnetic interactions. However, we could not stabilize any gapped localized state with

[23] Pouget, J.-P.; Alemany, P.; Canadell, E. *Mater. Horiz* **2018**, *5,* 590-640.
[24] Alemany, P.; Pouget J.-P.; Canadell, E. *Phys. Rev. B* **2012**, *85,* 195118.

ferromagnetic or antiferromagnetic interactions along the chain in the case of a 0.4 average charge.This is in agreement with more formal condensed matter approaches showing that the proclivity to localization because of electron repulsions is maximal for a half-filled band.[25] As results, we believe that the electronic repulsions are not especially relevant to understand the activated nature of the conductivity of (BVDT-TTF)$_{2.5}$(I_3) and conclude that the conductivity in this salt is essentially governed by the disorder due to local distortions induced by the H_{donor}···I interactions that break the uniformity of the donor chains.

4. (BVDT-TTF)$_2$(ReO_4)

4.1. Crystal structure

Upon combination of BVDT-TTF and $TBAReO_4$ in TCE solvent at RT with a 1 µA current for one week into an U-shaped cell, small plate crystals of (BVDT-TTF)$_2$(ReO_4) were obtained. Several crystalline plates were overlaid, thus the crystals were subject to twinning. Upon resolution of the SCXRD structure, it appears that the space group is monoclinic *C*2/m and crystal data are described in Table 4- 3. The presence of twinning, along with a low data completeness, have together led to a notable increase in the values of R_1 and wR_2.

Crystal system	monoclinic
Space group	*C*2/m
V/Å^3	1540.7(3)
a/Å	33.133(3)
b/Å	12.1739(14)
c/Å	3.8263(6)
α/°	90
β/°	93.360(11)
γ/°	90
R_{int} (%)	3.20
R_1,wR_2 (all data) (%)	22.02/55.18
Completeness (%)	81

Table 4- 3. Crystal data of (BVDT-TTF)$_2$(ReO_4).

[25] Lieb, E. H.; Wu, F. Y. *Phys. Rev. Lett.*, **1968**, *20*, 1445-1448

The asymmetric unit contains half of a BVDT-TTF and one molecule of disordered ReO_4^- with a 25% occupancy. The BVDT-TTF: anion ratio is therefore 2 : 1. The determination of the oxidation state of TTF through calculus is not possible due to the low X-ray data quality and precision on the central C=C and internal C–S bond lengths. The BVDT-TTF is bent with a 133.3° angle between the vinylene group and the plane defined by the 8 sulphur atoms (Figure 4- 9c). Here, the molecules form stacks along the *c*-axis, with intermolecular distances of 3.50 Å between the two molecular planes (Figure 4- 9a and c). As represented on Figure 4- 9, two BVDT-TTF molecules from adjacent stacks are engaged in a series of S-S interactions, with lateral S-S distance in the 3.43-3.81 Å range, thus creating a dispersive band in the *bc* plane. The perrhenate anions are disordered over 4 positions along the *c* axis, and are engaged in H-bonding through their oxygen atoms and the vinylic C-H, with distances d_{CH-O} in the 2.45-2.76 Å range.

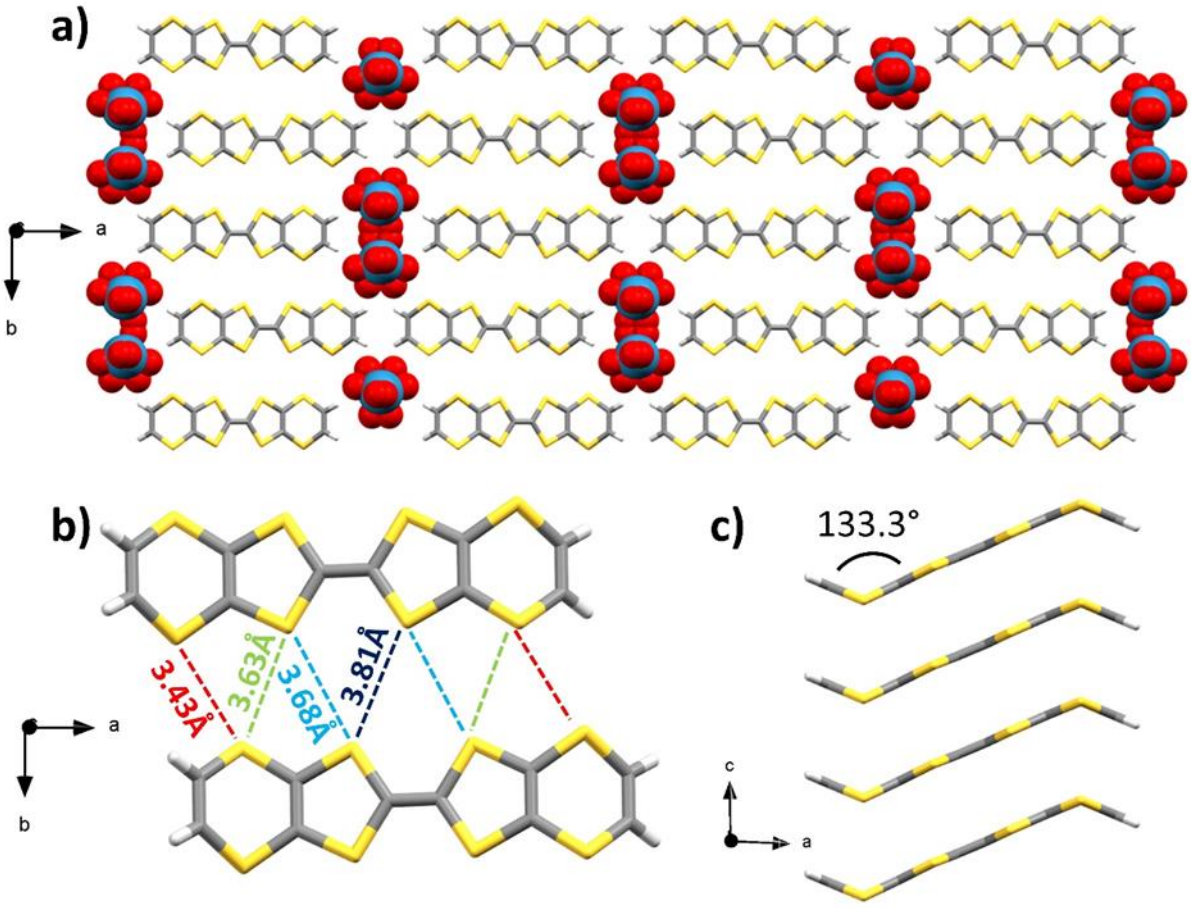


Figure 4- 9. X-ray crystal structure of $(BVDT\text{-}TTF)_2(ReO_4)$ (Carbon: grey ; Sulfur : yellow ; Rhenium : blue ; Oxygen : red ; Hydrogen : white).

4.2. Conductivity measurement

Single crystal conductivity measurement (two contact measurement) of $(BVDT\text{-}TTF)_2(ReO_4)$ shows a semi conductive behaviour, with a room temperature conductivity of $3.1 \cdot 10^{-3}$ $S \cdot cm^{-1}$. An activation energy (E_a) of 112 meV indicates a significant energy barrier for charge carriers to move through the crystal lattice (Figure 4- 10).

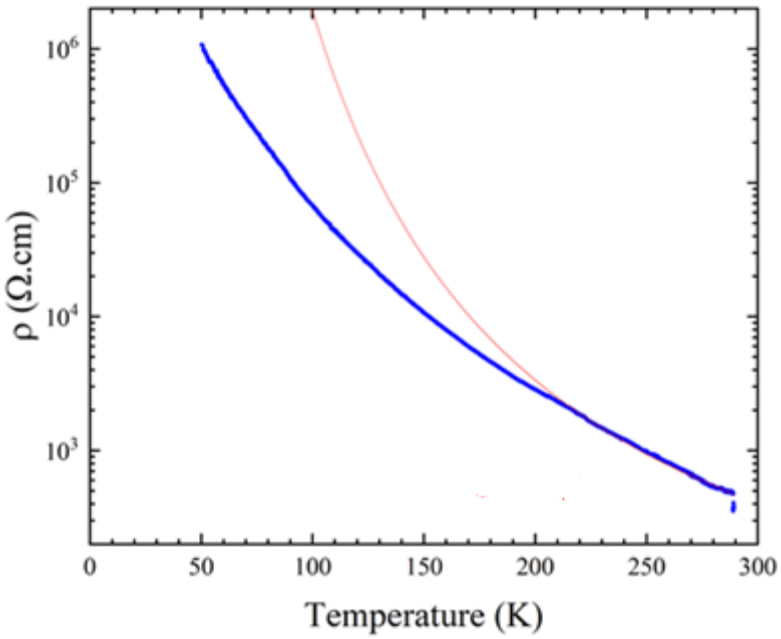


Figure 4- 10. Temperature dependent resistivity measurement on single crystal for $(BVDT\text{-}TTF)_2(ReO_4)$.

5. EVT-TTF

5.1. Synthesis and properties

The synthesis of EVT-TTF was conducted using the following procedure: a Diels-Alder reaction is performed between the trithione and phenyl vinyl sulfoxide to form the compound **3** (VDT). Compound **3** (VDT) was subjected to a cross-coupling reaction with 4,5-bis(2-cyanoethylthio)-1,3-dithiole-2-one using trimethyl phosphite as the coupling agent at a temperature of 120°C, resulting in the formation of compound **24**. Subsequently, treatment of the compound **24** with 3 equivalents of sodium ethoxide, followed by the addition of dibromoethane, yielded the compound **25** (Figure 4- 11). EVT-TTF is synthetized with an overall yield of 7%.

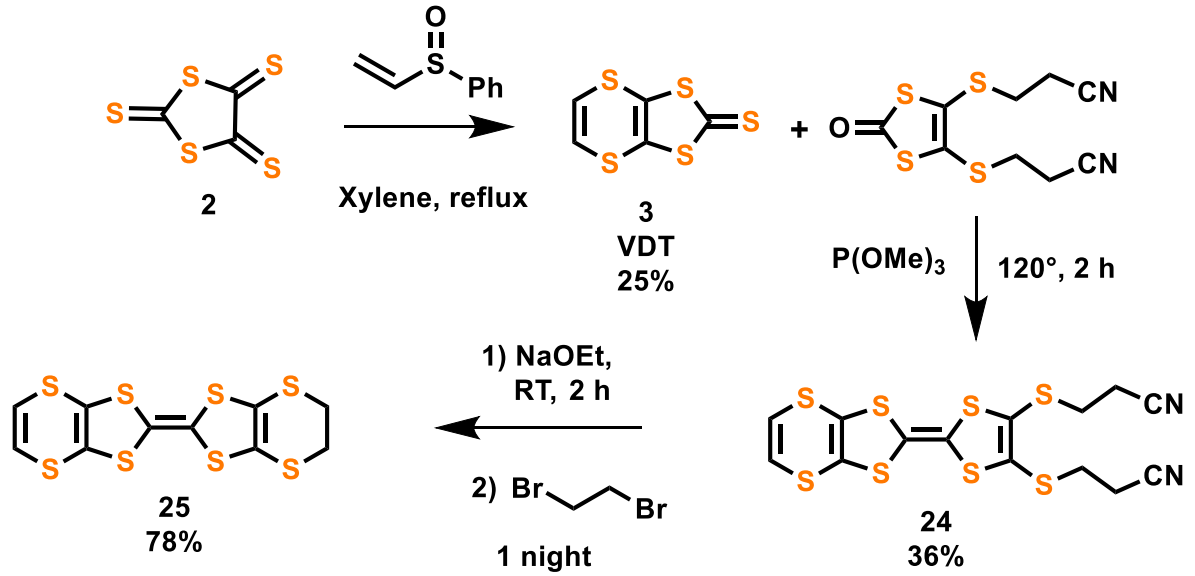


Figure 4- 11. Synthesis of EVT-TTF, **25**

The cyclic voltammogram of compound EVT-TTF **25** was measured at different scan rates (Figure 4- 12) and oxidation (E_{Ox}) and reduction (E_{Red}) potentials and $E_{1/2}$ are reported (Table 4- 4). The value of the $E^1_{1/2}$, which is 0.57 V and associated with the formation of the radical cation in EVT-TTF, falls within the range of BEDT-TTF and BVDT-TTF ($E^1_{1/2}$ 0.53 V and 0.59 V vs. SCE). While the first oxido-reduction wave is reversible, maintaining a constant $E^1_{1/2}$ at different scan rates, the second oxido-reduction exhibits a quasi-reversible nature characterized by less symmetrical redox peaks and a less pronounced reduction wave. This quasi-reversible behaviour becomes more evident as the scan rate increases, highlighting the interplay of kinetics in the electrochemical response.

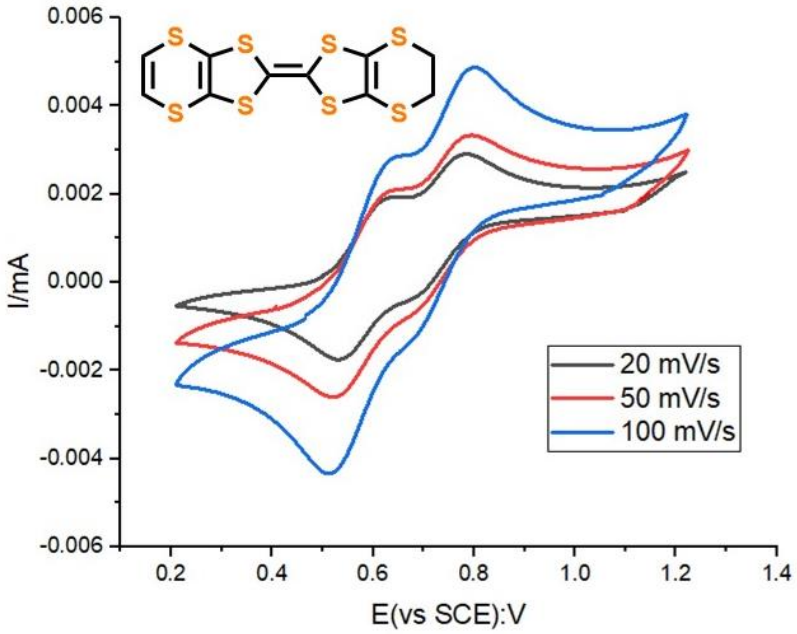


Figure 4- 12. Cyclic voltammetry of a **25** solution (10^{-3} M, $TBAPF_6$ 0.1M in THF). Platinum electrode as WE, platinum wire as CE and an Ag/AgCl/Saturated KCl electrode as RE at scan rate 20/50/100 $mV \cdot cm^{-1}$. Values were converted with respect to the standard calomel electrode (SCE).

Scan rate [$mV.s^{-1}$]	E^1_{Ox}	E^1_{Red}	$E^1_{1/2}$	E^2_{Ox}	E^2_{Red}
20	0.623	0.532	0.577	0.781	0.68
50	0. 628	0.530	0.783	0.790	0.70
100	0.631	0.615	0.779	0.795	0.70

Table 4- 4. Potential oxidation, E_{Ox} and reduction, E_{Red} potentials and $E_{1/2}$ of **25** vs SCE at different scan rates.

5.2. (EVT-TTF)(ClO_4) crystal structure description

EVT-TTF provided crystals with tetrabutylammonium perchlorate (TBAP) in DCM under a 1 μA current. The X-ray crystal structure is resolved in the monoclinic $P2_1/c$ space group and the crystal data are described in Table 4- 5.

Crystal system	monoclinic
Space group	$P2_1/c$
V/Å^3	1841.31(16)
a/Å	8.0005(4)
b/Å	23.8718(10)
c/Å	9.8100(5)
α/°	90
β/°	100.649(5)
γ/°	90
R_{int} (%)	3.25
R_1,wR_2 (all data) (%)	5.70/16.53
Completeness (%)	94.6

Table 4- 5. Crystal data of (EVT-TTF)(ClO_4).

The asymmetric unit contains one EVT-TTF along with a ClO_4^- anion disordered over two positions with 50%/50% occupancies, and half of a dichloromethane molecule. The ratio of EVT-TTF and perchlorate anion is 1:1. The calculated charge of the EVT-TTF is +1.09.[19] The central C=C and internal C–S bond lengths (Figure 4- 13) are in agreement with a +1 oxidation state of the TTF.

Bond length(Å)	
Central CE–CF	1.382(6)
Internal CE–S1	1.729(4)
Internal CE–S4	1.713(4)
Internal CF–S2	1.720(4)
Internal CF–S3	1.728(4)

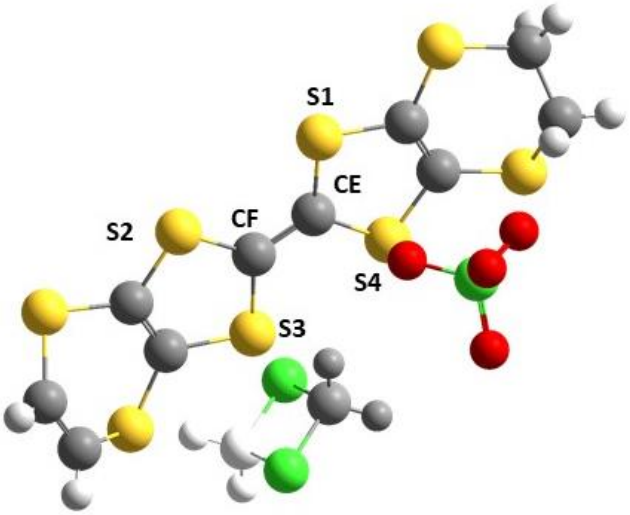


Figure 4- 13. Selected C–C and C–S internal bond distances for (EVT-TTF)(ClO_4). The carbon atom from DCM molecule is disordered over two positions with refined partial occupancy factors (0.5/0.5). One molecule appears grey, the other white, while the shared chlorine atoms are depicted in green for clarity. Only one out of the two disordered positions of the perchlorate anion is displayed for the sake of clarity.

The angle between the vinylidene moiety and the plane of the molecule is 130.9°. The ethylene group is not disordered. Two donors are forming a head-to-tail dimer whose planes are separated by 3.42 Å (Figure 4- 14b). Perchlorate and DCM molecules shield four sides of these dimers. Two adjacent dimers are connected through lateral S-S interactions along the *a* axis with distances in the 3.67-3.98 Å range.

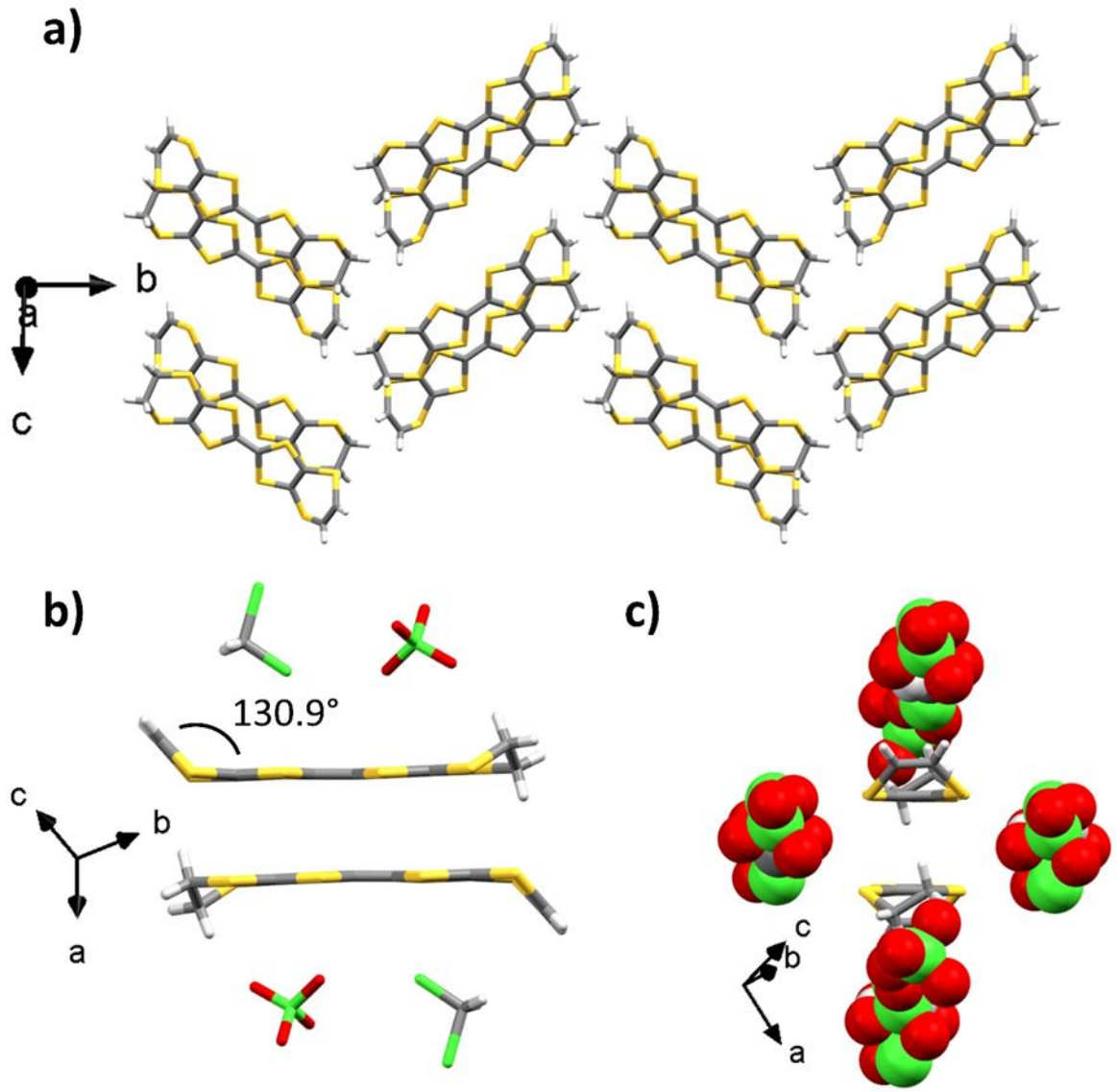


Figure 4- 14. X-ray crystal structure of (EVT-TTF)(ClO_4) (Carbon: grey ; Sulfur : yellow ; Chlorine : green; Oxygen : red ; Hydrogen : white). Solvent molecules and anions have been omitted for the sake of clarity on (a). Disordered solvent molecules and anions have been omitted for the sake of clarity on (b).

5.3. Conductivity measurement

Single crystal conductivity measurement (two-contact measurement) of (EVT-TTF)(ClO_4) shows that it is a semiconductor, with room temperature conductivity of $1.8 \cdot 10^{-2}$ $S \cdot cm^{-1}$. An activation energy (E_a) of 137 meV (two contact measurement) indicates a significant energy barrier for charge carriers to move through the crystal lattice of (EVT-TTF)(ClO_4) (Figure 4- 15).

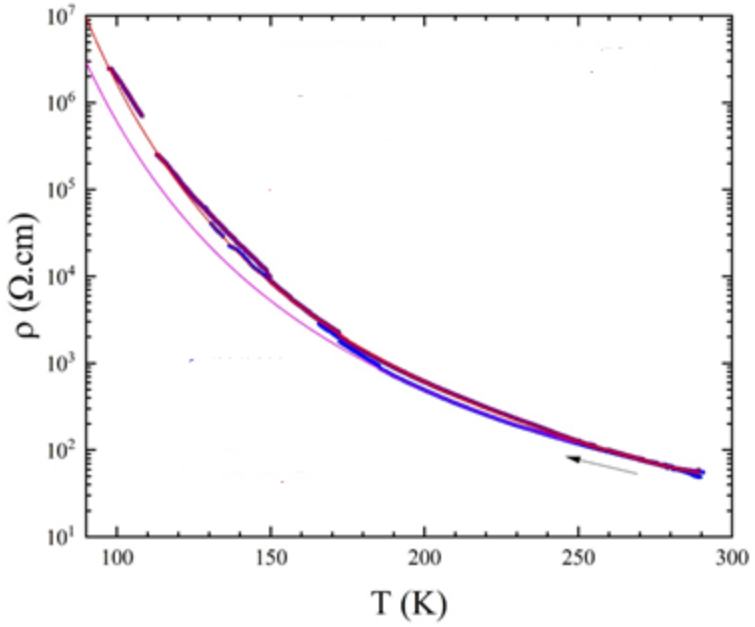


Figure 4- 15. Temperature dependent resistivity measurement on single crystal for (EVT-TTF)(ClO_4) in two and four contact measurements.

5.4. Band structure calculations

Band structure calculations were conducted in collaboration with Dr. E. Canadell from ICMAB, Spain, and Dr. P. Alemany from the University of Barcelona, Spain.

The calculated band structure for (EVT-TTF)(ClO_4) is shown on Figure 4- 16. Since the unit cell contains two layers of dimerized chains (four donor molecules per unit cell), the band structure contains two pairs of bands, each one associated with one layer and mostly build from the HOMO (highest occupied molecular orbital) of the donors. The two bands in each pair are practically degenerated because there are no short interlayer S···S contacts. The splitting between the two HOMO levels in an isolated dimer is calculated to be ≈ 0.48 eV and this is also the separation between the centres of the two pairs of bands in Figure 4- 16. Thus, the lower/upper pair of bands are built from the bonding/antibonding combinations of the HOMOs within the dimers. Because of substantial HOMO-HOMO overlaps, the two pairs of bands acquire dispersion along both the chain (Γ-X) and the inter-chain (Γ-Z) directions and because of the 1:1 stoichiometry only the lower pair of bands is filled. This confirms that EVT-TTF(ClO_4) is a direct gap semiconductor with an activation energy of ≈ 38 meV.

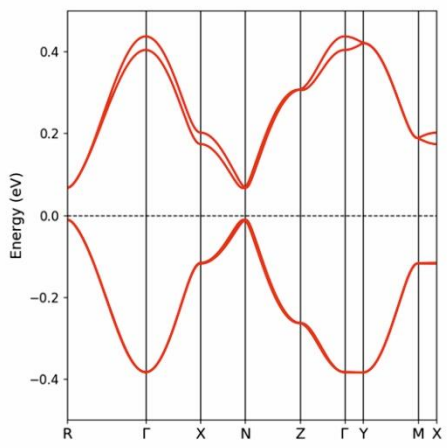


Figure 4- 16. Band structure for (EVT-TTF)(ClO_4) where Γ = (0, 0, 0), X = (a*/2, 0, 0), Y = (0, b*/2, 0), Z = (0, 0, c*/2), M= (a*/2, b*/2, 0), N= (a*/2, 0, c*/2) and R = (a*/2, b*/2, c*/2). Because of disorder, only donor molecules were included explicitly in the calculation while anions and solvent molecules were replaced by a uniform background charge.

6. Raman measurements

The BVDT-TTF and EVT-TTF salts were studied in collaboration with our colleagues at the Institute of Molecular Physics, Polish Academy of Sciences, specifically with Dr. Iwona Olejniczak, Dr. Arkadiusz Frąckowiak, and Dr. Bolesław Barszcz. This part of project was made possible through the support of the POLONIUM 2022 project, during which I had the privilege to work two weeks at their institute.

Similar to a wide range of low-dimensional molecular conductors,[26] the crystal structure of BVDT-TTF and EVT-TTF salts is characterized by the presence of two-dimensional interactions between donor molecules in the conducting layer. On the other hand, unlike BEDT-TTF and many others tetrathiafulvalene-derived donor molecules, both BVDT-TTF and EVT-TTF exhibit significant bending that leads to a unique arrangement of the donor molecule stacks in the crystal structure. Nevertheless, considering the shape of the frontier orbitals for BVDT-TTF (Figure 4- 17) and EVT-TTF (Figure 4- 18), which show a charge density mostly concentrated in the flat central part of the molecules, we can expect the presence of similar Mott or charge-ordered insulating phases which depend on the strength of the onsite and intersite electronic Coulomb correlations within the structure and differ in the charge distribution.[9]

[26] Seo, H.; Hotta, C.; Fukuyama, H. *Chem. Rev.* **2004**, *104*, 5005−5036.

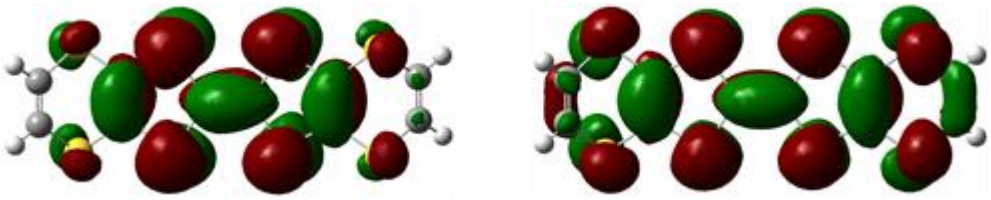


Figure 4- 17. Frontier molecular orbitals: HOMO (Highest Occupied Molecular Orbital) of the neutral BVDT-TTF (left), and α-SOMO (Single Occupied MO) of the BVDT-TTF^{*+} radical cation (right), calculated by DFT methods.

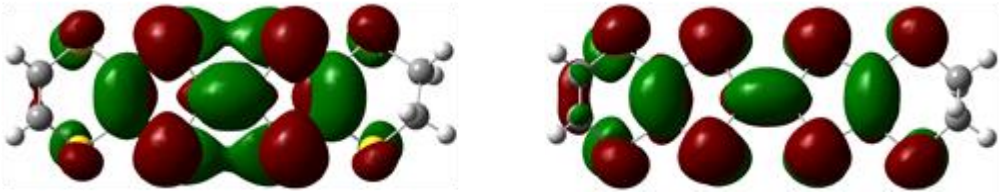


Figure 4- 18. Frontier molecular orbitals: HOMO (Highest Occupied Molecular Orbital) of the neutral EVT-TTF (left), and α-SOMO (Single Occupied MO) of the EVT-TTF^{*+} radical cation (right), calculated by DFT methods.

In order to estimate the oxidation states of the BVDT-TTF and EVT-TTF molecules in their salts, Raman spectroscopy was used which has been widely used in the case of BEDT-TTF salts,[27,28] in combination with the DFT calculations of vibrational modes for the neutral and the radical cation with the charge +1*e*. The focus lies in the examination of the C=C stretching mode, which is observed in the frequency range 1300 – 1600 cm^{-1}. This particular mode is distinguished by a robust and direct frequency correlation with charge variations.[29,30] The schematic pattern of the mode labeled as ν_C for the BVDT-TTF and EVT-TTF cations is shown in Figure 4- 19. While the ν_C mode is restricted to the central double C=C bond in the case of BVDT-TTF, it also involves out-of-phase stretching of the two lateral double C=C bonds for EVT-TTF.

[27] Yakushi, K. *Crystals.* **2012**, *2*, 1291-1346.
[28] Dressel, M.; Drichko, N. *Chem. Rev.* **2004**, *104* (11), 5689–5716
[29] Yamamoto, T.; Uruichi, M.; Yamamoto, K.; Yakushi, K.; Kawamoto, A.; Taniguchi, H. *J. Phys. Chem. B* **2005**, *109* (32), 15226–15235.
[30] Girlando, A. *J. Phys. Chem. C* **2011**, *115* (39), 19371–19378.

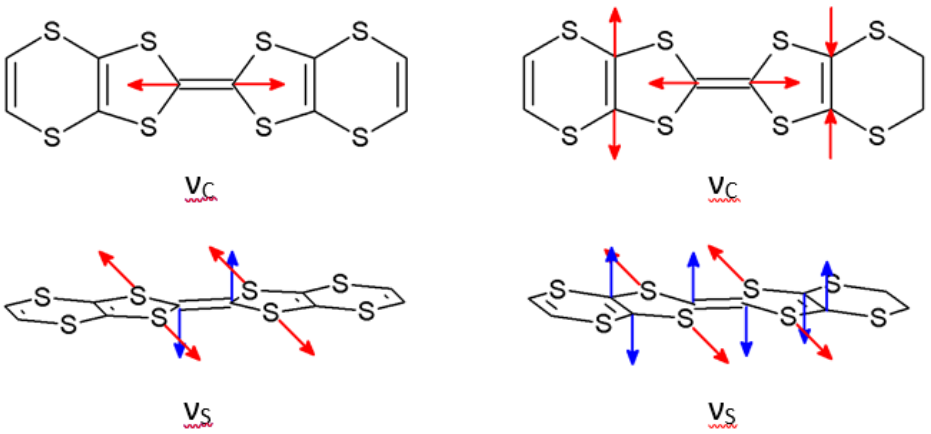


Figure 4- 19. The schematic patterns of the charge-sensitive C=C stretching ν_C mode (upper panels) and the out-of-plane C-S stretching ν_S mode (lower panels) of the BVDT-TTF^{*+} cation (left) and the EVT-TTF^{*+} cation (right), based on the DFT calculations.

Figure 4- 20 shows the room temperature Raman spectra of (BVDT-TTF)(TaF_6), (BVDT-TTF)$_2$(ReO_4), (BVDT-TTF)$_{2.5}$(I_3), and (EVT-TTF)(ClO_4) in the frequency range of the stretching C=C vibrations together with the theoretical Raman spectra of the isolated BVDT-TTF and EVT-TTF donor molecules, both the neutral and the cation. The ν_C mode appears in the theoretical spectra at about 1500 cm^{-1} for the neutral and at 1382 cm^{-1} for the cation, resulting in a frequency difference of about 120 cm^{-1} upon oxidation of BVDT-TTF/EVT-TTF, similar to BEDT-TTF.[27] The shapes of the Raman spectra shown in Figure 4- 20a are broader, and this indicates that the salts (BVDT-TTF)(TaF_6), (BVDT-TTF)$_2$(ReO_4) and (BVDT-TTF)$_{2.5}$(I_3) exhibit a semiconducting behaviour. Within these compounds, low-lying electronic charge transfer excitation phenomenon is present. This refers to small shifts of electron distribution because of the movement of electrons from one part of the molecule to another, and this process occurs a low energy. Low-lying electronic charge transfer excitation couples with C=C stretching modes due to the electron-molecular vibration (EMV).[27] We assign the broad features, at ~1416 cm^{-1} as the ν_C mode of BVDT-TTF^{+1}, and at ~1474 cm^{-1} as the ν_C mode of BVDT-TTF$^{+0.5/0.4}$ (Table 4- 6).

Taking stoichiometry into account, the formal charge on the BVDT-TTF donor molecule is +1*e* for (BVDT-TTF)(TaF_6), +0.5*e* for (BVDT-TTF)$_2$(ReO_4), and +0.4*e* for (BVDT-TTF)$_{2.5}$(I_3). Therefore, the presence of both BVDT-TTF^{+1} and BVDT-TTF$^{+0.5/0.4}$ molecules in the structure of these three salts with different stoichiometries suggests some degree of disorder and/or charge-ordering in the conducting plane. Unlike the other materials presented here, the Raman spectrum of (EVT-TTF)(ClO_4) (Figure 4- 20a) in the 1350 – 1500 cm^{-1} frequency range shows three relatively narrow features that are close to the corresponding modes in the theoretical spectrum of the EVT-TTF cation, both in terms of frequencies and relative intensities (Figure 4- 20b). The intriguing doublet bands around 1600 cm^{-1} in the experimental spectrum of (EVT-TTF)(ClO_4) is attributed to the presence of close contact interactions in the crystal structure, deviating from the isolated molecule scenarios in DFT calculations. Thus, only EVT-TTF^{+1} cations are present in the structure, in agreement with the stoichiometry.

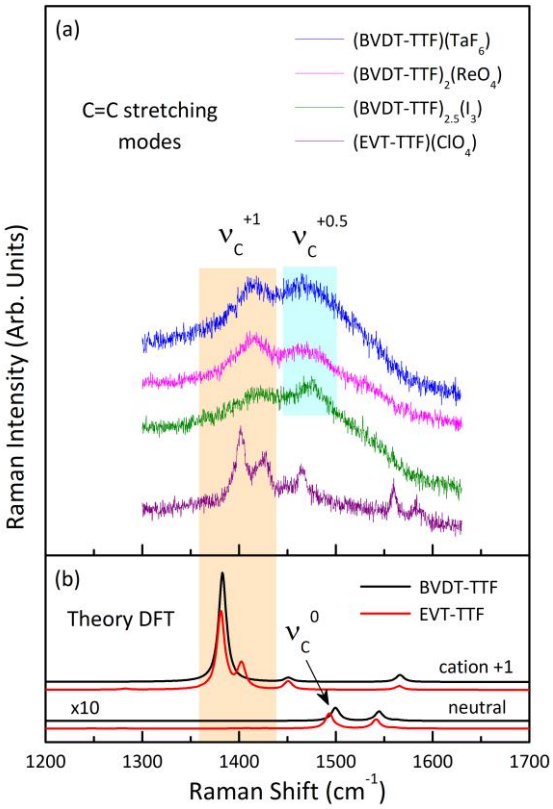


Figure 4- 20. (a) Raman spectra of (BVDT-TTF)(TaF_6), (BVDT-TTF)$_2$(ReO_4), (BVDT-TTF)$_{2.5}$(I_3), and (EVT-TTF)(ClO_4) measured at room temperature, in the frequency range of the C=C stretching vibrations; the spectra show the presence of the ν_C modes associated with the donor molecules of charge +1*e* and +0.5*e*; (b) theoretical Raman spectra of the isolated BVDT-TTF and EVT-TTF donor molecules, both the neutral and the cation, calculated at the B3LYP/6-31+ +G(d,p) level of theory.

	ν_C^0	$\nu_C^{+0.5/0.4}$	ν_C^{+1}
(BVDT-TTF)(TaF_6)	-	~1474	~1416
(BVDT-TTF)$_2$(ReO_4)	-	~1474	~1416
(BVDT-TTF)$_{2.5}$(I_3)	-	~1476	~1416
(EVT-TTF)(ClO_4)	-	-	1402
BVDT-TTF^0	1506	-	-
EVT-TTF^0	1504	-	-
BVDT-TTF (DFT)[a]	1500	-	1382
EVT-TTF (DFT)[a]	1493	-	1381

Table 4- 6. The position in cm^{-1} of the charge-sensitive C=C stretching ν_C mode of BVDT-TTF/EVT-TTF for the neutral ν_C^0, the cation $\nu_C^{+0.5/0.4}$, and the cation ν_C^{+1}, in experimental Raman spectra of (BVDT-TTF)(TaF_6), (BVDT-TTF)$_2$(ReO_4), (BVDT-TTF)$_{2.5}$(I_3), (EVT-TTF)(ClO_4), BVDT-TTF^0, and EVT-TTF^0, and calculated (DFT) Raman spectra BVDT-TTF, and EVT-TTF. [a]Theory level: B3LYP/6-31++G(d,p), scaled with a 0.9614 factor.

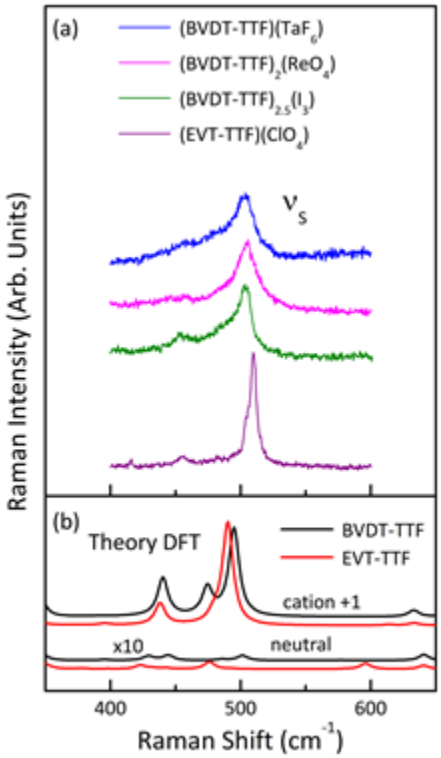


Figure 4- 21. (a) Raman spectra of (BVDT-TTF)(TaF_6), (BVDT-TTF)$_2$(ReO_4), (BVDT-TTF)$_{2.5}$(I_3), and (EVT-TTF)(ClO_4) measured at room temperature with the 632.8 nm excitation line, in the frequency range of the C=S stretching vibrations; (b) theoretical Raman spectra of the isolated BVDT-TTF and EVT-TTF donor molecules, both the neutral and the cation, calculated at the B3LYP/6-31+ +G(d,p) level of theory.

Figure 4- 21a shows the room temperature Raman spectra of (BVDT-TTF)(TaF_6), (BVDT-TTF)$_2$(ReO_4), (BVDT-TTF)$_{2.5}$(I_3), and (EVT-TTF)(ClO_4) in the frequency range of the stretching C=S vibrations. Here, the strong feature centered between 503 cm^{-1} in BVDT-TTF salts and 510 cm^{-1} in (EVT-TTF)(ClO_4) is attributed to the so-called "breathing mode" labeled ν_S (Figure 4- 19), which appears in the theoretical spectra at about 500 cm^{-1} (Figure 4- 21b). This mode is characteristic for the cation spectra. The equivalent of this vibration for BEDT-TTF is known to be strongly coupled to the electronic background.[30,31] Therefore, the significantly broadened shape in the case of (BVDT-TTF)(TaF_6), (BVDT-TTF)$_2$(ReO_4), and (BVDT-TTF)$_{2.5}$(I_3) suggests the proximity of the charge transfer excitation.

Figure 4- 22 shows the Raman spectrum of (BVDT-TTF)$_{2.5}$(I_3) in the frequency range of the stretching polyiodide modes. The spectrum reveals three distinct modes, the symmetric stretching of the centrosymmetric triiodide anion at 112 cm^{-1}, the asymmetric stretching mode of the asymmetric triiodide

[31] Visentini, G.; Masino, M.; Bellitto, C.; Girlando, A. *Phys. Rev. B* **1998**, *58*, 9460-9467.

ion at 143 cm^{-1}, and the band at 164 cm^{-1}, which is most likely related to the symmetric stretching of the L-shaped pentaiodide present in the structure.[32,33]

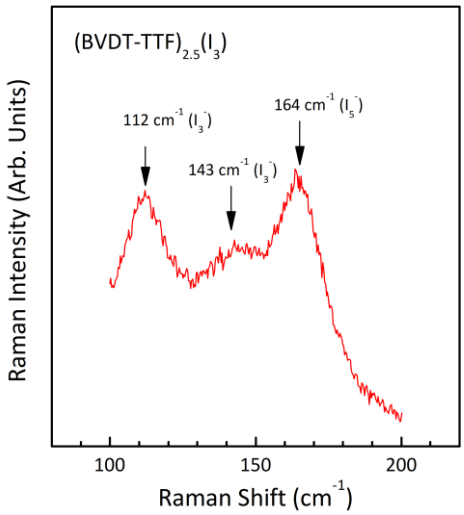


Figure 4- 22. Raman spectrum of $(BVDT\text{-}TTF)_{2.5}(I_3)$ measured at room temperature in the frequency range of the polyiodide stretching vibrations.

[32] Svensson, P. H.; Kloo, L. *Chem. Rev*. **2003**, *103*, 1649–1684.
[33] Jerman, I.; Jovanovski, V.; ŠurcaVuk, A.;. Hočevar, S. B.; Gaberšček, M.; Jesih, A.; Orel, B. *Electrochim. Acta* **2008**, *53*, 2281–2288.

7. Conclusions

Donor	Anion	Stoichiometry	Single crystal conductivity ($S \cdot cm^{-1}$, 290K)
BVDT-TTF	TaF_6^-	1 : 1	$4.4 \cdot 10^{-2}$
BVDT-TTF	I_3^-	2.5 : 1	$1.4 \cdot 10^{-1}$
BVDT-TTF	ReO_4^-	2 : 1	$3.1 \cdot 10^{-3}$
EVT-TTF	ClO_4^-	1 : 1	$1.8 \cdot 10^{-2}$
BEDT-TTF[34]	TaF_6^-	1 : 1	$5 \cdot 10^{-4}$
β-BEDT-TTF[13]	I_3^-	2 : 1	20
BEDT-TTF[35]	ReO_4^-	2 : 1	$5 \cdot 10^{-3}$
BEDT-TTF[36]	ClO_4^-	2 : 1	26.31

Table 4- 7. Stoichiometry and conductivity of BVDT-TTF, EVT-TTF and BEDT-TTF salts.

BVDT-TTF and EVT-TTF were investigated as donors for conductive salts. Conductive salts such as (BVDT-TTF) (TaF_6), (BVDT-TTF)$_{2.5}$(I_3), (BVDT-TTF)(ReO_4), and (EVT-TTF)(ClO_4) were synthesized and studied. Table 4- 7 summarizes the stoichiometry and conductivity data for the salts, including those reported in the literature for BEDT-TTF (see Chapter 1).

(BVDT-TTF)(TaF_6) displays 1-D stacks along with numerous lateral S-S interactions that provide pathways for charge movement and has a conductivity value of $4.4 \cdot 10^{-2}$ $S \cdot cm^{-1}$. In contrast, the donors in (BEDT-TTF)$_2$(TaF_6)$_2$(CH_2Cl_2)[34] form isolated dimers with a bond-over-ring structure. In this arrangement, the dimers are separated in the stacking direction by anions and solvent molecules, which reduces the transfer integrals between the molecules. As a result, the salt has a lower conductivity compared to (BVDT-TTF)(TaF_6).

(BVDT-TTF)$_{2.5}$(I_3) exhibits a conductivity of $1.4 \cdot 10^{-1}$ $S \cdot cm^{-1}$ and the mixed valence oxidation state of TTF suggests the presence of charge delocalization. The disorder caused by H_{donor}···I interactions appears to be the primary factor limiting its conductivity and preventing it from behaving as a true metal. The β-(BEDT-TTF)$_2$$I_3$[13] counterpart exhibits a higher conductivity because of its distinctive "corrugated sheet" network packing configuration. The close interactions between the sheets contribute to the enhanced conductivity of this material.

(BVDT-TTF)$_2$(ReO_4) and (BEDT-TTF)$_2$(ReO_4)[35] display similar conductivities with stoichiometry 2:1 respectively. (BEDT-TTF)$_2$(ReO_4) is stacked along a-axis. The similar conductivities can be attributed to several structural similarities between these two compounds. In both cases, the lateral S-S distances are comparable, falling within the range of 3.4 to 3.7 Å, with the shortest distances measured at approximately

[34] Allain, M.; Mézière, C.; Auban-Senzier, P.; Avarvari, N. *Crystals* **2021**, *11* (4), 386.
[35] Parkin, S. S. P.; Engler, E. M.; Schumaker, R. R. *Phys. Rev. Lett.* **1983**, *50* (4), 270–273.
[36] Saito, G.; Enoki, T.; Toriumi, K.; Inokuchi, H. *Solid State Commun.* **1982**, *42* (8), 557–560.

3.45 Å $(BEDT\text{-}TTF)_2(ReO_4)$ and 3.43 Å $(BVDT\text{-}TTF)_2(ReO_4)$ respectively. The intermolecular distances between donors in both structures are similar. The conductivity value of $(EVT\text{-}TTF)(ClO_4)$ is $1.8\cdot10^{-2}$ $S\cdot cm^{-1}$. The presence of well-defined pathways created by lateral S-S interactions contributes to the efficient movement of charge carriers. In contrast, when compared to $(BEDT\text{-}TTF)_2(ClO_4)$,[36] the conductivity of $(EVT\text{-}TTF)(ClO_4)$ is reduced because of the formation of dimers. In $(BEDT\text{-}TTF)_2(ClO_4)$, the donor molecules are stacked along the c-axis, resulting in short lateral and intermolecular S-S distances between them. This configuration enhances the efficient movement of charge carriers, leading to a higher conductivity.

According to the band structure calculations, the conductivity of the three examined salts relies on different mechanisms. The two salts with a 1:1 stoichiometry show distinct behaviors. In $(EVT\text{-}TTF)(ClO_4)$, there is a structural dimerization effect, while $(BVDT\text{-}TTF)(TaF_6)$ exhibits electronic dimerization (i.e. antiferromagnetism). Conductivity in $(BVDT\text{-}TTF)_{2.5}(I_3)$ is primarily due to small gaps caused by disorder. If it were not for this disorder, the compound would likely behave like a stable metal because of its robust chains and strong inter-chain interactions. Another possible hypothesis is that the material's conductivity is influenced by its relative instability with respect to the loss of iodine.

In summary, the several salts of these underexplored donors exhibit semiconducting behaviour with conductivities in the $1.4\cdot10^{-1}$ - $3.1\cdot10^{-3}$ $S\cdot cm^{-1}$ range at RT, comparable in magnitude to those measured for BEDT-TTF salts with similar anions. These first results highlight the promising potential for further exploration in the future. We are committed to conducting a comprehensive analysis of structure-property relationships, extending our investigations to include various anions such as AsF_6^-, Br_3^-, IBr_2^-, ClO_4^-, I_3^-, $Cu[N(CN)]_2X^-$, $Ag(CN)^-$ for both BVDT-TTF and EVT-TTF donors. In our group, the synthesis of enantiomeric salts was reported (specifically (R,R) and (S,S) forms of Dimethyl-ethylenedithio-tetrathiafulvalene dichlorate) along with the observation of the electrical magneto-chiral anisotropic effect in this structure.[37] One of our future objectives will be to replicate this approach with Dimethyl-ethylene-vinylenedithiotetrathiafulvalene to create chiral conductive salts in order to further investigate in depth their properties.

[37] Pop, F.; Auban-Senzier, P.; Frąckowiak, A.; Ptaszyński, K.; Olejniczak, I.; Wallis, J. D.; Canadell, E.; Avarvari, N. *J. Am. Chem. Soc.* **2013**, *135*, 17176–17186.

General Conclusion and Perspectives

In this work, we explored the realm of conductive Metal-Organic Frameworks by delving into the intricate relationship between the structural configurations of electroactive MOFs and their electronic attributes. We hypothesized that the introduction of extra sulphur atoms on the TTF scaffold could augment the likelihood of π-π stacking and S-S intermolecular interactions, resulting in enhanced electronic properties within these MOFs.

The synthesis of BVDT-TTF, tetrasubstituted with coordinating moieties, posed significant challenges. Several factors contributed to these difficulties, including the limited reactivity or decomposition of certain intermediates, as well as the low solubility of large unfunctionalized planar molecules. These constraints, along with generally low reaction yields, added complexity to the synthetic process.

A family of isostructural 2D MOFs has been synthesized with BVDTTTF-py_4. These MOFs, denoted as **L**-MCl_2, exhibited a 2D conducting path within their structure, which can make them more resistant to defects. 1-D channels are formed within the packing and are occupied by solvent molecules.

Using the same ligand and metal, i.e. copper(II) under different synthetic conditions, a different packing displayed 1D stacking motifs of the BVDT-TTF moieties along with larger pores. The coordinating nodes were herein composed of chlorine-bridged dinuclear copper clusters.

Post-synthetic oxidation resulted in an increase of conductivity. This enhancement is attributed to the improved charge transport pathways because of the partial filling of the conduction band.

Raman spectroscopy played a crucial role for distinguishing the oxidized state of the ligands within the materials. Obtaining high-quality single crystals is challenging, and the oxidation treatment reduced the crystallinity of the material. The extent of oxidation and the presence of iodine were in that case clearly assessed with Raman spectroscopy. Solid-state electrochemistry of the obtained networks was also performed, enabling us to observe the redox activity of the ligand.

H_8TTFOC and BVDT-TTF(Dipicolinic acid)$_4$ have been tried as ligands for networks synthesis. The choice of the metal ion and the presence of additional interactions, such as π-stacking or hydrogen bonding are crucial for obtaining stable and crystalline materials. The H_8TTFOC ligand has shown excellent performance as anodes in LIBs due to its non-coordinated carboxylic acid group, which enhances Li^+ mobility and capacity. In our case, crystalline coordination polymers were obtained, but they lacked stability under ambient conditions.

In the future of these researches, the use of high-valence metal clusters based on Al^{3+} or Fe^{3+} should improve the structural rigidity of the framework, and novel electroactive moieties such as TTF-TTP or metal-bisdithiolenes will be incorporated in coordination polymers, in order to finely tune the electronic properties

of the obtained materials. Their use as coatings for silicon electrodes in Lithium-ion Batteries (LIBs) is here a prominent long-term objective.[267]

A series of radical cation salts has been successfully synthesized using two donors molecules, BVDT-TTF and EVT-TTF, accompanied by anions of different shapes and sizes, such as ClO_4^-, ReO_4^-, TaF_6^-, or I_3^-. These anions play a crucial role in the arrangement of molecules and the electronic characteristics of the materials, as seen from the comprehensive analyses done with techniques such as SCXRD or conductivity measurements. The formation of radical cations has been unequivocally confirmed through Raman spectroscopy. These compounds displayed a semiconducting behaviour with room temperature conductivities comparable to the corresponding BEDT-TTF salts.

In order to enhance our comprehension of how anion size affects both the structural and electronic attributes of these materials, we will synthesize a fresh series of radical cation salts utilizing the same donor molecules. While several salts of EVT-TTF and BVDT-TTF have been reported with specific anions such as AsF_6^-, Br_3^-, ClO_4^-, or I_3^-, the papers often lack in a complete structure/property relationship analysis.[268,269] We intend to address this crucial knowledge gap. Novel anions well-studied with BEDTTTF, such as $Cu(NCS)_2^-$, should also yield interesting materials. Another research lead would be to introduce chiral centres on the EVT-TTF scaffold to study chirality related physical phenomenon in conductors.

[267] Devic, T.; Lestriez, B.; Roué, L. *ACS Energy Lett.* **2019**, *4* (2), 550–557.
[268] Iwasaka, S.; Nogami, T.; Shirota, Y. *Synth. Met.* **1988**, *26* (2), 177–184.
[269] Schumaker, R. R.; Lee, V. Y.; Engler, E. M. *J. Phys. Colloques* **1983**, *44* (C3), 1139-1145.

Experimental Section

Experimental Section

1. General Information

All reagents and chemicals from commercial sources were used without further purification. Solvents were dried and purified using standard techniques. Column chromatography was performed with analytical-grade solvents using Aldrich silica gel (technical grade, pore size 60 Å, 230-400 mesh particle size). Flexible plates ALUGRAM® Xtra SIL G UV254 from MACHEREY-NAGEL were used for TLC.

1.1. NMR spectra

NMR spectra were recorded with a Bruker AVANCE III 300 (^{1}H: 300 MHz; ^{13}C: 76 MHz) and BRUKER Avance III HD 500 MHz (^{1}H: 500 MHz ; ^{13}C: 126 MHz). Chemical shifts are given in ppm relative to tetramethylsilane (TMS) and coupling constants J in Hz. Residual non-deuterated solvent was used as an internal standard. The following abbreviations are used: s, singlet; d, doublet; t, triplet; q, quadruplet; m, multiplet.

1.2. Mass spectra

MS were obtained either by the MALDI/TOF-TOF technique using a JEOL JMS3000 apparatus, equipped with a 337 nm N_2 laser, and by electron impact methods using a JEOL JMS700 apparatus.

1.3. Elemental Analyses

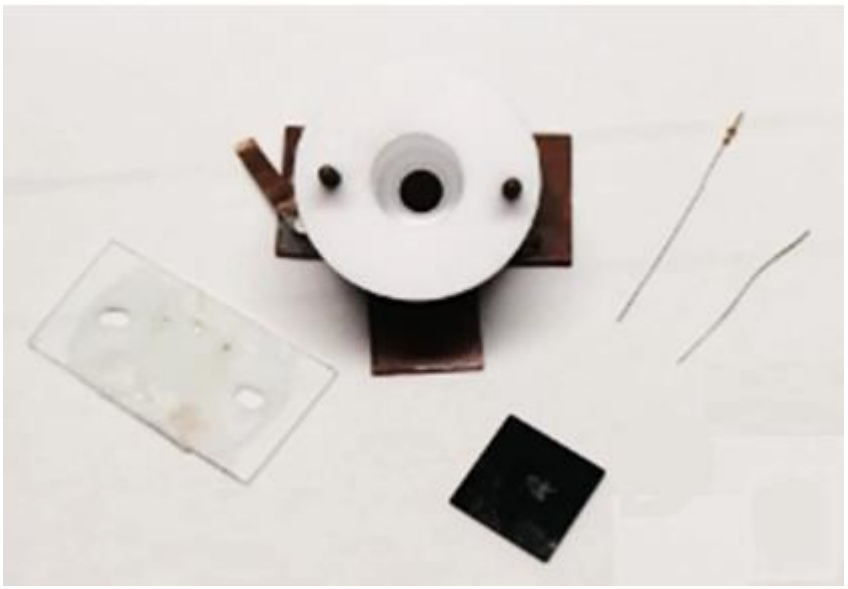
C, H, N, S measurements were performed with a Thermo Electron Analyser CHNS Flash 2000 analyser.

1.4. Cyclic voltammetry

Cyclic voltammetry was performed using a Biologic SP-150 potentiostat with a positive feedback compensation. Samples were dissolved in dichloromethane (HPLC grade, Carlo Erba) or in THF (HPLC grade, Carlo Erba, dried with SPBT-1 Benchtop Solvent Purification System). Tetrabutylammonium hexafluorophosphate (0.1 M as supporting electrolyte) was purchased from Sigma-Aldrich. Experiments were carried out in a one-compartment cell equipped with platinum working microelectrode (Ø = 2 mm) (WE) and a platinum wire counter electrode (CE). A silver wire immersed in 0.10 M Bu_4NPF_6/ACN was used as reference electrode (RE) and checked against ferrocene/ferrocenium couple (Fc/Fc^+) before and after each experiment.

1.5. Solid state cyclic voltammetry

Solid-state cyclic voltammetry was performed using a cylindrical Teflon cell featuring a hole (0.4 cm diameter) in the bottom in a vertical configuration. A glassy carbon plate was used as the WE and tightened from below. The cell was tightened on a copper plate as the electrical contact. A Pt wire and Ag wire were used as counter electrode (CE) and reference electrode (RE) respectively and placed at the top of the cylinder in contact with the electrolytic solution (0.1 M $TBAPF_6$ in ACN). The solid was placed over the WE and covered with a Nafion membrane (Nafion™ 117 from Sigma-Aldrich) to prevent the direct contact between the solid and the electrolytic solution.



Solid-state electrochemical configuration.

1.6. X-Ray Diffraction

Single crystals of the compounds were mounted on glass fibre loops using a viscous hydrocarbon oil to coat the crystal and then transferred directly to cold nitrogen stream for data collection. Data collection were performed on an Agilent Supernova with CuKα 172 (λ = 1.54184 Å). The structures were solved by direct methods with the ShelXT program and refined against all F2 values with the SHELXL-2013 program[1] using the Olex2 graphical user interface.[2]

1.7. Single Crystal Conductivity Measurements

Electrical conductivity measurements at room temperature were performed in two points on 0.2 to 0.3 mm long single crystals. Gold wires were glued with silver paste on both ends of the crystals. A Keithley 486 picoammeter was used to apply a constant voltage (up to 30 V) and measure the current.

1.8. Raman measurements

Crystalline samples selected for Raman measurements were between 0.1 and 0.2 mm in length. Raman spectra in the range 1100–1700 cm^{-1} were measured at room temperature using Renishaw inVia Raman microscope equipped with a thermoelectrically (TE)-cooled CCD detector and semiconductor laser emitting light in the near-infrared region at 785 nm wavelength. Low-frequency Raman spectra were measured at room temperature in a backward scattering geometry with a LABRAM HR800 Raman spectrometer equipped with a microscope and a He–Ne λ=632.8 nm laser line.

---

[1] Sheldrick, G. M. *Acta Cryst.* **2008**, *A64,* 112-122.
[2] Dolomanov, O. V.; Bourhis, L. J.; Gildea, R. J.; Howard, J. A. K.; Puschmann, H. *J. Appl. Crystallogr*. **2009**, *42* (2), 339–341.

1.9. Computational methods

Theoretical calculations of normal vibrational modes for the BVDT-TTF-Py_4 isolated molecule were performed with Gaussian 03,[3] using the standard 6-31++G(d,p) basis set and the hybrid density functional (B3LYP). The initial geometry used in calculations was prepared based on the experimental X-ray data. The result of the structure optimization corresponds to energy minima since no imaginary frequencies were found. On the basis of the optimized structure, vibrational frequencies as well as Raman scattering activities were calculated. The frequencies computed with a quantum harmonic oscillator approximation tend to be higher than experimental ones, and the scaling factor 0.9614 has been applied.[4]

1.10. Band structure calculations

The first-principles calculations for the solid were carried out using a numeric atomic orbitals density functional theory (DFT) approach[5,6] developed for efficient calculations in large systems and implemented in the SIESTA code.[7,8] The generalized gradient approximation (GGA) to DFT was used and, in particular, the functional of Perdew, Burke, and Ernzerhof.[9] To study the relative energies of states with localized electrons, spin polarized band calculations have been undertaken. All calculations included a Hubbard correction term U_{eff} = U–J = 6.0 eV for the S 3p states.[10,11] Only the valence electrons are considered in the calculation, with the core being replaced by norm-conserving scalar relativistic pseudopotentials[12] factorized in the Kleinman-Bylander form.[13] A split-valence double-ζ basis set was used, including polarization orbitals with an energy shift of 10 meV for S, C, N, Cl,

---

[3] Gaussian 03, (Revision D.01), Frisch, M. J.; Trucks, G. W.; Schlegel, H. B.; Scuseria, G. E.; Robb, M. A.; Cheeseman, J. R.; Montgomery, Jr., J. A.; Vreven, T.; Kudin, K. N.; Burant, J. C.; Millam, J. M.; Iyengar, S. S.; Tomasi, J.; Barone, V.; Mennucci, B.; Cossi, M.; Scalmani, G.; Rega, N.; Petersson, G. A.; Nakatsuji, H.; Hada, M.; Ehara, M.; Toyota, K.; Fukuda, R.; Hasegawa, J.; Ishida, M.; Nakajima, T.; Honda, Y.; Kitao, O.; Nakai, H.; Klene, M.; Li, X.; Knox, J. E.; Hratchian, H. P.; Cross, J. B.; Bakken, V.; Adamo, C.; Jaramillo, J.; Gomperts, R.; Stratmann, R. E.; Yazyev, O.; Austin, A. J.; Cammi, R.; Pomelli, C.; Ochterski, J. W.; Ayala, P. Y.; Morokuma, K.; Voth, G. A.; Salvador, P.; Dannenberg, J. J.; Zakrzewski, V. G.; Dapprich, S.; Daniels, A. D.; Strain, M. C.; Farkas, O.; Malick, D. K.; Rabuck, A. D.; Raghavachari, K.; Foresman, J. B.; Ortiz, J. V.; Cui, Q.; Baboul, A. G.; Clifford, S.; Cioslowski, J.; Stefanov, B. B.; Liu, G.; Liashenko, A.; Piskorz, P.; Komaromi, I.; Martin, R. L.; Fox, D. J.; Keith, T.; Al-Laham, M. A.; Peng, C. Y.; Nanayakkara, A.; Challacombe, M.; Gill, P. M. W.; Johnson, B.; Chen, W.; Wong, M. W.; Gonzalez, C.; Pople, J. A.; Gaussian, Inc. Wallingford CT, **2004**.
[4] Scott, A. P.; Radom, L.; *J. Phys. Chem.* **1996**, *100*, 16502– 16513.
[5] Hohenberg, P.; Kohn, W. *Phys. Rev.* **1964**, *136*, B864– B871
[6] Kohn, W.; Sham, L. J. *Phys. Rev.* **1965**, *140*, A1133– A1138.
[7] Soler, J. M.; Artacho, E.; Gale, J. D.; García, A.; Junquera, J.; Ordejón, P.; Sánchez-Portal, D. *J. Phys. Condens. Matter* **2002**, *14*, 2745– 2779.
[8] Artacho, E.; Anglada, E.; Diéguez, O.; Gale, J. D.; García, A.; Junquera, J.; Martin, R. M.; Ordejón, P.; Pruneda, J. M.; Sánchez-Portal, D.; Soler, J. M. *J. Phys. Condens. Matter* **2008**, *20*, 064208.
[9] Perdew, J. P.; Burke, K.; Ernzerhof, M. *Phys. Rev. Lett.* **1996**, *77*, 3865– 3868.
[10] Dudarev, S. L.; Botton, G. A.; Savrasov, S. Y.; Humphreys, C. J.; Sutton, A. P. *Phys. Rev. B* **1998**, *57*, 1505–1509.
[11] Kiyota, Y.; Jeon, I.-R.; Jeannin, O.; Beau, M.; Kawamoto, T.; Alemany, P.; Canadell, E.; Mori, T.; Fourmigué, M. *Phys. Chem. Chem. Phys.* **2019**, *21,* 22639– 22646.
[12] Troullier, N.; Martins, J. L. *Phys. Rev. B* **1991**, *43*, 1993– 2006.
[13] Kleinman, L.; Bylander, D. M. *Phys. Rev. Lett.* **1982**, *48*, 1425– 1428.

I, Cd and H atoms.[14] The energy cut-off of the real space integration mesh was 350 Ry. The Brillouin zone was sampled using grids of (7×7×7) k-points.[15]

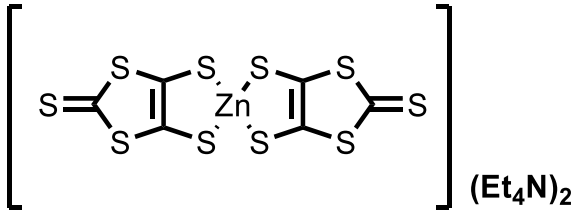
The Brillouin zone was sampled using grids[15] of (15×5×10) *k*-points for EVT-TTF(ClO_4) and BVDT-TTF(TaF_6). For $(BVDT\text{-}TTF)_{2.5}(I_3)$ (15×10×5), (10×7×15) and (10×1×1) *k*-point grids were used for calculations with a single cell, 2a double cell and single chains along *a*.

[14] Artacho, E. ; Sánchez-Portal, D.; Ordejón, P.; García, A.; Soler, J. M. *Phys. Status Solidi B* **1999**, *215*, 809–817.

[15] Monkhorst, H. J.; Pack, J. D. *Phys. Rev. B* **1976**, *13*, 5188– 5192.

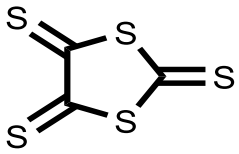
2. Experimental Procedures

Compound 1 : Bis(tetraethylammonium)bis(1,3-dithiole-2-thione-4,5-dithiolato) zincate



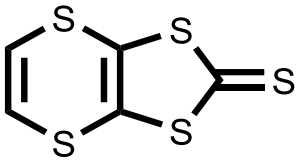
Synthesized according to the reported procedure.[16]

Compound 2 : 1,3-dithiolane-2,4,5-trithione



Synthesized according to the reported procedure.[16]

Compound 3 : [1,3]dithiolo[4,5-b][1,4]dithiine-2-thione, VDT



Compound **2** (3 g, 0.015 mol, 1 equiv.) was added into a round-bottom flask containing xylene (140 mL). Vinylsulfinylbenzene (2.28 g, 0.015 mol, 1 equiv.) was introduced and the mixture was heated for 5 hours at 120 °C. The solvent was removed under reduced pressure and the product was purified by column chromatography using petroleum ether: dichloromethane (2:1) to afford **3** as a brown solid (0.883 g, 25%).

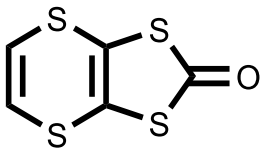
^{1}H NMR (300 MHz, $CDCl_3$): δ (ppm) 6.64 (s, 2H).

^{13}C NMR (76 MHz, $CDCl_3$): δ (ppm) 214.35, 126.99, 124.39.

MS (EI) m/z**:** 221.8754, $M_{theo.}$ ($C_5H_2S_5$) = 221.8750.

[16] Svenstrup, N.; Becher, J. *Synth.* **1995**, *1995*(3), 215-235.

Compound 4 : [1,3]dithiolo[4,5-b][1,4]dithiin-2-one



Compound **3** (0.83 g, 3.74 mmol, 1 equiv.) and Mercury (II) acetate (2.66 g, 8.35 mmol, 2.22 equiv.) were suspended in chloroform (100 mL) and acetic acid (100 mL). The reaction mixture was stirred for 3 hours at room temperature. The white precipitate was filtered through Celite and the filtrate was washed with water (2 x 100 mL), then treated with a saturated solution of $NaHCO_3$ (100 mL), and dried with $MgSO_4$. After evaporating the solvent, the product was purified by flash column chromatography using petroleum ether: DCM (1:1) to afford **4** as a yellowish solid (0.54 g, 70%).

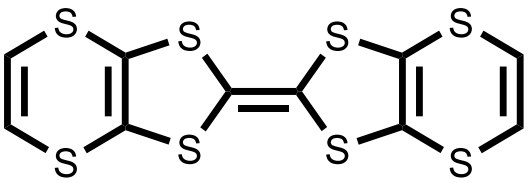
^{1}H NMR (300 MHz, $CDCl_3$): δ (ppm) 6.62 (s, 2H).

^{13}C NMR (76 MHz, $CDCl_3$): δ (ppm) 192.43, 124.05, 117.31.

MS (MALDI-TOF) m/z**:** 205.8983, $M_{theo.}$ ($C_5H_2OS_4$) = 205.8975.

Elemental analysis calcd. (%): C 29.11; H 0.98; O 7.75 ; S 62.16; found: C 28.70; H 0.98; O 7.51 ; S 62.11.

Compound 5 : 2,2'-bi[1,3]dithiolo[4,5-b][1,4]dithiinylidene, BVDT-TTF



Compound **4** (0.4 g, 1.94 mmol, 1 equiv.) was dissolved in triethyl phosphite (10 mL) in a Schlenk flask under an argon atmosphere and refluxed. An orange precipitate was observed after 1 h, and the reaction was maintained at this temperature for five hours. The reaction was cooled down to room temperature and methanol (5 mL) was added. The resulting precipitate was isolated through filtration and subsequently washed with diethyl ether (15 mL) to obtain **4** (0.27 g, 70 %).

^{1}H NMR (300 MHz, $CDCl_3$): δ (ppm) 6.55 (s, 4H).

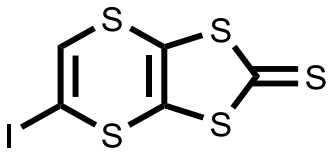
^{1}H NMR (300 MHz, DMSO-d_6): δ (ppm) 6.90 (s, 4H).

The compound was not soluble enough in any of the usual deuterated solvents for ^{13}C NMR analysis.

MS (MALDI-TOF) m/z**:** 379.8074, $M_{theo.}$ ($C_{10}H_4S_8$) = 379.8073.

Elemental analysis calcd. (%): C 31.56; H 1.06; S 67.38; found: C 31.13; H 1.35; S 66.11.

Compound 6 : 5-iodo-[1,3]dithiolo[4,5-b][1,4]dithiine-2-thione

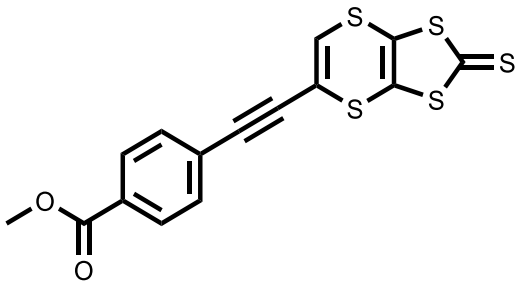


To a −78 °C cooled solution of the compound **3** (100 mg, 0.45 mmol, 1 equiv.) in 15 mL of dry THF was added a solution of freshly prepared LDA (2.1 equiv., diisopropylamine (96 µL, 0.945 mmol) and 1.6 M n-BuLi in hexane (0.58 mL, 0.945 mmol) in 10 ml of dry THF). The reaction mixture was stirred for 30 min at −78 °C and perfluorohexyl iodide (1.1 mL, 5.2 mmol, 2.1 equiv.) was added. The mixture was stirred overnight at room temperature. The solvent was removed under reduced pressure. The concentrated solution was purified by chromatography on silica gel using petroleum ether: DCM (3:1) as eluent to yield a mixture of **6** and **3** (1:0.31 ratio according to NMR), (23 mg, 15.25% of **6** and 4.7 mg, 4.7% of **3**).

^{1}H NMR (300 MHz, $CDCl_3$): δ (ppm) mix of product 6.86 (s, 1 H) and starting 6.64 (s, 2H) ratio 1 : 0.31.

MS (MALDI-TOF) m/z**:** 347.77, $M_{theo.}$ (C_5HIS_5) = 347.77.

Compound 7 : Methyl 4-((2-thioxo-[1,3]dithiolo[4,5-b][1,4]dithiin-5-yl)ethynyl)benzoate



Compound **6** (76 mg, 0.22 mmol, 1 equiv., mixture with compound **3**), methyl 4-ethynylbenzoate (56 mg, 0.35 mmol, 1.59 equiv.), $Pd(PPh_3)_4$ (25 mg, 10% mol) and CuI (4 mg, 10% mol) were added into a Schlenk flask containing Et_3N (10 mL) and Toluene (10 mL). The suspension was degassed with Argon for 15 min and stirred at 70° for 2 days. The solvent was removed under reduced pressure and the resulting solid was dissolved in DCM (40 mL), washed with water (50 mL) and brine (50 mL), and dried with $MgSO_4$. The residue was purified by chromatography on silica gel using petroleum ether: DCM (2:1) to afford compound **7** (25 mg, 30%).

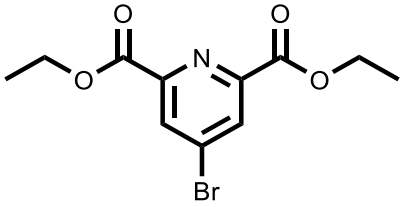
^{1}H NMR (300 MHz, $CDCl_3$): δ (ppm) 8.02 (d, J = 8.7 Hz, 2H), 7.53 (d, J = 8.7 Hz, 2H), 6.94 (s, 1H), 3.93 (s, 3H).

^{13}C NMR (76 MHz, $CDCl_3$): δ (ppm) 213.14, 166.26, 131.73, 130.68, 129.65, 128.64, 128.16, 127.35, 125.95, 121.12, 93.28, 85.71, 52.43.

MS (MALDI-TOF) m/z**:** 379.9132, $M_{theo.}$ ($C_{15}H_8O_2S_5$) = 379.9128.

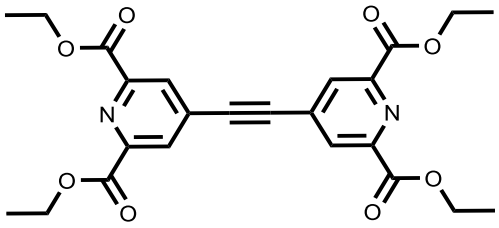
Elemental analysis calcd. (%): $C_{15}H_8O_2S_5$ ($CHCl_3$) C 38.44; H 1.81; O 6.40; S 37.07 found: C 38.89; H 2.16; S 37.11.

Compound 8 : Diethyl 4-bromopyridine-2,6-dicarboxylate



Synthesized according to the reported procedure.[17]

Compound 9 : Tetraethyl 4,4'-(ethyne-1,2-diyl)bis(pyridine-2,6-dicarboxylate)

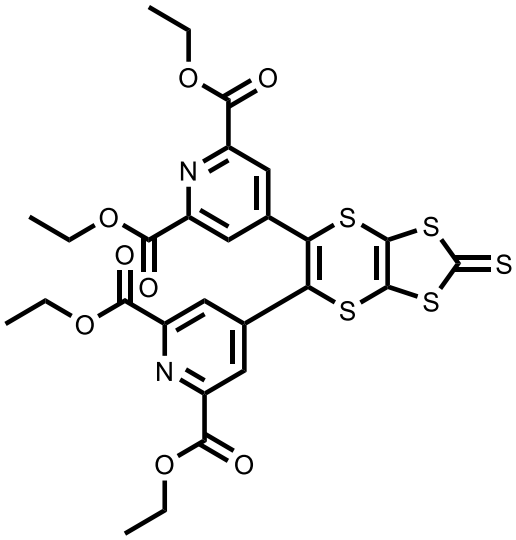


Compound **8** (5.4 g, 0.02 mol, 1 equiv.), $PdCl_2(PPh_3)_2$ (0.45 g, 6 mol%) and CuI (0.68 g, 18 mol%) were dissolved in a mixture of Et_3N (10 mL) and dry THF (50 mL) into a Schlenk flask. The solution was degassed for 15 min, then trimethylsilylacetylene (1.36 mL, 0.01 mol, 0.5 equiv.) was added and the mixture was stirred for 4 hours at 70°C. TBAF (1 M, 20 mL, 0.02 mol, 1 equiv.) was added and the reaction monitored by TLC. After 2 days at 70°C, the reaction was cooled to room temperature and the beige precipitate was filtered and washed with 50 mL of THF (2.67 g, 57%).

^{1}H NMR (300 MHz, $CDCl_3$): δ (ppm) 8.39 (s, 4H), 4.52 (q, J = 7.1 Hz, 8H), 1.48 (t, J = 7.1 Hz, 12H).
^{13}C NMR (76 MHz, $CDCl_3$): δ (ppm) 164.03, 149.35, 132.40, 129.66, 91.30, 62.81, 14.35.
MS (MALDI-TOF) m/z: 491.1424; $M_{theo.}$ ($C_{24}H_{24}N_2O_8Na_1$) = 491.1429.

[17] Nettekoven, M.; Jenny, C. *Org. Process Res. Dev.* **2003**, *7* (1), 38–43.

Compound 10 : Tetraethyl 4,4'-(2-thioxo-[1,3]dithiolo[4,5-b][1,4]dithiine-5,6-diyl)bis(pyridine-2,6-dicarboxylate)



A mixture of **9** (2 g, 4.27 mmol, 1 equiv.) and **2** (4.18 g, 21 mmol, 5 equiv.) in toluene (70 mL) was refluxed overnight into a Schlenk flask under Argon. The mixture was cooled to room temperature and the solution was evaporated and purified by column chromatography using petroleum ether: DCM (2:1) to afford the compound **10** as a brown solid (2 g, 70%).

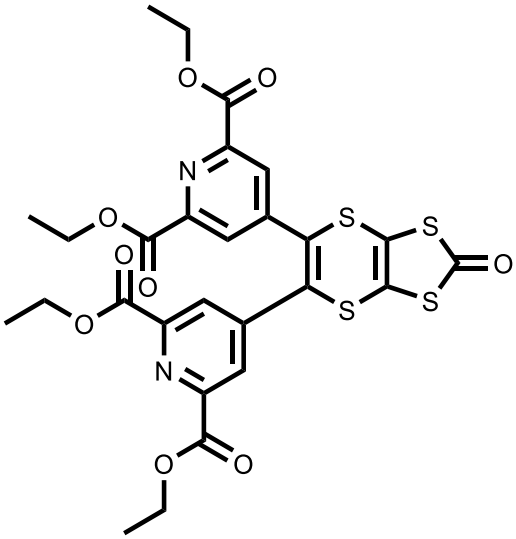
^{1}H NMR (300 MHz, $CDCl_3$): δ (ppm) 7.98 (s, 4H), 4.43 (q, J = 7.1 Hz, 8H), 1.41 (t, J = 7.1 Hz, 12H).

^{13}C NMR (76 MHz, $CDCl_3$): δ (ppm) 212.1, 163.69, 148.79, 145.70, 135.98, 128.52, 127.48, 62.87, 14.27.

MS (MALDI-TOF) m/z: 664.0129 M_{theo}. ($C_{27}H_{24}N_2O_8S_5$) =664.0136.

Elemental analysis calcd. (%): C 48.78; H 3.64; N 4.21; O 19.25; S 24.11 found C 48.99; H 3.90; N 3.84 S 25.30.

Compound 11 : Tetraethyl 4,4'-(2-oxo-[1,3]dithiolo[4,5-b][1,4]dithiine-5,6-diyl)bis(pyridine-2,6-dicarboxylate)



Mercuric acetate (1.86 g, 5.85 mmol, 3.9 equiv.) was added to a solution of **10** (1 g, 1.5 mmol, 1 equiv.) in chloroform (24 mL). The mixture was stirred for 4 hours at room temperature. The white precipitate was filtered off on Celite and the filtrate was washed with water (2 x 80 mL) and saturated $NaHCO_3$ (80 mL) and dried with $MgSO_4$. After removing the solvent under reduced pressure, the product was purified by flash column chromatography using petroleum ether: DCM (1:2) to afford **11** as a yellowish solid (0.84 g, 86%).

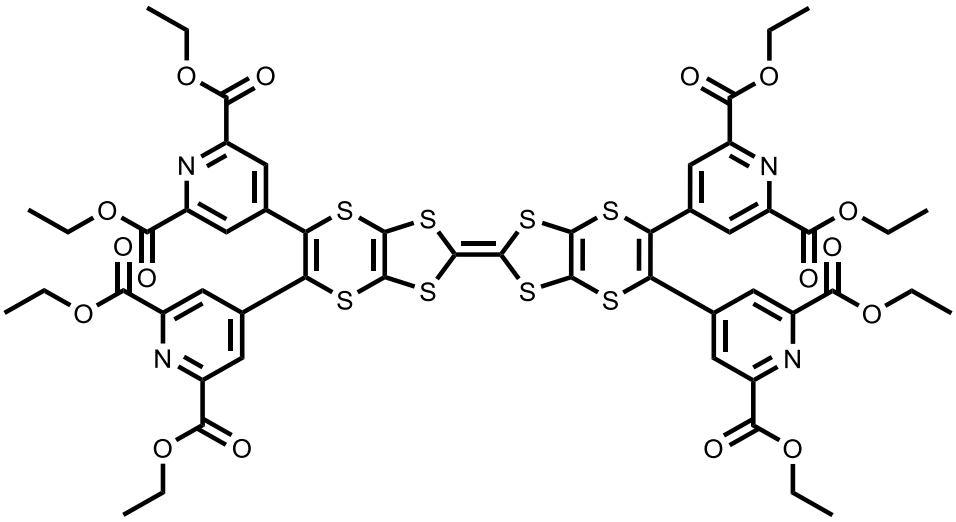
^{1}H NMR (300 MHz, $CDCl_3$): δ (ppm) 7.98 (s, 4H), 4.42 (q, J = 7.1 Hz, 8H), 1.38 (t, J = 7.4 Hz, 12H).

^{13}C NMR (76 MHz, $CDCl_3$): δ (ppm) 190.61, 163.68, 149.88, 145.75, 135.77, 127.25, 120.19, 62.87, 14.23.

MS (MALDI-TOF) m/z: 671.0260 ; $M_{theo.}$ ($C_{27}H_{24}N_2O_9S_4Na_1$) = 671.0256.

Elemental analysis calcd. (%): C 49.99; H 3.73; N 4.32; O 22.20; S 19.77 ; found C 50.10; H 2.98; N 4.99; S 19.32.

Compound 12 : Octaethyl 4,4',4'',4'''-([2,2'-bi[1,3]dithiolo[4,5-b][1,4]dithiinylidene]-5,5',6,6' tetrayl)tetrakis(pyridine-2,6-dicarboxylate)



Compound **11** (0.41 g, 0.63 mmol) was heated in triethyl phosphite (4 mL) under Argon at 110 °C for five hours into a Schlenk flask. The reaction was cooled down to room temperature and diethyl ether (3 mL) was added into the solution. The resulting orange precipitate was filtered, and then it was washed once with 15 mL of diethyl ether to afford **12** as an orange solid (0.06 g, 15 %).

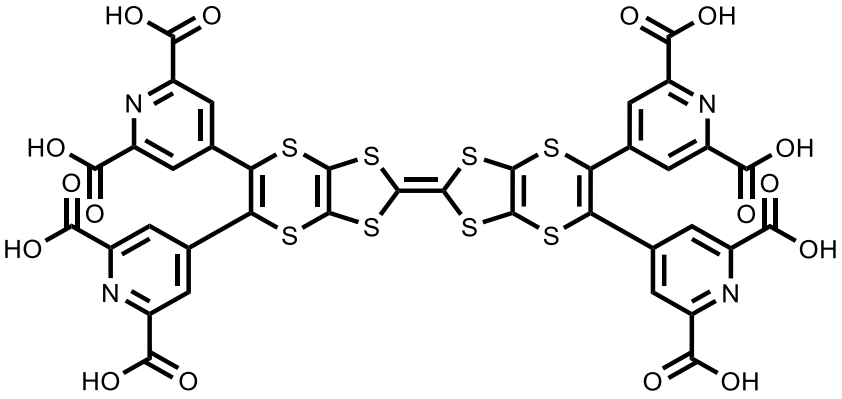
^{1}H NMR (300 MHz, $CDCl_3$): δ (ppm) 7.98 (s, 8H), 4.43 (q, J = 7.1 Hz, 16H), 1.41 (t, J = 7.1 Hz, 24H).

^{13}C NMR (76 MHz, $CDCl_3$): δ (ppm) 163.78, 149.69, 146.05, 136.58, 127.50, 122.77, 119.72, 62.86, 14.27.

MS (MALDI-TOF) m/z: 1264.0825; $M_{theo.}$ ($C_{54}H_{48}N_4O_{16}S_8$) = 1264.0834.

Elemental analysis calcd. (%): C 51.25; H 3.82; N 4.43; O 20.23; S 20.27 found C 51.85; H 3.87; N 4.02; S 20.01.

Compound 13 : 4,4',4'',4'''-(3a,3'a,7a,7'a-tetrahydro-[2,2'-bi[1,3]dithiolo[4,5-b][1,4]dithiinylidene]-5,5',6,6'-tetrayl)tetrakis(pyridine-2,6-dicarboxylic acid)



A solution of compound **13** (0.14 g, 0.11 mmol, 1 equiv) in THF (8 mL) was combined with a 4 mL aqueous solution of LiOH (0.113 g, 4.7 mmol, 43 equiv.) into a Schlenk flask. The mixture was refluxed for 1 night. The THF was removed under reduced pressure and the oily residue oil was dissolved in water (5 mL). The aqueous solution was adjusted to a pH of 5 by addition of 1 M HCl, leading to the precipitation of a black solid that was filtered and dried (57 mg, 50%).

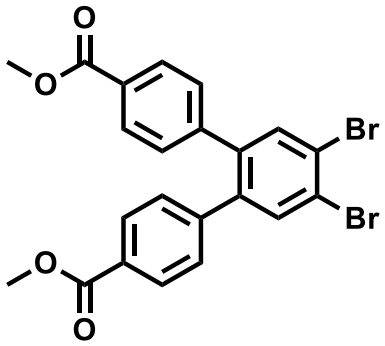
^{1}H NMR (300 MHz, DMSO-d_6): δ (ppm) 8.03 (s, 8H).

The compound was not soluble enough in any of the usual deuterated solvents for ^{13}C NMR analysis.

MS (MALDI-TOF) m/z: 1039.8369 ; $M_{theo.}$ ($C_{38}H_{16}N_4O_{16}S_8$) = 1039.8327.

Elemental analysis calcd. (%): C 43.84; H 1.55; N 5.38; O 24.59; S 24.64 found C 43.12; H 1.55; N 4.98; S 23.95.

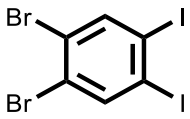
Compound 14 : Dimethyl 4',5'-dibromo-[1,1':2',1''-terphenyl]-4,4''-dicarboxylate



Synthesized according to the reported procedure.[18]

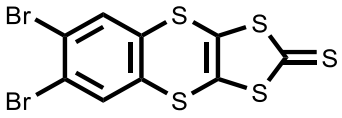
[18] Hisaki, I.; Nakagawa, S.; Tohnai, N.; Miyata, M. *Angew. Chem. Int. Ed.* **2015**, *54* (10), 3008–3012.

Compound 15 : 1,2-dibromo-4,5-diiodobenzene



Synthesized according to the reported procedure.[19]

Compound 16 : 6,7-dibromobenzo[b][1,3]dithiolo[4,5-e][1,4]dithiine-2-thione



Compound **1** (2.13 g, 2.98 mmol, 1 equiv.), compound **15** (3.94 g, 8.13 mmol, 2.73 equiv.), Cu_2O (85 mg, 0.59 mmol, 20 mol%), ethyl acetoacetate (0.15 mL, 1.19 mmol, 40 mol%), and DMF (6 mL) were placed in a Schlenk flask and heated at 120 °C for one night. The mixture was cooled down to room temperature and poured into dichloromethane (30 mL). The resulting mixture was washed with water (100 mL) and brine (100 mL), and then dried over $MgSO_4$.The crude product was purified by column chromatography on silica gel using petroleum ether: DCM (3:1) to afford **16** as a yellow solid (0.5 g, 20 %).

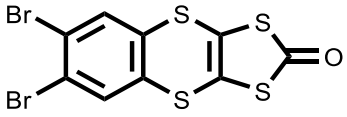
^{1}H NMR (300 MHz, $CDCl_3$): δ (ppm) 7.72 (s, 2H).

^{13}C NMR (76 MHz, $CDCl_3$): δ (ppm) 211.64, 134.78, 133.17, 130.17, 125.54.

MS (MALDI-TOF) m/z**:** 427.7111, $M_{theo.}$ ($C_9H_2Br_2S_5$) = 427.7127.

Elemental analysis calcd. (%): C 25.13; H 0.47; Br 37.15; S 37.26 ; found C 25.13; H 0.52; S 37.14.

Compound 17 : 6,7-dibromobenzo[b][1,3]dithiolo[4,5-e][1,4]dithiin-2-one



Compound **16** (1.6 g, 3.75 mmol, 1 equiv.) and Mercury (II) acetate (4.66 g, 14.6 mmol, 3.9 equiv.) were poured in chloroform (100 mL) into a round-bottom flask. The mixture was stirred for 3 hours at room temperature. The white precipitate was filtered off on Celite and the filtrate was washed with water (2 x 100 mL) and saturated $NaHCO_3$ (100 mL), and dried with $MgSO_4$. After evaporating the solvent, the product was purified by flash column chromatography using petroleum ether: DCM (2:1) to afford **17** as a yellowish solid (1.24 g, 80%).

^{1}H NMR (300 MHz, $CDCl_3$): δ (ppm) 7.74 (s, 2H).

---

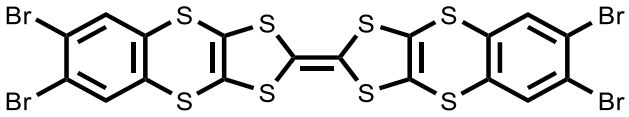
[19] Juríček, M.; Kouwer, P. H. J.; Rehák, J.; Sly, J.; Rowan, A. E. *J. Org. Chem.* **2009**, *74* (1), 21–25.

^{13}C NMR (76 MHz, $CDCl_3$): δ (ppm) 187.31, 134.4, 130.00, 123.10, 121.23.

MS (MALDI-TOF) m/z**:** 411.7361, $M_{theo.}$ ($C_9H_2Br_2OS_4$) = 411.7355.

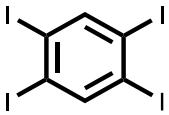
Elemental analysis calcd. (%): C 26.10; H 0.49; Br 38.59; O 3.86; S 30.96 ; found C 25.13; H, 0.52; S 31.16.

Compound 18 : 6,6',7,7'-tetrabromo-2,2'-bibenzo[b][1,3]dithiolo[4,5-e][1,4]dithiinylidene



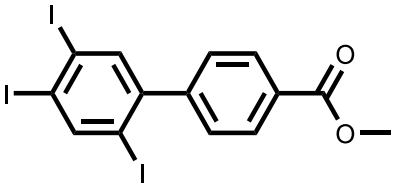
Compound **17** (0.3 g, 0.72 mmol, 1 equiv.) was dissolved in trimethyl phosphite (4 mL, 33.8 mmol., 47 equiv.) into a Schlenk flask. The suspension was degassed for 15 min and stirred at 120 °C. An orange precipitate was observed after 1 hour of reaction. The reaction was maintained at this temperature for one night. The reaction flask was cooled down to room temperature and 10 mL of diethyl ether were added into the flask. The solid was filtered and washed, one time, with diethyl ether (20 mL) to afford the compound **18** (0.05 g, 17%).
The compound was not soluble enough in any of the usual deuterated solvents for ^{1}H- and ^{13}C-NMR analysis.
MS (MALDI-TOF) m/z: 791.4806; $M_{theo.}$ ($C_{18}H_4Br_4S_8$) = 791.4889.
Elemental analysis calcd. (%): C 27.15; H 0.51; S 32.21; found: C 27.31; H 0.55; S 31.87.

Compound 19 : 1,2,4,5-tetraiodobenzene



Synthesized according to the reported procedure.[20]

Compound 20 : Methyl 2',4',5'-triiodo-[1,1'-biphenyl]-4-carboxylate



Compound **19** (3.66 g, 6.30 mmol, 1 equiv.), $Pd(PPh_3)_4$ (728 mg, 0.63 mmol, 10%mol), (4-(methoxycarbonyl)phenyl)boronic acid (1.7 g, 9.45 mmol, 1.5 equiv), and sodium carbonate (2 g, 18.9 mmol, 3 equiv.) were suspended in a mixture of toluene (50 mL), methanol (50 mL) and 1,4-dioxane (60 mL) into a

[20] Papke, Roger L.; Crooks, Peter A.; Dwoskin, Linda P.; Hernandez, Gretchen Lopez; Zhang, Zhenfa; Thinschmidt, Jeffrey S.; Zheng, Guangrong. Patent US 20090143424 2010-07-15

Schlenk flask. The solution was degassed with Argon for 15 min and stirred at 90° for one night. After cooling to room temperature, the solvents were removed under reduced pressure. The residue was dissolved in dichloromethane (50 mL), the solution was washed with water (50 mL) and brine (50 mL), and dried with $MgSO_4$. The organic phase was concentrated under reduced pressure and the obtained residue was purified by chromatography on silica gel using petroleum ether: DCM (1:2) to obtain the compound **20** (743 mg, 20%).

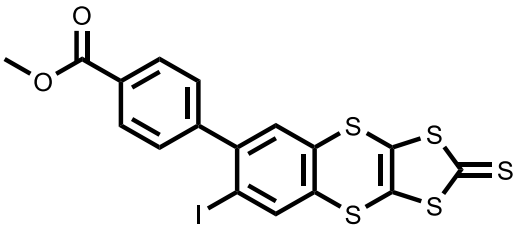
^{1}H NMR (300 MHz, $CDCl_3$): δ (ppm) 8.39 (s, 1H), 8.09 (d, J = 8.4 Hz, 2H), 7.74 (s, 1H), 7.37 (d, J = 8.2, 3.8 Hz, 2H), 3.94 (s, 3H).

^{13}C NMR (76 MHz, $CDCl_3$): δ (ppm) 166.69, 148.44, 146.85, 146.12, 139.66, 130.04, 129.60, 129.17, 108.34, 107.83, 98.05, 52.41.

MS (EI) m/z: 589.7715; $M_{theo.}$ ($C_{14}H_9I_3O_2$) = 589.7737.

Elemental analysis calcd. (%): C 28.50; H 1.54; found: C 29.33; H 1.58.

Compound 21 : Methyl 4-(7-iodo-2-thioxobenzo[b][1,3]dithiolo[4,5-e][1,4]dithiin-6-yl)benzoate



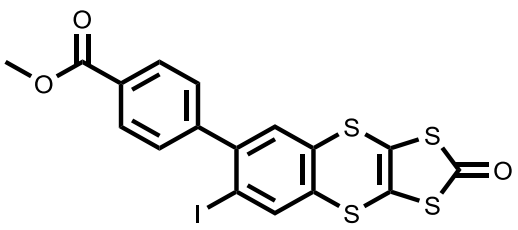
Compound **1** (2.13 g, 2.98 mmol, 1 equiv.), compound **19** (2.37 g, 4.47 mmol, 1.5 equiv.), Cu_2O (85 mg, 0.60 mmol, 20 mol%), and ethyl acetoacetate (0.15 mL, 1.19 mmol, 40 mol%) were placed in DMF (6 mL) under Argon into a Schlenk flask. The mixture was heated at 120 °C for four hours, then it was cooled down to room temperature and poured into DCM (30 mL). The resulting mixture was washed with water (100 mL) and brine (100 mL), and then dried over $MgSO_4$. The crude product was purified by column chromatography on silica gel using petroleum ether: DCM (5:1) to afford **21** as a yellow solid (0.5 g, 20%).

^{1}H NMR (300 MHz, $CDCl_3$): δ (ppm) 8.12 (d, J = 8.2 Hz, 2H), 8.07 (s, 1H), 7.39 (s, 1H), 7.38 (d, J = 7.7 Hz, 2H), 3.95 (s, 3H).

^{13}C NMR (76 MHz, $CDCl_3$): δ (ppm) 208.3, 167.49, 146.41, 143.21, 140.82, 139.18, 135.59, 135.12, 130.26, 129.75, 129.34, 123.75, 121.07, 98.31, 52.59.

MS (MALDI-TOF) m/z: 531.8299 ; $M_{theo.}$ ($C_{17}H_9IO_2S_5$) = 531.8251.

Compound 22 : Methyl 4-(7-iodo-2-oxobenzo[b][1,3]dithiolo[4,5-e][1,4]dithiin-6-yl)benzoate



Compound **21** (1.6 g, 3.75 mmol, 1 equiv.) and Mercury(II) acetate (4.66 g, 14.62 mmol, 3.9 equiv.) were placed in chloroform (100 mL). The solution was stirred for 3 hours at room temperature. The white precipitate was

filtered off on Celite and the filtrate was washed with water (2 x 40 mL) then once with saturated $NaHCO_3$ (40 mL) and dried with $MgSO_4$. The solvent was removed and the product was purified by flash column chromatography using petroleum ether: DCM (1:1) to afford **15** as a yellowish solid (1.24 g, 80%).

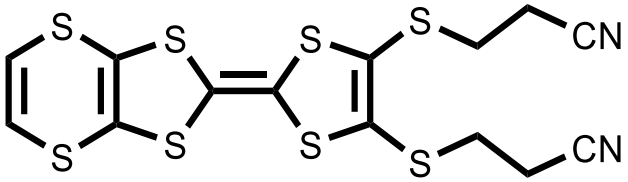
^{1}H NMR (300 MHz, $CDCl_3$): δ (ppm) 8.12 (d, J = 8.2 Hz, 2H), 8.07 (s, 1H), 7.40 (s, 1H), 7.38 (d, J = 7.7 Hz, 2H), 3.95 (s, 3H).

^{13}C NMR (76 MHz, $CDCl_3$): δ (ppm) 190.73, 166.02, 146.60, 146.13, 156.33, 139.07, 135.23, 134.89, 130.47, 129.71, 129.30, 129.01, 120.76, 121.02, 52.59.

MS (MALDI-TOF) m/z: 515.8482 ; $M_{theo.}$ ($C_{17}H_9IO_3S_4$) = 515.8479.

Elemental analysis calcd. (%): C 39.54; H 1.76; S 24.83; found: C 39.42; H 1.63; S 24.99.

Compound 24 : 3,3'-((2-([1,3]dithiolo[4,5-b][1,4]dithiin-2-ylidene)-1,3-dithiole-4,5 diyl)bis(sulfanediyl))dipropanenitrile



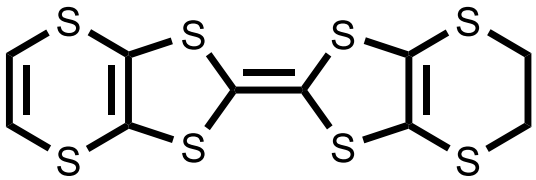
Compound **3** (0.83 g, 3.75 mmol, 1 equiv.), and 3,3'-((2-oxo-1,3-dithiole-4,5-diyl)bis(sulfanediyl))dipropanenitrile[21] (2.1 g, 7.5 mmol, 2 equiv.) were mixed under Argon in trimethyl phosphite (12 mL) in a Schlenk flask, and the mixture was heated at 110° for 2 hours. The precipitate was filtered off and the filtrate was evaporated to dryness. Co-evaporation with toluene was repeated four times (4 x 50 mL). The residue was submitted to column chromatography using dichloromethane as the eluent to afford **24** as an orange solid (0.61 g, 36%).

^{1}H NMR (300 MHz, $CDCl_3$): δ (ppm) 6.56 (s, 2H), 3.09 (t, J = 7.1 Hz, 4H), 2.74 (t, J = 7.1 Hz, 4H).

^{13}C NMR (76 MHz, $CDCl_3$): δ (ppm) 128.14, 124.78, 119.19, 118.12, 117.51, 113.06, 31.51, 19.05.

MS (MALDI-TOF) m/z: 461.8604 ; $M_{theo.}$ ($C_{14}H_{10}N_2S_8$)= 461.8605.

Compound 25 : 5,6-dihydro-2,2'-bi[1,3]dithiolo[4,5-b][1,4]dithiinylidene, EVT



Compound **24** (0.61 g, 1.59 mmol, 1 equiv.) was suspended in degassed THF (35 mL) under argon and a solution of NaOEt (1 M in EtOH, 4.77 mL, 3 equiv.) was added into a schlenk flask. After stirring at room temperature for

[21] Fang, Q.; Chen, H.; Lei, H.; Xue, G.; Chen, X. *CrystEngComm* **2015**, *17* (4), 787–796.

2 hours, a solution of 1,2-dibromoethane (0.32 g, 1.74 mmol, 1.1 eq) in THF (5 mL) was introduced. After 10 min., an orange precipitate appeared and the mixture was left overnight at RT. The solvent was removed under reduced pressure and the solid was washed with EtOH (0.47 g, 78%).

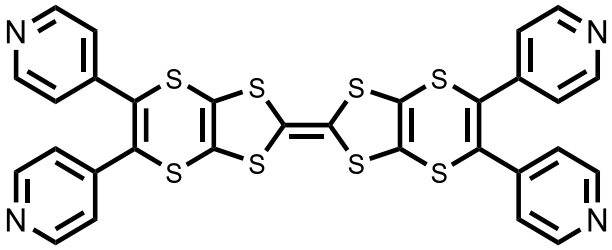
^{1}H NMR (300 MHz, $CDCl_3$): δ (ppm) 6.55 (s, 2H), 3.30 (s, 4H).

^{1}H NMR (500 MHz, DMSO): δ (ppm) 6.90 (s, 2H), 3.40 (s, 4H).

^{13}C NMR (126 MHz, DMSO): δ (ppm) 124.42, 118.57, 115.30, 113.15, 112.84, 29.55.

MS (MALDI-TOF) m/z: 381.8229; $M_{theo.}$ ($C_{10}H_6S_8$)= 381.8232.

Compound 26 : 5,5',6,6'-tetra(pyridin-4-yl)-2,2'-bi[1,3]dithiolo[4,5-b][1,4]dithiinylidenen, L



Synthesized according to the reported procedure.[22]

Compound L-$CdCl_2$:

Compound 26 (1 mg, 1.54×10^{-3} mmol) was dissolved in 1 mL of DCM and placed in a tube (13 cm height, 1 cm diameter). A buffer solution of DCM/MeOH 1/1 (0.5 mL) and a solution of metal CdCl2 (2 mg, 0.010 mmol) in MeOH (2 mL) were successively layered. After 5 days, red crystals appeared. The crystals were washed several times with ethanol and DCM.

Elemental analysis calcd. (%): $C_{30}H_{16}N_4S_8Cl_2Cd$, 2(CH_2Cl_2) theor.: C, 36.88; H, 1.93; N, 5.38; S, 24.61. Found: C, 36.40; H, 1.88; N, 5.20; S, 25.67.

Compound L-$HgCl_2$:

Compound 26 (1 mg, 1.54×10^{-3} mmol) was dissolvedin 1 ml of DCM and placed in a tube (13 cm height, 1 cm diameter). A buffer solution of DCM/MeOH 1/1 (0.5 mL) and a solution of metal $HgCl_2$ (2 mg, 7.36×10□ 3 mmol) in MeOH (2 mL) were successively layered. After 5 days, red crystals appeared. The crystals were washed several times with ethanol and DCM.

Elemental analysis calcd. (%): $C_{30}H_{16}N_4S_8Cl_2Hg$, (CH_2Cl_2) theor.: C, 35.62; H, 1.74; N, 5.36; S, 24.54. Found: C, 34.53; H, 1.67; N, 5.05; S, 24.70.

Compound L-$CuCl_2$:

[22] Brooks, A. C.; Day, P.; Dias, S. I. G.; Rabaça, S.; Santos, I. C.; Henriques, R. T.; Wallis, J. D.; Almeida, M. *Eur. J. Inorg. Chem.* **2009**, 10.

Compound 26 (1 mg, 1.54×10^{-3} mmol) was dissolved in 1 ml of $CHCl_3$ and placed in a tube (13 cm height, 1 cm diameter). A buffer solution of $CHCl_3$/MeOH 1/1 (0.5 mL) and a solution of metal $CuCl_2$ (2 mg, 0.014 mmol) in MeOH (2 mL) were successively layered. After 5 days, red crystals appeared. The crystals were washed several times with ethanol and $CHCl_3$.

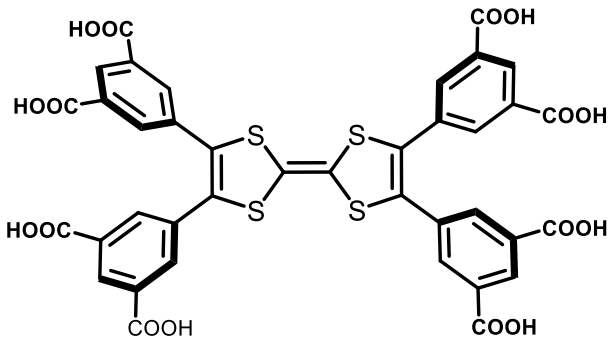
Elemental analysis calcd. (%): $C_{30}H_{16}N_4S_8Cl_2Cu$, ($CHCl_3$) theor.: C, 39.49; H, 1.82; N, 5.94; S, 27.21. Found: C, 39.58; H, 1.96; N, 5.63; S, 27.43.

Compound L-$ZnCl_2$:

Compound 26 (1 mg, 1.54×10^{-3} mmol) was dissolved in 1 ml of DCM and placed in a tube (13 cm height, 1 cm diameter). A buffer solution of DCM/MeOH 1/1 (0.5 mL) and a solution of metal ZnCl2 (2 mg, 0.014 mmol) in MeOH (2 mL) were successively layered. After 5 days, red crystals appeared. The crystals were washed several times with ethanol and DCM.

Elemental analysis calcd. (%): $C_{30}H_{16}N_4S_8Cl_2Zn$,3(CH_2Cl_2) theor.: C, 36.70; H, 2.05; N, 5.19; S, 23.75. Found: C, 35.05 H, 1.74; N, 5.12; S, 25.13.

Compound 27 : 5,5',5'',5'''-([2,2'-bi(1,3-dithiolylidene)]-4,4',5,5'-tetrayl)tetraisophthalic acid



Synthesized according to the reported procedure.[23]

Compound Zn_2-TTFOC :

Compound 27 (2 mg, $2.32\text{x}10^{-3}$ mmol, 1 equiv.) was dissolved in 1 mL of DMF. Subsequently, $Zn(NO_3)_2{\cdot}6H_2O$ (1.5 mg, 5.10×10^{-3} mmol, 2.2 equiv.) was dissolved in EtOH (0.5 mL) and H_2O (0.5 mL). Both solutions were combined in a Teflon liner, and a single drop of 12 M NaOH was introduced. The resulting mixture was placed in a Parr bomb and subjected to an oven at 120°C for 2 days. The resulting red crystals were retained within the solution.

Compound Ni_3-TTFOC :

[23] Su, J.; He, W.; Li, X.-M.; Sun, L.; Wang, H.-Y.; Lan, Y.-Q.; Ding, M.; Zuo, J.-L. *Matter* **2020**, *2* (3), 711–722.

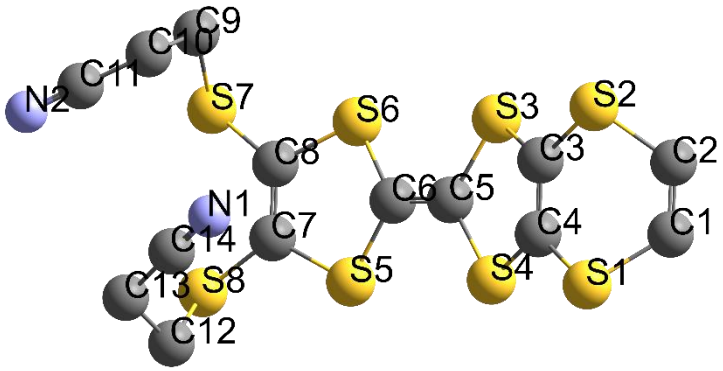
Compound 27 (2 mg, $2.32x10^{-3}$ mmol, 1 equiv.) was dissolved in 1 mL of DMF. Subsequently, $Ni(NO_3)_2 \cdot 6H_2O$ (1.38 mg, 5.10×10^{-3}, 2.2 equiv.) was dissolved in EtOH (0.5 mL) and H_2O (0.5 mL). Both solutions were combined in a Teflon liner, and a single drop of 12 M NaOH was introduced. The resulting mixture was placed in a Parr bomb and subjected to an oven at 120°C for 2 days. The resulting red crystals were retained within the solution.

Compound Cu_3-TTFOC :

Compound 27 (2 mg, $2.32x10^{-3}$ mmol, 1 equiv.) was dissolved in 1 mL of DMF. Subsequently, $Cu(NO_3)_2 \cdot H_2O$ (0.9 mg, 5.10×10^{-3}mmol, 2.2 equiv.) was dissolved in EtOH (0.5 mL) and H_2O (0.5 mL). Both solutions were combined in a Teflon liner, and a single drop of 12 M NaOH was introduced. The resulting mixture was placed in a Parr bomb and subjected to an oven at 120°C for 2 days. The resulting red crystals were retained within the solution.

3. Crystallographic Data

Compound 24 : 3,3'-((2-([1,3]dithiolo[4,5-b][1,4]dithiin-2-ylidene)-1,3-dithiole-4,5 diyl)bis(sulfanediyl))dipropanenitrile



Empirical formula	$C_{14}N_2S_8$
Formula weight	452.64
Temperature/K	290(3)
Crystal system	triclinic
Space group	P-1
a/Å	7.7102(5)
b/Å	11.3430(7)
c/Å	12.3103(8)
α/°	64.255(6)
β/°	84.672(5)
γ/°	77.483(5)
Volume/Å^3	946.70(11)
Z	2
ρ_{calc}/g·cm^{-3}	1.588
μ/mm^{-1}	8.739
F(000)	452.0
Crystal size/mm^3	0.26 × 0.15 × 0.09
Radiation	Cu Kα (λ = 1.54184)
2Θ range for data collection/°	7.974 to 101.556
Completeness to theta = 100.8°/%	99.9
Index ranges	-7 ≤ h ≤ 7, -11 ≤ k ≤ 11, -9 ≤ l ≤ 12
Reflections collected	3797
Independent reflections	1998 [R_{int} = 0.0256, R_{sigma} = 0.0284]
Data/restraints/parameters	1998/0/98
Goodness-of-fit on F^2	1.066
Final R indexes [I>=2σ (I)]	R_1 = 0.1046, wR_2 = 0.2780
Final R indexes [all data]	R_1 = 0.1069, wR_2 = 0.2807
Largest diff. peak/hole / e Å^{-3}	1.50/-1.49

Bond Lengths

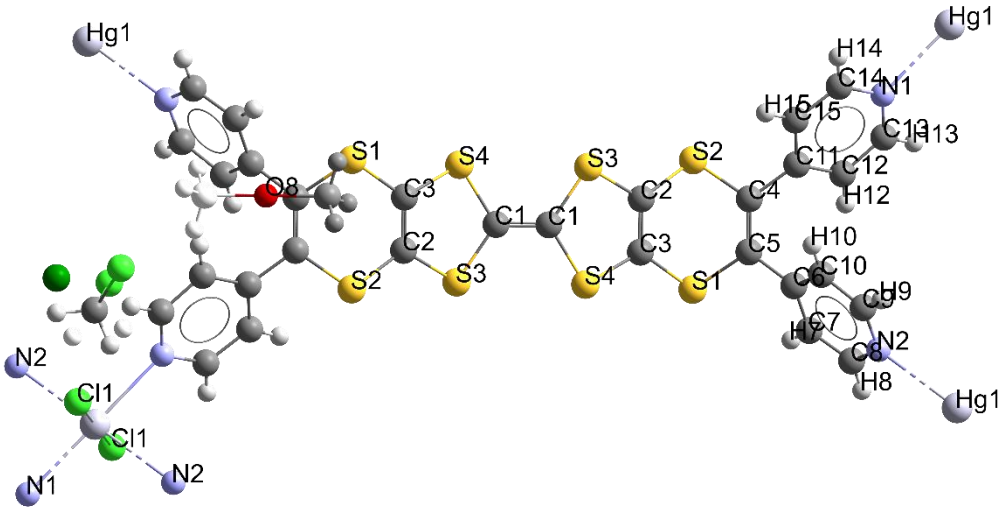
Atom	Atom	Length/Å	Atom	Atom	Length/Å
$S_{(3)}$	$C_{(5)}$	1.769(9)	$S_{(8)}$	$C_{(12)}$	1.819(12)
$S_{(3)}$	$C_{(3)}$	1.751(10)	$S_{(1)}$	$C_{(4)}$	1.727(10)
$S_{(5)}$	$C_{(7)}$	1.750(10)	$S_{(1)}$	$C_{(1)}$	1.773(11)
$S_{(5)}$	$C_{(6)}$	1.752(10)	$C_{(5)}$	$C_{(6)}$	1.341(14)
$S_{(6)}$	$C_{(8)}$	1.755(10)	$C_{(8)}$	$C_{(7)}$	1.352(14)
$S_{(6)}$	$C_{(6)}$	1.743(10)	$C_{(3)}$	$C_{(4)}$	1.347(14)
$S_{(4)}$	$C_{(5)}$	1.755(10)	$C_{(12)}$	$C_{(13)}$	1.549(18)
$S_{(4)}$	$C_{(4)}$	1.758(10)	$C_{(9)}$	$C_{(10)}$	1.518(17)
$S_{(2)}$	$C_{(3)}$	1.745(10)	$C_{(2)}$	$C_{(1)}$	1.308(15)
$S_{(2)}$	$C_{(2)}$	1.771(11)	$N_{(1)}$	$C_{(14)}$	1.139(15)
$S_{(7)}$	$C_{(8)}$	1.745(10)	$C_{(10)}$	$C_{(11)}$	1.441(19)
$S_{(7)}$	$C_{(9)}$	1.834(11)	$C_{(14)}$	$C_{(13)}$	1.441(19)
$S_{(8)}$	$C_{(7)}$	1.737(10)	$C_{(11)}$	$N_{(2)}$	1.154(18)

Bond Angles

Atom	Atom	Atom	Angle/°	Atom	Atom	Atom	Angle/°
$C_{(3)}$	$S_{(3)}$	$C_{(5)}$	94.1(5)	$S_{(6)}$	$C_{(6)}$	$S_{(5)}$	113.7(5)
$C_{(7)}$	$S_{(5)}$	$C_{(6)}$	94.7(5)	$C_{(5)}$	$C_{(6)}$	$S_{(5)}$	122.7(8)
$C_{(6)}$	$S_{(6)}$	$C_{(8)}$	94.6(5)	$C_{(5)}$	$C_{(6)}$	$S_{(6)}$	123.5(8)
$C_{(5)}$	$S_{(4)}$	$C_{(4)}$	94.4(5)	$S_{(2)}$	$C_{(3)}$	$S_{(3)}$	119.5(6)
$C_{(3)}$	$S_{(2)}$	$C_{(2)}$	99.2(5)	$C_{(4)}$	$C_{(3)}$	$S_{(3)}$	117.4(8)
$C_{(8)}$	$S_{(7)}$	$C_{(9)}$	103.0(5)	$C_{(4)}$	$C_{(3)}$	$S_{(2)}$	122.7(8)
$C_{(7)}$	$S_{(8)}$	$C_{(12)}$	102.7(5)	$S_{(1)}$	$C_{(4)}$	$S_{(4)}$	119.2(6)
$C_{(4)}$	$S_{(1)}$	$C_{(1)}$	99.1(5)	$C_{(3)}$	$C_{(4)}$	$S_{(4)}$	116.5(8)
$S_{(4)}$	$C_{(5)}$	$S_{(3)}$	113.0(5)	$C_{(3)}$	$C_{(4)}$	$S_{(1)}$	123.7(8)
$C_{(6)}$	$C_{(5)}$	$S_{(3)}$	123.3(8)	$C_{(13)}$	$C_{(12)}$	$S_{(8)}$	114.4(9)
$C_{(6)}$	$C_{(5)}$	$S_{(4)}$	123.6(8)	$C_{(10)}$	$C_{(9)}$	$S_{(7)}$	113.2(8)
$S_{(7)}$	$C_{(8)}$	$S_{(6)}$	117.1(5)	$C_{(1)}$	$C_{(2)}$	$S_{(2)}$	122.9(9)

Atom	Atom	Atom	Angle/°	Atom	Atom	Atom	Angle/°
$C_{(7)}$	$C_{(8)}$	$S_{(6)}$	116.8(8)	$C_{(2)}$	$C_{(1)}$	$S_{(1)}$	123.5(9)
$C_{(7)}$	$C_{(8)}$	$S_{(7)}$	125.2(8)	$C_{(11)}$	$C_{(10)}$	$C_{(9)}$	110.6(11)
$S_{(8)}$	$C_{(7)}$	$S_{(5)}$	118.0(6)	$N_{(1)}$	$C_{(14)}$	$C_{(13)}$	178.3(15)
$C_{(8)}$	$C_{(7)}$	$S_{(5)}$	116.6(8)	$C_{(14)}$	$C_{(13)}$	$C_{(12)}$	111.8(11)
$C_{(8)}$	$C_{(7)}$	$S_{(8)}$	124.8(8)	$N_{(2)}$	$C_{(11)}$	$C_{(10)}$	179.1(16)

BVDT-TTF-Py$_4$ -HgCl$_2$



Empirical formula	$C_{16.35}H_{10.96}Cl_3Hg_{0.5}N_2O_{0.35}S_4$
Formula weight	575.91
Temperature/K	150.00(10)
Crystal system	monoclinic
Space group	$P2_1/c$
a/Å	13.0601(3)
b/Å	9.7826(2)
c/Å	16.0640(3)
α/°	90
β/°	95.873(2)
γ/°	90
Volume/Å^3	2041.59(7)
Z	4
ρ_{calc}/g·cm^{-3}	1.874
μ/mm^{-1}	14.485
F(000)	1123.0
Crystal size/mm^3	0.271 × 0.108 × 0.091
Radiation	Cu Kα (λ = 1.54184)
2Θ range for data collection/°	6.804 to 152.756
Completeness to theta = 135.4°/%	100.0
Index ranges	-13 ≤ h ≤ 16, -11 ≤ k ≤ 12, -18 ≤ l ≤ 20
Reflections collected	9841
Independent reflections	4192 [R_{int} = 0.0324, R_{sigma} = 0.0380]
Data/restraints/parameters	4192/0/258
Goodness-of-fit on F^2	1.029
Final R indexes [I>=2σ (I)]	R_1 = 0.0354, wR_2 = 0.0936
Final R indexes [all data]	R_1 = 0.0391, wR_2 = 0.0985
Largest diff. peak/hole / e Å^{-3}	0.93/-2.30

Bond Lengths

Atom	Atom	Length/Å	Atom	Atom	Length/Å
Hg1	N1[1]	2.437(3)	C3	S4	1.754(4)
Hg1	N1	2.437(3)	C4	C5	1.334(7)
Hg1	Cl1	2.5286(10)	C4	C11	1.486(5)
Hg1	Cl1[1]	2.5286(10)	Cl4	C16A	1.729(7)
Hg1	N2[2]	2.547(3)	Cl4	C16B	1.729(7)
Hg1	N2[3]	2.547(3)	C5	C6	1.483(5)
S1	C3	1.747(4)	C6	C7	1.389(6)
S1	C5	1.791(4)	C6	C10	1.394(5)
N1	C13	1.331(5)	C7	C8	1.383(6)
N1	C14	1.342(5)	C9	C10	1.389(5)
C1	C1[4]	1.340(9)	C11	C12	1.393(5)
C1	S3	1.759(4)	C11	C15	1.389(6)
C1	S4	1.770(4)	C12	C13	1.391(5)
C2	S2	1.738(4)	C14	C15	1.390(5)
C2	S3	1.758(4)	O8	C17[5]	1.589(14)
C2	C3	1.340(7)	O8	C17	1.589(14)
S2	C4	1.769(4)	C17	Cl5A[6]	1.983(15)
N2	C8	1.342(5)	Cl5A	C16A	1.734(7)
N2	C9	1.329(5)	Cl5B	C16B	1.669(10)

[1]1-X,-Y,1-Z; [2]1-X,1-Y,1-Z; [3]+X,-1+Y,+Z; [4]2-X,1-Y,-Z; [5]2-X,1-Y,1-Z; [6]1+X,+Y,+Z

Bond Angles

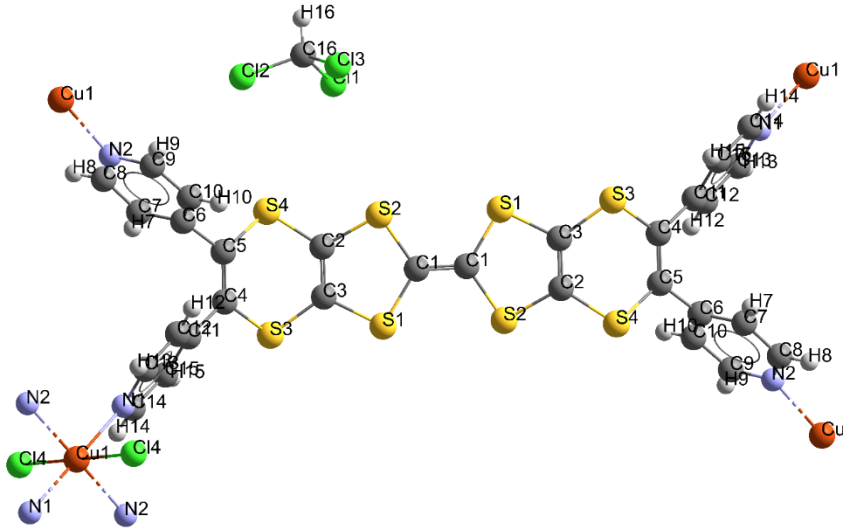
Atom	Atom	Atom	Angle/°	Atom	Atom	Atom	Angle/°
N1[1]	Hg1	N1	180.0	C2	S3	C1	93.3(2)
N1[1]	Hg1	Cl1	90.57(8)	S1	C3	S4	119.8(3)
N1	Hg1	Cl1	89.42(8)	C2	C3	S1	122.7(3)
N1[1]	Hg1	Cl1[1]	89.43(8)	C2	C3	S4	117.4(3)
N1	Hg1	Cl1[1]	90.57(8)	C5	C4	S2	123.3(3)
N1	Hg1	N2[2]	96.65(13)	C5	C4	C11	125.7(3)
N1[1]	Hg1	N2[2]	83.35(13)	C11	C4	S2	110.7(3)
N1[1]	Hg1	N2[3]	96.65(13)	C3	S4	C1	93.4(2)
N1	Hg1	N2[3]	83.35(13)	C4	C5	S1	121.9(3)
Cl1	Hg1	Cl1[1]	180.00(4)	C4	C5	C6	124.9(3)
Cl1[1]	Hg1	N2[2]	90.59(8)	C6	C5	S1	113.2(3)

Bond Angles

Atom	Atom	Atom	Angle/°	Atom	Atom	Atom	Angle/°
Cl1	Hg1	N2[2]	89.41(8)	C7	C6	C5	121.5(3)
Cl1[1]	Hg1	N2[3]	89.41(8)	C7	C6	C10	117.5(4)
Cl1	Hg1	N2[3]	90.59(8)	C10	C6	C5	121.0(3)
N2[2]	Hg1	N2[3]	180.00(13)	C8	C7	C6	120.1(4)
C3	S1	C5	101.23(18)	N2	C8	C7	122.4(4)
C13	N1	Hg1	122.9(3)	N2	C9	C10	124.2(3)
C13	N1	C14	118.0(3)	C9	C10	C6	118.4(4)
C14	N1	Hg1	118.4(3)	C12	C11	C4	119.9(3)
C1[4]	C1	S3	123.8(4)	C15	C11	C4	121.5(3)
C1[4]	C1	S4	122.3(4)	C15	C11	C12	118.3(3)
S3	C1	S4	114.0(3)	C13	C12	C11	118.4(4)
S2	C2	S3	118.5(2)	N1	C13	C12	123.5(4)
C3	C2	S2	123.9(3)	N1	C14	C15	122.6(4)
C3	C2	S3	117.5(3)	C11	C15	C14	119.2(4)
C2	S2	C4	101.99(19)	C17	O8	C17[6]	180.0
C8	N2	Hg1[5]	119.4(3)	O8	C17	Cl5A[7]	169.4(10)
C9	N2	Hg1[5]	123.2(3)	Cl4	C16A	Cl5A	114.2(4)
C9	N2	C8	117.4(3)	Cl5B	C16B	Cl4	106.3(5)

[1]1-X,-Y,1-Z; [2]1-X,1-Y,1-Z; [3]+X,-1+Y,+Z; [4]2-X,1-Y,-Z; [5]+X,1+Y,+Z; [6]2-X,1-Y,1-Z; [7]1+X,+Y,+Z

BVDT-TTF-Py$_4$ -CuCl$_2$



Empirical formula	$C_{16}H_9Cl_4Cu_{0.5}N_2S_4$
Formula weight	531.06
Temperature/K	288(14)
Crystal system	monoclinic
Space group	$P2_1/c$
a/Å	12.7692(6)
b/Å	9.5235(5)
c/Å	16.6155(8)
α/°	90
β/°	90.673(4)
γ/°	90
Volume/Å^3	2020.43(17)
Z	4
ρ_{calc} /g·cm^{-3}	1.746
μ/mm^{-1}	9.773
F(000)	1062.0
Crystal size/mm^3	0.1 × 0.05 × 0.04
Radiation	CuKα (λ = 1.54184)
2Θ range for data collection/°	6.922 to 144.362
Completeness to theta = 135.4°/%	98.6
Index ranges	-15 ≤ h ≤ 15, -11 ≤ k ≤ 11, -20 ≤ l ≤ 20
Reflections collected	8362
Independent reflections	3819 [R_{int} = 0.0359, R_{sigma} = 0.0435]
Data/restraints/parameters	3819/0/241
Goodness-of-fit on F^2	1.026
Final R indexes [I>=2σ (I)]	R_1 = 0.0435, wR_2 = 0.1109
Final R indexes [all data]	R_1 = 0.0631, wR_2 = 0.1241
Largest diff. peak/hole / e Å^{-3}	0.62/-0.47

Bond Lengths

Atom	Atom	Length/Å	Atom	Atom	Length/Å
Cu1	N1[1]	2.062(3)	N1	C14	1.344(5)
Cu1	N1	2.062(3)	N2	C9	1.328(5)
Cu1	N2[2]	2.085(3)	N2	C8	1.317(5)
Cu1	N2[3]	2.085(3)	C5	C6	1.488(4)
S2	C2	1.755(3)	C5	C4	1.322(5)
S2	C1	1.764(4)	C6	C7	1.369(5)
S3	C4	1.788(3)	C6	C10	1.368(5)
S3	C3	1.747(3)	C4	C11	1.483(4)
S4	C5	1.772(3)	C3	C2	1.325(5)
S4	C2	1.744(3)	C11	C15	1.387(5)
S1	C3	1.755(3)	C11	C12	1.385(5)
S1	C1	1.755(4)	C1	C1[4]	1.338(6)
Cl3	C16	1.769(8)	C15	C14	1.377(5)
Cl1	C16	1.766(8)	C12	C13	1.385(5)
Cl2	C16	1.729(6)	C7	C8	1.387(5)
N1	C13	1.331(5)	C9	C10	1.387(5)

[1]1-X,-Y,1-Z; [2]1-X,1-Y,1-Z; [3]+X,-1+Y,+Z; [4]2-X,1-Y,2-Z

Bond Angles

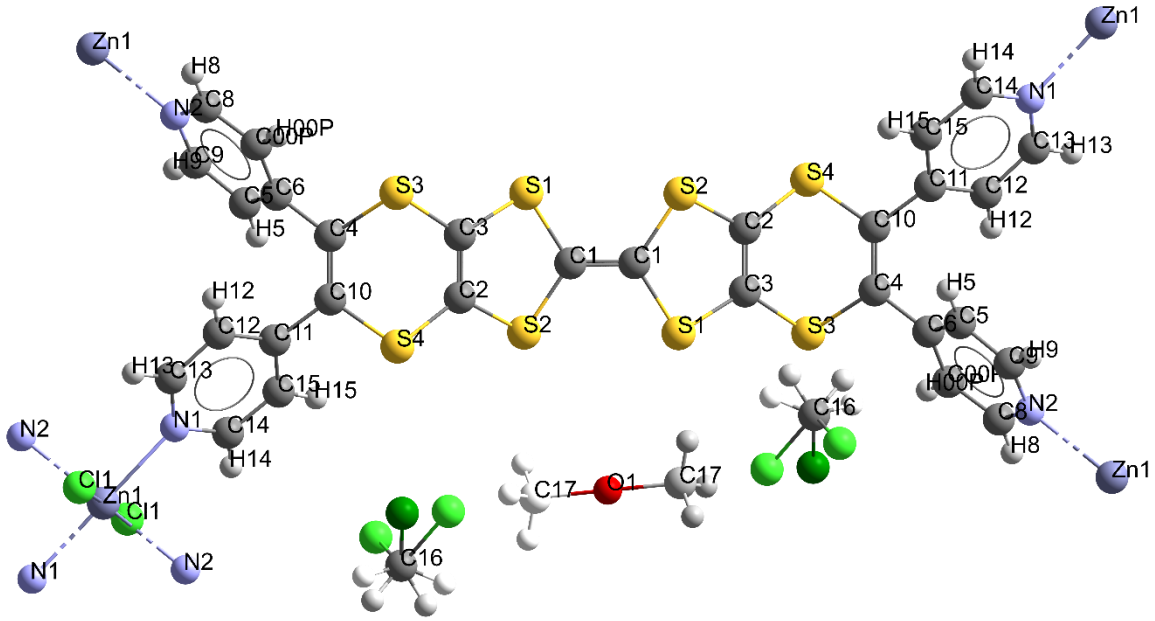
Atom	Atom	Atom	Angle/˚	Atom	Atom	Atom	Angle/˚
N1[1]	Cu1	N1	180.0	C11	C4	S3	111.9(2)
N1[1]	Cu1	N2[2]	88.43(10)	S3	C3	S1	118.5(2)
N1[1]	Cu1	N2[3]	91.57(10)	C2	C3	S3	124.0(2)
N1	Cu1	N2[2]	91.57(10)	C2	C3	S1	117.3(2)
N1	Cu1	N2[3]	88.43(10)	C15	C11	C4	120.2(3)
N2[2]	Cu1	N2[3]	180.0	C12	C11	C4	122.6(3)
C2	S2	C1	93.64(16)	C12	C11	C15	117.2(3)
C3	S3	C4	101.92(15)	S4	C2	S2	117.8(2)
C2	S4	C5	101.70(15)	C3	C2	S2	117.8(2)

Bond Angles

Atom	Atom	Atom	Angle/°	Atom	Atom	Atom	Angle/°
C1	S1	C3	94.02(16)	C3	C2	S4	124.2(2)
C13	N1	Cu1	122.9(2)	S1	C1	S2	113.94(17)
C13	N1	C14	117.5(3)	C1[5]	C1	S2	122.7(4)
C14	N1	Cu1	119.6(2)	C1[5]	C1	S1	123.3(4)
C9	N2	Cu1[4]	119.8(3)	C14	C15	C11	120.1(3)
C8	N2	Cu1[4]	122.8(2)	C11	C12	C13	119.3(3)
C8	N2	C9	117.2(3)	N1	C13	C12	123.4(3)
C6	C5	S4	109.7(2)	N1	C14	C15	122.5(3)
C4	C5	S4	124.2(2)	C6	C7	C8	119.2(4)
C4	C5	C6	125.8(3)	N2	C9	C10	123.0(4)
C7	C6	C5	119.6(3)	C6	C10	C9	119.4(4)
C10	C6	C5	122.4(3)	N2	C8	C7	123.4(4)
C10	C6	C7	117.8(3)	Cl1	C16	Cl3	110.7(3)
C5	C4	S3	122.6(2)	Cl2	C16	Cl3	108.5(4)
C5	C4	C11	125.5(3)	Cl2	C16	Cl1	112.3(4)

[1]1-X,-Y,1-Z; [2]1-X,1-Y,1-Z; [3]+X,-1+Y,+Z; [4]+X,1+Y,+Z; [5]2-X,1-Y,2-Z

BVDT-TTF-Py_4 -$ZnCl_2$



Empirical formula	$C_{16.25}H_{10.75}Cl_3N_2O_{0.25}S_4Zn_{0.5}$
Formula weight	505.29
Temperature/K	150.00(10)
Crystal system	monoclinic
Space group	$P2_1/c$
a/Å	12.8519(2)
b/Å	9.6095(2)
c/Å	15.9424(3)
α/°	90
β/°	94.469(2)
γ/°	90
Volume/Å^3	1962.91(6)
Z	4
ρ_{calc}/g·cm^{-3}	1.710
μ/mm^{-1}	8.892
F(000)	1017.0
Crystal size/mm^3	0.25 × 0.1 × 0.09
Radiation	CuKα (λ = 1.54184)
2Θ range for data collection/°	6.898 to 144.016
Completeness to theta = 135.4°/%	99.9
Index ranges	-15 ≤ h ≤ 15, -11 ≤ k ≤ 11, -19 ≤ l ≤ 17
Reflections collected	8295
Independent reflections	3780 [R_{int} = 0.0287, R_{sigma} = 0.0353]
Data/restraints/parameters	3780/12/257
Goodness-of-fit on F^2	1.046
Final R indexes [I>=2σ (I)]	R_1 = 0.0440, wR_2 = 0.1149
Final R indexes [all data]	R_1 = 0.0486, wR_2 = 0.1188
Largest diff. peak/hole / e Å^{-3}	2.13/-1.66

Bond Lengths

Atom	Atom	Length/Å	Atom	Atom	Length/Å
Zn1	Cl8[1]	2.4466(7)	N2	C9	1.340(4)
Zn1	Cl8	2.4466(7)	N2	C8	1.339(4)
Zn1	N1[1]	2.193(3)	C11	C10	1.481(4)
Zn1	N1	2.193(3)	C11	C12	1.394(4)
Zn1	N2[2]	2.290(3)	C11	C15	1.395(5)
Zn1	N2[3]	2.290(3)	C6	C4	1.480(4)
S3	C4	1.789(3)	C6	C5	1.390(5)
S3	C3	1.746(3)	C6	C00P	1.396(5)
S4	C10	1.772(3)	C4	C10	1.338(5)
S4	C2	1.742(3)	C9	C5	1.389(5)
S2	C1	1.756(3)	C3	C2	1.329(5)
S2	C2	1.754(3)	C13	C12	1.386(5)
S1	C3	1.763(3)	C1	C1[4]	1.351(6)
S1	C1	1.763(3)	C15	C14	1.377(5)
Cl07	C16	1.745(5)	C8	C00P	1.384(5)
Cl9	C16	1.747(5)	C16	Cl1	1.548(8)
N1	C13	1.338(4)	C17	O1	1.578(14)
N1	C14	1.344(4)			

[1]1-X,-Y,1-Z; [2]+X,-1+Y,+Z; [3]1-X,1-Y,1-Z; [4]2-X,1-Y,-Z

Bond Angles

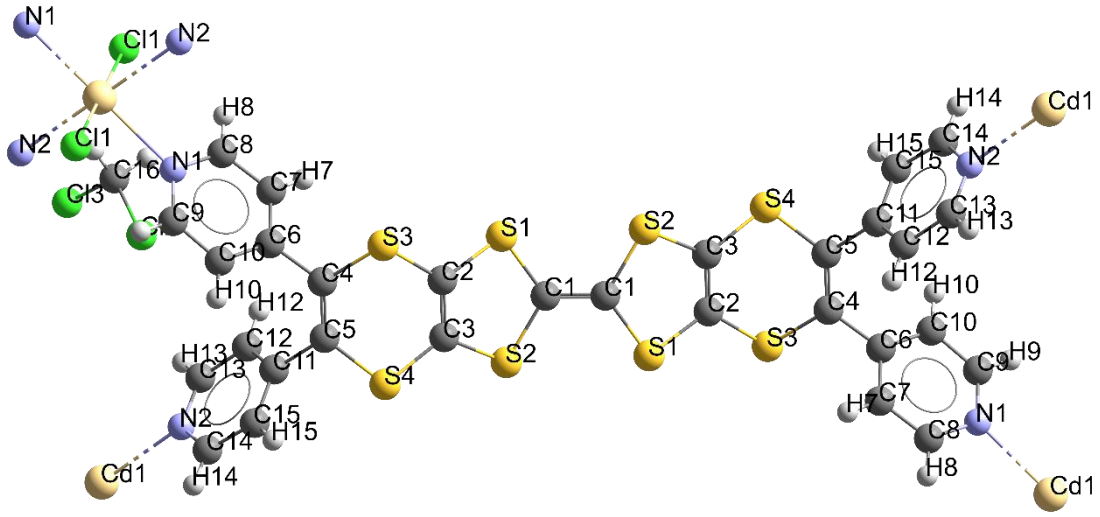
Atom	Atom	Atom	Angle/°	Atom	Atom	Atom	Angle/°
Cl8[1]	Zn1	Cl8	180.0	C5	C6	C00P	117.1(3)
N1[1]	Zn1	Cl8[1]	89.98(7)	C00P	C6	C4	121.2(3)
N1	Zn1	Cl8[1]	90.02(7)	C6	C4	S3	113.6(2)
N1	Zn1	Cl8	89.98(7)	C10	C4	S3	121.8(2)
N1[1]	Zn1	Cl8	90.02(7)	C10	C4	C6	124.6(3)
N1[1]	Zn1	N1	180.0	C11	C10	S4	110.4(2)
N1[1]	Zn1	N2[2]	85.28(10)	C4	C10	S4	123.0(2)
N1[1]	Zn1	N2[3]	94.72(10)	C4	C10	C11	126.3(3)
N1	Zn1	N2[3]	85.28(10)	N2	C9	C5	123.8(3)
N1	Zn1	N2[2]	94.72(10)	S3	C3	S1	119.61(19)
N2[2]	Zn1	Cl8[1]	89.65(7)	C2	C3	S3	123.4(2)
N2[2]	Zn1	Cl8	90.35(7)	C2	C3	S1	116.9(2)
N2[3]	Zn1	Cl8[1]	90.35(7)	N1	C13	C12	123.6(3)

Bond Angles

Atom	Atom	Atom	Angle/°	Atom	Atom	Atom	Angle/°
N2[3]	Zn1	Cl8	89.65(7)	S2	C1	S1	114.37(18)
N2[2]	Zn1	N2[3]	180.00(11)	C1[5]	C1	S2	123.4(4)
C3	S3	C4	101.08(15)	C1[5]	C1	S1	122.3(4)
C2	S4	C10	101.81(15)	C13	C12	C11	119.0(3)
C2	S2	C1	92.77(15)	C14	C15	C11	119.5(3)
C3	S1	C1	93.04(15)	N1	C14	C15	123.3(3)
C13	N1	Zn1	123.4(2)	C9	C5	C6	119.2(3)
C13	N1	C14	117.1(3)	S4	C2	S2	118.33(19)
C14	N1	Zn1	119.2(2)	C3	C2	S4	123.4(2)
C9	N2	Zn1[4]	123.6(2)	C3	C2	S2	118.2(2)
C8	N2	Zn1[4]	119.6(2)	N2	C8	C00P	123.4(3)
C8	N2	C9	116.8(3)	C8	C00P	C6	119.7(3)
C12	C11	C10	120.4(3)	Cl07	C16	Cl9	113.1(3)
C12	C11	C15	117.5(3)	Cl1	C16	Cl07	112.5(4)
C15	C11	C10	121.6(3)	C17	O1	C17[6]	180.0
C5	C6	C4	121.6(3)				

[1]1-X,-Y,1-Z; [2]1-X,1-Y,1-Z; [3]+X,-1+Y,+Z; [4]+X,1+Y,+Z; [5]2-X,1-Y,-Z; [6]2-X,1-Y,1-Z

BVDT-TTF-Py_4 -$CdCl_2$



Empirical formula	$C_{16}H_{10}Cd_{0.5}Cl_3N_2S_4$
Formula weight	521.05
Temperature/K	293(2)
Crystal system	monoclinic
Space group	$P2_1/c$
a/Å	13.1301(15)
b/Å	9.5611(10)
c/Å	16.1205(12)
α/°	90
β/°	94.781(8)
γ/°	90
Volume/$Å^3$	2016.7(3)
Z	4
$\rho_{calc}/g \cdot cm^{-3}$	1.716
μ/mm^{-1}	12.127
F(000)	1036.0
Crystal size/mm^3	0.154 × 0.086 × 0.067
Radiation	CuKα (λ = 1.54184)
2Θ range for data collection/°	6.756 to 134.132
Completeness to theta = 134.1°/%	97.0
Index ranges	-15 ≤ h ≤ 13, -11 ≤ k ≤ 9, -19 ≤ l ≤ 19
Reflections collected	6561
Independent reflections	3501 [R_{int} = 0.0888, R_{sigma} = 0.1246]
Data/restraints/parameters	3501/0/232
Goodness-of-fit on F^2	1.065
Final R indexes [I>=2σ (I)]	R_1 = 0.1091, wR_2 = 0.2851
Final R indexes [all data]	R_1 = 0.1647, wR_2 = 0.3488
Largest diff. peak/hole / e $Å^{-3}$	3.62/-1.30

Bond Length

Atom	Atom	Length/Å	Atom	Atom	Length/Å
Cd1	Cl1[1]	2.563(3)	N2	C13	1.280(18)
Cd1	Cl1	2.563(3)	Cl3	C16	1.73(5)
Cd1	N1	2.374(12)	C5	C11	1.52(2)
Cd1	N1[1]	2.374(12)	C5	C4	1.34(2)
Cd1	N2[2]	2.443(10)	C11	C12	1.35(2)
Cd1	N2[3]	2.443(10)	C11	C15	1.38(2)
S3	C4	1.757(13)	C4	C6	1.481(19)
S3	C2	1.761(15)	Cl2	C16	1.76(4)
S4	C5	1.765(14)	C3	C2	1.33(2)
S4	C3	1.744(13)	C6	C10	1.38(2)
S1	C2	1.747(14)	C6	C7	1.36(2)
S1	C1	1.727(19)	C8	C7	1.41(2)
S2	C3	1.733(13)	C12	C13	1.41(2)
S2	C1	1.775(16)	C9	C10	1.40(2)
N1	C8	1.339(18)	C14	C15	1.38(2)
N1	C9	1.31(2)	C1	C1[4]	1.36(3)
N2	C14	1.35(2)			

[1]1-X,2-Y,1-Z; [2]+X,1+Y,+Z; [3]1-X,1-Y,1-Z; [4]2-X,1-Y,-Z

Bond Angles

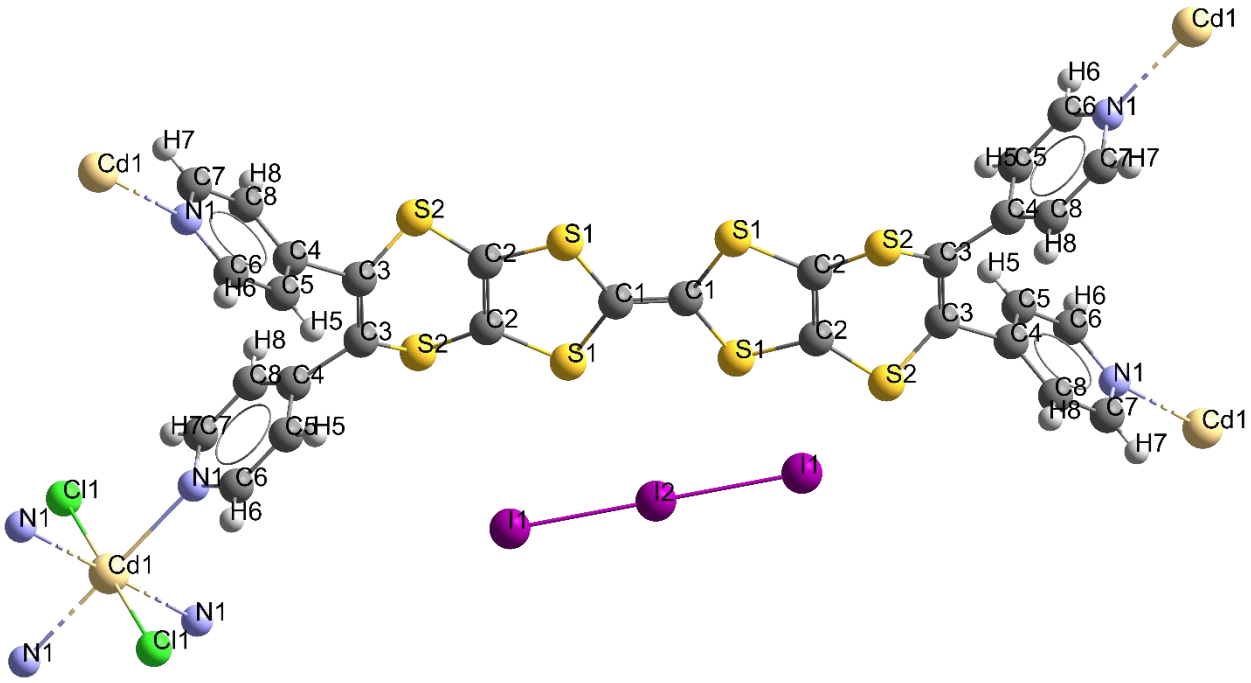
Atom	Atom	Atom	Angle/°	Atom	Atom	Atom	Angle/°
Cl1[1]	Cd1	Cl1	180.0	C12	C11	C5	122.0(13)
N1[1]	Cd1	Cl1[1]	90.6(3)	C12	C11	C15	118.5(14)
N1	Cd1	Cl1[1]	89.4(3)	C15	C11	C5	119.5(14)
N1	Cd1	Cl1	90.6(3)	C5	C4	S3	122.4(10)
N1[1]	Cd1	Cl1	89.4(3)	C5	C4	C6	125.4(12)
N1[1]	Cd1	N1	180.0	C6	C4	S3	112.2(10)
N1	Cd1	N2[2]	84.8(4)	S2	C3	S4	120.9(9)
N1[1]	Cd1	N2[2]	95.2(4)	C2	C3	S4	122.6(10)
N1	Cd1	N2[3]	95.2(4)	C2	C3	S2	116.4(10)

Bond Angles

Atom	Atom	Atom	Angle/°	Atom	Atom	Atom	Angle/°
N1[1]	Cd1	N2[3]	84.8(4)	C10	C6	C4	118.6(13)
N2[2]	Cd1	Cl1	89.6(3)	C7	C6	C4	121.8(12)
N2[2]	Cd1	Cl1[1]	90.4(3)	C7	C6	C10	119.6(13)
N2[3]	Cd1	Cl1[1]	89.6(3)	N1	C8	C7	122.6(15)
N2[3]	Cd1	Cl1	90.4(3)	S1	C2	S3	117.2(11)
N2[3]	Cd1	N2[2]	180.0(4)	C3	C2	S3	124.0(10)
C4	S3	C2	102.0(7)	C3	C2	S1	118.8(11)
C3	S4	C5	101.7(6)	C11	C12	C13	119.6(14)
C1	S1	C2	92.9(8)	N1	C9	C10	122.9(13)
C3	S2	C1	93.5(7)	C6	C10	C9	118.4(16)
C8	N1	Cd1	117.8(10)	N2	C14	C15	121.9(15)
C9	N1	Cd1	123.1(8)	S1	C1	S2	114.4(9)
C9	N1	C8	118.0(12)	C1[5]	C1	S1	125.9(18)
C14	N2	Cd1[4]	118.1(9)	C1[5]	C1	S2	119.7(19)
C13	N2	Cd1[4]	122.8(10)	N2	C13	C12	122.4(14)
C13	N2	C14	119.0(12)	C14	C15	C11	118.6(15)
C11	C5	S4	112.9(11)	C6	C7	C8	118.0(14)
C4	C5	S4	123.4(10)	Cl3	C16	Cl2	113.3(17)
C4	C5	C11	123.7(12)				

[1]1-X,2-Y,1-Z; [2]+X,1+Y,+Z; [3]1-X,1-Y,1-Z; [4]+X,-1+Y,+Z; [5]2-X,1-Y,-Z

(BVDT-TTF-Py$_4$) $^{\bullet+}$CdCl$_2$ I$_3^-$



Empirical formula	$C_{15}H_8Cd_{0.5}ClI_{1.5}N_2S_4$
Formula weight	626.47
Temperature/K	150.01(10)
Crystal system	monoclinic
Space group	C2/m
a/Å	16.216(6)
b/Å	9.725(3)
c/Å	12.885(5)
α/°	90
β/°	94.80(3)
γ/°	90
Volume/Å^3	2024.8(12)
Z	4
ρ_{calc}/g·cm^{-3}	2.055
μ/mm^{-1}	27.582
F(000)	1186.0
Crystal size/mm^3	0.1 × 0.08 × 0.05
Radiation	Cu Kα (λ = 1.54184)
2Θ range for data collection/°	10.618 to 100.87
Completeness to theta = 100.9°/%	98.0
Index ranges	-9 ≤ h ≤ 16, -8 ≤ k ≤ 9, -12 ≤ l ≤ 12
Reflections collected	1934
Independent reflections	1124 [R_{int} = 0.1519, R_{sigma} = 0.1847]
Data/restraints/parameters	1124/130/106
Goodness-of-fit on F^2	1.800
Final R indexes [I>=2σ (I)]	R_1 = 0.2114, wR_2 = 0.5038
Final R indexes [all data]	R_1 = 0.2265, wR_2 = 0.5198
Largest diff. peak/hole / e Å^{-3}	5.54/-1.94

Bond Length

Atom	Atom	Length/Å	Atom	Atom	Length/Å
I1	I2	2.938(6)	S2	C3	1.60(4)
Cl1	Cd1	2.583(15)	C2	C2[5]	1.59(9)
Cd1	N1[1]	2.42(5)	C3	C3[5]	1.48(10)
Cd1	N1[2]	2.42(2)	C3	C4	1.56(5)
Cd1	N1	2.42(2)	C6	C5	1.3900
Cd1	N1[3]	2.42(5)	C6	N1	1.3900
S1	C1	1.73(3)	C5	C4	1.3900
S1	C2	1.72(4)	C4	C8	1.3900
C1	C1[4]	1.36(11)	C8	C7	1.3900
S2	C2	1.62(5)	C7	N1	1.3900

[1]+X,1-Y,+Z; [2]2-X,1-Y,1-Z; [3]2-X,+Y,1-Z; [4]1-X,2-Y,2-Z; [5]+X,2-Y,+Z

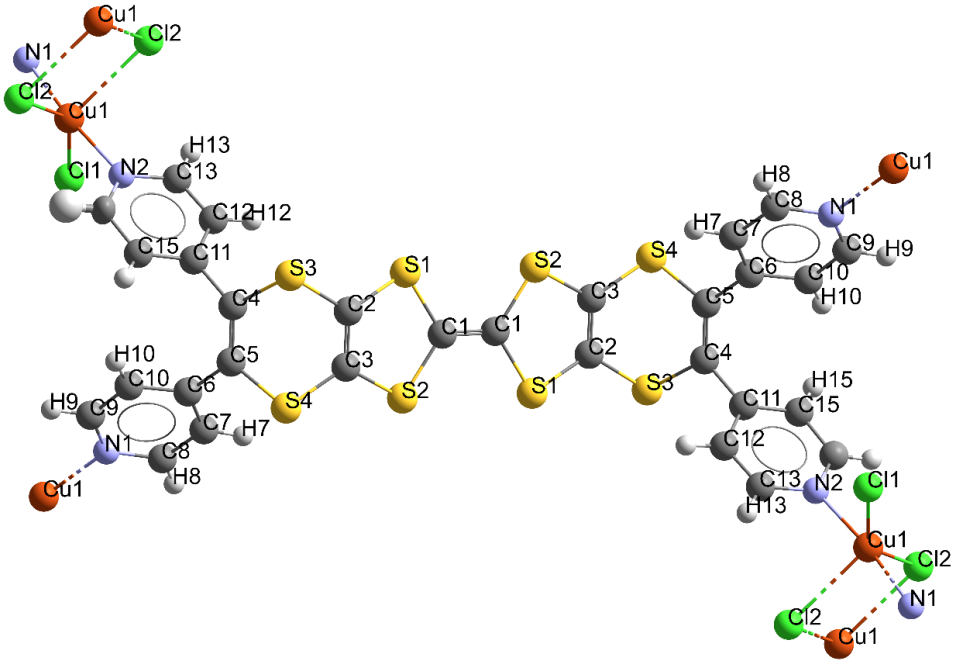
Bond Angle

Atom	Atom	Atom	Angle/°	Atom	Atom	Atom	Angle/°
Cl1	Cd1	Cl1[1]	180.0	I1	I2	I1[6]	180.0
N1[2]	Cd1	Cl1[1]	90(2)	C3	S2	C2	100(2)
N1[1]	Cd1	Cl1	90(2)	S2	C2	S1	127(3)
N1[3]	Cd1	Cl1[1]	90(2)	C2[4]	C2	S1	112.3(16)
N1	Cd1	Cl1	90.2(6)	C2[4]	C2	S2	121.0(16)
N1[2]	Cd1	Cl1	90(2)	C3[4]	C3	S2	124(2)
N1[3]	Cd1	Cl1	90(2)	C3[4]	C3	C4	119(2)
N1[1]	Cd1	Cl1[1]	90(2)	C4	C3	S2	114(4)
N1	Cd1	Cl1[1]	89.8(6)	C5	C6	N1	120.0
N1	Cd1	N1[2]	95(2)	C6	C5	C4	120.0
N1	Cd1	N1[3]	85(2)	C5	C4	C3	112(3)
N1[1]	Cd1	N1[2]	85(5)	C8	C4	C3	127(3)

Atom	Atom	Atom	Angle/°	Atom	Atom	Atom	Angle/°
N1[1]	Cd1	N1[3]	95(5)	C8	C4	C5	120.0
N1	Cd1	N1[1]	180(3)	C4	C8	C7	120.0
N1[3]	Cd1	N1[2]	180(5)	N1	C7	C8	120.0
C2	S1	C1	100(2)	C6	N1	Cd1	125.1(13)
S1	C1	S1[4]	114(3)	C7	N1	Cd1	114.8(13)
C1[5]	C1	S1[4]	123.1(15)	C7	N1	C6	120.0
C1[5]	C1	S1	123.1(15)				

[1]2-X,1-Y,1-Z; [2]2-X,+Y,1-Z; [3]+X,1-Y,+Z; [4]+X,2-Y,+Z; [5]1-X,2-Y,2-Z; [6]1-X,1-Y,2-Z

BVDT-TTF-Py$_4$-[CuCl$_2$]$_2$



Empirical formula	$C_{17.14}H_{9.14}Cl_{2.29}Cu_{1.14}N_{2.29}S_{4.57}$
Formula weight	547.33
Temperature/K	230.00(10)
Crystal system	monoclinic
Space group	I2/a
a/Å	8.9751(7)
b/Å	17.3241(15)
c/Å	38.861(3)
α/°	90
β/°	90.014(7)
γ/°	90
Volume/Å^3	6042.4(9)
Z	7
ρ_{calc}/g·cm^{-3}	1.053
μ/mm^{-1}	5.234
F(000)	1912.0
Crystal size/mm^3	0.25 × 0.14 × 0.12
Radiation	Cu Kα (λ = 1.54184)
2Θ range for data collection/°	5.586 to 100.858
Completeness to theta = 100.9°/%	97.2
Index ranges	-8 ≤ h ≤ 6, -16 ≤ k ≤ 17, -38 ≤ l ≤ 36
Reflections collected	7264
Independent reflections	3073 [R_{int} = 0.0558, R_{sigma} = 0.0699]
Data/restraints/parameters	3073/0/217
Goodness-of-fit on F^2	1.054
Final R indexes [I>=2σ (I)]	R_1 = 0.0669, wR_2 = 0.1830
Final R indexes [all data]	R_1 = 0.0764, wR_2 = 0.1909
Largest diff. peak/hole / e Å^{-3}	0.79/-0.42

Bond Lenght

Atom	Atom	Length/Å	Atom	Atom	Length/Å
Cu1	Cl2[1]	2.625(2)	N2	C14	1.306(10)
Cu1	Cl2	2.354(2)	N2	C13	1.360(10)
Cu1	Cl1	2.252(2)	C4	C11	1.494(11)
Cu1	N1[2]	2.016(6)	C4	C5	1.344(10)
Cu1	N2	2.018(6)	C11	C12	1.388(10)
S3	C4	1.780(7)	C11	C15	1.384(10)
S3	C2	1.748(7)	C12	C13	1.351(11)
S4	C5	1.798(7)	C6	C5	1.473(11)
S4	C3	1.730(8)	C6	C7	1.390(11)
S1	C2	1.752(7)	C6	C10	1.396(11)
S1	C1	1.772(8)	C15	C14	1.393(11)
S2	C3	1.781(7)	C2	C3	1.320(11)
S2	C1	1.760(8)	C1	C1[3]	1.336(15)
N1	C9	1.311(10)	C7	C8	1.394(11)
N1	C8	1.336(10)	C9	C10	1.371(11)

[1]3/2-X,1/2-Y,3/2-Z; [2]1-X,-1/2+Y,3/2-Z; [3]1-X,1-Y,1-Z

Bond Angles

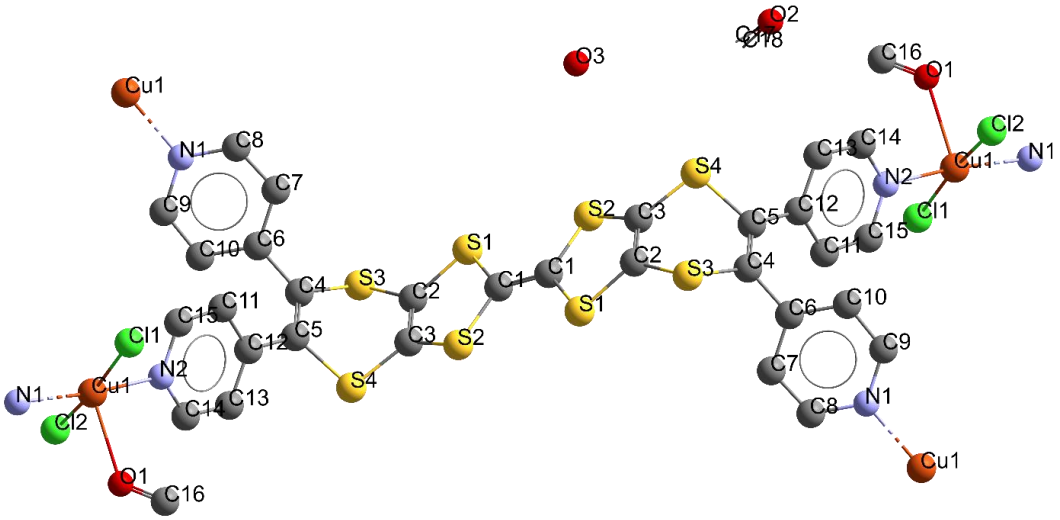
Atom	Atom	Atom	Angle/°	Atom	Atom	Atom	Angle/°
Cl2	Cu1	Cl2[1]	94.44(7)	C15	C11	C4	122.0(7)
Cl1	Cu1	Cl2	141.49(10)	C15	C11	C12	117.2(7)
Cl1	Cu1	Cl2[1]	123.95(9)	C13	C12	C11	119.8(7)
N1[2]	Cu1	Cl2	94.63(18)	C7	C6	C5	121.2(6)
N1[2]	Cu1	Cl2[1]	88.5(2)	C7	C6	C10	115.7(7)
N1[2]	Cu1	Cl1	89.76(19)	C10	C6	C5	123.1(7)
N1[2]	Cu1	N2	171.7(3)	C4	C5	S4	119.0(6)
N2	Cu1	Cl2[1]	86.90(19)	C4	C5	C6	126.7(6)
N2	Cu1	Cl2	92.61(19)	C6	C5	S4	114.3(5)
N2	Cu1	Cl1	87.06(19)	C11	C15	C14	119.9(7)
C2	S3	C4	100.1(3)	N2	C14	C15	121.5(7)

Bond Angles

Atom	Atom	Atom	Angle/°	Atom	Atom	Atom	Angle/°
C3	S4	C5	99.6(4)	C12	C13	N2	122.3(7)
Cu1	Cl2	Cu1[1]	85.56(7)	S3	C2	S1	120.3(4)
C2	S1	C1	94.1(3)	C3	C2	S3	120.1(6)
C1	S2	C3	94.3(4)	C3	C2	S1	118.9(6)
C9	N1	Cu1[3]	116.8(5)	S4	C3	S2	119.3(4)
C9	N1	C8	118.8(7)	C2	C3	S4	123.0(6)
C8	N1	Cu1[3]	124.2(6)	C2	C3	S2	116.9(6)
C14	N2	Cu1	122.1(5)	S2	C1	S1	114.6(4)
C14	N2	C13	119.0(6)	C1[4]	C1	S1	122.1(8)
C13	N2	Cu1	118.7(5)	C1[4]	C1	S2	123.2(8)
C11	C4	S3	111.0(5)	C6	C7	C8	120.3(7)
C5	C4	S3	121.3(6)	N1	C9	C10	122.9(7)
C5	C4	C11	127.5(7)	N1	C8	C7	121.7(7)
C12	C11	C4	120.7(6)	C9	C10	C6	120.7(7)

[1]3/2-X,1/2-Y,3/2-Z; [2]1-X,-1/2+Y,3/2-Z; [3]1-X,1/2+Y,3/2-Z; [4]1-X,1-Y,1-Z

BVDT-TTF-Py$_4$-(CuCl$_2$)$_2$(CH$_3$OH)$_2$



Empirical formula	$C_{40}Cl_4Cu_2N_5S_8O_{0.25}$
Formula weight	1079.81
Temperature/K	293(2)
Crystal system	monoclinic
Space group	I2/a
a/Å	8.6098(3)
b/Å	17.5168(6)
c/Å	38.8522(11)
α/°	90
β/°	91.111(3)
γ/°	90
Volume/Å^3	5858.4(3)
Z	4
ρ_{calc}/g·cm^{-3}	1.224
μ/mm^{-1}	1.043
F(000)	2124.0
Radiation	synchrotron (λ = 0.67056)
2Θ range for data collection/°	3.69 to 61.336
Completeness to theta = 47.4/%	98.6
Index ranges	-12 ≤ h ≤ 13, -15 ≤ k ≤ 23, -58 ≤ l ≤ 58
Reflections collected	41062
Independent reflections	9509 [R_{int} = 0.1679, R_{sigma} = 0.0912]
Data/restraints/parameters	9509/30/268
Goodness-of-fit on F^2	1.412
Final R indexes [I>=2σ (I)]	R_1 = 0.1432, wR_2 = 0.3820
Final R indexes [all data]	R_1 = 0.1809, wR_2 = 0.4158
Largest diff. peak/hole / e Å^{-3}	2.81/-1.67

Bond Lengths

Atom	Atom	Length/Å	Atom	Atom	Length/Å
Cu1	Cl1	2.275(3)	C6	C4	1.483(8)
Cu1	Cl2	2.211(3)	C6	C7	1.388(8)
Cu1	N2	2.005(5)	C6	C10	1.400(8)
Cu1	N1[1]	2.009(5)	C4	C5	1.327(9)
Cu1	O1	2.314(7)	C5	C12	1.468(8)
S1	C1	1.745(6)	C1	C1[2]	1.339(11)
S1	C2	1.746(6)	C12	C11	1.384(8)
S4	C5	1.787(5)	C12	C13	1.398(8)
S4	C3	1.728(6)	C2	C3	1.348(9)
S2	C1	1.772(6)	C8	C7	1.386(9)
S2	C3	1.749(6)	C10	C9	1.372(8)
S3	C4	1.789(5)	O1	C16	1.210(13)
S3	C2	1.734(6)	C15	C11	1.397(8)
N2	C15	1.343(9)	C14	C13	1.369(9)
N2	C14	1.331(9)	C17	O2	1.11(3)
N1	C8	1.345(9)	O2	C18	1.32(3)
N1	C9	1.342(8)			

[1]1-X,1/2+Y,3/2-Z; [2]1-X,1-Y,1-Z

Bond Angles

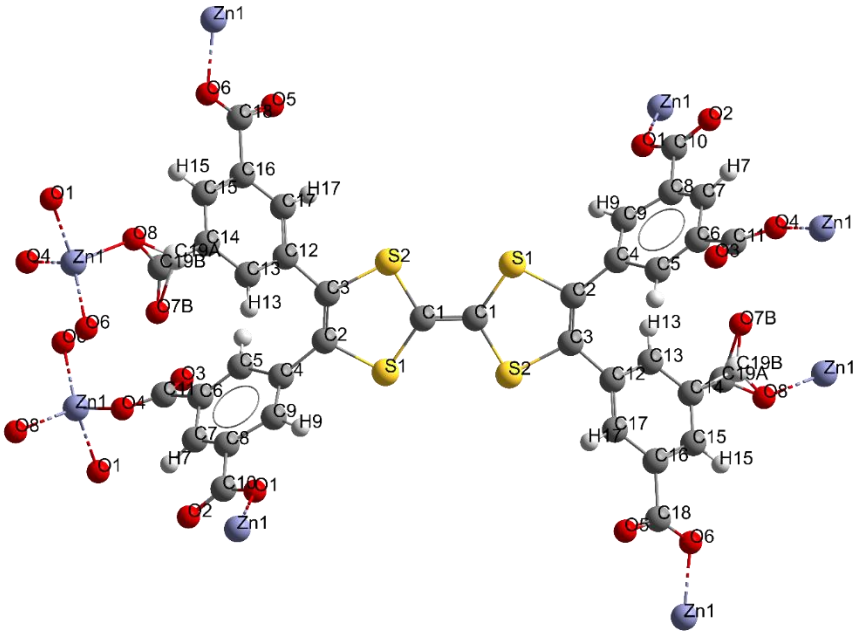
Atom	Atom	Atom	Angle/˚	Atom	Atom	Atom	Angle/˚
Cl1	Cu1	O1	100.6(3)	C5	C4	C6	127.3(5)
Cl2	Cu1	Cl1	171.66(17)	C4	C5	S4	120.7(4)
Cl2	Cu1	O1	87.4(3)	C4	C5	C12	126.9(5)
N2	Cu1	Cl1	90.51(19)	C12	C5	S4	112.4(4)
N2	Cu1	Cl2	86.43(19)	S1	C1	S2	115.2(3)
N2	Cu1	N1[1]	171.7(2)	C1[3]	C1	S1	124.0(7)
N2	Cu1	O1	94.6(2)	C1[3]	C1	S2	120.8(7)
N1[1]	Cu1	Cl1	92.68(18)	C11	C12	C5	121.9(5)
N1[1]	Cu1	Cl2	89.35(18)	C11	C12	C13	117.7(5)
N1[1]	Cu1	O1	92.4(2)	C13	C12	C5	120.4(5)

Bond Angles

Atom	Atom	Atom	Angle/°	Atom	Atom	Atom	Angle/°
C1	S1	C2	94.4(3)	S3	C2	S1	120.4(4)
C3	S4	C5	99.5(3)	C3	C2	S1	118.2(5)
C3	S2	C1	94.2(3)	C3	C2	S3	120.7(5)
C2	S3	C4	99.4(3)	N1	C8	C7	123.0(6)
C15	N2	Cu1	119.1(4)	S4	C3	S2	120.7(4)
C14	N2	Cu1	121.8(5)	C2	C3	S4	121.6(5)
C14	N2	C15	118.4(5)	C2	C3	S2	117.1(5)
C8	N1	Cu1[2]	120.4(4)	C8	C7	C6	119.1(6)
C9	N1	Cu1[2]	121.9(4)	C9	C10	C6	119.5(6)
C9	N1	C8	117.6(5)	C16	O1	Cu1	131.1(8)
C7	C6	C4	120.2(5)	N2	C15	C11	121.6(6)
C7	C6	C10	117.7(5)	C12	C11	C15	119.6(6)
C10	C6	C4	122.1(5)	N1	C9	C10	123.0(6)
C6	C4	S3	112.5(4)	N2	C14	C13	123.4(6)
C5	C4	S3	120.2(4)	C14	C13	C12	119.2(6)

[1]1-X,1/2+Y,3/2-Z; [2]1-X,-1/2+Y,3/2-Z; [3]1-X,1-Y,1-Z

Zn_2-TTFOC



Empirical formula	$C_{19}H_6O_{7.5}S_2Zn$
Formula weight	483.73
Temperature/K	210(15)
Crystal system	monoclinic
Space group	$P2_1/c$
a/Å	17.823(5)
b/Å	13.825(3)
c/Å	15.847(4)
α/°	90
β/°	109.13(3)
γ/°	90
Volume/Å^3	3688.9(17)
Z	4
ρ_{calc}/g·cm^{-3}	0.871
μ/mm^{-1}	2.193
F(000)	968.0
Radiation	Cu Kα (λ = 1.54184)
2Θ range for data collection/°	18.258 to 100.764
Completeness to theta = 100.8°/%	99.0
Index ranges	-17 ≤ h ≤ 17, -13 ≤ k ≤ 13, -15 ≤ l ≤ 10
Reflections collected	6800
Independent reflections	3783 [R_{int} = 0.1113, R_{sigma} = 0.2068]
Data/restraints/parameters	3783/89/113
Goodness-of-fit on F^2	2.025
Final R indexes [I>=2σ (I)]	R_1 = 0.3433, wR_2 = 0.6562
Final R indexes [all data]	R_1 = 0.4310, wR_2 = 0.7019
Largest diff. peak/hole / e Å^{-3}	2.21/-1.48

Bond Lenght

Atom	Atom	Length/Å	Atom	Atom	Length/Å
Zn1	O1[1]	2.00(2)	C6	C7	1.42(4)
Zn1	O4[2]	1.93(2)	C6	C11	1.56(2)
Zn1	O6[3]	1.96(2)	O6	C18	1.182(16)
Zn1	O8	1.92(2)	C7	C8	1.33(3)
O1	C10	1.178(16)	C8	C9	1.42(4)
S1	C2	1.81(4)	C8	C10	1.55(2)
S1	C1	1.756(12)	C1	C1[4]	1.367(18)
S2	C3	1.81(4)	C12	C17	1.3900
S2	C1	1.740(12)	C12	C13	1.3900
O2	C10	1.181(16)	C17	C16	1.3900
C2	C4	1.48(4)	C16	C15	1.3900
C2	C3	1.29(4)	C16	C18	1.57(2)
O4	C11	1.166(17)	C15	C14	1.3900
C4	C5	1.47(4)	C14	C13	1.3900
C4	C9	1.34(4)	C14	C19A	1.57(2)
C3	C12	1.48(4)	C14	C19B	1.56(3)
O3	C11	1.181(17)	O8	C19A	1.182(19)
C5	C6	1.32(4)	O8	C19B	1.180(17)
O5	C18	1.181(16)	C19B	O7B	1.184(17)

[1]1-X,1/2+Y,1/2-Z; [2]1-X,1-Y,-Z; [3]1-X,-1/2+Y,1/2-Z; [4]2-X,1-Y,1-Z

Bond Angles

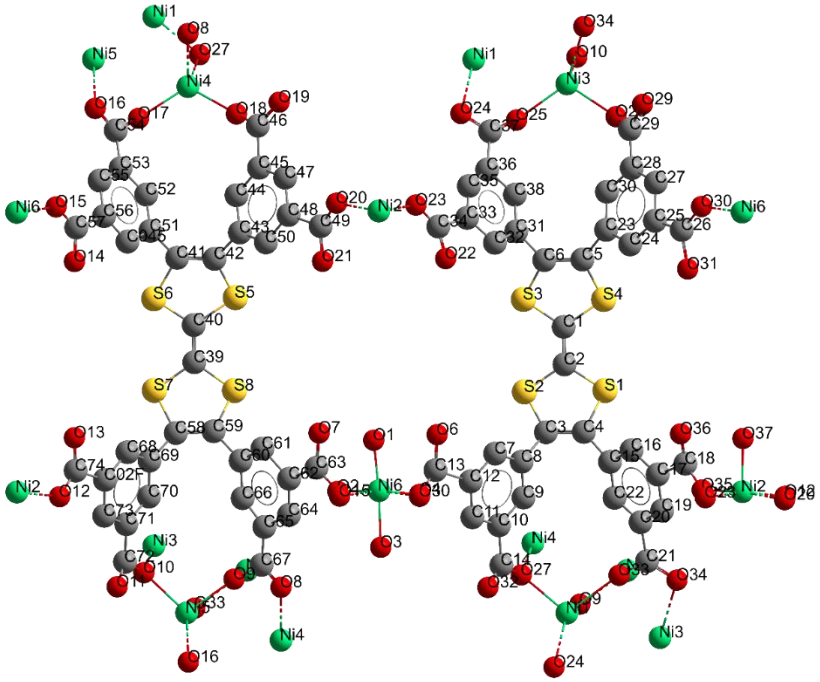
Atom	Atom	Atom	Angle/°	Atom	Atom	Atom	Angle/°
O4[1]	Zn1	O1[2]	100.0(9)	C1[4]	C1	S2	120.3(18)
O4[1]	Zn1	O6[3]	118.1(9)	O1	C10	O2	127(3)
O6[3]	Zn1	O1[2]	124.4(9)	O1	C10	C8	118(2)
O8	Zn1	O1[2]	101.2(10)	O2	C10	C8	115(2)
O8	Zn1	O4[1]	98.2(9)	O4	C11	O3	128(3)
O8	Zn1	O6[3]	110.8(10)	O4	C11	C6	115(2)
C10	O1	Zn1[3]	117.4(18)	O3	C11	C6	117(2)
C1	S1	C2	95.1(15)	C17	C12	C3	126(2)
C1	S2	C3	93.9(14)	C17	C12	C13	120.0
C4	C2	S1	112(3)	C13	C12	C3	114(2)

Bond Angles

Atom	Atom	Atom	Angle/°	Atom	Atom	Atom	Angle/°
C3	C2	S1	116(3)	C12	C17	C16	120.0
C3	C2	C4	132(4)	C17	C16	C15	120.0
C11	O4	Zn1[1]	117(2)	C17	C16	C18	122.3(16)
C5	C4	C2	121(3)	C15	C16	C18	117.5(16)
C9	C4	C2	123(3)	C14	C15	C16	120.0
C9	C4	C5	116(3)	C15	C14	C13	120.0
C2	C3	S2	119(3)	C15	C14	C19A	118(2)
C2	C3	C12	129(4)	C15	C14	C19B	120.5(18)
C12	C3	S2	111(3)	C13	C14	C19A	119(2)
C6	C5	C4	122(4)	C13	C14	C19B	118.6(18)
C5	C6	C7	120(3)	C14	C13	C12	120.0
C5	C6	C11	123(3)	O5	C18	O6	132(3)
C7	C6	C11	117(2)	O5	C18	C16	113(2)
C18	O6	Zn1[2]	115.5(18)	O6	C18	C16	114(2)
C8	C7	C6	119(3)	C19A	O8	Zn1	131(3)
C7	C8	C9	120(3)	C19B	O8	Zn1	121.5(19)
C7	C8	C10	123(3)	O8	C19A	C14	116(2)
C9	C8	C10	115(3)	O8	C19B	C14	117(2)
C4	C9	C8	121(3)	O8	C19B	O7B	130(3)
S2	C1	S1	115.0(8)	O7B	C19B	C14	114(2)
C1[4]	C1	S1	124.3(18)				

[1]1-X,1-Y,-Z; [2]1-X,1/2+Y,1/2-Z; [3]1-X,-1/2+Y,1/2-Z; [4]2-X,1-Y,1-Z

Ni_3-TTFOC



Empirical formula	$C_{15.2}HO_{6.73}S_{1.6}Ni_{1.33}N$
Formula weight	419.76
Temperature/K	220.00(10)
Crystal system	triclinic
Space group	P-1
a/Å	18.7428(17)
b/Å	19.9818(17)
c/Å	20.6304(16)
α/°	76.768(7)
β/°	81.721(7)
γ/°	88.602(7)
Volume/Å^3	7442.6(11)
Z	10
ρ_{calc}/g·cm^{-3}	0.937
μ/mm^{-1}	2.379
F(000)	2080.0
Radiation	Cu Kα (λ = 1.54184)
2Θ range for data collection/°	6.556 to 72.742
Completeness to theta = 72.7°/%	98.4
Index ranges	-14 ≤ h ≤ 11, -15 ≤ k ≤ 13, -15 ≤ l ≤ 15
Reflections collected	18656
Independent reflections	6972 [R_{int} = 0.1925, R_{sigma} = 0.1955]
Data/restraints/parameters	6972/70/441
Goodness-of-fit on F^2	1.852
Final R indexes [I>=2σ (I)]	R_1 = 0.2516, wR_2 = 0.5556
Final R indexes [all data]	R_1 = 0.3005, wR_2 = 0.6091
Largest diff. peak/hole / e Å^{-3}	2.61/-1.43

Bond Lenght

Atom	Atom	Length/Å	Atom	Atom	Length/Å
Ni2	O35	2.060(19)	C20	C19	1.3900
Ni2	O23[1]	2.04(3)	C20	C21	1.59(3)
Ni2	O12[2]	2.08(2)	C19	C17	1.3900
Ni2	O37	1.88(10)	C17	C16	1.3900
Ni2	O20[1]	2.06(2)	C51	C52	1.40(5)
Ni6	O1	1.80(7)	C51	C045	1.37(5)
Ni6	O15[3]	2.00(2)	C51	C41	1.498(14)
Ni6	O2	2.07(2)	C52	C53	1.41(5)
Ni6	O30[1]	2.03(2)	C53	C55	1.50(5)
Ni6	O3	2.02(2)	C53	C54	1.45(5)
Ni6	O4	2.01(2)	C55	C56	1.34(4)
S6	C41	1.73(3)	C56	C045	1.39(5)
S6	C40	1.715(16)	C56	C57	1.63(5)
S7	C58	1.81(3)	O31	C26	1.44(4)
S7	C39	1.744(17)	C69	C68	1.3900
S3	C6	1.68(3)	C69	C70	1.3900
S3	C1	1.737(17)	C69	C58	1.419(18)
S4	C5	1.73(3)	C68	C02F	1.3900
S4	C1	1.723(17)	C02F	C73	1.3900
S8	C39	1.762(17)	C02F	C74	1.518(19)
S8	C59	1.71(2)	C73	C71	1.3900
S2	C2	1.732(17)	C71	C70	1.3900
S2	C3	1.69(3)	C8	C7	1.3900
S5	C42	1.72(2)	C8	C9	1.3900
S5	C40	1.771(16)	C8	C3	1.503(18)
S1	C4	1.75(2)	C7	C12	1.3900
S1	C2	1.718(17)	C12	C11	1.3900
O35	C18	1.27(5)	C12	C13	1.65(4)
O33	C21	1.29(3)	C11	C10	1.3900
O33	Ni1	2.30(2)	C10	C9	1.3900
O33	Ni5[4]	2.40(3)	C10	C14	1.51(3)
O27	C14	1.27(4)	C13	O6	1.28(4)

Atom	Atom	Length/Å	Atom	Atom	Length/Å
O27	Ni1	2.12(3)	C13	O4	1.19(3)
O27	Ni4^{5}	2.34(3)	O7	C63	1.30(4)
O23	C34	1.197(14)	C34	C33	1.477(19)
O9	C67	1.26(3)	C34	O22	1.194(19)
O9	Ni1^{4}	2.22(3)	C23	C24	1.3900
O9	Ni5	2.068(17)	C23	C30	1.3900
O15	C57	1.15(3)	C23	C5	1.499(17)
O2	C63	1.258(18)	C24	C25	1.3900
O12	C74	1.220(18)	C25	C27	1.3900
O17	C54	1.38(4)	C25	C26	1.41(4)
O17	Ni4	2.093(17)	C27	C28	1.3900
O10	C72	1.267(17)	C28	C30	1.3900
O10	Ni3^{5}	2.33(3)	C28	C29	1.42(3)
O10	Ni5	2.102(17)	C6	C5	1.358(18)
O30	C26	1.34(4)	C6	C31	1.504(19)
O34	C21	1.32(3)	C4	C3	1.354(18)
O34	Ni3^{6}	2.38(3)	C42	C43	1.427(17)
O13	C74	1.211(14)	C42	C41	1.334(14)
O18	C46	1.503(18)	O32	C14	1.07(4)
O18	Ni4	2.071(17)	C43	C50	1.3900
O16	C54	1.222(19)	C43	C44	1.3900
O28	C29	1.256(18)	C50	C48	1.3900
O28	Ni3	2.19(3)	C48	C47	1.3900
C72	O11	1.263(18)	C48	C49	1.493(18)
C72	C71	1.515(17)	C47	C45	1.3900
O36	C18	1.17(5)	C45	C44	1.3900
O19	C46	1.21(3)	C45	C46	1.501(14)
C60	C66	1.39(4)	C1	C2	1.350(17)
C60	C61	1.30(4)	C31	C38	1.41(4)
C60	C59	1.498(18)	C31	C32	1.39(5)
C66	C65	1.34(4)	C38	C36	1.46(5)
C65	C64	1.35(4)	C36	C35	1.39(4)
C65	C67	1.505(17)	C36	C37	1.52(4)

Atom	Atom	Length/Å	Atom	Atom	Length/Å
C64	C62	1.40(4)	C35	C33	1.21(4)
C62	C61	1.53(5)	C33	C32	1.40(5)
C62	C63	1.51(4)	C58	C59	1.356(18)
O29	C29	1.244(18)	C39	C40	1.326(13)
O8	C67	1.25(3)	C57	O14	1.22(3)
O8	Ni4[6]	2.35(4)	O25	C37	1.29(3)
C18	C17	1.498(19)	O25	Ni3	2.20(2)
C15	C22	1.3900	O24	C37	1.249(18)
C15	C16	1.3900	O24	Ni1[7]	2.40(3)
C15	C4	1.500(17)	O20	C49	1.24(3)
C22	C20	1.3900	C49	O21	1.28(4)

[1]1-X,1-Y,2-Z; [2]-1+X,+Y,1+Z; [3]2-X,1-Y,1-Z; [4]1-X,2-Y,1-Z; [5]1-X,1-Y,1-Z; [6]+X,1+Y,+Z; [7]+X,-1+Y,+Z

Bond Angles

Atom	Atom	Atom	Angle/°	Atom	Atom	Atom	Angle/°
O35	Ni2	O12[1]	91.1(8)	O23	C34	C33	127(4)
O35	Ni2	O20[2]	173.1(10)	O22	C34	O23	132(4)
O23[2]	Ni2	O35	95.6(9)	O22	C34	C33	101(4)
O23[2]	Ni2	O12[1]	167.8(11)	C24	C23	C30	120.0
O23[2]	Ni2	O20[2]	87.2(10)	C24	C23	C5	112.8(19)
O37	Ni2	O35	90(3)	C30	C23	C5	127.2(19)
O37	Ni2	O23[2]	95(4)	C23	C24	C25	120.0
O37	Ni2	O12[1]	95(3)	C24	C25	C27	120.0
O37	Ni2	O20[2]	96(3)	C24	C25	C26	129(2)
O20[2]	Ni2	O12[1]	85.0(9)	C27	C25	C26	111(2)
O1	Ni6	O15[3]	91(2)	C28	C27	C25	120.0
O1	Ni6	O2	87(2)	C27	C28	C30	120.0
O1	Ni6	O30[2]	99(2)	C27	C28	C29	122.6(18)
O1	Ni6	O3	176(2)	C30	C28	C29	117.3(18)
O1	Ni6	O4	99(2)	C28	C30	C23	120.0
O15[3]	Ni6	O2	90.1(8)	C5	C6	S3	116(2)
O15[3]	Ni6	O30[2]	89.7(9)	C5	C6	C31	131(2)
O15[3]	Ni6	O3	85.9(9)	C31	C6	S3	112(2)

Bond Angles

Atom	Atom	Atom	Angle/°	Atom	Atom	Atom	Angle/°
O15[3]	Ni6	O4	170.6(10)	C15	C4	S1	115.6(17)
O30[2]	Ni6	O2	173.7(9)	C3	C4	S1	113.9(16)
O3	Ni6	O2	90.3(9)	C3	C4	C15	130(2)
O3	Ni6	O30[2]	83.4(9)	C23	C5	S4	119.5(19)
O4	Ni6	O2	91.3(9)	C6	C5	S4	115.8(18)
O4	Ni6	O30[2]	87.9(9)	C6	C5	C23	124(2)
O4	Ni6	O3	84.8(10)	O12	C74	C02F	118(2)
C40	S6	C41	95.1(12)	O13	C74	O12	127(3)
C39	S7	C58	95.9(12)	O13	C74	C02F	114(2)
C6	S3	C1	97.5(12)	C43	C42	S5	115.1(18)
C1	S4	C5	96.1(11)	C41	C42	S5	114.5(19)
C59	S8	C39	95.2(12)	C41	C42	C43	130(2)
C3	S2	C2	94.8(12)	O9	C67	C65	129(3)
C42	S5	C40	95.1(11)	O8	C67	O9	116(3)
C2	S1	C4	94.3(11)	O8	C67	C65	108(3)
C18	O35	Ni2	134.4(19)	C50	C43	C42	122.9(19)
C21	O33	Ni1	155(3)	C50	C43	C44	120.0
C21	O33	Ni5[4]	112(3)	C44	C43	C42	117.0(19)
Ni1	O33	Ni5[4]	91.4(8)	C43	C50	C48	120.0
C14	O27	Ni1	127(3)	C50	C48	C49	120(2)
C14	O27	Ni4[5]	130(3)	C47	C48	C50	120.0
Ni1	O27	Ni4[5]	100.2(14)	C47	C48	C49	119.2(19)
C34	O23	Ni2[2]	132(2)	C48	C47	C45	120.0
C67	O9	Ni1[4]	104(2)	C47	C45	C46	108.0(18)
C67	O9	Ni5	151(3)	C44	C45	C47	120.0
Ni5	O9	Ni1[4]	103.6(11)	C44	C45	C46	131.3(18)
C57	O15	Ni6[3]	134(3)	C45	C44	C43	120.0
C63	O2	Ni6	137(2)	S4	C1	S3	111.2(11)
C74	O12	Ni2[6]	126.2(19)	C2	C1	S3	125.8(14)
C54	O17	Ni4	136(2)	C2	C1	S4	122.9(14)
C72	O10	Ni3[5]	131.8(19)	C38	C31	C6	122(3)

Bond Angles

Atom	Atom	Atom	Angle/°	Atom	Atom	Atom	Angle/°
C72	O10	Ni5	120(2)	C32	C31	C6	114(3)
Ni5	O10	Ni3[5]	106.1(11)	C32	C31	C38	124(3)
C26	O30	Ni6[2]	136(2)	C31	C38	C36	116(3)
C21	O34	Ni3[7]	96(2)	C38	C36	C37	109(3)
C46	O18	Ni4	142(2)	C35	C36	C38	112(3)
C29	O28	Ni3	138(2)	C35	C36	C37	139(4)
O10	C72	C71	128(3)	C33	C35	C36	133(4)
O11	C72	O10	116(2)	C35	C33	C34	118(4)
O11	C72	C71	108(2)	C35	C33	C32	117(3)
C66	C60	C59	128(3)	C32	C33	C34	125(3)
C61	C60	C66	120(3)	C31	C32	C33	116(3)
C61	C60	C59	112(3)	O2	C63	C62	122(3)
C65	C66	C60	133(3)	O2	C63	O7	117(3)
C66	C65	C64	109(3)	O7	C63	C62	121(3)
C66	C65	C67	121(3)	C51	C41	S6	110(2)
C64	C65	C67	129(3)	C42	C41	S6	119(2)
C65	C64	C62	125(3)	C42	C41	C51	128(3)
C64	C62	C61	120(3)	C69	C58	S7	114.1(19)
C64	C62	C63	122(3)	C59	C58	S7	109.6(17)
C63	C62	C61	118(3)	C59	C58	C69	136(3)
C60	C61	C62	113(3)	O19	C46	O18	114(2)
C67	O8	Ni4[7]	101(2)	O19	C46	C45	131(3)
O35	C18	C17	118(4)	C45	C46	O18	110(2)
O36	C18	O35	124(3)	O27	C14	C10	124(4)
O36	C18	C17	114(4)	O32	C14	O27	116(4)
C22	C15	C16	120.0	O32	C14	C10	120(4)
C22	C15	C4	127(2)	S7	C39	S8	108.8(11)
C16	C15	C4	113(2)	C40	C39	S7	124.2(14)
C20	C22	C15	120.0	C40	C39	S8	125.7(14)
C22	C20	C19	120.0	S1	C2	S2	112.5(11)
C22	C20	C21	117(2)	C1	C2	S2	123.5(14)

Bond Angles

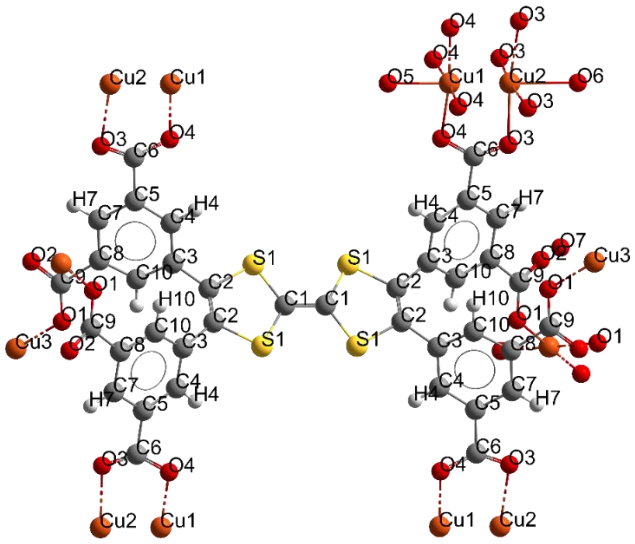
Atom	Atom	Atom	Angle/°	Atom	Atom	Atom	Angle/°
C19	C20	C21	123(2)	C1	C2	S1	124.0(13)
C20	C19	C17	120.0	O28	C29	C28	123(3)
C19	C17	C18	115(3)	O29	C29	O28	114(3)
C19	C17	C16	120.0	O29	C29	C28	123(3)
C16	C17	C18	125(3)	S6	C40	S5	113.0(11)
C17	C16	C15	120.0	C39	C40	S6	123.9(14)
C52	C51	C41	120(4)	C39	C40	S5	122.6(14)
C045	C51	C52	118(3)	C60	C59	S8	114.1(18)
C045	C51	C41	122(4)	C58	C59	S8	120.4(19)
C51	C52	C53	122(4)	C58	C59	C60	124(2)
C52	C53	C55	117(4)	O15	C57	C56	124(4)
C52	C53	C54	124(4)	O15	C57	O14	124(4)
C54	C53	C55	119(4)	O14	C57	C56	111(4)
C56	C55	C53	118(4)	C8	C3	S2	116.8(19)
C55	C56	C045	123(4)	C4	C3	S2	118.1(17)
C55	C56	C57	114(3)	C4	C3	C8	122(2)
C045	C56	C57	123(3)	C37	O25	Ni3	143(2)
C51	C045	C56	121(3)	C37	O24	Ni1^{8}	97(2)
O33	C21	O34	125(3)	O25	C37	C36	127(3)
O33	C21	C20	118(3)	O24	C37	C36	108(3)
O34	C21	C20	116(3)	O24	C37	O25	125(3)
C68	C69	C70	120.0	C13	O4	Ni6	130(2)
C68	C69	C58	117(3)	O10^{5}	Ni3	O34^{8}	90.5(10)
C70	C69	C58	122(2)	O28	Ni3	O10^{5}	110.8(10)
C02F	C68	C69	120.0	O28	Ni3	O34^{8}	97.4(10)
C68	C02F	C73	120.0	O28	Ni3	O25	109.1(10)
C68	C02F	C74	122(2)	O25	Ni3	O10^{5}	113.1(9)
C73	C02F	C74	117(2)	O25	Ni3	O34^{8}	133.7(11)
C71	C73	C02F	120.0	O33	Ni1	O24^{7}	123.8(10)
C73	C71	C72	123(2)	O27	Ni1	O33	104.0(10)
C70	C71	C72	117(2)	O27	Ni1	O9^{4}	93.8(12)

Bond Angles

Atom	Atom	Atom	Angle/°	Atom	Atom	Atom	Angle/°
C70	C71	C73	120.0	O27	Ni1	O24[7]	111.6(12)
C71	C70	C69	120.0	O9[4]	Ni1	O33	82.1(8)
C7	C8	C9	120.0	O9[4]	Ni1	O24[7]	134.7(11)
C7	C8	C3	123(2)	O9	Ni5	O33[4]	82.9(9)
C9	C8	C3	116(2)	O9	Ni5	O10	101.4(11)
C12	C7	C8	120.0	O10	Ni5	O33[4]	85.5(10)
C7	C12	C11	120.0	O27[5]	Ni4	O8[8]	97.3(12)
C7	C12	C13	120(2)	O17	Ni4	O27[5]	118.8(11)
C11	C12	C13	120(2)	O17	Ni4	O8[8]	112.4(12)
C10	C11	C12	120.0	O18	Ni4	O27[5]	109.2(13)
C11	C10	C9	120.0	O18	Ni4	O17	114.7(12)
C11	C10	C14	118(3)	O18	Ni4	O8[8]	101.7(13)
C9	C10	C14	122(3)	O30	C26	O31	113(3)
C10	C9	C8	120.0	O30	C26	C25	129(3)
O17	C54	C53	118(3)	C25	C26	O31	118(3)
O16	C54	O17	121(4)	C49	O20	Ni2[2]	130(2)
O16	C54	C53	120(4)	O20	C49	C48	122(3)
O6	C13	C12	108(3)	O20	C49	O21	120(3)
O4	C13	C12	119(3)	O21	C49	C48	115(3)
O4	C13	O6	131(4)				

[1]-1+X,+Y,1+Z; [2]1-X,1-Y,2-Z; [3]2-X,1-Y,1-Z; [4]1-X,2-Y,1-Z; [5]1-X,1-Y,1-Z; [6]1+X,+Y,-1+Z; [7]+X,1+Y,+Z; [8]+X,-1+Y,+Z

Cu_3-TTFOC



Empirical formula	$C_{25.33}H_8Cu_2O_{12}S_{2.67}$
Formula weight	716.89
Temperature/K	220.00(10)
Crystal system	orthorhombic
Space group	Fmmm
a/Å	14.3486(15)
b/Å	25.669(3)
c/Å	36.130(3)
α/°	90
β/°	90
γ/°	90
Volume/Å^3	13307(2)
Z	12
ρ_{calc}/g·cm^{-3}	1.073
μ/mm^{-1}	2.716
F(000)	4280.0
Crystal size/mm^3	0.26 × 0.08 × 0.04
Radiation	Cu Kα (λ = 1.54184)
2Θ range for data collection/°	4.892 to 101.716
Completeness to theta = 100.8°/%	99.6
Index ranges	-8 ≤ h ≤ 14, -21 ≤ k ≤ 25, -20 ≤ l ≤ 36
Reflections collected	5471
Independent reflections	1944 [R_{int} = 0.1759, R_{sigma} = 0.2213]
Data/restraints/parameters	1944/17/71
Goodness-of-fit on F^2	1.437
Final R indexes [I>=2σ (I)]	R_1 = 0.1959, wR_2 = 0.4666
Final R indexes [all data]	R_1 = 0.2607, wR_2 = 0.5260
Largest diff. peak/hole / e Å^{-3}	1.37/-1.30

Bond Length

Atom	Atom	Length/Å	Atom	Atom	Length/Å
Cu3	O1	1.900(12)	Cu2	O6	2.30(2)
Cu3	O1[1]	1.900(12)	O1	C9	1.253(14)
Cu3	O1[2]	1.900(12)	O4	C6	1.32(2)
Cu3	O1[3]	1.900(12)	O3	C6	1.209(19)
Cu1	Cu2	2.05(2)	O2	C9	1.266(15)
Cu1	O4	1.949(15)	C7	C5	1.381(15)
Cu1	O4[4]	1.949(15)	C7	C8	1.403(16)
Cu1	O4[5]	1.949(15)	C5	C6	1.509(16)
Cu1	O4[6]	1.949(15)	C5	C4	1.397(15)
Cu1	O5	2.08(5)	C10	C3	1.353(15)
S1	C1	1.739(10)	C10	C8	1.384(15)
S1	C2	1.782(15)	C3	C4	1.376(16)
Cu2	O3[6]	2.205(15)	C3	C2	1.456(16)
Cu2	O3[4]	2.205(15)	C8	C9	1.537(16)
Cu2	O3	2.205(15)	C1	C1[7]	1.38(4)
Cu2	O3[5]	2.205(15)	C2	C2[8]	1.30(4)

[1]+X,1/2-Y,3/2-Z; [2]2-X,+Y,+Z; [3]2-X,1/2-Y,3/2-Z; [4]+X,1-Y,+Z; [5]1-X,+Y,+Z; [6]1-X,1-Y,+Z; [7]3/2-X,1/2-Y,1-Z; [8]3/2-X,1/2-Y,+Z

Bond Angles

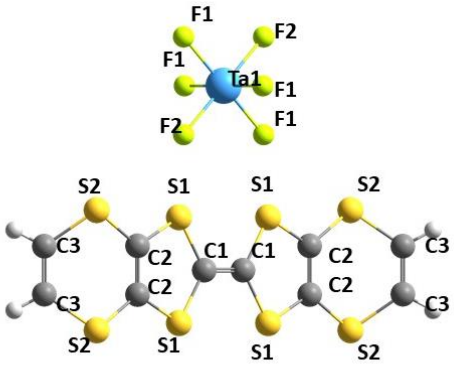
Atom	Atom	Atom	Angle/˚	Atom	Atom	Atom	Angle/˚
O1	Cu3	O1[1]	180.0(8)	O3	Cu2	O3[4]	89.7(8)
O1[1]	Cu3	O1[2]	86.3(8)	O3	Cu2	O6	86.6(7)
O1	Cu3	O1[3]	86.3(8)	O3[4]	Cu2	O6	86.6(7)
O1[3]	Cu3	O1[2]	180.0	O3[6]	Cu2	O6	86.6(7)

Bond Angles

Atom	Atom	Atom	Angle/°	Atom	Atom	Atom	Angle/°
O1	Cu3	O1[2]	93.7(8)	O3[5]	Cu2	O6	86.6(7)
O1[1]	Cu3	O1[3]	93.7(8)	C9	O1	Cu3	118.3(12)
Cu2	Cu1	O5	180.000(12)	C6	O4	Cu1	115.3(11)
O4[4]	Cu1	Cu2	93.7(5)	C6	O3	Cu2	105.2(13)
O4[5]	Cu1	Cu2	93.7(5)	C5	C7	C8	117.6(15)
O4[6]	Cu1	Cu2	93.7(5)	C7	C5	C6	117.7(13)
O4	Cu1	Cu2	93.7(5)	C7	C5	C4	120.1(15)
O4[4]	Cu1	O4[5]	86.6(9)	C4	C5	C6	122.1(14)
O4	Cu1	O4[5]	172.6(10)	C3	C10	C8	126.3(19)
O4[6]	Cu1	O4[4]	172.6(10)	C10	C3	C4	113.7(17)
O4	Cu1	O4[6]	86.6(9)	C10	C3	C2	121.2(17)
O4[6]	Cu1	O4[5]	92.9(9)	C4	C3	C2	124.8(18)
O4	Cu1	O4[4]	92.9(9)	O4	C6	C5	114.0(14)
O4	Cu1	O5	86.3(5)	O3	C6	O4	132.4(17)
O4[6]	Cu1	O5	86.3(5)	O3	C6	C5	113.5(16)
O4[5]	Cu1	O5	86.3(5)	C3	C4	C5	123.7(16)
O4[4]	Cu1	O5	86.3(5)	C7	C8	C9	122.6(14)
C1	S1	C2	94.1(9)	C10	C8	C7	118.2(16)
Cu1	Cu2	O3[5]	93.4(7)	C10	C8	C9	119.2(15)
Cu1	Cu2	O3	93.4(7)	S1	C1	S1[7]	116.2(11)
Cu1	Cu2	O3[4]	93.4(7)	C1[8]	C1	S1	121.9(6)
Cu1	Cu2	O3[6]	93.4(7)	C1[8]	C1	S1[7]	121.9(6)
Cu1	Cu2	O6	180.0	C3	C2	S1	113.2(14)
O3	Cu2	O3[6]	89.9(8)	C2[7]	C2	S1	117.2(8)
O3[4]	Cu2	O3[5]	89.9(8)	C2[7]	C2	C3	128.5(11)
O3	Cu2	O3[5]	173.2(13)	O1	C9	O2	125.0(16)
O3[6]	Cu2	O3[5]	89.7(8)	O1	C9	C8	119.7(15)
O3[4]	Cu2	O3[6]	173.2(13)	O2	C9	C8	114.8(14)

[1]2-X,1/2-Y,3/2-Z; [2]+X,1/2-Y,3/2-Z; [3]2-X,+Y,+Z; [4]+X,1-Y,+Z; [5]1-X,1-Y,+Z; [6]1-X,+Y,+Z; [7]3/2-X,1/2-Y,+Z; [8]3/2-X,1/2-Y,1-Z

(BVDT-TTF)(TaF_6)



Empirical formula	$C_{10}H_4F_6S_8Ta$
Formula weight	675.56
Temperature/K	200.00(10)
Crystal system	orthorhombic
Space group	Pnnm
a/Å	4.8259(3)
b/Å	17.8935(9)
c/Å	10.1805(5)
α/°	90
β/°	90
γ/°	90
Volume/$Å^3$	879.11(8)
Z	2
$\rho_{calc}/g\cdot cm^{-3}$	2.552
μ/mm^{-1}	20.964
F(000)	638.0
Crystal size/mm^3	0.319 × 0.095 × 0.05
Radiation	Cu Kα (λ = 1.54184)
2Θ range for data collection/°	9.886 to 143.606
Completeness to theta = 135.4°/%	99.2
Index ranges	-5 ≤ h ≤ 5, -22 ≤ k ≤ 19, -12 ≤ l ≤ 11
Reflections collected	1810
Independent reflections	883 [R_{int} = 0.0321, R_{sigma} = 0.0268]
Data/restraints/parameters	883/0/62
Goodness-of-fit on F^2	1.099
Final R indexes [I>=2σ (I)]	R_1 = 0.0393, wR_2 = 0.1129
Final R indexes [all data]	R_1 = 0.0408, wR_2 = 0.1141
Largest diff. peak/hole / e $Å^{-3}$	2.17/-1.30

Bond Length

Atom	Atom	Length/Å	Atom	Atom	Length/Å
Ta1	F1[1]	1.902(4)	S1	C2	1.737(5)
Ta1	F1	1.902(4)	S2	C2	1.748(5)
Ta1	F1[2]	1.902(4)	S2	C3	1.769(6)
Ta1	F1[3]	1.902(4)	C1	C1[4]	1.399(14)
Ta1	F2[3]	1.848(6)	C2	C2[5]	1.346(11)
Ta1	F2	1.848(6)	C3	C3[5]	1.325(13)
S1	C1	1.719(4)			

[1]+X,+Y,-Z; [2]1-X,-Y,+Z; [3]1-X,-Y,-Z; [4]-X,-Y,1-Z; [5]+X,+Y,1-Z

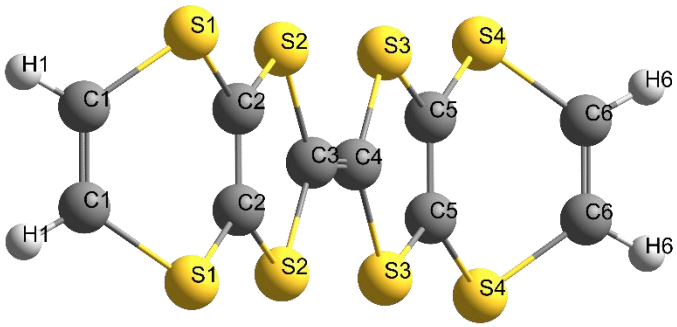
Bond Angles

Atom	Atom	Atom	Angle/°	Atom	Atom	Atom	Angle/°
F1	Ta1	F1[1]	180.0	F2[1]	Ta1	F1[3]	88.9(2)
F1	Ta1	F1[2]	90.4(2)	F2[1]	Ta1	F1[2]	91.1(2)
F1	Ta1	F1[3]	89.6(2)	F2[1]	Ta1	F2	180.0
F1[3]	Ta1	F1[2]	180.0(2)	C1	S1	C2	94.9(3)
F1[1]	Ta1	F1[2]	89.6(2)	C2	S2	C3	98.8(3)
F1[1]	Ta1	F1[3]	90.4(2)	S1	C1	S1[4]	116.2(4)
F2	Ta1	F1	88.9(2)	C1[5]	C1	S1	121.9(2)
F2[1]	Ta1	F1[1]	88.9(2)	C1[5]	C1	S1[4]	121.9(2)
F2	Ta1	F1[3]	91.1(2)	S1	C2	S2	118.7(3)
F2	Ta1	F1[2]	88.9(2)	C2[4]	C2	S1	116.92(19)
F2[1]	Ta1	F1	91.1(2)	C2[4]	C2	S2	124.31(19)
F2	Ta1	F1[1]	91.1(2)	C3[4]	C3	S2	124.3(2)

[1]1-X,-Y,-Z; [2]+X,+Y,-Z; [3]1-X,-Y,+Z; [4]+X,+Y,1-Z; [5]-X,-Y,1-Z

$(BVDT\text{-}TTF)_{2.5}(I_3)$





Empirical formula	$C_{10}H_4I_{1.2}S_8$
Formula weight	532.89
Temperature/K	200.00(10)
Crystal system	orthorhombic
Space group	Pnma
a/Å	3.777(19)
b/Å	12.18(14)
c/Å	33.1(9)
α/°	90
β/°	90
γ/°	90
Volume/Å^3	1523(44)
Z	4
ρ_{calc}/g·cm^{-3}	2.324
μ/mm^{-1}	29.814
F(000)	1022.0
Crystal size/mm^3	0.28 × 0.09 × 0.03
Radiation	Cu Kα (λ = 1.54184)
2Θ range for data collection/°	5.34 to 146.512
Completeness to theta = 135.4°/%	98.1
Index ranges	-4 ≤ h ≤ 4, -14 ≤ k ≤ 14, -39 ≤ l ≤ 35
Reflections collected	3568
Independent reflections	1518 [R_{int} = 0.0592, R_{sigma} = 0.0561]
Data/restraints/parameters	1518/15/103
Goodness-of-fit on F^2	1.131
Final R indexes [I>=2σ (I)]	R_1 = 0.0795, wR_2 = 0.2430
Final R indexes [all data]	R_1 = 0.0943, wR_2 = 0.2540
Largest diff. peak/hole / e Å^{-3}	1.26/-0.76

Bond Length

Atom	Atom	Length/Å	Atom	Atom	Length/Å
I1	I2	2.834(15)	S4	C5	1.77(3)
S2	C2	1.76(3)	S4	C6	1.77(3)
S2	C3	1.75(2)	C4	C3	1.37(4)
S3	C4	1.745(19)	C5	C5[1]	1.32(2)
S3	C5	1.76(3)	C2	C2[1]	1.32(2)
S1	C2	1.77(3)	C6	C6[1]	1.29(3)
S1	C1	1.77(3)	C1	C1[1]	1.32(3)

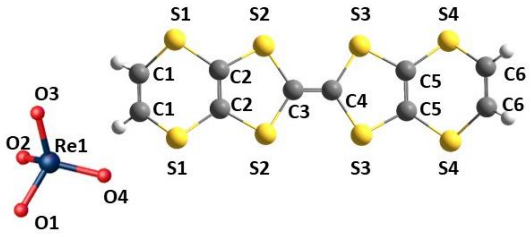
[1]+X,3/2-Y,+Z

Bond Angles

Atom	Atom	Atom	Angle/˚	Atom	Atom	Atom	Angle/˚
C3	S2	C2	95.3(13)	C5[1]	C5	S4	123.9(7)
C4	S3	C5	95.1(13)	S2	C2	S1	119.2(13)
C2	S1	C1	100.3(16)	C2[1]	C2	S2	117.4(6)
C5	S4	C6	99.7(16)	C2[1]	C2	S1	123.3(7)
S3[1]	C4	S3	114.9(15)	S2[1]	C3	S2	114.6(15)
C3	C4	S3	122.6(7)	C4	C3	S2	122.7(7)
C3	C4	S3[1]	122.6(7)	C4	C3	S2[1]	122.7(7)
S3	C5	S4	118.6(14)	C6[1]	C6	S4	124.4(7)
C5[1]	C5	S3	117.4(6)	C1[1]	C1	S1	123.3(7)

[1]+X,3/2-Y,+Z

$(BVDT\text{-}TTF)_2(ReO_4)$



Empirical formula	$C_{10}H_4O_2Re_{0.5}S_8$
Formula weight	781.05
Temperature/K	200.15
Crystal system	monoclinic
Space group	C2/m
a/Å	33.133(3)
b/Å	12.1739(14)
c/Å	3.8263(6)
α/°	90
β/°	93.360(11)
γ/°	90
Volume/Å^3	1540.7(3)
Z	4
ρ_{calc} /g·cm^{-3}	3.367
μ/mm^{-1}	37.016
F(000)	1417.0
Crystal size/mm^3	0.22 × 0.1 × 0.03
Radiation	Cu Kα (λ = 1.54184)
2Θ range for data collection/°	5.344 to 133.178
Completeness to theta = 133.2°/%	81.0
Index ranges	-39 ≤ h ≤ 28, -14 ≤ k ≤ 13, -4 ≤ l ≤ 4
Reflections collected	1714
Independent reflections	1166 [R_{int} = 0.0320, R_{sigma} = 0.0347]
Data/restraints/parameters	1166/129/131
Goodness-of-fit on F^2	1.006
Final R indexes [I>=2σ (I)]	R_1 = 0.2201, wR_2 = 0.5502
Final R indexes [all data]	R_1 = 0.2266, wR_2 = 0.5519
Largest diff. peak/hole / e Å^{-3}	2.32/-1.74

Bond Length

Atom	Atom	Length/Å	Atom	Atom	Length/Å
Re1	O4	1.70(2)	S3	C5	1.73(4)
Re1	O2	1.70(2)	C2	C2[1]	1.28(6)
Re1	O1	1.69(2)	C2	S1	1.78(3)
Re1	O3	1.70(2)	C1	C1[1]	1.26(6)
S2	C3	1.75(2)	C1	S1	1.77(3)
S2	C2	1.75(3)	S4	C6	1.77(4)
C4	S3	1.77(3)	S4	C5	1.76(3)
C4	S3[1]	1.77(3)	C6	C6[1]	1.33(9)
C4	C3	1.30(7)	C5	C5[1]	1.33(7)

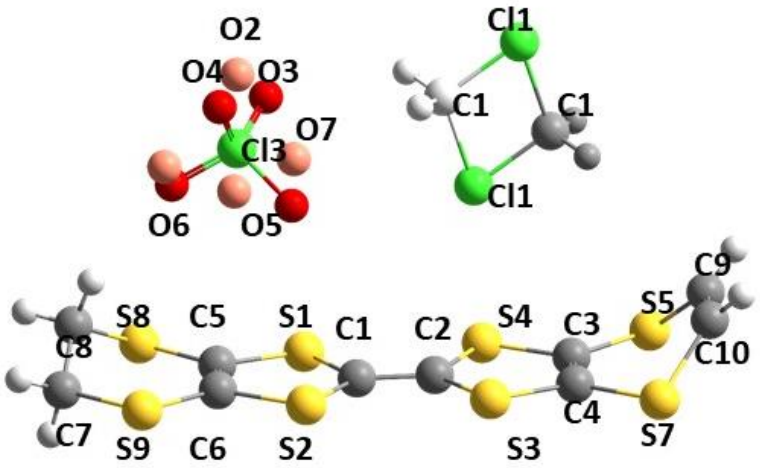
[1]+X,1-Y,+Z

Bond Angles

Atom	Atom	Atom	Angle/°	Atom	Atom	Atom	Angle/°
O4	Re1	O2	122(4)	C4	C3	S2	122.8(13)
O4	Re1	O1	106(9)	C4	C3	S2[1]	122.8(13)
O4	Re1	O3	112(8)	C2[1]	C2	S2	118.2(10)
O2	Re1	O3	102(8)	C2[1]	C2	S1	124.0(10)
O1	Re1	O2	90(10)	S1	C2	S2	117.8(17)
O1	Re1	O3	124(8)	C1[1]	C1	S1	124.9(10)
C3	S2	C2	94.5(16)	C5	S4	C6	99.2(18)
S3	C4	S3[1]	113(3)	C6[1]	C6	S4	124.4(14)
C3	C4	S3	123.5(13)	S3	C5	S4	117.6(19)
C3	C4	S3[1]	123.5(13)	C5[1]	C5	S3	117.9(11)
C5	S3	C4	95.6(17)	C5[1]	C5	S4	124.5(12)
S2[1]	C3	S2	114(2)	C2	S1	C1	97.8(15)

[1]+X,1-Y,+Z

EVT-TTF ClO_4



Empirical formula	$C_{10.5}H_7Cl_2O_4S_8$
Formula weight	524.54
Temperature/K	297.15
Crystal system	monoclinic
Space group	$P2_1/c$
a/Å	8.0005(4)
b/Å	23.8718(10)
c/Å	9.8100(5)
α/°	90
β/°	100.649(5)
γ/°	90
Volume/Å^3	1841.31(16)
Z	4
ρ_{calc}/g·cm^{-3}	1.892
μ/mm^{-1}	11.819
F(000)	1056.0
Crystal size/mm^3	0.409 × 0.27 × 0.088
Radiation	CuKα (λ = 1.54184)
2Θ range for data collection/°	7.406 to 133.174
Completeness to theta = 133.2°/%	94.6
Index ranges	-9 ≤ h ≤ 9, -18 ≤ k ≤ 26, -10 ≤ l ≤ 11
Reflections collected	6003
Independent reflections	3084 [R_{int} = 0.0325, R_{sigma} = 0.0396]
Data/restraints/parameters	3084/186/262
Goodness-of-fit on F^2	1.055
Final R indexes [I>=2σ (I)]	R_1 = 0.0570, wR_2 = 0.1564
Final R indexes [all data]	R_1 = 0.0646, wR_2 = 0.1653
Largest diff. peak/hole / e Å^{-3}	0.98/-0.94

Bond Length

Atom	Atom	Length/Å	Atom	Atom	Length/Å
S1	C5	1.742(4)	S9	C6	1.732(4)
S1	C1	1.729(5)	S9	C7	1.798(7)
C11	Cl1	1.68(2)	C3	C4	1.362(6)
C11	Cl1[1]	1.85(3)	C6	C5	1.372(6)
S4	C3	1.729(4)	C1	C2	1.382(6)
S4	C2	1.719(4)	C10	C9	1.323(8)
S3	C2	1.728(4)	C8	C7	1.493(9)
S3	C4	1.732(4)	O3	Cl2	1.412(13)
S2	C6	1.722(5)	Cl2	O4	1.392(11)
S2	C1	1.713(4)	Cl2	O5	1.433(11)
S5	C3	1.747(4)	Cl2	O6	1.351(14)
S5	C9	1.755(6)	Cl3	O1	1.422(11)
S8	C5	1.735(5)	Cl3	O2	1.411(11)
S8	C8	1.803(5)	Cl3	O7	1.428(10)
S7	C4	1.740(5)	Cl3	O8	1.353(10)
S7	C10	1.762(6)			

[1]1-X,1-Y,2-Z

Bond Angles

Atom	Atom	Atom	Angle/˚	Atom	Atom	Atom	Angle/˚
C1	S1	C5	95.3(2)	S4	C2	S3	115.9(2)
Cl1	C11	Cl1[1]	107.9(9)	C1	C2	S4	123.4(3)
C11	Cl1	C11[1]	72.1(9)	C1	C2	S3	120.6(3)
C2	S4	C3	95.2(2)	S3	C4	S7	118.8(3)
C2	S3	C4	95.1(2)	C3	C4	S3	116.6(3)
C1	S2	C6	96.3(2)	C3	C4	S7	124.5(3)
C3	S5	C9	98.7(2)	C9	C10	S7	124.3(4)
C5	S8	C8	102.4(2)	C10	C9	S5	124.4(4)
C4	S7	C10	98.7(3)	C7	C8	S8	114.4(4)
C6	S9	C7	98.1(3)	C8	C7	S9	114.1(4)

Bond Angles

Atom	Atom	Atom	Angle/°	Atom	Atom	Atom	Angle/°
S4	C3	S5	119.5(3)	O3	Cl2	O5	110.4(8)
C4	C3	S4	117.0(3)	O4	Cl2	O3	106.6(9)
C4	C3	S5	123.4(3)	O4	Cl2	O5	110.7(9)
S2	C6	S9	116.0(3)	O6	Cl2	O3	118.4(12)
C5	C6	S2	116.5(3)	O6	Cl2	O4	104.1(11)
C5	C6	S9	127.6(4)	O6	Cl2	O5	106.6(10)
S8	C5	S1	114.7(2)	O1	Cl3	O7	99.2(8)
C6	C5	S1	116.4(3)	O2	Cl3	O1	110.8(12)
C6	C5	S8	129.0(3)	O2	Cl3	O7	100.3(9)
S2	C1	S1	115.6(2)	O8	Cl3	O1	113.6(9)
C2	C1	S1	122.7(3)	O8	Cl3	O2	111.5(11)
C2	C1	S2	121.7(3)	O8	Cl3	O7	120.1(11)

[1]1- X,1-Y,2-Z

ENGAGEMENT DE NON PLAGIAT

Je, soussigné(e) Federico Solano
déclare être pleinement conscient(e) que le plagiat de documents ou d'une partie d'un document publiée sur toutes formes de support, y compris l'internet, constitue une violation des droits d'auteur ainsi qu'une fraude caractérisée.
En conséquence, je m'engage à citer toutes les sources que j'ai utilisées pour écrire ce rapport ou mémoire.

signé par l'étudiant(e) le **30** / **09** / **2023**

Présidence de l'université
40 rue de rennes – BP 73532
49035 Angers cedex
Tél. 02 41 96 23 23 | Fax 02 41 96 23 00

université angers

COLLEGE DOCTORAL PAYS DE LA LOIRE
ED MATIERE, MOLECULES MATERIAUX ET GEOSCIENCES

université angers

Titre : BVDT-TTF fonctionnalisé pour les polymères de coordination électroactifs et les conducteurs moléculaires

MOTS-CLÉS : matériaux métallo-organiques (MOFs), dérivés de TTF, conductivité, sels de transfert de charge

Résumé: Les polymères de coordination (MOFs) sont des matériaux cristallins formés par la combinaison de métaux et de ligands polytopiques. Ils sont généralement poreux mais pas ou peu conducteurs.

Les travaux décrits dans cette thèse portent sur la conception et l'étude de MOFs électroactifs. Ils visent à comprendre la relation entre leur structure et leurs propriétés électroniques, ainsi que le rôle joué par les interactions π-π dans la mobilité des porteurs de charge. Dans le cadre de notre étude, nous nous sommes particulièrement intéressés aux réseaux basés sur la structure du BVDT-TTF, qui est une structure dérivée du tétrathiafulvalène (TTF) par l'incorporation de vinylènes soufrés supplémentaires. La surface π et le nombre d'atomes de soufre plus importants confèrent en théorie aux structures obtenues une meilleure dispersion de leur bande de conduction. Ce cœur électroactif a été fonctionnalisé par des sites de coordination, puis combiné avec des métaux pour former des polymères de coordination. L'analyse structurale aux rayons X, la spectroscopie Raman et l'analyse computationnelle ont permis de comprendre les voies de transport de charge au sein de ces réseaux. Un matériau conducteur poreux serait en effet un atout majeur dans diverses applications telles que les électrodes de batteries ou de piles à combustible, ainsi que les supercondensateurs. Dans le domaine des sels à transfert de charge, nous avons exploré des variantes insaturées du BEDT-TTF : BVDT-TTF (Bis(Vinylenedithio)-Tetrathiafulvalene) et EVT-TTF (Ethylène vinylenedithiotetrathiafulvalene). Quatre nouveaux sels conducteurs ont été synthétisés et caractérisés. Ces composés présentent un comportement semi-conducteur, avec des conductivités à température ambiante comparables aux sels BEDT-TTF avec des anions similaires.

Titre: Functionalized BVDT-TTF for electro-active coordination polymers and molecular conductors

Keywords: Metal-organic frameworks (MOFs), tetrathiafulvalene derivatives, conductivity, charge salts.

Résumé: Metal-organic frameworks (MOFs) are a class of crystalline materials formed by the combination of metals and polytopic ligands. They display usually a high porosity but no conductivity. This thesis deals with the design and study of electroactive MOFs. Understanding the relation between their structure and their electronic properties, with a specific emphasis on the influential role of π-stacking interactions in charge carrier mobility, is of the outmost interest. In our study, we were particularly interested in networks based on the BVDT-TTF scaffold, which is an extension of the tetrathiafulvalene (TTF) by the incorporation of additional sulphur vinylenes. The larger π-surface and number of sulphur atoms should impart the obtained structures with a better dispersion of the conduction band. X-ray structural analysis, Raman spectroscopy and computational analysis uncovered unique pathways for charge carriers within these networks. Porous conductive materials possess a significant potential for various applications such as battery and fuel cell electrodes, as well as supercapacitors. In the domain of charge transfer salts, our research delves into unsaturated variants of BEDT-TTF: BVDT-TTF (Bis(Vinylenedithio)-Tetrathiafulvalene) and EVT-TTF (Ethylene-vinylenedithiotetrathiafulvalene). Four new conductive salts were synthetized and characterised by X-ray and Raman spectroscopy. These compounds exhibit semiconducting behaviour, with room temperature conductivities comparable to BEDT-TTF salts with similar anions, indicating exciting possibilities for further exploration in this field.